National Uranium Resource Evaluation

URANIUM IN GRANITES FROM THE SOUTHWESTERN UNITED STATES: ACTINIDE PARENT-DAUGHTER SYSTEMS, SITES AND MOBILIZATION

FIRST YEAR REPORT

By: L.T. Silver, I.S. Williams, J.A. Woodhead

DIVISION OF GEOLOGICAL AND PLANETARY SCIENCES
CALIFORNIA INSTITUTE OF TECHNOLOGY
Pasadena, California 91125

October 1980

PREPARED FOR U.S. DEPARTMENT OF ENERGY
Assistant Secretary for Resource Applications
Grand Junction Office, Colorado

URANIUM IN GRANITES FROM THE SOUTHWESTERN UNITED STATES: ACTINIDE PARENT-DAUGHTER SYSTEMS, SITES AND MOBILIZATION

FIRST YEAR REPORT

L.T. Silver, I.S. Williams, J.A. Woodhead

DIVISION OF GEOLOGICAL AND PLANETARY SCIENCES
CALIFORNIA INSTITUTE OF TECHNOLOGY
Pasadena, California 91125

October 1980

PREPARED FOR THE U.S. DEPARTMENT OF ENERGY
ASSISTANT SECRETARY FOR RESOURCE APPLICATIONS
GRAND JUNCTION OFFICE, COLORADO
UNDER CONTRACT NO. DE-AC13-76GJ01664
AND BENDIX FIELD ENGINEERING CORPORATION
SUBCONTRACT NO. 79-384-E

CONTENTS

TABLES

FIGURES

SUMMARY

In this first annual report for subcontract BFEC 79-384-E (Uranium in Granites of Southwestern North America) we have established the general geological and geochemical background for our investigations. We describe the regional setting and some important geochemical patterns, constituting a major uranium anomaly, of the Precambrian basement in the Colorado Plateau region. Three of our investigated samples were derived from a portion of this region in central and northern Arizona. We describe the tectonic and petrologic setting for a fourth sample, a granite from the young (Cretaceous) Peninsular Ranges Batholith of southern California.

We present the results of a detailed investigation of a sample of the Lawler Peak Granite, Bagdad district, Yavapai County, Arizona, and preliminary results of studies on granites near Prescott, Arizona and Globe, Arizona, as well as the California granite.

The sample selection of the Lawler Peak Granite was made on the basis that this granite body is part of the great regional uranium anomaly in the Precambrian basement of the southwestern United States; that it is one of a continent-wide generation of anorogenic granites; and that it has several associated uranium prospects and potential ore deposits. The principal findings of the study are:

1) The granite is dated precisely by this work at 1411 ± 3 m.y., confirming its synchroneity with a great regional terrane of granites.

2) Uranium is presently 8-10 times crustal abundance in this granite. Thorium is presently 2-3 times crustal abundance. Th/U is distinctively low at 1.3, compared to a crustal average of about 4.0. $^{238}U/^{204}Pb$ is 45, compared to the terrestrial average of approximately 9.

3) a) Uranium is found to be enriched in at least eight, possibly ten, primary igneous mineral species over the whole-rock values. In addition uranium apparently also is present as a dispersed component in submicroscopic interstitial sites, particularly fractures, cleavages and grain boundaries.

b) Individual mineral species show distinct levels in, and characteristic ranges of, uranium concentration. Collectively, uranium concentrations in the various minerals range through at least seven orders of magnitude, from less than 0.1 ppm in the feldspars and quartz, up to 50 percent UO_2 in a complex U-Ca titanate (Brannerite?) and up to 63 percent in a metamict uranosilicate (Coffinite?). ThO_2 covers a similar range, attaining 48 percent in thorite.

c) Material balance calculations can be only crudely approximated because of difficulty in obtaining precise abundance data for the several high uranium and thorium concentration phases present. Limiting calculations can be made.

d) It appears that in a uraniferous granite such as this, conventional accessory mineral suites (e.g. zircon, sphene, allanite, apatite,

monazite, xenotime) probably cannot account for most of the uranium in the rock, and more rare, high U-concentration phases also are present and are significant uranium hosts.

e) The conventional accessory mineral phases have abundances which are determined by the concentrations of their major stoichiometric components (non-actinide). Their contributions to the total uranium and thorium in the rock are governed by this consideration more than by the uranium and thorium concentrations in the rock.

f) With respect to uranium mobilization from granites under various geological conditions, it is necessary to know the stability field of each radioactive accessory species, including the rare high uranium and thorium concentration phases, for every type of superimposed geochemical or geological set of conditions.

4) This whole-rock sample, like others in the region, apparently has been subject to a loss of uranium; and apparently has not been open to the migration of thorium or radiogenic leads.

5) All mineral species and dispersed surficial sites investigated give discordant daughter-parent isotope relations indicating that they have been open on the scale of individual grains (centimeters) for uranium, radiogenic lead and thorium.

6) For the Lawler Peak Granite, it appears that at least two different geological episodes have contributed to the disturbance of the U-Th-Pb isotope systems: 230 ± 10 m.y., 75 ± 25 m.y. and, in addition, possibly a recent event (weathering?, volcanism?). Candidates for the last two events can be recognized.

7) Studies of various sites for transient dispersal of uranium, thorium and radiogenic lead isotopes indicate a non-uniform dispersal of these components. It is possible to estimate the comparative mean migration ranges for these components.

8) It appears that the bulk rock has lost at least 24 percent of its original uranium endowment, accepting limited or no radiogenic lead or thorium migration from the sample. This loss is equivalent to 5 µg/g of rock. For the exposed surface area of the Lawler Peak pluton, this is equivalent to migration of 100,000 metric tonnes of uranium from the present zone of relief (400+ meters).

Our studies of three other granite samples carefully selected for comparisons with the Lawler Peak Granite complement the findings for that rock:

1) All four granites are similar in that high uranium and/or thorium accessory minerals are important sites for their contained uranium and thorium.

2) The Ruin and Dells Granites, shown in this work to be very similar in age (1400-1440 m.y.) to the Lawler Peak Granite, possess important differences in mineral assemblages and in the long term stability of their contained uranium-thorium-lead isotope systems.

3) Both the Dells and Ruin Granites appear to be effectively closed systems for thorium migration. The Dells Granite does not appear to have suffered major uranium loss; the Ruin Granite appears to have lost nearly 60 percent of its original uranium (about 6 g/tonne).

4) Zircons in the Precambrian granites appear to be perhaps the most reliable indicators of the primary igneous uranium endowment.

5) The Dells Granite is one of the most radioactive granites identified in the southwestern United States (uranium, 39 ppm; thorium, 31 ppm). Its accessory mineral assemblage should provide important information on processes of uranium enrichment during igneous differentiation.

6) The Rubidoux Mountain Granite, one of the most highly differentiated rocks in the great Peninsular Ranges Batholith, does not suggest this batholith would be a favorable source for uranium deposits. It has only two times the uranium concentration found in average crustal rocks. Although the granite may have lost half its uranium at the time of crystallization, it has not lost uranium subsequently. This is attributed to its youth, stable geologic setting and comparatively modest radiation damage effects in its key uraniferous accessory minerals.

INTRODUCTION

BACKGROUND

The principles which govern the primary distribution of the actinide elements, uranium and thorium, in various types of granites in the earth's crust are only partly understood. Because, in geologic time, their several isotopes undergo radioactive transformations to measurable quantities of stable daughter lead isotopes, the geochemistry of these elements provides important insights into the timing and the mechanisms of formation of continental crust, clues to the source regions from which such granites are derived, and tracers for the incorporation of granitic components into the sedimentary cycle. The economic significance of uranium and thorium in nuclear power generation further justifies investigation of their geochemistry in granites, not only in terms of their primary igneous behavior, but to understand better those processes which can subsequently mobilize and, perhaps, concentrate uranium and thorium into useful ore deposits.

Although granitic rocks have only rarely proven to be of uranium ore grade, they have been identified as clearly important in many models for uranium exploration, both as potential uranium sources and/or as hosts for uranium ore formation in diverse geologic settings. Basic information is required on the distribution of uraniferous granites; on their tectonic and petrologic settings; on the principles of petrology and trace-element geochemistry which govern uranium fractionation in individual granite masses and among suites of granitic bodies during igneous processes; and on various processes for mobilization of uranium from its initial igneous sites.

The importance of accessory minerals as local hosts for a large fraction of the uranium in granites was established in the 1950's (e.g. Larsen et al., 1956; Tilton, et al., 1955; Picciotto, 1950; Brown et al., 1953a,b; Brown and Silver, 1956). The existence of some of the uranium in submicroscopic dispersed sites, particularly as interstitial material on fractures and grain boundaries, was also recognized by some early workers (Picciotto, 1950; Brown et al.,1953a,b; Brown and Silver, 1956). Subsequent work by numerous other investigators has underscored the evidence for both classes of uranium sites in many granites.

Only a few research groups have recognized the utility of the integrated radiogenic daughter/actinide parent isotope systems ($^{206}Pb/^{238}U$; $^{207}Pb/^{235}U$; $^{208}Pb/^{232}Th$) as well as the ratios $^{207}Pb/^{206}Pb$, $^{232}Th/^{238}U$ and $^{238}U/^{204}Pb$ in establishing unique isotopic parameters for characterizing the primary igneous rock and mineral endowments, and to evaluate possible secondary open-system geochemical events and their timing (e.g. Tilton, et al., 1955; Silver and Deutsch, 1963; Banks, 1963; Banks and Silver, 1964, 1966; Rosholt and Bartel, 1969; Rosholt et al., 1973; Ludwig and Silver, 1977; Ludwig and Stuckless, 1978; Stuckless and Nkomo, 1978, 1980; Zartman, 1979).

In all of these works, one or more individual mineral species, as well as the whole-rock isotope systems, were investigated, but none of these studies attempted a comprehensive mineralogical, as well as isotopic, study of all accessible radioactive species. This is a difficult, if not impossible, task, because of the low abundances of many species, the large samples required, the time-consuming, painstaking mineral separations and preparations, and the

extended, complicated isotope chemistry. These earlier works made it clear, however, that the more detailed the investigation of actinide mineral sites, the more effective was the evaluation of the geochemical behavior of uranium and thorium in the total-rock system.

OBJECTIVES

For this study we have the following specific objectives:

(1) We wish to determine the primary distribution of U and Th during the crystallization of granitic magmas, establish partitioning principles for these and related elements and compare the effects of major and trace element melt composition on these principles.

(2) We hope to establish the timing, nature and extent of secondary mobilization of uranium and thorium in hypogene and supergene settings to which various granites are introduced by utilizing the radiogenic and common lead systematics of various mineral and rock systems.

APPROACH

In this report we have examined four granitic rocks from different geographic settings, and to various degrees from different geological and geochemical settings (Figs. 1,2), for their whole-rock and selected accessory mineral isotopic properties. For one sample, from the Lawler Peak pluton in the Bagdad area, west-central Arizona, we have conducted the most detailed study of the uranium and thorium content, distribution, host mineralogy and isotopic systematics in a granite of which we are aware.

For each of the other granites, the Cretaceous Rubidoux Mountain Granite of Riverside, California, the Precambrian Dells Granite, north of Prescott, Arizona, and the Precambrian Ruin Granite from south of Roosevelt Reservoir, Gila Co, Arizona, we present significant new whole-rock and mineralogical data. From the work on these four rocks, from preceding published works and our own unpublished studies, we have made a number of findings and developed some interpretations we believe provide important insights into the processes and principles which govern the primary distribution and secondary mobilization of uranium, thorium and their associated radiogenic leads.

The report is organized to provide (1) petrologic and geologic contexts for each sample, (2) petrography and uranium and thorium mineralogy, (3) isotopic studies, and (4) an interpretation of the geochemistry and history of the actinide elements in the sample. The findings for the first three samples must be considered in the light of the extended observations made on the Lawler Peak Granite sample which will be presented last. Generalizations from all four studies follow.

Figure 1
Location map of the Rubidoux Mountain Leucogranite in the Southern California region, its relation to the Peninsular Ranges Batholith, and to the other granites sampled for this study.

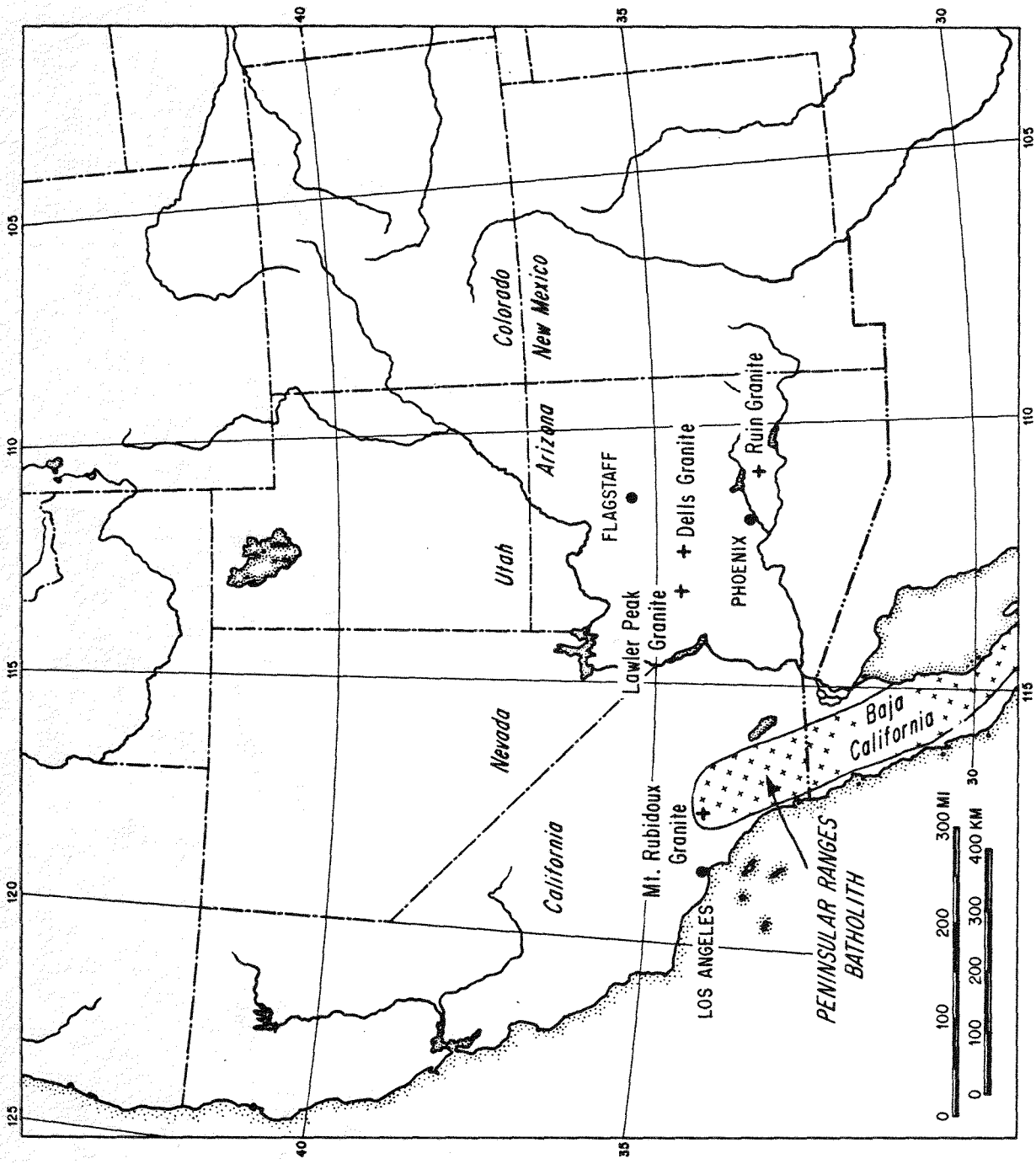
Colorado
New Mexico
Arizona
Utah
Nevada
California
Baja California
FLAGSTAFF
PHOENIX
Dells Granite
Ruin Granite
Lawler Peak Granite
Mt. Rubidoux Granite
LOS ANGELES
PENINSULAR RANGES BATHOLITH
0 100 200 300 400 KM
0 100 200 300 MI

Figure 1

Figure 2
Location map for the Bagdad area and the three Precambrian granite samples from Arizona studied in this work. The location of the Bagdad-Prescott strip map (Fig. 8) is also shown.

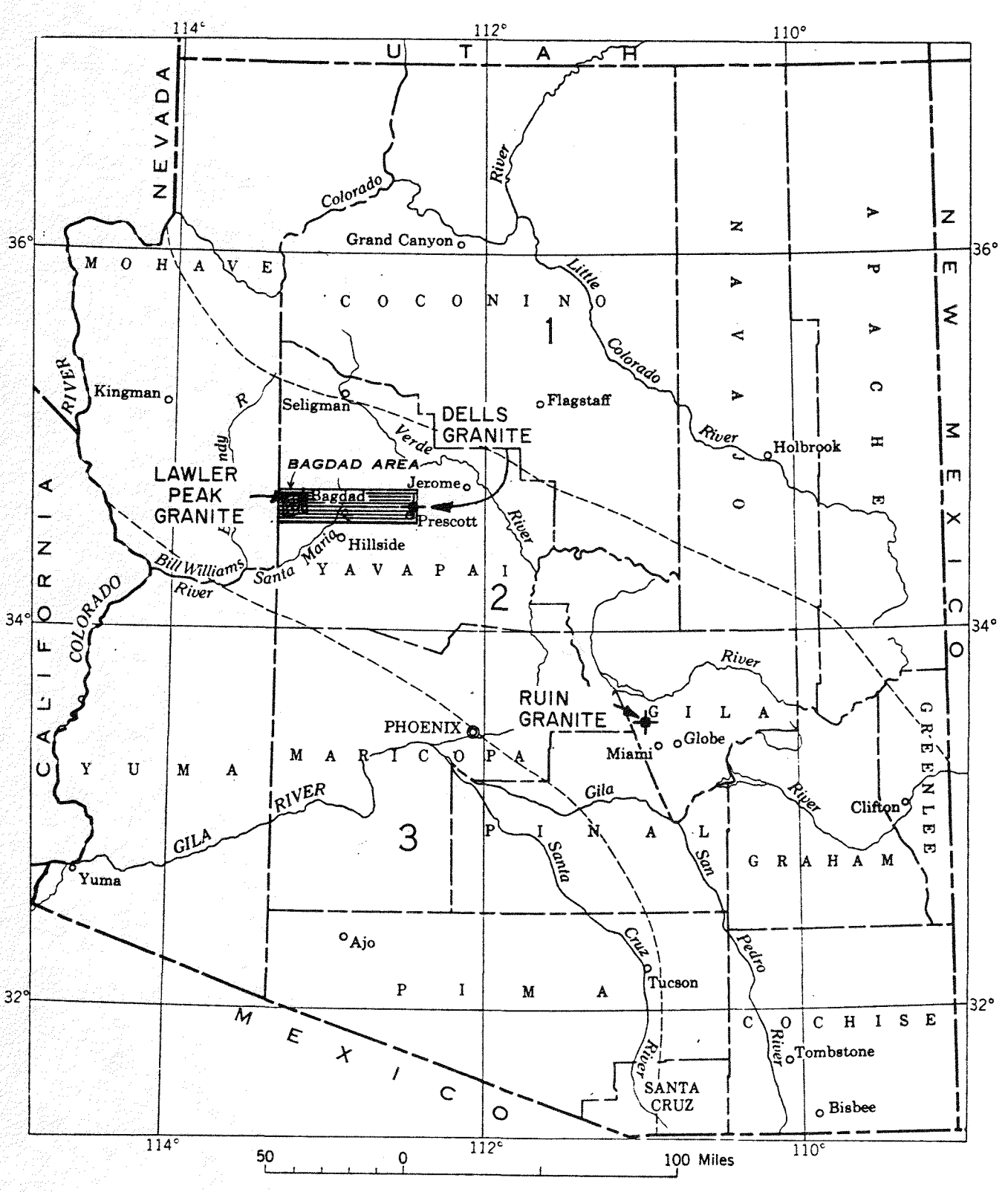
114°
112°
110°
U T A H
NEVADA
Colorado River
Grand Canyon
36°
M O H A V E
C O C O N I N O
1
Little Colorado River
N A V A J O
A P A C H E
N E W M E X I C O
Kingman
RIVER
Seligman
Flagstaff
DELLS GRANITE
Verde River
Holbrook
BAGDAD AREA
LAWLER PEAK GRANITE
Bagdad
Jerome
Prescott
Hillside
Bill Williams River
Santa Maria River
Y A V A P A I
2
34°
CALIFORNIA
COLORADO RIVER
RUIN GRANITE
PHOENIX
G I L A
M A R I C O P A
Miami
Globe
Y U M A
GILA RIVER
Gila River
Clifton
GREENLEE
3
P I N A L
G R A H A M
Santa Cruz River
San Pedro River
Yuma
Ajo
Tucson
32°
P I M A
C O C H I S E
Tombstone
M E X I C O
SANTA CRUZ
Bisbee
50
0
100 Miles

Figure 2

GEOLOGIC CONTEXT FOR SAMPLE SELECTION

MAGMATIC EPISODICITY IN THE SOUTHWESTERN UNITED STATES

In the southwestern United States, where this continuing investigation of uranium in granites has drawn its samples, granite magmatism has been prominent in at least three major Precambrian episodes, in Middle Proterozoic time and in several great episodes in the Mesozoic and Cenozoic. Following Precambrian intervals of batholithic development which culminated at about 1710, 1630, and 1425 million years ago (Silver, 1968a; Silver et al. 1977a,b), cratonic consolidation and general stability was achieved and maintained for more than a billion years in the region. From the beginning of the Mesozoic era (~240 million years ago) to the present, each geologic period has seen one or more major granite-forming episodes in the Southwest, each with different time-space relations and different geochemical characteristics.

For this work, the selected samples represent some of the more radioactive granites from the two most prolific plutonic generations. The Lawler Peak, Dells and Ruin Granites (Fig. 2) all formed 1400 to 1440 m.y. ago, as part of what was probably the greatest magmatic episode in the geologic history of the Southwest, (Silver, 1968a, Silver, Bickford et al., 1977b). This batholith-forming event was anorogenic in character, represented principally by large plutons of characteristically coarse porphyritic alkali-calcic quartz monzonites and granites. Large, sometimes rapakivitic, potassium feldspar megacrysts are a distinctive feature of these granites (e.g. Lawler Peak and Ruin Granites) but they are not always present (Dells Granite). Over large regions of the Southwest, these massive granites form individual plutonic centers up to 5000 km^2 in exposed areas, with well preserved primary structures, textures, and mineralogy.

Some of these granites have an unusually radioactive character (e.g. Dells, Lawler Peak) and others (Ruin) apparently have common crustal values for U and Th. Our three samples were selected, in part for their different combinations of properties and settings within this generation.

In contrast, the Rubidoux Mountain Granite is a highly differentiated end member of the great Peninsular Ranges Batholith which extends from its northern terminus near Riverside, California (Fig. 1) nearly 1500 km south to the southern tip of Baja California, Mexico. The magmatic arc is the product of convergent plate interactions, located on and near the Cretaceous continental margin of southwestern North America, and it is found on a classical orogenic site in which it is a significant element in the tectonic record. The batholith is one of the most calcic suites reported anywhere (Silver, et al., 1979) and is in marked chemical contrast to the Precambrian anorogenic suite in Arizona from which our other samples are taken. Rubidoux Mountain, on the western outskirts of Riverside, California was identified as underlain by perhaps the most highly fractionated lithology in the southern California portion of the batholith by Larsen (1948) in his classical petrographic study. Preliminary data has indicated it is also one of the most radioactive granites in the batholith (based on a study of more than 300 samples). By virtue of its comparative youthfulness, the radioactive mineral assemblage in the Rubidoux Mountain Granite can be expected to present a contrast in radiation damage and its consequent influence on U, Th and Pb lability, compared to the Precambrian granite suites.

Further, a comparatively simple geological history, and the presence of certain unique mineral indicators of past redox history, provide useful controls not available in most Precambrian suites.

URANIUM GEOCHEMICAL ANOMALY IN THE PRECAMBRIAN BASEMENT OF THE SOUTHWESTERN UNITED STATES

A major consideration in the selection of our Precambrian study samples is the evidence for a great regional geochemical anomaly in the Precambrian basement in a portion of the Colorado Plateau and adjacent regions. (Silver, 1968b; 1976).

The anomaly is expressed in unusual uranium concentrations in zircons contained in several generations of Precambrian plutonic and volcanic rocks ranging from 1100 to nearly 1800 million years in age. Data gathered by the principal investigator in the course of continuing regional geochronological studies have reinforced the initial observations and have defined the approximate geographic limits of the anomaly. They bear an interesting geographic spatial relation to the distribution of Mesozoic sandstone-type uranium ore deposits whose distribution in the Colorado Plateau region and proximity to Precambrian basement exposures is shown in Figure 3.

The limited exposure of basement within the southern Colorado Plateau is partially compensated for by the presence of numerous Cenozoic volcanic centers which have sampled the buried basement during explosive phases of their eruptions. Basement xenoliths are widely available in the Navajo and Hopi volcanic fields, as well as in the San Francisco Mountains, Mt. Taylor and other volcanic complexes. These sites together with the basement exposures have provided a significant sample population for examination of the anomaly.

In most of the igneous rocks from which zircons have been extracted in North America, average zircon uranium concentrations have ranged from 200 to 800 ppm with a mean value of approximately 500 ± 100 ppm. Only a few percent show values in excess of 1000 ppm. Corresponding igneous whole-rock uranium values range from less than 2 to more than 5 ppm, with a crustal average of 2.5 to 3 ppm, suggesting that on the average, zircons are enriched in uranium 150 to 200 times over their host rocks.

With these relations in mind, an examination of Figure 4 indicates the anomaly in the Colorado Plateau region. The geographic distribution of more than a hundred Precambrian igneous zircon suites represented by their composite uranium concentrations (in ppm) is shown on a regional base map. An irregular NE-SW trending belt of values consistently in excess of 1000 ppm is outlined by a dotted contour for 1000 ppm. Inside the dotted outline, values range from rarely less than 1000 to 12,000 ppm. Outside the outline, only a few samples exceed 1000 ppm. The coincidence of the anomaly with the geographic distribution of many of the productive uranium districts of the southern San Juan Basin, New Mexico and the Four Corners area (Fig. 3) is apparent.

In Figure 5, the contrast in uranium level between sample populations from inside and outside the anomaly belt is shown in a frequency plot of zircon uranium concentrations with general locations indicated by symbols. More than

Figure 3
Distribution of uranium deposits and basement exposures in the Colorado Plateau region (Adapted from Butler, 1972, in Geologic Atlas of the Rocky Mountain Region).

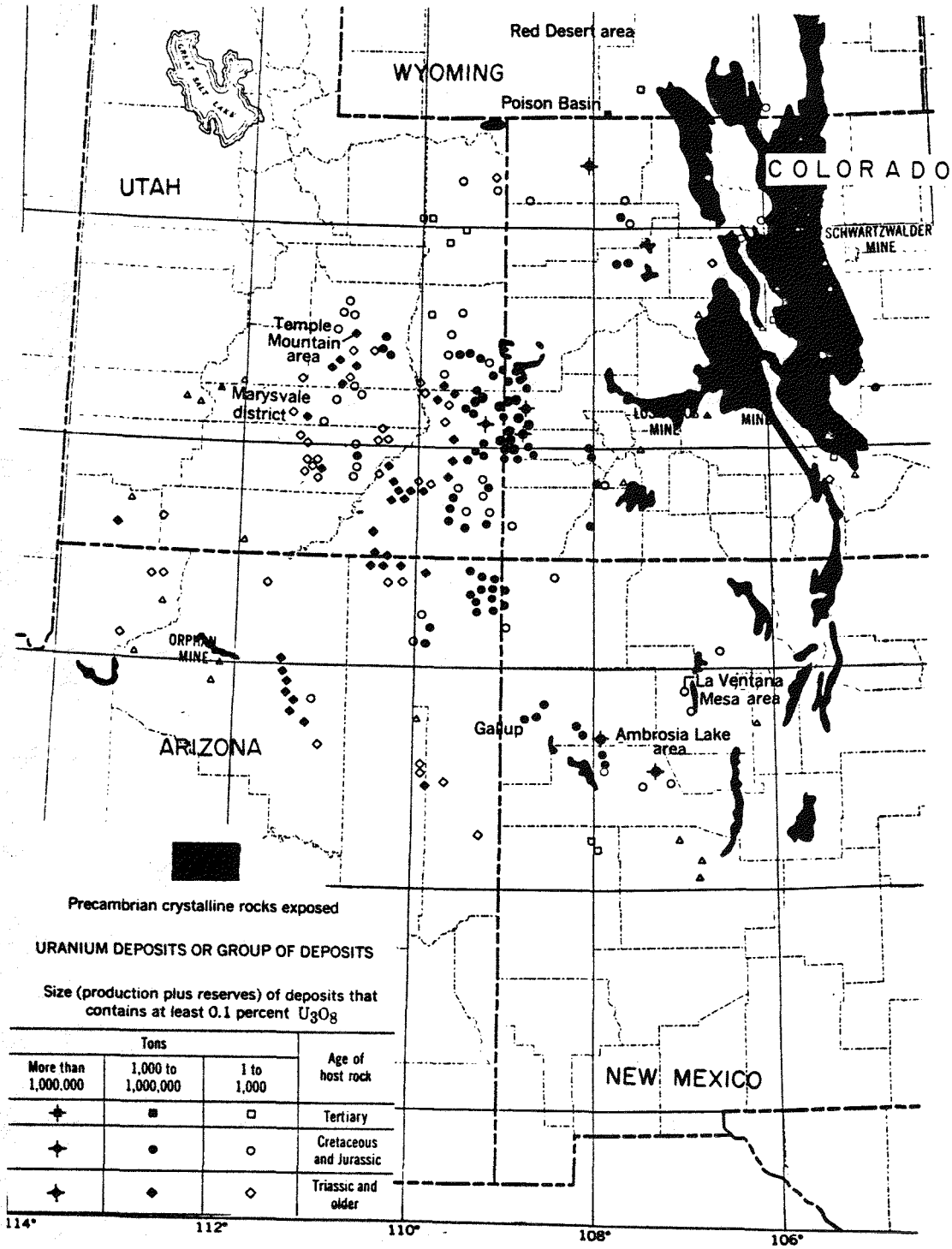

LOCATION AND SIZE OF URANIUM DEPOSITS

Adapted from A.P. Butler, Jr. in the Rocky Mtn. Atlas of Geology (1972)

Figure 3

Figure 4
Average uranium concentrations for zircon populations in Precambrian igneous rocks in the basement of the Colorado Plateau and adjacent regions. The dotted line defines a region within which zircon populations have uranium concentrations predominantly above 1000 ppm, constituting a significant uranium geochemical anomaly remarkably similar in geographic distribution to the location of important sandstone-type uranium ore deposits.

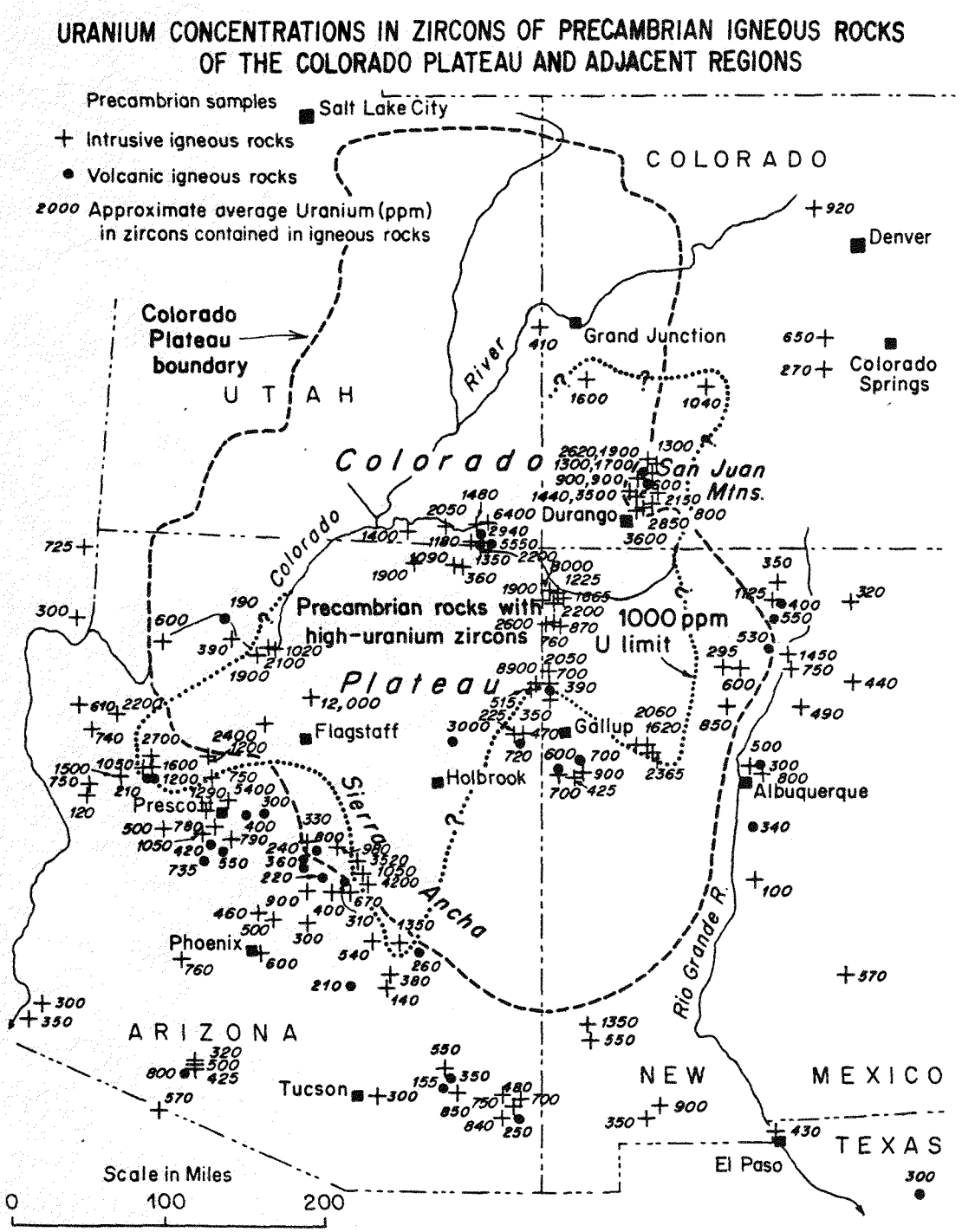
URANIUM CONCENTRATIONS IN ZIRCONS OF PRECAMBRIAN IGNEOUS ROCKS
OF THE COLORADO PLATEAU AND ADJACENT REGIONS
Precambrian samples
Salt Lake City
Intrusive igneous rocks
Volcanic igneous rocks
2000 Approximate average Uranium (ppm) in zircons contained in igneous rocks
COLORADO
Denver
Colorado Plateau boundary
UTAH
Grand Junction
Colorado River
Colorado Springs
Colorado Plateau
San Juan Mtns.
Durango
Precambrian rocks with high-uranium zircons
1000 ppm U limit
Flagstaff
Gallup
Holbrook
Albuquerque
Prescott
Sierra Ancha
Phoenix
Rio Grande R.
ARIZONA
NEW MEXICO
Tucson
El Paso
TEXAS
Scale in Miles
0
100
200

Figure 4

Figure 5
Frequency distribution diagram for average uranium concentrations in zircon populations in Precambrian igneous rocks of the Colorado Plateau and adjacent regions.

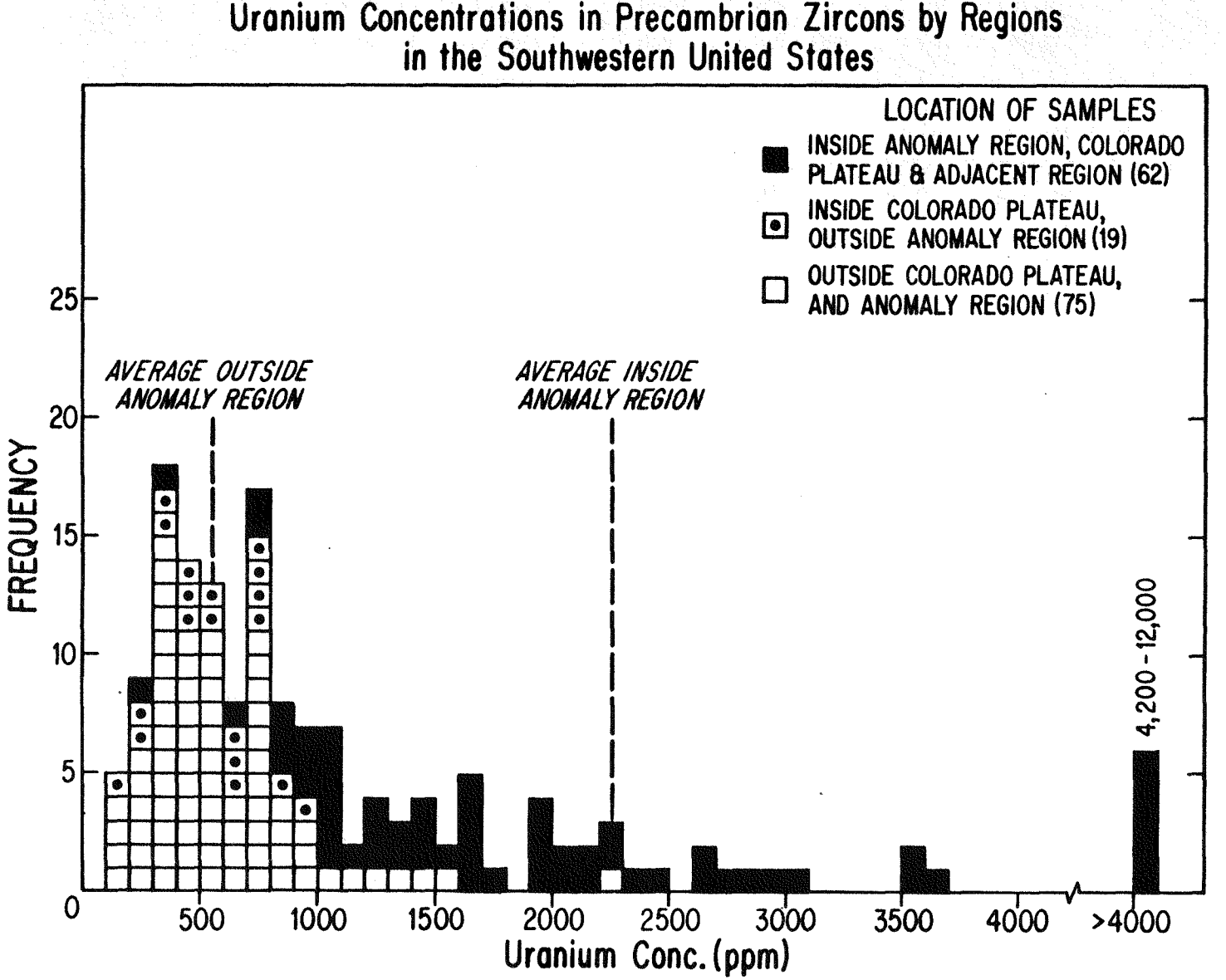
Uranium Concentrations in Precambrian Zircons by Regions
in the Southwestern United States
LOCATION OF SAMPLES
INSIDE ANOMALY REGION, COLORADO PLATEAU & ADJACENT REGION (62)
INSIDE COLORADO PLATEAU, OUTSIDE ANOMALY REGION (19)
OUTSIDE COLORADO PLATEAU, AND ANOMALY REGION (75)
AVERAGE OUTSIDE ANOMALY REGION
AVERAGE INSIDE ANOMALY REGION
4,200 - 12,000
FREQUENCY
0
5
10
15
20
25
500
1000
1500
2000
2500
3000
3500
4000
>4000
Uranium Conc. (ppm)

Figure 5

80 percent of the samples inside the anomaly have uranium concentrations in excess of 1000 ppm with an average of 2250 ± 50 ppm. Outside the anomaly region, only seven percent are in excess of 1000 ppm and the average of the population is about 550 ± 50 ppm.

Until recently very little whole-rock uranium data has been available for the samples displaying very uraniferous zircons. The nature and the possible relations of this geochemical anomaly to source regions for the Colorado Plateau deposits of uranium are clearly a matter of considerable interest. Therefore in the selection of our samples, we have chosen to examine three significant samples with different zircon uranium values: Dells (zircon uranium = 5400 ppm), Lawler Peak (2700 ppm) and Ruin (1350 ppm) Granites.

The comparison with the Rubidoux Mountain sample (2150 ppm) and its quite different tectonic and petrographic association is particularly appropriate. It is demonstrably one of the least weathered and oxidized samples, with a simple post-emplacement history, available for this type of investigation in the southwestern United States.

RUBIDOUX MOUNTAIN GRANITE

GEOLOGY, PETROGRAPHY AND CHEMISTRY

Rubidoux Mountain (Mt. Rubidoux) is located on the northwest side of the city of Riverside, California. It is a low, isolated, pale red-brown ridge, northeast-trending, about 1 mile in length and 1/2 mile wide bounded on its northwest side by the channel of the Santa Ana River. It is one of the most northerly exposures of the Peninsular Ranges Batholith.

Larsen (1948) recognized two facies of granite on Rubidoux Mountain which he called coarse and fine phases of leucogranite. Banks (1963) mapped the mountain and established that the fine phase occurred as dike-like masses cutting the much more extensive coarse phase. External contacts of the coarse phase are concealed by younger cover. Banks and Silver (1966) established the minimum age for the coarse phase as 112 m.y. and the best age of about 118 ± 3 m.y. from an extensive study of slightly discordant U-Pb isotopic systems in zircons and other accessory minerals. Similar studies on the sequentially younger fine-grained phase showed that within the uncertainties reflected in the slightly discordant systems the coarse and fine phases are indistinguishable in age. Subsequent changes in decay constant usage now indicate a "best" age of 116 ± 3 m.y. A distinctly younger pyroxene granodiorite cuts both phases of the granite and has yielded a precise age of 108 ± 1 m.y. from several zircon fractions. It is the last recorded thermal event visible on the mountain.

A newly blasted block of Rubidoux Granite (coarse phase) on the southwest flank of Mt. Rubidoux provided our sample #36. Geographic coordinates for this locality are latitude 33° 59' 39" N, longitude 117° 23' 23" W. This split boulder exposure revealed a striking blue-green interior with a remarkably well preserved lithology of leucocratic adamellite bulk composition (Fig. 6). A petrographic mode for this rock based on 12 thin sections gave the assemblage shown in Table 1.

A major and trace element analysis of the bulk rock has been provided by Dr. Bruce Chappell, Australian National University, Canberra (Table 2).

The texture of the granite is coarse (averaging 1 cm for the feldspar and quartz) and equigranular. Microcline microperthite is anhedral to subhedral; oligoclase is generally euhedral to subhedral; quartz is anhedral, as are most of the mafic mineral grains. There is no apparent foliation. Xenoliths are sparse, small (<5 cm), equant and unoriented. The granite is generally massive with widely spaced joints. The entire mountain looks remarkably like a weathered monadnock.

The mafic mineralogy is quite distinctive, and particularly significant for this study. Larsen (1948) established the very high Fe/(Fe + Mg + Mn) ratios which characterize the biotite (0.72, annite) and the hornblende (0.74, ferropargasite). He further recognized the presence of an Fe-rich hypersthene (0.76). Banks pointed out the additional presence of fayalite (0.91).

All of the mafic minerals are very susceptible to oxidation; the sample #36 is remarkable for their largely unoxidized state, although locally small

Figure 6
Photograph of a hand specimen of the Rubidoux Mountain Leucogranite sample, showing the distinctive blue-green hue found only in very fresh samples.

Figure 6

TABLE 1

Modal analysis*

Rubidoux Mountain Coarse Granite

Mineral	Wt. percent
Quartz	35.8
Plagioclase (An_{18})	30.5
Microcline-microperthite	27.0
Myrmekite	2.5
Biotite	2.5
Hornblende	1.4
Hypersthene	Trace
Fayalite	Trace
Opaques	0.1
Fe-rich alteration minerals	0.2
Accessories	
Zircon	Trace
Allanite	Trace
Apatite	Trace
Thorite	Trace

* Based on 12 thin-sections, 20,000 points

TABLE 2

Major and trace element chemistry of

Rubidoux Mountain Leucogranite #36

(Analyst - B. Chappell, A.N.U.)

Major Elements	Weight %
SiO_2	74.52
TiO_2	0.17
Al_2O_3	13.08
Fe_2O_3	0.60
FeO	1.26
MnO	0.04
MgO	0.22
CaO	1.35
Na_2O	3.67
K_2O	4.25
P_2O_5	0.03
S	<0.02
H_2O^+	0.33
H_2O^-	0.11
CO_2	0.16
rest	0.17
	99.96

Trace Elements	ppm
Ba	880
Rb	163
Sr	95
Pb	12.0
Th	24.4
U	5.0
Zr	140
Nb	7.0
Y	18
La	-
Ce	47
Nd	16
Sc	5
V	7
Cr	28
Mn	280
Ni	6.5
Cu	1.5
Zn	30
Ga	14.4

quantities of reddish-brown "iddingsite" alteration material were found associated with hypersthene and fayalite.

The most sensitive indicator of the lack of oxidation is the material responsible for the pervasive greenish tints of this sample. A very fine-grained blue-green Fe-rich sheet-structure mineral is deposited in thin films penetrating many fractures and cleavages of all the major transparent to translucent minerals (quartz and feldspars). This mineral, tentatively identified as an Fe-rich chlorite or a smectite is seen as very thin green filaments in thin section. On the outer weathered surfaces of the large bouldery blocks which yield the green lithology, these filaments are altered within a transition zone of a few millimeters to a red-brown color which dominates the hues of all the weathered exposures of the coarse phase of the Rubidoux Mountain Granite.

We believe this disseminated Fe-rich material, as well as the residual fayalite and hypersthene, argues uniquely against any significant supergene weathering during the history of our sample #36, and eliminates that process from consideration in our analysis of the stability of uranium, thorium and lead systems in this sample. On the other hand, the pervasive distribution of a hydrous sheet-structure mineral does call for a pervasive deuteric or hypogene hydrothermal episode.

URANIUM AND THORIUM DISTRIBUTION

Uranium and thorium are concentrated in at least four accessory minerals, apatite, allanite, zircon and uranothorite (Banks, 1963). Silver (quoted in Banks) conducted an extensive α-particle track mapping study (1955) of four polished thin-sections of this sample and found that the α-particles emitted collectively from the ^{238}U, ^{235}U and ^{232}Th decay chains were spatially related to the mineral phases as follows: quartz and feldspars, 10 percent; biotite, 1 percent; hornblende 0.5 percent; apatite, 23 percent; zircon, 22 percent; allanite, 40 percent; uranothorite, 14 percent, and other sites (fractures, grain boundaries, unidentified material), up to 10 percent.

Banks (1963) reported the following average uranium concentrations (in ppm) for zircon (2150), allanite (450) and uranothorite (81,000). Banks did not measure thorium concentrations. We have not yet attempted isotope dilution measurements for Th in various minerals, but we have examined the more radioactive species by radiometry and electron microprobe studies. Each species shows a range of uranium and thorium concentrations.

Zircon ranges from less than 200 to more than 9000 ppm uranium, with a large part of that range observed among zones in single crystals. Thorium ranges from less than 200 to more than 3000 ppm, averaging about 800 ppm. The average Th/U ratio in ziron is about 0.27. Allanite shows significant but more restricted ranges, again, commonly, in zonal distribution within crystals. The uranium ranges from less than 200 to 800 ppm and thorium from 6000 to 11,000 ppm, averaging 9500 ppm. The average Th/U ratio is about 21.

Uranothorite shows a moderate range and zonation in both uranium, 65,000 - 120,000 ppm, and thorium, 360,000-520,000 ppm. Thorium averages about 440,000 ppm and the average Th/U ratio is about 5.4.

Systematic daughter-parent isotopic studies were completed by Banks (1963) for the lead-uranium system in several phases plus the whole-rock system. Utilizing the same blasted boulder for our sample source, we have analyzed the whole-rock system and a carefully prepared feldspar concentrate for U, Th and Pb. Chappell has also determined U and Th by X-ray fluorescence analysis on a large representative sample (Table 2).

From the several types of observations it is possible to identify and crudely estimate the contributions of the principal sites to uranium and thorium in the rock. It is not possible to complete a material balance analysis because much of our accessory mineral species abundance data is based largely on inefficient yields from the mineral separation processes. Our estimate for allanite abundance, 250 ± 100 ppm, shows that allanite can account for up to 80 or 90 percent of the thorium in the rock with uranothorite (10 ± 5 ppm) probably the only other significant site (10 percent). Uranothorite can account for up to 25 to 30 percent of the total uranium, zircon (150 ± 50 ppm abundance) may contain up to 10 percent, allanite only 2-3 percent. It is clear that, even with the larger abundance uncertainties, perhaps 60 percent of the uranium must be present in other sites.

The α-track studies suggest that perhaps 20 to 25 percent of the total activity is distributed among major phases or in dispersed sites such as fractures and grain boundaries. If this were all uranium-derived α-activity, it might account for a large fraction of the remaining uranium in the total rock. On the other hand, our detailed study of the Lawler Peak Granite which follows suggests to us the real possibility that still another high concentration uranium phase at the abundance level of 1-3 ppm may be present in this rock. At that level, such a phase may be overlooked. We are now reviewing our mineral separates.

URANIUM-THORIUM-LEAD ISOTOPE SYSTEMATICS

The isotopic systematics of some of the radioactive minerals have been reported in Banks and Silver (1966). Two fractions of zircons were each apparently internally concordant for the paired Pb-U isotope systems. However, the more radioactive fraction yielded very slightly lower ages (Tables 3a,b), a characteristic observed in a number of samples from the Rubidoux Mountain intrusive complex. Uranothorite was also analyzed. The fractions with 8,000 ppm uranium and 440,000 ppm thorium yielded Pb-U ages of 97 ± 2 m.y., internally concordant but 15 m.y. less than the zircons. A single fraction with 108,000 ppm uranium and approximately 400,000 ppm thorium yielded concordant ages Pb-U of 87 ± 2 m.y. Silver (1963) has pointed out the well-defined correlation between radioactivity and degree of normal discordance in many zircon populations. It is presumed here that young, isostructural thorite is similar to zircon in its dependence between radiation damage and discordance, with lead loss rather than uranium gain as the significant process. There can be no unique interpretation concerning actinide migration from this data. However Banks also noted that allanite yielded Pb-U ages up to 40 percent greater than the zircon ages. The zircon ages are the most consistent among several populations from this pluton (and probably more correct). Although $^{207}Pb/^{206}Pb$ ages are not sensitive in this age range, the allanite appears to have seen uranium loss in excess of any lead loss. This is consistent with observations of Pb-U isotope systems in allanite we have made in a number of other rock suites.

TABLE 3a

Rubidoux Mtn. Leucogranite #36

Isotopic data for whole rock, feldspar and zircon

Sample	Weight (g)	Observed Lead Ratios			Radiogenic Pb Atom%			Concentrations (ppm)			
		206/204	207/204	208/204	206	207	208	Pb^{rad}	U	Th	Th/U Ratio
Whole Rock I[1]	12.68	19.47	15.70	39.26	47.6	5.5	46.9	0.196	4.65	--	--
Whole Rock II[2]	0.850	19.57	15.69	39.50	44.4	3.7	51.9	0.263	7.38	23.9	--
Perthite[2]	0.342	18.86	15.63	38.67	--	--	--	--	0.138	0.160	1.16
Zircons[1]											
Fraction #1	0.383	1786	101.02	185.98	88.32	4.27	7.41	32.21	1882	--	--
Fraction #2	0.733	1414	82.93	158.97	88.99	4.29	6.71	38.97	2307	--	--
Estimated Total Zircon Population									2150 ±100		

[1] Data from Banks (1963) and Banks and Silver (1966).

[2] Data from this study.

TABLE 3b

Rubidoux Mtn. Leucogranite #36

Atomic ratios and apparent ages

Sample	Atomic Ratios			Apparent Ages (m.y.)		
	$^{206}Pb/^{238}U$	$^{207}Pb/^{235}U$	$^{208}Pb/^{232}Th$	$^{206}Pb/^{238}U$	$^{207}Pb/^{235}U$	$^{208}Pb/^{232}Th$
Whole Rock I[1]	0.167	--	--	107	--	--
Whole Rock II[2]	0.0174	--	0.00638	111	--	128
Perthite[2]	--	--	--	--	--	--
Zircons[1]						
Fraction #1	0.01759	0.1172	--	112.4	112.6	--
Fraction #2	0.01749	0.1163	--	111.9	111.8	--

[1] Data from Banks (1963) and Banks and Silver (1966).

[2] Data from this study.

The whole-rock Pb-U system was first measured by Banks (1963) and the data is shown in Table 3a for an unusually large aliquot of crushed rock (12.7g), taken to maximize representative sampling of the accessories. Uranium was 4.65 ppm. We have reanalyzed material from the same block but have utilized sample-splitters and a Spex Shatterbox to obtain more homogeneous and representative samples. Our uranium and thorium for a 0.85g sample is U, 7.38 ppm and Th, 23.9 ppm. Chappell's values for U and Th, 5.0 ppm and 24.4 ppm, respectively, are shown in Table 2 in the trace element compilation.

The dispersion of various values for uranium reflects more the difficulty of obtaining a completely representative sample than analytical errors. The more profound chemical attack was probably performed in the second isotope dilution (ID) analysis in Table 3, minimizing the probability of undigested zircon, for example. The XRF value for uranium should also have been obtained from an effective attack. The occurrence of uranothorite (a key mineral), and perhaps another phase, at levels of 10 ppm or less makes vigorous physical homogenization a necessary but difficult requirement.

The good agreement between XRF and ID values for thorium probably reflects the much greater abundance of allanite.

The nominal ages calculated for the whole-rock system are subject to uncertainties of 10 percent or more. They can be considered to demonstrate that the bulk U-Th-Pb system has been closed throughout the history of the rock within the 10 percent uncertainty, despite the internal open-system evidence from zircon, uranothorite and allanite as reported by Banks.

SOME DISCUSSION AND CONCLUSIONS

(1) The Cretaceous Rubidoux Mountain Granite (coarse phase) appears, within analytical uncertainty to have been a closed bulk-rock U-Th-Pb isotope system throughout its post-emplacement history. This is consistent with the lack of evidence for recent weathering and oxidation in the selected sample. It appears that the penetrative development of fracture-filling hydrous sheet structure minerals was more apt to be a product of deuteric post-crystallization processes rather than subsequent oxidizing hydrothermal alteration. This is consistent with the retention of fayalite and ferrohypersthene as well as fresh annitic biotite and ferropargasitic amphibole.

(2) Nevertheless, almost all phases show some evidence of relative lead loss. No specific episode of geochemical disturbance has been independently identified. If such a disturbance is responsible for the extreme cases of uranothorite relative lead loss (>25 percent) and allanite relative uranium loss (>30 percent), it seems plausible it took place in the more recent history of the rock (late Cenozoic?) when the effects of cumulative radiation damage were more significant. Evidence for radiation damage exists in at least the uranothorite and the allanite from optical and X-ray diffraction studies.

(3) The ratio of the general levels of uranium in the composite zircon population to the average whole-rock value is approximately 375. This is higher by a factor of about two than values observed in most rocks of the Peninsular Ranges Batholith in which zircon is a conspicuous accessory. Either zircon

has had an unusual role in the paragenesis of this assemblage, or there exists a distinct possibility that in the deuteric episode in which the dispersed blue-green sheet structure mineral formed, a significant fraction (~50 percent) of the primary endowment of uranium in the rock was lost before significant radioactive decay and radiogenic accumulation could take place.

(4) Even with moderate uranium and thorium levels of 5-7 and 24 ppm respectively, the accessory mineral suite in the crystallizing magma was augmented by a high uranium and thorium phase, uranothorite, in which U and Th are stoichiometric components rather than trace elements substituting for other components. It is clear that at a significant point in the crystallization history of this granite, despite the presence of enriched receptors such as zircon and allanite, the melt became saturated for U and Th and euhedral uranothorite appeared. It is also suspected that another high uranium phase may have crystallized.

(5) Rocks of Rubidoux Mountain lithology comprise considerably less than one percent of the Peninsular Ranges Batholith. It is the most differentiated and uraniferous granite identified in the batholith thus far, at a level of 5-7 ppm, which is only about twice the average crustal values and about 2-3 times the average batholith value. It therefore does not appear that the calcic batholith suite, at least on the western, older side of the magmatic arc, has been effective in providing a significant crustal enrichment in uranium. A similar argument can be made for thorium, which is also only twice average crustal abundance.

RUIN GRANITE

GEOLOGY, PETROGRAPHY AND GEOCHEMISTRY

The Ruin Granite is one of the largest apparently continuous masses of Precambrian granite in Arizona. Named by Ransome (1903) for the famous ancient Indian ruins of Tonto National Monument, the mass underlies significant portions of the basins of the Gila River and Tonto Creek near their confluence in west-central Gila County. The minimum dimensions are 90 km in a northwest direction from north of Miami to the central Mazatzal Mountains and 50-60 km in a northeast direction from Apache Lake to the Sierra Ancha. Large portions of the plutonic complex are concealed under younger cover and the complete extent and internal structures are not well mapped. In the Sierra Ancha, a small, productive uranium district is located in Apache Group and associated diabase, probably resting directly on Ruin Granite.

The pluton is comprised predominantly of a coarse porphyritic granite whose minor minerals vary among combinations of biotite, biotite and hornblende, and biotite and muscovite. The pluton is generally unfoliated and only locally deformed. It is exposed on broad deeply weathered surfaces, some of which are exhumed and stripped Late Proterozoic surfaces developed pre- or post-Apache Group time.

The pluton is very well dated at several places as having an age of 1440 ± 20 m.y.. Zircon data have been obtained for the sample discussed here, from the central Mazatzal Mountains and from the Sierra Ancha. Livingston (1969) has derived essentially identical Rb-Sr and K-Ar data in the Haystack Buttes area near the Salt River, northeast of Globe.

Our study sample (Fig. 7) was obtained from a blasted ledge at the base of a road cut with an excellent deep weathering profile, on the west side of Arizona state route #88, from Globe to Roosevelt Reservoir, about 0.7 miles south of the junction with route #288 to Young, Arizona. The U.S. land coordinates are NE 1/4, SW 1/4, Sec. 33, T. 3 N, R. 14 E. The total sample collected was about 80 kg and appears macroscopically quite fresh. It is estimated that the sample position was a minimum of 200, and probably more than 500, meters below the late Proterozoic weathering surfaces.

The sample is a coarse porphyritic muscovite-biotite granite (Fig. 7) with euhedral, flesh-colored microcline-microperthite megacrysts up to 3 cm in major dimension. An estimated mode based on hand specimens and thin-sections is: quartz, 28 volume percent; perthite, 39 percent; oligoclase (An_{24}), 21 percent; biotite, 8.2 percent; muscovite, 1.2 percent; opaque minerals, 1.0 percent; others, 0.7 percent. A major and trace element analysis of Ruin Granite #2 is given in Table 4.

Evidence of alteration in the major minerals is modest. Chlorite makes up less than 10 percent of the biotite. Plagioclase shows cores dusted with clay minerals and some sericite. Traces of epidote are present in the plagioclase and along the margins and cleavages of biotite to the extent of 0.2-0.3 percent.

Figure 7
Photograph of a hand specimen of the Ruin Granite sample showing typical flesh-colored microcline-microperthite megacrysts.

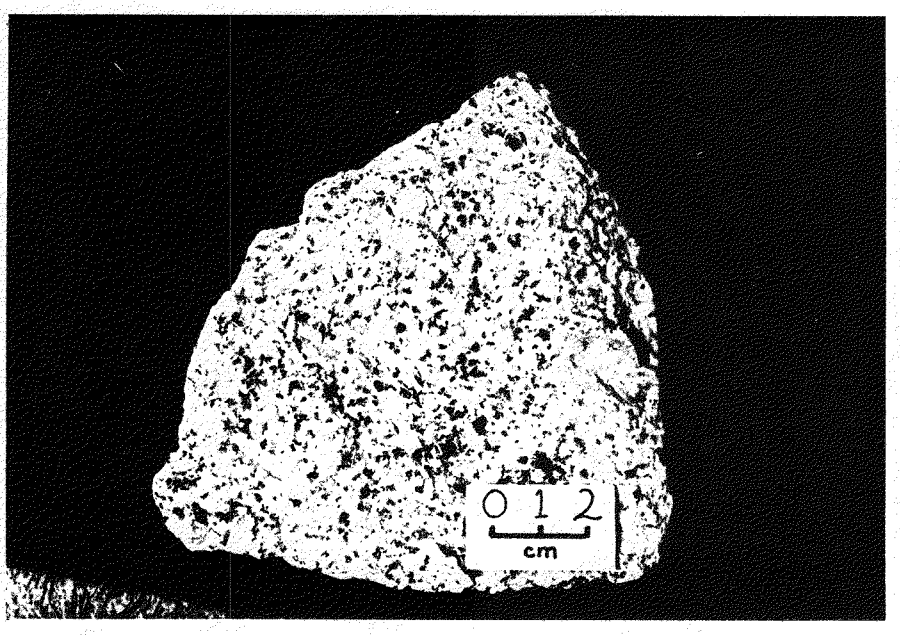

Figure 7

TABLE 4

Major and trace element chemistry of

Ruin Granite #2

(Analyst - B. Chappell, A.N.U.)

Major Elements	Weight %
SiO_2	71.02
TiO_2	0.43
Al_2O_3	13.65
Fe_2O_3	1.18
FeO	1.45
MnO	0.07
MgO	1.11
CaO	1.80
Na_2O	2.92
K_2O	4.62
P_2O_5	0.15
S	<0.02
H_2O^+	0.84
H_2O^-	0.09
CO_2	0.22
rest	0.17
	99.72

Trace Elements	ppm
Ba	455
Rb	275
Sr	136
Pb	26.5
Th	29.6
U	4.4
Zr	175
Nb	17.0
Y	42
La	35
Ce	85
Nd	30
Sc	9
V	32
Cr	6
Mn	520
Ni	6.0
Cu	23.0
Zn	49
Ga	15.0

Accessory minerals include: magnetite, ilmenite, epidote, allanite, a complex oxide (to be identified), zircon, apatite, fluorite and probably, thorite.

URANIUM-THORIUM-LEAD ISOTOPE SYSTEMATICS

We have concentrated on studying the whole-rock uranium, thorium and lead system, for comparison with analyses of feldspar (Ludwig and Silver, 1977) and zircon reported here.

The zircon isotopic data are shown in Tables 5a,b. The average uranium concentration is 1350 ± 100 ppm. Thorium has not been determined by isotope dilution. The zircons form a two-point chord on a Concordia diagram leading to an apparent age of 1440 ± 20 m.y., in excellent agreement with two other zircon studies and the Rb-Sr and K-Ar studies in the same plutonic complex.

It is significant to note that zircons in the Ruin Granite are very euhedral externally and in internal zones, and vary in color from pale to deep transparent hyacinth in whole grains or in inner zones to grayish-white and opaque in thin outer zones. The range of uranium concentration is from less than 100 to more than 5000 ppm. The two fractions differ in that the hyacinth zircons, concentrated in fraction #1, average 557 ppm U, while those zircons with maximum development of gray opaque outer zones, concentrated in fraction #2, average 2205 ppm U.

The difference in degree of discordance of these zircons (Table 5b) is remarkable. The lower radioactivity fraction is 15 percent discordant in a normal sense, i.e. $^{206}Pb/^{238}U$ age < $^{207}Pb/^{235}U$ age < $^{207}Pb/^{206}Pb$ age, and in a relative sense lead appears to have been lost from the zircons compared to uranium. The more radioactive fraction is about 75 percent discordant, yielding a very large spread between the two data points on a Concordia diagram. The observed relation between radioactivity and discordance is part of a now well-known phenomenon (Silver, 1963), but it is also an extreme example.

The zircons provide evidence for U-Th-Pb open system behavior internal to the whole-rock system. Other phases which should be examined to evaluate the full extent for this sample are allanite, apatite and thorite?.

The whole-rock U-Th-Pb isotope system has been measured in two distinct aliquots differing in size by a factor of two. The sample was prepared with great care to achieve fine grinding and homogenization from 2 kg of rock. The analytical results in Table 5a, show very good agreement. Utilizing preferred values for initial lead composition ($^{206}Pb/^{204}Pb$, 16.15; $^{207}Pb/^{204}Pb$, 15.38; $^{208}Pb/^{204}Pb$, 35.75) determined from potassium-rich feldspar (Ludwig and Silver, 1977), the daughter-parent systematics and model ages are given in Table 5b.

DISCUSSION WITH SOME CONCLUSIONS AND INTERPRETATIONS

The whole-rock U values average 4.00 ppm; Th averages 27.35 ppm; and Th/U averages 6.8. These may be compared with XRF values in Table 4. The radiogenic lead appears very consistent; however, for a 1440 m.y. old system, the radiogenic

TABLE 5a

Ruin Granite #2

Isotopic data for whole rock and zircon

Sample	Weight (mg)	Observed Lead Ratios			Radiogenic Pb Atom%			Concentrations (ppm)			
		206/204	207/204	208/204	206	207	208	Pb^{rad}	U	Th	Th/U Ratio
Whole Rock #1	1016.	20.77	15.78	39.98	49.89	4.430	45.68	4.06	3.925	28.17	7.177
Whole Rock #2	1998.	20.75	15.79	39.97	49.89	4.441	45.68	4.07	4.082	26.52	6.497
Zircons											
Fraction #1	32.3	219.3	33.49	67.35	81.01	7.193	11.80	115.4	557.2	--	--
Fraction #2	26.0	1442.7	133.34	181.55	84.50	6.982	8.51	154.3	2205.	--	--
Estimated Total Zircon Population									1350 ±100		

TABLE 5b

Ruin Granite #2

Atomic ratios and apparent ages

Sample	Atomic Ratios				Apparent Ages (m.y.)			
	$^{206}Pb/^{238}U$	$^{207}Pb/^{235}U$	$^{207}Pb/^{206}Pb$	$^{208}Pb/^{232}Th$	$^{206}Pb/^{238}U$	$^{207}Pb/^{235}U$	$^{207}Pb/^{206}Pb$	$^{208}Pb/^{232}Th$
Whole Rock #1	0.5982	7.131	0.08645	0.07387	3051	2156	1371	1441
Whole Rock #2	0.5749	7.040	0.08881	0.07842	2928	2117	1398	1526
Zircons								
Fraction #1	0.1949	2.386	0.08880	--	1148	1238	1400	--
Fraction #2	0.0687	0.7830	0.08262	--	432	595	1282	--

isotopic composition suggests a long term Th/U ratio of 3.1 in the parental system. This is a profound discrepancy with the observed value of 6.8, and potentially a clue to a large fractional loss of uranium from the bulk-rock system.

Comparison of the $^{206}Pb/^{238}U$ and $^{208}Pb/^{232}Th$ isotope ratios and apparent ages with the emplacement age inferred from zircons shows another major discrepancy. The observed $^{206}Pb/^{238}U$ ratio is 2.4 times the value expected from the zircon age for the rock. This can also be plausibly explained by loss of uranium which was present throughout most of the history of the sample. If the loss were recent, the $^{206}Pb/^{238}U$ ratio would imply a pre-loss uranium concentration of 9.6 ppm.

In contrast, the observed $^{208}Pb/^{232}Th$ ratios range from precisely those expected for a closed system to values only 6 percent high. Given the magnitude of the common lead correction for the observed whole-rock lead and their combined uncertainties, this can be taken as indicating essentially a closed system for both radiogenic lead and thorium, during the life of the rock. This supports further the concept that the anomalous Pb-U ratio reflects whole-rock uranium loss.

There is an additional test which may be applied. The ratio of average zircon concentration to observed whole-rock uranium is 338. If the rock system once possessed a uranium concentration of 9.6 ppm, the same ratio would have been 140. This is a much more typical value for closed granite systems.

The whole-rock $^{207}Pb/^{206}Pb$ radiogenic ratios appear somewhat low but within the uncertainty are what would be expected for a closed Pb-U system. This does not support the concept of a major uranium loss at anytime except in the geologically recent history (last 50-75 million years) of the sample.

In summarizing these data and observations, it may be concluded:

(1) Zircons in the Ruin Granite have higher than average uranium concentrations and show evidence of extreme uranium fractionation during crystallization of the host melt.

(2) Other accessory minerals particularly thorite? and allanite must be investigated to establish the principal sites for thorium and uranium in the bulk rock.

(3) The whole rock has a "normal" crustal value for uranium, but a twice normal value for thorium. From the Th/U ratio, the evidence of unsupported radiogenic ^{206}Pb, and the anomalous zircon : whole-rock uranium ratio, it appears the bulk sample may have lost up to 50-60 percent of its original and long-term uranium endowment during its recent geological history.

(4) There appears to be no evidence of radiogenic lead loss or thorium loss comparable in magnitude to the inferred uranium loss.

(5) The analysis of whole-rock uranium loss, suggests the Ruin Granite may indeed belong in the uranium geochemical anomaly region as suggested by its zircon uranium concentrations.

DELLS GRANITE

GEOLOGY, PETROGRAPHY AND CHEMISTRY

The Dells Granite sample is derived from a boldly outcropping granite pluton, located about 6-8 km northeast of Prescott, Yavapai County, Arizona. The distinctive bouldery terrain, which is called the Granite Dells locally, is exposed over 12 km^2. It is surrounded and unconformably overlain by Cenozoic rocks so that the true dimensions of the pluton are not known (see the strip geologic map in Figure 8).

The Dells Granite has been identified by aeroradiometric surveys as one of the most radioactive granites known in Arizona. In Figure 8, the area covered by the geologic strip map is represented by a succession of uranium and thorium profiles derived from gamma-ray spectroscopy (Aero Service, 1979) The positions of the Dells and Lawler Peak plutons are clearly identified by the strong uranium and thorium gamma-ray signal-to-background values they generate.

The exposed granite is quite massive and structureless (Krieger, 1965) except for broadly spaced joint systems which control the weathering and erosion patterns. Xenoliths are sparse and comprised of randomly oriented schist and gneiss fragments up to 30-50 cm in diameter.

The Dells Granite is consistently a two-mica granite, usually equigranular but occasionally with large potassium feldspar megacrysts. The quartz is consistently a dark, smoky, gray-brown. Our sample is quite typical, but fresher than any other exposures found.

Our sample was taken from a quarried block in an old roadside quarry on the north side of the exposed granite on the east side of U.S. route #89, 0.3 km north of the junction with route #89A. The U.S. land coordinates are NW 1/4, NE 1/4, Sec. 12 T. 14 N, R 2 W. About 50 kg was taken.

The sample is an inequigranular medium-grained, leucocratic muscovite-biotite adamellite (Fig. 9). An estimated mode for the rock is: quartz, 35 percent; microcline-microperthite, 27 percent; plagioclase (An_{10}), 34 percent; biotite (chlorite), 2 percent; muscovite, 1 percent; opaques 0.5 percent; others, 0.5 percent.

Accessory minerals are numerous and diverse: magnetite, ilmenite, hematite, garnet, tourmaline, epidote, clinozoisite, allanite, fluorite, apatite, zircon, thorite, xenotime?, a black complex oxide that appears metamict and several other metamict? unidentified phases.

The zircon and xenotime? are all well-formed but in more magnetic fractions show distinct rusty-colored coatings. Fluorite shows a range from colorless to pale-green to pink to purple.

The alteration mineral suite includes a dust of clay and occasional sericite flakes in the plagioclase; extensive chloritization of biotite; development of late epidote-allanite aggregates in the plagioclase, and chlorite-like replacement of opaques and garnets along fractures.

Figure 8

A geological strip map and characteristic gamma-ray intensity maps for uranium and thorium for the region extending from east of Prescott, Arizona, to west of Bagdad, a distance of 75 km. Shown on the geological map in solid black are two of the radioactive granite bodies sampled and discussed in this report. The pluton of Lawler Peak is NE of Bagdad and the adjacent radioactive pluton of Blue Mountain (not studied) is in turn immediately east of that. The very radioactive granite of the Dells is seen 6 km NE of Prescott. The gamma-ray profile maps have been synthesized from aeroradiometric gamma-ray spectrometer flight lines (Aero Service, 1979) flown under BFEC project No. 44-77-4118, Western Geophysical Co. of America, AeroService Div. contractor. The base map is simplified from the Arizona state geological map. Each flight line reflects the characteristic U or Th gamma-ray intensity (in counts per second) encountered, shown as height of the signal above the reference line. It can be seen clearly that the plutons of Lawler Peak, Blue Mountain and the Dells are the most prominent anomalies in this strip.

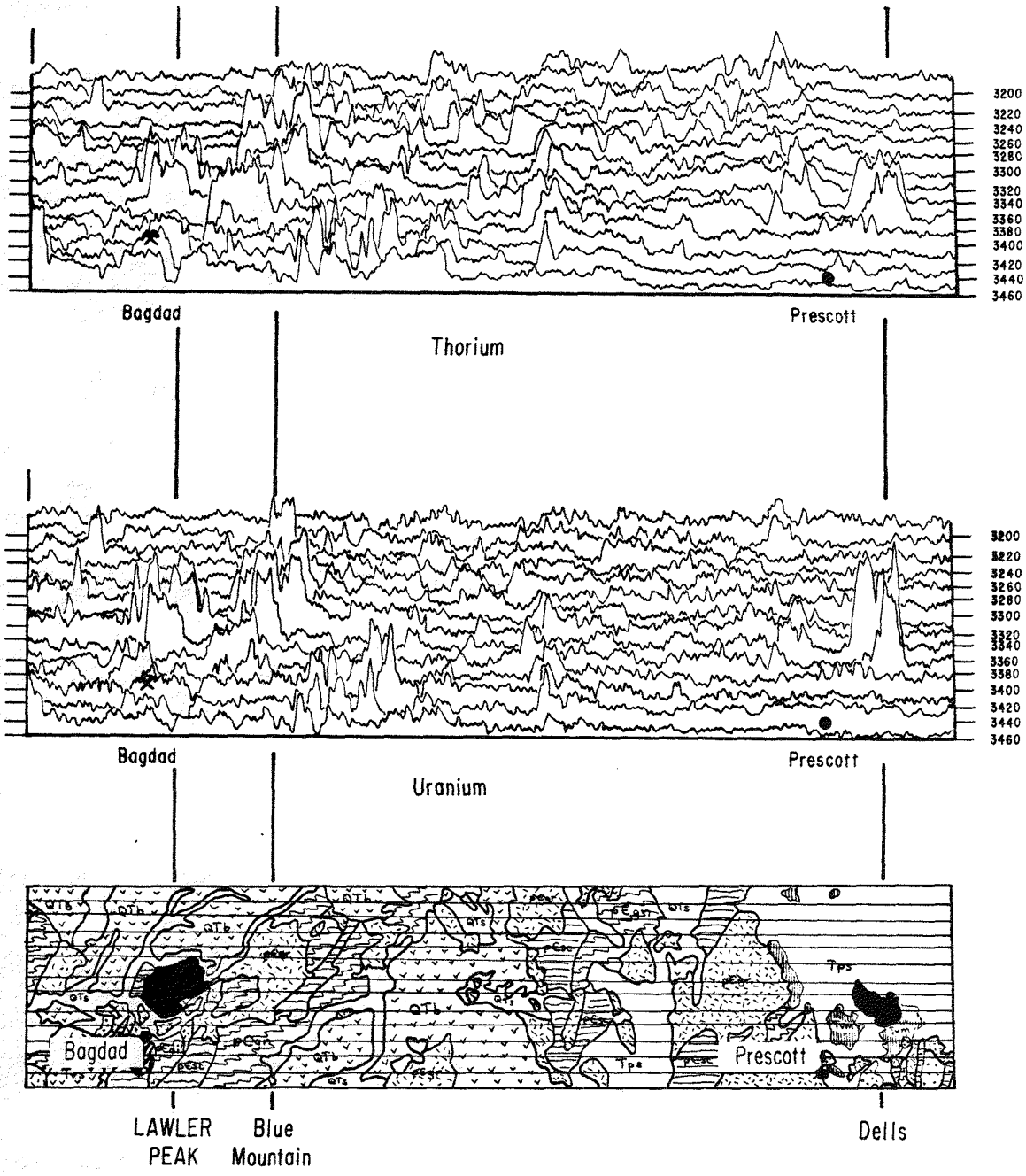
3200
3220
3240
3260
3280
3300
3320
3340
3360
3380
3400
3420
3440
3460
Bagdad
Prescott
Thorium
Uranium
Bagdad
Prescott
LAWLER PEAK
Blue Mountain
Dells

Figure 8

Figure 9
Photograph of a hand specimen of the Dells Granite sample displaying the characteristic dark, smoky quartz.

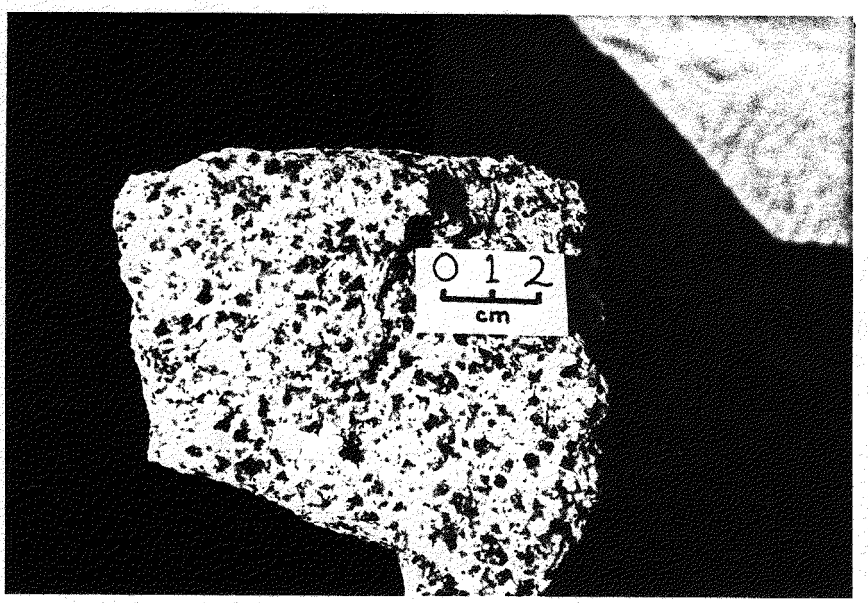

Figure 9

The whole-rock major and trace element chemistries are given in Table 6. The siliceous and high Fe/(Fe + Mg + Mn) character of the granite is noteworthy. The elevated levels of the actinides, the heavy lanthanides, rubidium and niobium, as well as the low levels of Ba, Sr and the transition metals are also conspicuous.

URANIUM-THORIUM-LEAD ISOTOPIC STUDIES

We have completed isotopic analyses of a whole-rock sample and two zircon fractions. A major analytical investigation of this rock is currently in progress.

The data for the two zircon fractions are given in Table 7a. The zircon fractions, although among the least radioactive in the rock, have uranium values between 4400 and 4760 ppm, thorium values of 1000 to 1140 ppm and Th/U ratios of ~0.23. Other fractions of zircon appear to range to more than 7000 ppm uranium, and our preliminary estimate for the average of the total population is 5400 ppm. Composite thorium is 1350 and composite Th/U is 0.25.

The whole-rock uranium from isotope dilution is 38.9 (39.6 by XRF) and the thorium is 31.2 (35.6 by XRF). The observed Th/U ratio is 0.80 (0.90 by XRF), an unusually low value.

DISCUSSION AND SOME CONCLUSIONS

The isotope systematics of the zircon are somewhat surprising (Table 7b). Despite the extreme radioactivity levels, the Pb-U systems are only 13 to 30 percent normally discordant. Plotted on a Concordia diagram, the Pb-U systems generate an age of 1400 ± 15 m.y. for the Dells Granite.

The $^{208}Pb/^{232}Th$ system in the zircons displays a rare example of reverse discordance, with values 12-28 percent too high for a 1400 m.y. closed system. At this point no unique explanation of these excessive ratios is possible. One may consider the alternative of mobility of Th which would have had to exceed the mobility of lead and uranium according to the observations. The possibility of impure zircon separates containing small quantities of other very radioactive and reverse-discordant phases must be considered, although special precautions against such a possibility were taken.

The whole-rock isotope systematics are also surprising in their near concordance for both Pb-U and Pb-Th systems. The $^{207}Pb/^{206}Pb$ radiogenic ratio gives an age in close agreement with the zircon intercept age. The $^{206}Pb/^{238}U$ age is about 15 percent low, the $^{208}Pb/^{232}Th$ age is about 8 percent low. Unless coupled U, Th and Pb loss has occurred, it appears the whole-rock system has been nearly closed for all of these elements throughout its history. Relatively slight lead loss is indicated. This geochemical stability is obviously in marked contrast to our observations for the Ruin Granite, and for the Lawler Peak Granite (to follow).

Our preliminary studies of the Dells Granite #400 sample do not permit us to resolve the comprehensive questions of uranium and thorium siting at this

TABLE 6

Major and trace element chemistry of

Dells Granite #400

(Analyst - B. Chappell, A.N.U.)

Major Elements	Weight %
SiO_2	75.61
TiO_2	0.03
Al_2O_3	13.09
Fe_2O_3	0.46
FeO	0.32
MnO	0.03
MgO	0.05
CaO	0.62
Na_2O	4.14
K_2O	4.53
P_2O_5	<0.01
S	<0.02
H_2O^+	0.37
H_2O^-	0.15
CO_2	0.22
rest	0.10
	99.72

Trace Elements	ppm
Ba	25
Rb	294
Sr	11.0
Pb	53
Th	35.6
U	39.6
Zr	107
Nb	77
Y	111
La	8
Ce	16
Nd	13
Sc	1
V	<1
Cr	7
Mn	255
Ni	<0.5
Cu	1.5
Zn	34
Ga	19.2

TABLE 7a

Dells Granite #400

Isotopic data for whole rock, feldspar and zircon

Sample	Weight (mg)	Observed Lead Ratios			Radiogenic Pb* Atom%			Concentrations (ppm)			
		206/204	207/204	208/204	206	207	208	Pb^{rad}	U	Th	Th/U Ratio
Whole Rock	1032.	26.92	16.34	38.60	73.88	6.590	19.53	9.65	38.92	31.18	0.801
Zircons											
Fraction #1	3.04	440.2	52.57	86.82	83.09	7.286	9.621	983.	4417	1137	0.257
Fraction #2	4.32	325.4	41.86	69.48	84.16	7.205	8.636	841.	4757	997	0.209
Estimated Total Zircon Population									5400 ±300	1350 ±100	0.250
*Assumed Common Pb.		16.15	15.38	35.75							

TABLE 7b

Dells Granite #400

Atomic ratios and apparent ages

Sample	Atomic Ratios				Apparent Ages (m.y.)			
	$^{206}Pb/^{238}U$	$^{207}Pb/^{235}U$	$^{207}Pb/^{206}Pb$	$^{208}Pb/^{232}Th$	$^{206}Pb/^{238}U$	$^{207}Pb/^{235}U$	$^{207}Pb/^{206}Pb$	$^{208}Pb/^{232}Th$
Whole Rock	0.2121	2.609	0.08921	0.06772	1240	1303	1406	1324
Zircons								
Fraction #1	0.2149	2.599	0.08768	0.09358	1255	1300	1375	1808
Fraction #2	0.1730	2.042	0.08561	0.08192	1028	1130	1329	1591

time. It is our intention to pursue the mineralogy, the lability, and the material balance in the next phase of our investigations. We can note the following points, however:

(1) The zircons are the most radioactive and the least discordant of the three 1400-1440 m.y. old rocks we have examined in this work. However, they display a puzzling reverse discordance for the $^{208}Pb/^{232}Th$ system.

(2) The whole-rock system is the most radioactive and the most nearly closed, apparently, of the three Precambrian rocks.

(3) The ratio of zircon average uranium to whole-rock uranium of 140 is a normal value and argues independently for an essentially closed whole-rock uranium system.

(4) The Dells pluton is the pluton most clearly separated from Mesozoic and Cenozoic plutonic and tectonic activity among the three Precambrian samples. It should be noted that it is overlapped by Late Tertiary volcanic rocks, however.

(5) The Dells appears to have a radioactive accessory mineral assemblage and crystallization history distinctly different from those of the Ruin and Lawler Peak Granites. Examination, identification and analysis of the complete mineral assemblage should be illuminating as to the origins of the differences in bulk character and behavior.

LAWLER PEAK GRANITE

GEOGRAPHIC AND GEOLOGIC SETTING

The sample is derived from the granite pluton of Lawler Peak, two miles northeast of the Bagdad mining district, in Yavapai County, west-central Arizona (see Figs. 1 and 2 for the general location). The precise location is from a boulder broken in road construction, on the road to the Hillside Mine in the NE 1/4, SW 1/4, Sec. 27, T. 15 N., R. 9 W. about 800 m S 70° W from Lawler Peak. This location is shown as 1 in the southwestern portion of the pluton in the attached simplified geologic map of the Bagdad area (Fig. 10).

Anderson, et al. (1955) provided detailed descriptions of the geological setting and a petrographic description of a portion of this pluton. Aldrich, et al. (1958) suggested an approximate age of 1350 m.y. (Table 8) for the granite of Lawler Peak, from studies of several different isotopic systems in several granite and pegmatite minerals. Silver (1966, 1967) established a more precise age of the pluton as slightly more than 1400 million years. He defined the host terrane for the pluton as part of a great regional volcano-plutonic complex which formed between 1700 and 1800 million years ago and which is temporally correlative with the type Yavapai Series in the Jerome-Bradshaw Mountains, 100 km to the east. This interpretation was supported by further work reported in Anderson, et al. (1971) and in Anderson and Silver (1976).

In the course of these investigations it was noted (Silver, 1968a, 1976) that the Lawler Peak Granite and the surrounding Bagdad terrane are part of a great regional Precambrian uranium geochemical anomaly extending from western Arizona northeast to central Colorado (Fig. 4). The initial recognition of this anomaly derived from observations of unusually high uranium concentrations in granitic and rhyolitic zircon separates used for U-Th-Pb isotopic studies investigating the geochronology of the Precambrian terranes in the southwestern United States.

The field geology context of the Lawler Peak pluton is well-documented, by virtue of the work of Anderson et al. (1955). In the wall rock on its northwest flank, and elsewhere in the vicinity, several uranium prospects (including the Hillside Mine) have been identified which may owe their geologic development to their proximity to the uraniferous granite. Thus an extensive geochemical study of the pluton appears justified and is in progress in our laboratory.

A large exposure of Lawler Peak Granite, approximately 25 km^2 in area, is found in a window nearly surrounded by overlapping late Tertiary-Quaternary volcanic and terrigenous sedimentary rocks 2 to 8 km northeast of the Bagdad Mine (Fig. 10). A probable extension of the pluton with approximately twice the areal exposure reappears on the northeast side of Blue Mountain. The entire intrusive area displays anomalous high U and Th radioactivities observed in a recent airborne survey (Aero Service, 1979; Fig. 8). Unconformable younger volcanics conceal the northern intrusive contact under Bozarth Mesa and indicate the total pluton may be significantly larger than the approximately 80 square km exposed. Other porphyritic biotite-rich granites south of Bagdad also were called Lawler Peak by Anderson et al. (1955) but Silver (1966, unpubl.) has shown most of these to be a distinctly older generation. The name Waters Peak Granite is now suggested for these other granites.

Figure 10
Simplified geological map of the Bagdad, Arizona, area, modified from the work of Anderson, Scholtz and Strobell, 1955. The granite sample investigated in this report came from the locality indicated by a filled triangle labelled 1.

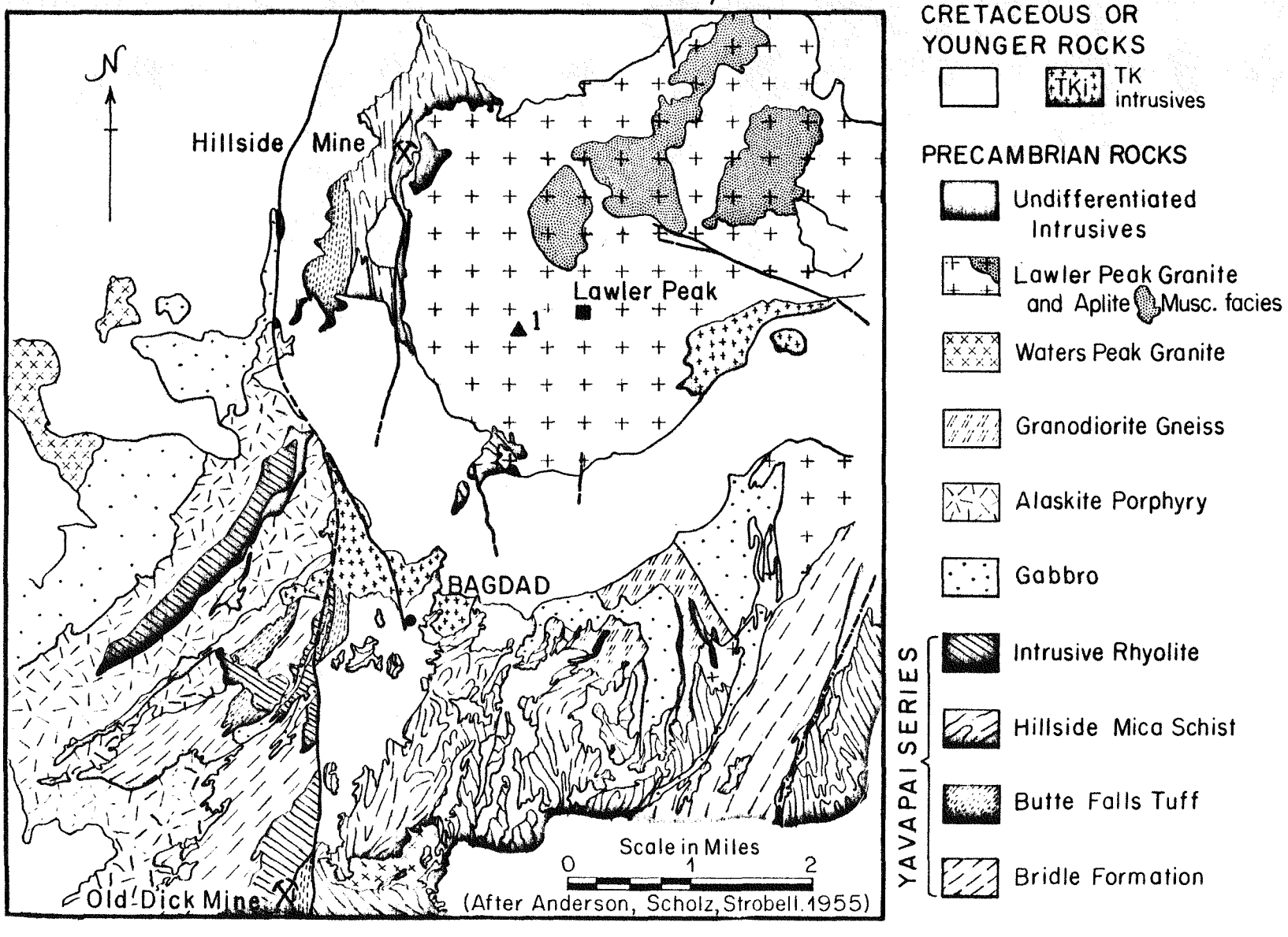
GEOLOGIC MAP OF THE BAGDAD, ARIZONA AREA
N
Hillside Mine
Lawler Peak
1
BAGDAD
Old Dick Mine
Scale in Miles
0
1
2
(After Anderson, Scholz, Strobell. 1955)
CRETACEOUS OR YOUNGER ROCKS
TKi
TK intrusives
PRECAMBRIAN ROCKS
Undifferentiated Intrusives
Lawler Peak Granite and Aplite
Musc. facies
Waters Peak Granite
Granodiorite Gneiss
Alaskite Porphyry
Gabbro
YAVAPAI SERIES
Intrusive Rhyolite
Hillside Mica Schist
Butte Falls Tuff
Bridle Formation

Figure 10

TABLE 8

Isotopic ages measured on the Lawler Peak Granite, recalculated from the data of Aldrich et al., 1958.

Rock type	Mineral	Apparent Ages (m.y.)*					
		$^{40}Ar-^{40}K$	$^{87}Sr-^{87}Rb$	$^{206}Pb-^{238}U$	$^{207}Pb-^{235}U$	$^{207}Pb-^{206}Pb$	$^{208}Pb-^{232}Th$
Granite	zircon			625	760	1180	273
	muscovite	1390	1361				
Pegmatite	lepidolite	1409	1468				

*All ages recalculated to the constants recommended by the Subcommission on Geochronology of the IUGS Commission of Stratigraphy (Steiger & Jäger, 1977).

The Lawler Peak body was intruded discordantly into older Precambrian rocks with which it is in visible contact on its west and southwest sides. No Paleozoic or Mesozoic stratified rocks are present on or near the pluton, but regional structural considerations suggest they may have been present at elevations 1000 to 3000 ft (300 - 900 m) higher than present surface exposures of the granite. The granite is intruded in turn by late Cretaceous or Tertiary? porphyries along its southern and eastern margins. A late Tertiary erosion surface with 1400 ft (400 m) of relief was cut on the crystalline rocks of the Bagdad region. Conglomeratic sedimentary rocks with intercalated and capping volcanic strata subsequently filled and subdued most of this relief. Much of the western lobe of the Lawler Peak Granite (from which this sample was taken) stood high above the general erosion surface and the inundating fill. It is possible, indeed probable, that the present sampling sites have underlain a stripped erosion surface for most of Cenozoic time. Quaternary erosion has exhumed the pluton and incised much of the major drainage of Boulder Creek within it so that present relief is in excess of 500 m.

GENERAL PETROGRAPHY OF THE GRANITE

Anderson et al. (1955) describe the granite as comprised of a main facies and a muscovite facies. The main facies is typically a coarse porphyritic biotite-muscovite granite with large tabular zoned potassium feldspar phenocrysts 3 to 8 cm in diameter. The tabular phenocrysts commonly show distinct to strong planar orientation, sharing that foliation with uncommon xenoliths. The megacrysts are locally concentrated into pods of nearly pure alkali-feldspar. Other minerals of the granite lack any evidence of preferred orientation even at the margins of the pluton where the texture becomes somewhat finer grained and apparently was chilled early in the emplacement history.

We have noted portions of the pluton in which biotite is essentially the only mica, although the granite is otherwise similar to the main facies.

The muscovite facies is a somewhat lighter colored granite in which biotite is absent and muscovite is more abundant than in the main facies (Fig. 10). It occurs as masses up to 2 km in diameter within the main facies, with contacts that are locally sharp but elsewhere are quite gradational. Numerous late aplites, pegmatites and fluorite-beryl-wolframite-bearing quartz veins are present in and near the muscovite facies. Anderson and his colleagues (p. 19, op. cit.) inferred the muscovite granite probably to represent a pneumatolytic alteration facies of the principal two-mica granite or a late crystallization phase.

PETROGRAPHY OF THE LAWLER PEAK GRANITE #1 SAMPLE

A large sample (75 kg) of main facies granite was collected in 1962. The megascopic mineralogy consists of dark gray smoky quartz, cream to yellowish, slightly altered, plagioclase, large phenocrysts of pale flesh-brown potassium feldspar and distinct books of muscovite and biotite (Fig. 11). Texturally all minerals form an unfoliated, coarse, inequigranular texture with average grain size between 5 and 10 mm, spotted with the conspicuous megacrysts of platy potassium feldspar, 3 to 8 cm in largest dimensions.

Figure 11
Photograph of a hand specimen of the Lawler Peak Granite #1 sample which displays the abundant potassium feldspar megacrysts and the smoky gray quartz.

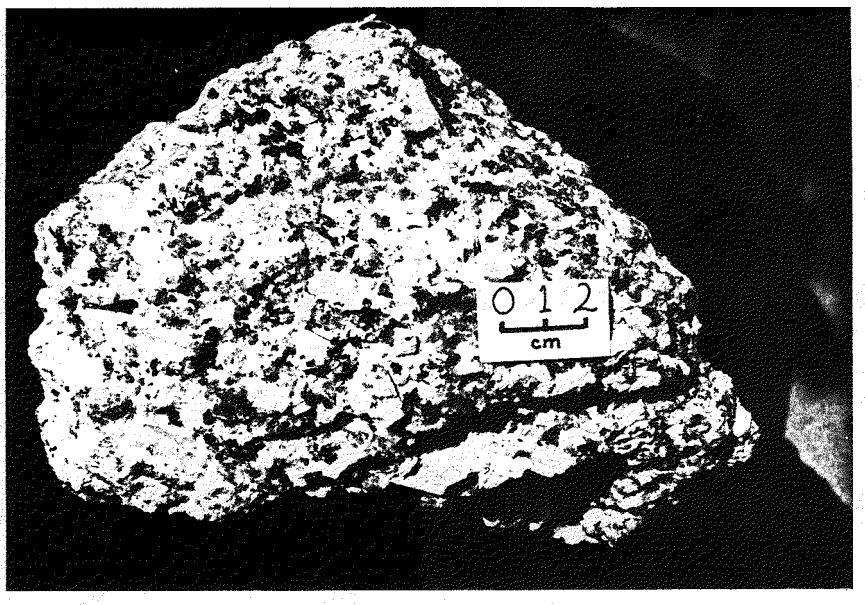

Figure 11

In thin-section (Figs. 12,13), quartz forms coarse unstrained anhedral aggregates. Plagioclase is subhedral, twinned and weakly zoned, with compositions ranging from sodic oligoclase cores to albite rims. The cores show a dispersed cloud of fine oriented flakes of white mica (Fig. 17) with sparse epidote and dusty yellowish clays. The potassium feldspar is anhedral in the groundmass, subhedral to euhedral in phenocrysts. It is a coarse perthitic microcline with two or more generations of exsolved sodic phases visible (Figs. 14-16). Alteration is slight to absent. The coarse perthite megacrysts are commonly Carlsbad-twinned, with small euhedral plagioclose crystals dispersed in concentric internal zones. The biotite is platy, pleochroic from dark greenish-brown to pale yellow, partly chloritized and with numerous minute, high index to opaque inclusions, many of which are surrounded by strong pleochroic haloes (Figs. 18-20). The muscovite is generally somewhat coarser than the biotite, tends to form thicker books and is sometimes found with intercalated layers of biotite in its structure (Figs. 22-24,27). It too displays pleochroic haloes (pale brown) around minute inclusions (Fig. 25). Epidote, chlorite and fluorite commonly form replacement layers up to 0.5 mm thick in, and coronas around, the biotite (Fig. 21). Opaque minerals with outlines ranging from anhedral to euhedral form small, widely distributed grains. The opaque minerals commonly are aggregated (Figs. 12,22).

Zircon, monazite, and a variety of minute (0.3 mm) unidentified brown, high-relief isotropic minerals are included among the radioactive accessory mineral assemblages (Figs. 24,25). The zircon grains commonly show well-defined euhedral forms and internal zones with a wide range of metamictization reflected in variable opacity and reduction of interference colors (Figs. 48-50). Monazite is pale yellow to colorless and euhedral to subhedral (Figs. 24,25,56). The close association between opaque mineral aggregates and assemblages of radioactive accessory minerals is pronounced (Figs. 24,25).

Fluorite is usually colorless but in many places it shows tints of pale to deep purple, particularly near contacts with accessory minerals inferred to be radioactive.

Although many accessory minerals are spatially associated with the mica plates and opaque mineral aggregates (Figs. 26-28) a significant number are dispersed among and included in the feldspars and quartz (Figs. 22,23).

In summary, the sample displays a typical undeformed plutonic igneous texture. The estimated mineral abundances from counts on four thin sections and from two cut slabs totalling 125 cm^2 are given in Table 9. A major and trace element analysis from a large homogenized bulk sample is given in Table 10. A calculated CIPW normative analysis is given in Table 11. From these data, the rock is called a biotite muscovite adamellite, close to a true granite in composition. Field observations on the variable abundances of the alkali feldspar phenocrysts suggest that variations between adamellite and granite on a local scale are commonplace.

Figure 12
Photomicrograph of typical Lawler Peak Granite #1 groundmass mineralogy and texture. The coarse opaque aggregates are made up of magnetite and ilmenite. The olive-brown biotite at the upper edge of the field, left of center, is 1mm long. Thin section, plane light.

Figure 13
Photomicrograph of the same field as Fig. 12. Note the albite-twinned oligoclase, "tartan" twinned microcline-perthite, coarse book muscovite (pink interference color) intergrown with biotite at the upper edge, and the undulatory extinction in the yellow-gray quartz at the lower right. Sericite is present in the cores of dusty plagioclase, center right. Thin section, crossed nicols.

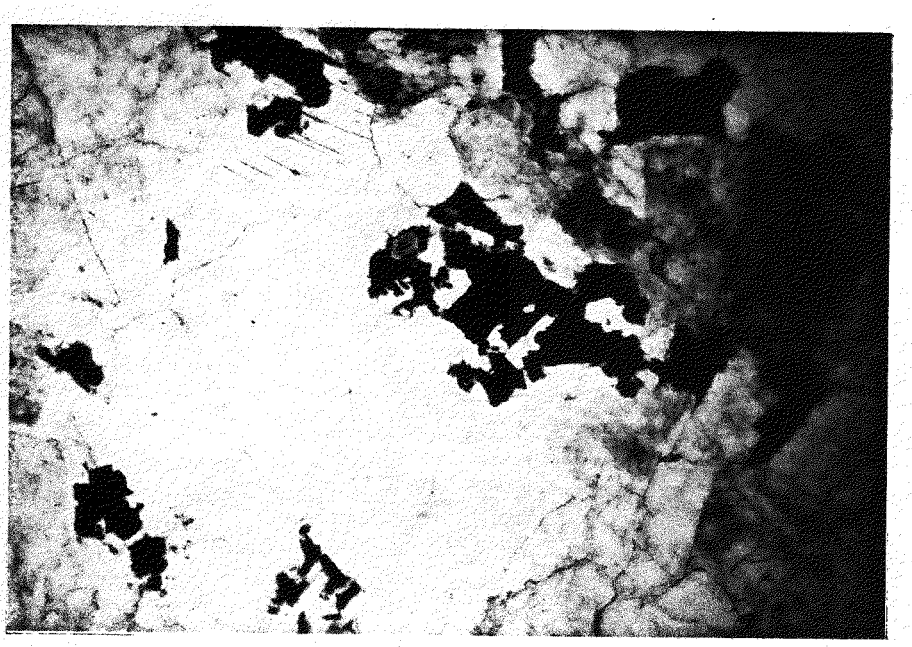

Figure 12

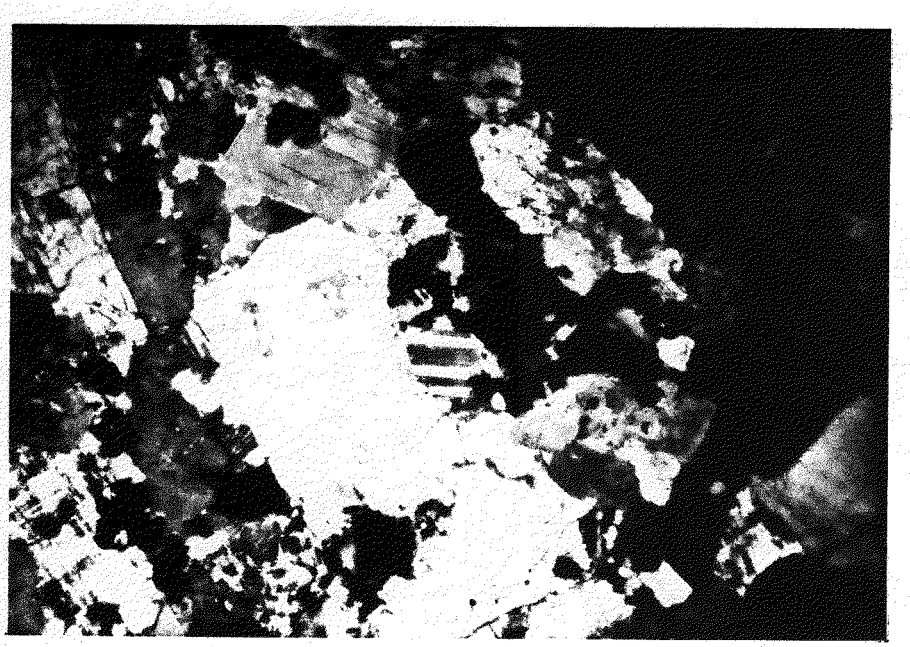

Figure 13

Figure 14
Photomicrograph of a typical Carlsbad twinned microcline-perthite megacryst, Lawler Peak Granite #1. Note late stage minerals following transverse fractures. Thin section, plane light.

Figure 15
Same field as Fig. 14, thin section, crossed nicols. Note plagioclase inclusions in the perthite megacryst. Sericite is a conspicuous mineral in the transverse fractures.

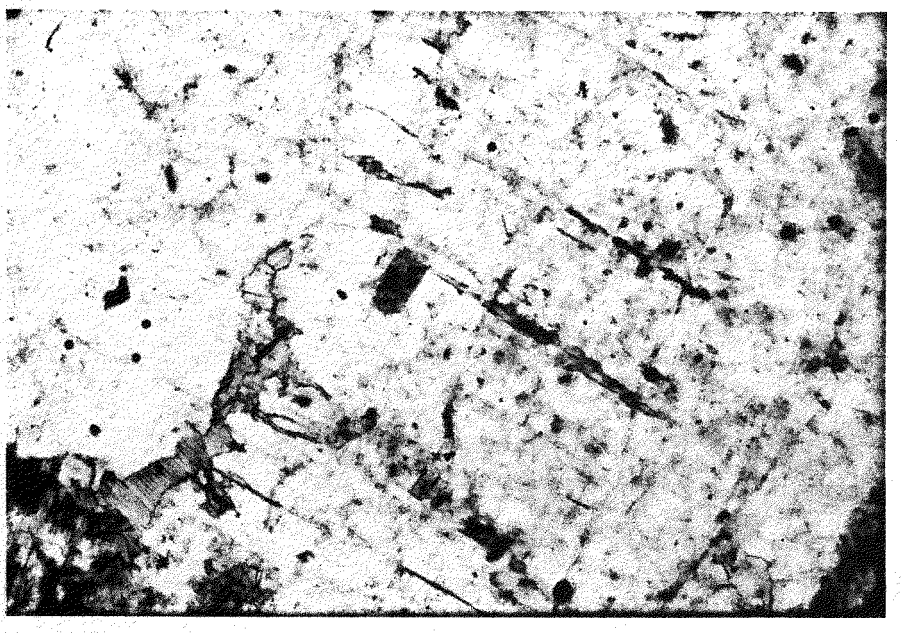

Figure 14

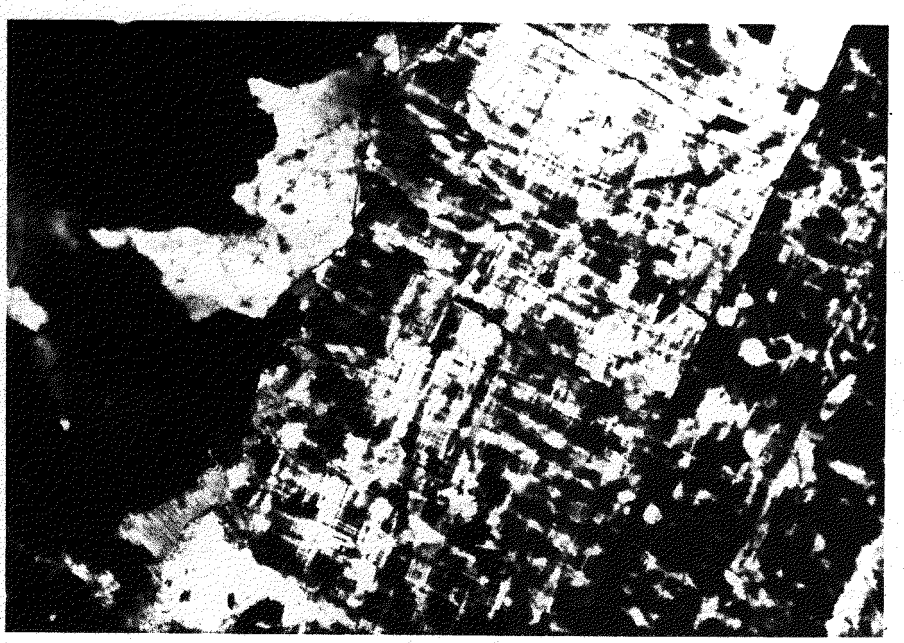

Figure 15

Figure 16
Photomicrograph of a perthite megacryst and subhedral to euhedral plagioclase inclusions analyzed by electron microprobe. The field of view is 2.5 mm by 1.8 mm. Thin section, crossed nicols.

Figure 17
Photomicrograph of albite-twinned oligoclase with characteristic inclusions of late stage alteration fluorite (isotropic, black) and muscovite. The field of view is 650 µm by 450 µm. Thin section, crossed nicols.

Figure 16

Figure 17

Figure 18
Photomicrograph of a biotite crystal with characteristic opaque and radioactive mineral inclusions. The latter are surrounded by dark pleochroic halos. The crystal is 2 mm across. Thin section, plane light.

Figure 19
Photomicrograph of a zircon inclusion in biotite showing characteristic form, zonation, and pleochroic halos. The zircon is 150 μm long. Thin section, plane light.

Figure 18

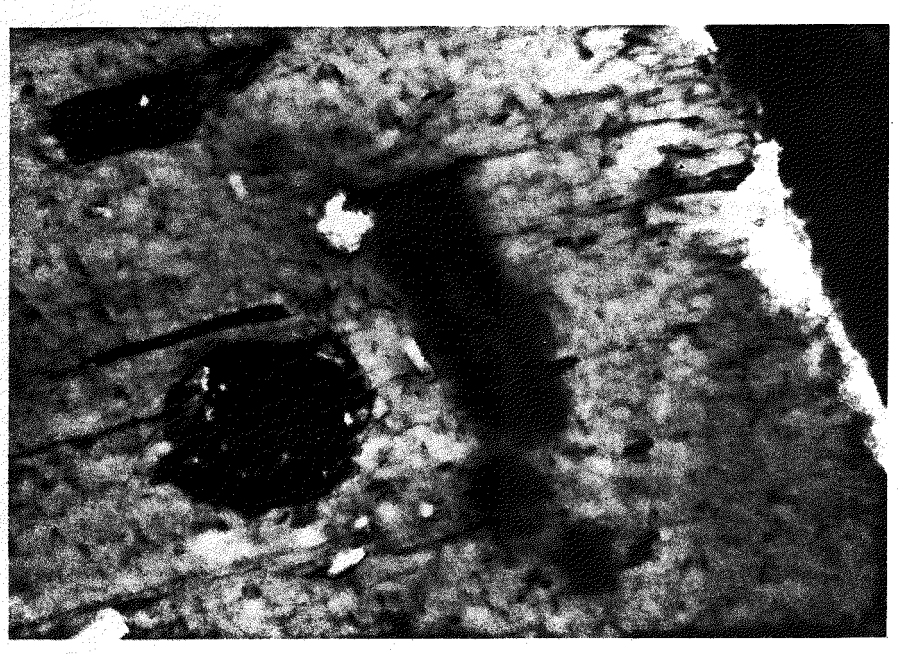

Figure 19

Figure 20
Photomicrograph of clear euhedral apatite, late epidote and zircon? inclusions in biotite. The larger epidote aggregate at the right and the ones at the top and lower left have allanite cores. The epidote adjacent to the apatite at the upper left is nearly free of allanite. Note the absence of pleochroic haloes around apatite and epidote in contrast to the zircon?. The apatite in the upper left corner of the field is 200 μm long. Thin section, plane light.

Figure 21
Photomicrograph of biotite with interlayers of paler chlorite and colorless muscovite. In the center of the field a zircon crystal in a muscovite layer has been analyzed by electron microprobe. In the upper right corner a monazite crystal has been analyzed similarly. The opaque grain at lower right is a partially skeletal manganilmenite. Rectangular brown surface stains around the zircon and monazite indicate electron microprobe (EMP) scan areas. The field of view is 2.2 mm by 1.5 mm. Polished thin section, plane light.

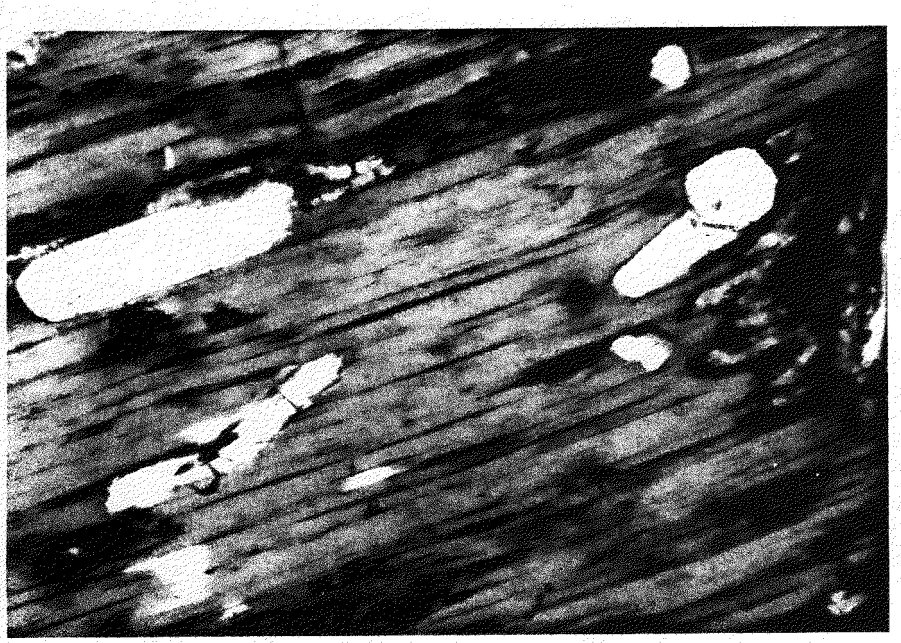

Figure 20

Figure 21

Figure 22
Photomicrograph showing the clustering of radioactive accessory minerals in several hosts including muscovite and quartz and in intimate association with opaque mineral aggregates. The aggregate of opaque minerals in the lower center of the field is 1 mm across. Thin section, plane light.

Figure 23
Photomicrograph of the same field as Figure 22, showing accessory minerals in muscovite (upper center), quartz (middle right), and altered plagioclase (middle left). Note that the opaque aggregate is confined to the albite rim of the plagioclase. Thin section, crossed nicols.

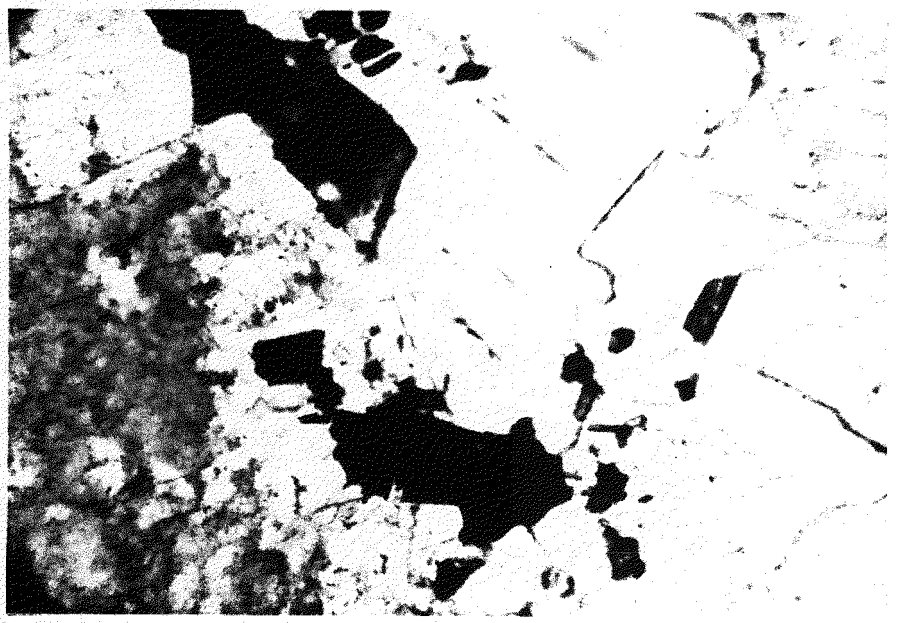

Figure 22

Figure 23

Figure 24
Photomicrograph of the right portion of Figs. 22 and 23 showing details of zircon and monazite crystals near a triple contact point of quartz, muscovite and opaque grains. The large zircon in the upper right of the field is 100 µm long. Thin section, plane light.

Figure 25
Photomicrograph of equant monazite and prismatic zircon inclusions in muscovite displaying distinct pale brown pleochroic haloes. Note the abundance of opaque minerals. The large monazite in the center of the field is 50 µm across. Thin section, plane light.

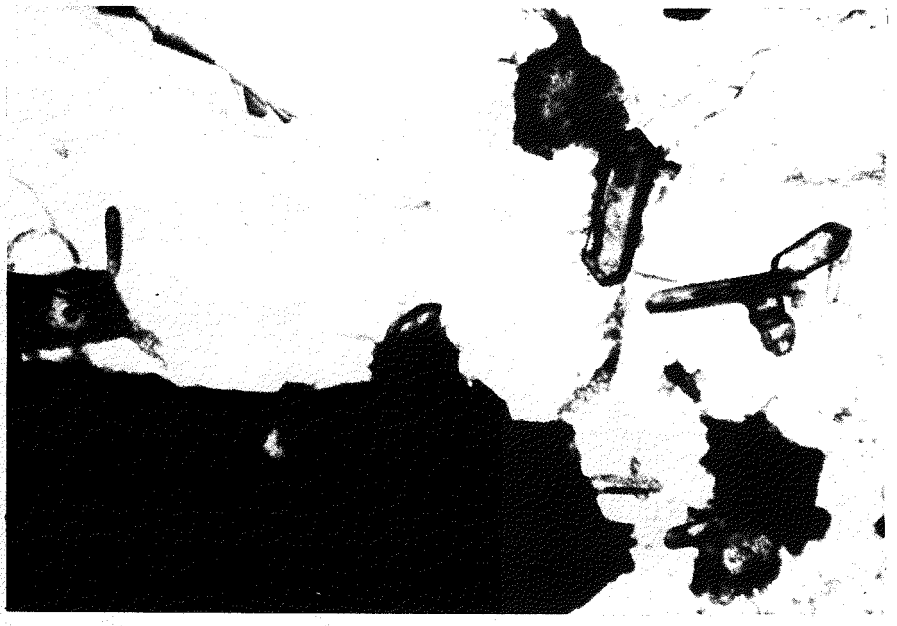

Figure 24

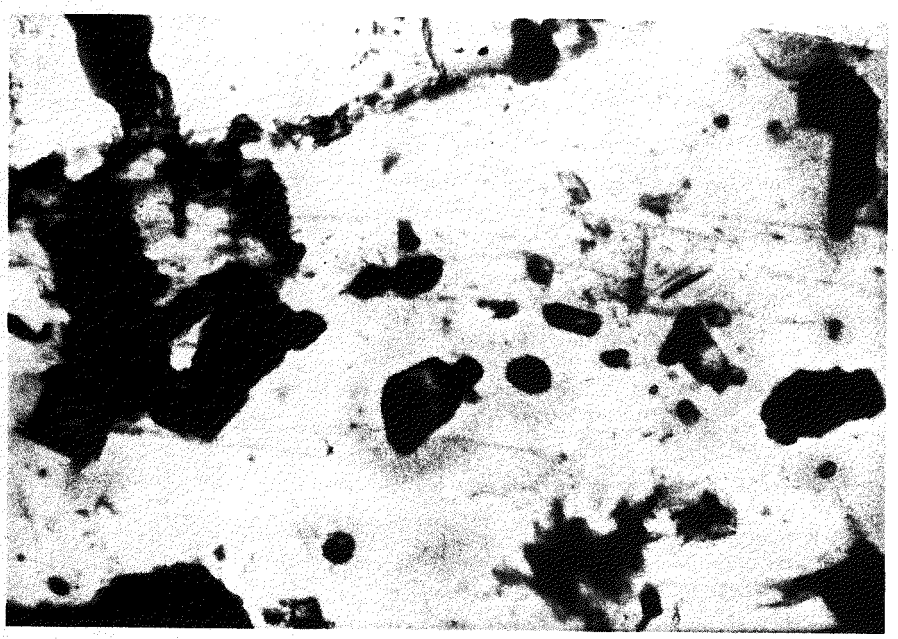

Figure 25

Figure 26
Photomicrograph showing the complex distribution of trace mineral inclusions in the biotite-chlorite intergrowths. Numerous opaque grains, sphene-ilmenite intergrowths, and radioactive zircon, apatite and monazite crowd the biotite host. The radiating aggregate at the top is epidote. The field of view is 3 mm by 2 mm. Thin section, plane light.

Figure 27
Photomicrograph showing detail of the center lower edge of the field of Fig. 12, showing intergrown biotite and muscovite. In the center, biotite replacement of muscovite is inferred. The field of view is 3 mm by 2 mm. Thin section, plane light.

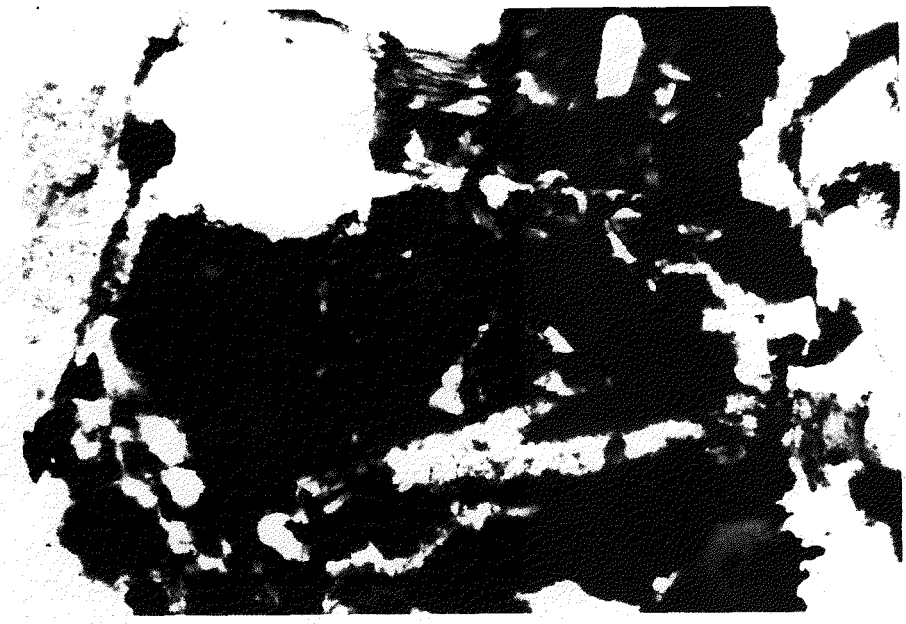

Figure 26

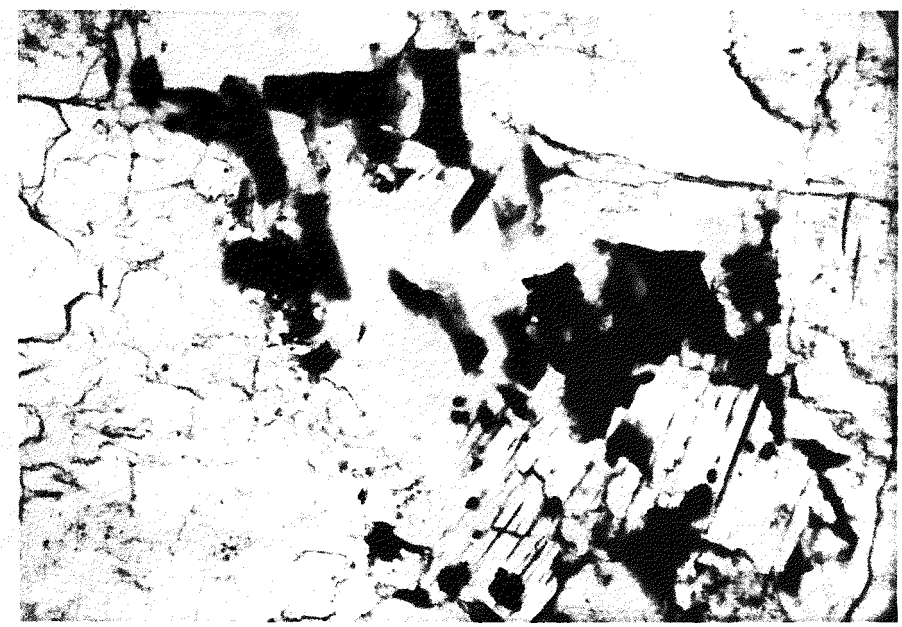

Figure 27

Figure 28
Photomicrograph, in oblique reflected light, of magnetite with inclusions of monazite (yellow, right of center) and other minerals. The monazite is 30 μm across. Polished thin section.

Figure 29
Photomicrograph of a hand-picked mineral separate of niobian rutile crystals. The mean crystal diameter is about 200 μm. Unmounted.

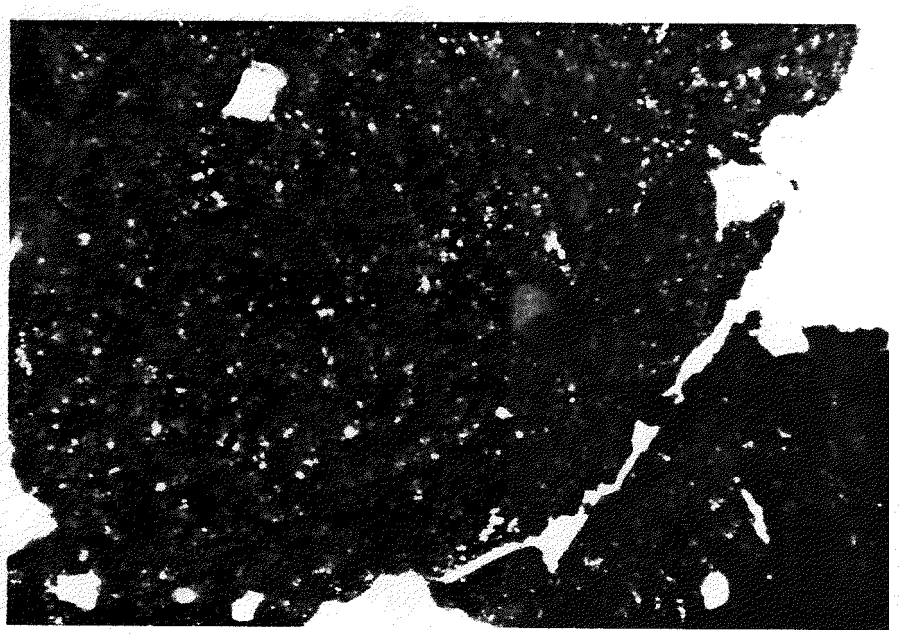

Figure 28

Figure 29

TABLE 9

Combined thin section and slab mode[1]

Lawler Peak Granite #1

	Volume %	Weight %
Quartz	34.0	34.1
K-feldspar	37.5	36.3
Plagioclase	21.7	21.5
Muscovite	3.7	4.1
Biotite	2.1	2.6
Opaques	0.390	0.728
Epidote	0.296	0.358
Fluorite	0.180	0.216
Apatite	0.074	0.090
Zircon	0.035	0.057
Monazite + Xenotime	0.002	0.004
Brannerite?	0.002	0.004

[1] Quartz : K-feldspar : Plagioclase determined on slab (1180 points)

Muscovite : Biotite determined on thin section (8000 points)

Minor minerals determined on thin section (31,540 points)

TABLE 10

Major and trace element chemistry of

Lawler Peak Granite #1

(Analyst - B. Chappell, A.N.U.)

Major Elements	Weight %
SiO_2	75.33
TiO_2	0.22
Al_2O_3	12.77
Fe_2O_3	0.79
FeO	0.64
MnO	0.07
MgO	0.42
CaO	1.07
Na_2O	3.09
K_2O	4.31
P_2O_5	0.09
S	<0.02
H_2O^+	0.07
H_2O^-	0.11
CO_2	0.29
rest	0.15
	100.05

Trace Elements	ppm
Ba	280
Rb	339
Sr	103
Pb	27.5
Th	30.2
U	19.8
Zr	128
Nb	36.5
Y	51
La	39
Ce	91
Nd	30
Sc	7
V	10
Cr	<1
Mn	540
Ni	<0.5
Cu	9.0
Zn	47
Ga	17.0

TABLE 11

CIPW normative composition of Lawler Peak Granite #1

Quartz	38.53
Orthoclase	25.78
Albite	26.45
Anorthite	4.78
Corundum	1.31
Hypersthene	1.35
Magnetite	1.16
Hematite	0.00
Ilmenite	0.42
Apatite	0.22
An content	15.3%
Differentiation Index	90.8
Color Index	2.93

Determination of Modal Composition

Because of the considerable range in the grain size and abundance of the minerals in the granite, a combination of methods was employed in obtaining an estimate of its modal composition.

The relative abundance of the principal rock-forming minerals (quartz, plagioclase, K-feldspar and mica) was determined by point counting rock slabs. Low-density point-counting of thin sections cut from areas interstitial to the K-feldspar phenocrysts gave the proportions of muscovite, biotite-chlorite and opaque minerals relative to quartz and the feldspars. High density counting of the same sections provided an indication of the relative abundance of the more common of the accessory minerals: epidote, apatite, fluorite, monazite, xenotime, sphene-ilmenite, U-titanate, zircon and opaque minerals. The modal composition calculated from the combined point-counting data is listed above in Table 9.

The point-count mode is considered to be a relatively reliable determination of the major mineral mode, but it provides only a crude estimate of the accessory mineral abundances. As will be discussed below, if the relative importance of the various accessory minerals as sites for uranium, thorium and radiogenic lead in this rock is to be assessed even semi-quantitatively, alternative methods of placing limits on trace mineral abundances must be used.

MINERALOGICAL INVESTIGATIONS

Introduction

The minerals in the Lawler Peak Granite #1 were identified and studied optically, by electron microprobe (EMP), scanning electron microscopy (SEM) and X-ray diffractometry. Most of the EMP analyses were done on grains *in situ* in polished thin sections, but analyses also were made of grains selected from high-density mineral separates prepared especially for that purpose or for the isotopic studies.

An alphabetical listing of the minor and trace minerals identified in the granite is given in Table 12. Of the twenty-five minor and trace minerals recognized, fifteen (marked in Table 12 by asterisks) contain uranium or thorium in greater concentrations than does the bulk rock. Table 12 probably does not include all accessory minerals in the rock; some of the high-density mineral separates show as yet unaccounted for high radioactivity levels, indicating the possible presence of additional radioactive species which still remain to be isolated and identified.

Individual grains of most of the identified radioactive species commonly are complex. Physically, they may be mixtures of phases and states due to mutual inclusions, epitaxial growth relations among isomorphous species, exsolution, secondary replacement and radiation damage. Chemically, they usually represent multi-component solid solution series.

The variation in uranium and thorium concentrations within a given species and even within single crystals may be considerable. Uranium concentrations in zircon for example, range from much less than 1000 to more than 20,000 ppm, about two orders of magnitude, within some single grains. Determined efforts were made to purify and characterize fractions of each mineral species selected to represent major portions of the compositional range within that species. It is the recognition and characterization of such variability within mineral species in the Lawler Peak Granite that is a major facet of this research. It has made possible the utilization of intra-species variability to explore correlations between chemical composition and susceptibility to chemical and/or isotopic mobilization; to examine the crystallization history of each species in the context of the general rock paragenesis; and to obtain some unique information bearing on the timing of significant alteration episodes in the history of this granite sample.

Mineral Separations and the Problem of Representative Mineral Populations

The high-density mineral concentrates from which specific minerals were selected for EMP characterization and for isotopic analysis were prepared by procedures used routinely in this laboratory. Those procedures were designed to produce a high yield of high-purity concentrate at the expense of achieving quantitative recovery. At every step, some loss of sample and some fractionation of the mineralogical composition of the product relative to that of the starting material occurred. It is possible to make a qualitative assessment of the sense of fractionation caused by each operation, as is done below, but the involved procedure of continuous monitoring of mineralogical and isotopic mass balance was not attempted.

TABLE 12

Minor and trace mineral species identified in Lawler Peak Granite #1

*Allanite
**Anatase
*Apatite
**Biotite
Bismuthinite
*Bismutite
**Chlorite
*Epidote
Fluorite
Hematite
**Magnetite
Manganilmenite
*Monazite
Muscovite
Pyrite
Rutile
Niobian rutile
Scheelite
Sericite
*Sphene
*Thorite
*Uranium titanate, Brannerite?
*Uranosilicate, Coffinite?
*Xenotime
*Zircon

*Radioactive species
**Radioactivity probably due to surficial U, Th

Fifty-nine pounds (26.8 kg) of granite were reduced from fist size to chips and then to pass an 0.015 inch slit (380 μm) by jaw crusher and disc mill. A maximum crushed grain size of 0.015 inches was chosen as optimum for achieving adequate liberation of inclusions while preserving a large proportion of the high-density crystals intact. Both crushing operations were more efficient in the disaggregation of the brittle framework silicates (quartz and the feldspars) than in the breakdown of the more flexible sheet silicates (biotite-chlorite and muscovite). In the final concentrate therefore, accessory minerals which occurred in the granite as inclusions in sheet silicates were probably relatively depleted.

A first-order concentrate of high-density minerals was prepared from the crushed rock using a Wilfley shaking table. As a dynamic hydraulic process, the Wilfley table separation strongly discriminated against minerals with finer grain sizes, to the extent that most grains finer than about 0.001 inches (25 μm) were lost from the concentrate. Tests carried out using other samples have shown that this loss would have removed a disproportionately large fraction of radioactive phases.

The high-density mineral concentrate was purified further by settling in high-density liquids, ethylene tetrabromide (density 2.96 g/cc) and methylene iodide (density 3.33 g/cc). These procedures also discriminated against finer grained particles, which separated more slowly and were more readily entrained in the floating fractions.

Subdivision of the high-density concentrate to assist in the isolation of individual mineral species was achieved by utilizing the minerals' different magnetic properties. Ferromagnetic minerals were extracted with a powerful hand magnet. The remaining concentrate was then subdivided on the basis of paramagnetic susceptibility using a Frantz isodynamic separator. In part to improve the efficiency of the magnetic separations, the concentrate first was sized on 30, 50, 100 and 200 meshes (600, 300, 150 and 75 μm respectively).

Separates of the greatest mineralogical purity were obtained for grain sizes finer than 100 mesh (150 μm), below which size limit relatively few crystal aggregates survived the crushing procedures. Nevertheless, overlapping intrinsic magnetic properties of some minerals and the common presence of fine inclusions which caused a smearing of the magnetic properties of others necessitated the hand purification of all separates intended for analysis. Consequently, most of the analytical work was performed on fractions which were sufficiently coarse grained for effective hand picking (coarser than 200 mesh, 75 μm).

In summary, problems of incomplete liberation and recovery, of sacrificing assurance that the sample is completely representative for assurance of high purity and of working on a restricted range of grain sizes prevent the analyzed samples of each mineral species from representing the complete range of variability within that species in the rock. Nevertheless, the samples analyzed are considered to represent a major fraction of each species, certainly sufficient to establish their principal chemical and isotopic characteristics.

Major Minerals

Quartz

About thirty-four volume percent of the granite is quartz (Fig. 11). The large, gray, anhedral crystals are nearly pure SiO_2 (Tables 13,14), although a trace of iron may be present in grains juxtaposed to iron-rich accessory minerals. Commonly the quartz is permeated with swarms of extremely fine rutile needles, especially near the grain centers. The rutile is too fine for EMP spot analysis but scan photographs suggest it to be almost pure TiO_2, in contrast to the larger crystals of niobian rutile which occur as discrete grains.

Alkali Feldspar

About twenty-two volume percent of the granite is alkali feldspar. Alkali feldspar is present as very large, tabular, Carlsbad-twinned megacrysts (Figs. 11,14,15), which reach up to several centimeters in length, and also as a coarse-grained groundmass constituent (Fig. 13). The alkali feldspar is microperthitic, with the exsolution lamellae becoming broader and more numerous toward the crystals' margins.

The composition of the alkali feldspar is $Ab_5\ Or_{95}$, with virtually no An component (Tables 13,14). The sodium feldspar exsolution lamellae are $Ab_{94}\ Or_5$ with an An component of less than 1 percent. The composition of the lamellae therefore is in marked contrast to that of the microcrystalline plagioclase inclusions in the K-spar (Fig. 16) even though the Ab contents of the two are similar.

Plagioclase

About thirty-seven volume percent of the granite is plagioclase. Plagioclase is present in two principal forms, as a major mineral with grain size up to a centimeter (Fig. 11) and as euhedral, randomly oriented inclusions in alkali feldspar an order of magnitude smaller (Figs. 15,16).

The coarser plagioclase crystals are zoned normally from about Ab_{80} to Ab_{90} core to rim, with less than 1 percent orthoclase (Or) component (Tables 13,14). In contrast, the finer plagioclase crystal inclusions are zoned normally from Ab_{93} to Ab_{98} core to rim, also with less than 1 percent Or component. Plagioclase in both occurrences may show sericitization and extensive clay dust (Fig. 23), and in the coarser grains the sericite may be accompanied by fluorite and epidote (Figs. 17,34).

Micas

Sheet silicates (muscovite, biotite and chlorite) comprise slightly less than six volume percent of the granite (Fig. 11).

White mica is about twice as abundant as biotite-chlorite. It occurs principally as books of muscovite up to several millimeters in diameter (Figs. 22,31) but it also is present as fine-grained muscovite inclusions in the

TABLE 13

Selected major mineral microprobe analyses

Mineral	Quartz	Alkali Feldspar		Coarse-grained Plagioclase		Fine-grained Plagioclase		Muscovite		Biotite	Chlorite
		K-Spar	Exsolution Lamellae	Central	Edge	Central	Edge	Coarse-grained	Fine-grained		
SiO_2	100.0	65.3	68.5	64.5	66.0	67.1	68.8	46.5	46.1	36.7	28.3
TiO_2	—	—	—	—	—	—	0.1	0.7	0.1	2.1	0.2
Al_2O_3	—	18.3	19.3	22.4	21.0	21.0	19.7	28.2	30.3	16.3	19.3
FeO[1]	—	0.1	—	—[2]	—	—	—	5.6	3.9	18.3	25.2
MnO	—	na	na	na[3]	na	na	na	0.2	0.1	1.0	1.6
MgO	—	—	—	—	—	—	—	2.2	0.6	10.2	13.1
CaO	—	—	0.1	3.5	2.1	1.4	0.3	—	tr[4]	—	0.1
Na_2O	—	0.5	10.3	9.9	9.1	11.5	12.3	0.2	0.3	tr	—
K_2O	—	15.0	0.8	0.1	0.1	0.1	0.1	10.9	10.5	10.4	tr
P_2O_5	—	na	na	na	na	na	na	na	na	na	na
F	na	na	na	na	na	na	na	0.6	0.1	1.3	tr
Cl	na	na	na	na	na	na	na	tr	tr	tr	—
BaO	0.1	—	—	—	0.1	0.1	—	na	na	na	na
TOTAL	100.3	99.2	99.2	100.5	98.5	101.3	101.2	95.0	92.0	96.1[5]	88.3[5]

[1] cation oxidation state not determined

[2] below detection limit

[3] na; not analyzed for

[4] tr; trace amount detected

[5] trace Zn also detected

TABLE 14

Approximate formulae of major minerals based on microprobe analyses

QUARTZ	$Si_{1.00}O_2$			
ALKALI FELDSPAR				
K-spar	$(K_{.88}Na_{.04}Ca_{.00})Al_{1.00}Si_{3.02}O_8$	Ab-4.8	An-0.0	Or-95.2
exsolution lamellae	$(K_{.05}Na_{.88}Ca_{.01})Al_{1.00}Si_{3.01}O_8$	Ab-94.4	An-0.7	Or-4.9
COARSE PLAGIOCLASE				
central	$(K_{.01}Na_{.85}Ca_{.16})Al_{1.16}Si_{2.83}O_8$	Ab-83.0	An-16.2	Or-0.8
edge	$(K_{.01}Na_{.78}Ca_{.10})Al_{1.10}Si_{2.93}O_8$	Ab-88.0	An-11.3	Or-0.6
FINE PLAGIOCLASE				
central	$(K_{.01}Na_{.97}Ca_{.07})Al_{1.08}Si_{2.91}O_8$	Ab-93.1	An-6.3	Or-0.5
edge	$(K_{.00}Na_{1.03}Ca_{.01})Al_{1.00}Si_{2.98}O_8$	Ab-98.3	An1.3	Or-0.4

MUSCOVITE

coarse-grained

$(K_{.95}Na_{.03})Mg_{.22}Fe_{.32}Ti_{.03}Mn_{.01}Al_{1.41}[Al_{.85}Si_{3.15}]O_{10}F_{.14}(OH)_{2.28}$*

fine-grained

$(K_{.94}Na_{.05})Mg_{.06}Fe_{.23}Al_{1.70}[Al_{.79}Si_{3.21}]O_{10}F_{.02}(OH)_{3.73}$*

BIOTITE

$(K_{1.04}Na_{.01})Mg_{1.19}Fe_{1.20}Ti_{.13}Mn_{.06}Zn_{.02}Al_{.40}[Al_{1.12}Si_{2.89}]O_{10}F_{.32}(OH)_{2.05}$*

CHLORITE

$Ca_{.01}Mg_{2.09}Fe_{2.25}Ti_{.02}Mn_{.15}Zn_{.03}Cr_{.01}Al_{1.46}[Al_{.97}Si_{3.03}]O_{10}F_{.10}(OH)_{8.33}$*

*(OH) determined by difference

sericitized central zones of plagioclase crystals, commonly in association with fluorite and epidote (Fig. 17). These fine-grained inclusions differ significantly in chemical composition (Tables 13,14) from the coarse books of muscovite, being significantly poorer in magnesium, iron, titanium, and manganese, richer in sodium and strongly depleted in fluorine. This is consistent with their having formed by secondary replacement of feldspar, as has the sericite.

Biotite and chlorite commonly are mutually intergrown in apparent crystallographic continuity (Figs. 21,30)—and sometimes are themselves intergrown with muscovite Fig. 27. They are very similar in their proportions of magnesium, iron and manganese relative to total iron plus magnesium plus manganese (Tables 13,14). This is consistent with the textural evidence that chlorite has formed as a secondary replacement of biotite. However, the total Fe + Mg + Mn in the chlorite is enriched by about 35 percent relative to the biotite. In comparison to biotite-chlorite, muscovite is slightly enriched in iron relative to Fe + Mg + Mn probably because Fe^{3+} is more readily accepted in the dioctahedral sites, but the proportions of ferromagnesian elements are otherwise similar. Both the biotite and chlorite are unusually rich in manganese. Chlorite differs from biotite in having greater substitution of aluminum in the octahedral site and significantly lower titanium.

The sheet silicates are of particular interest in that they are a major host for included radioactive accessory minerals (Table 17; Figs. 18-21). Pleochroic haloes in the micas due to radiation damage are conspicuous (Figs. 18,19,25,26) as are both aggregates and isolated inclusions of zircon, monazite, xenotime, thorite and apatite. In the immediate vicinity of such radioactive inclusions, marked expansion of the host mica along its basal cleavage locally is observed. There is an additional close spatial association between the micas and large aggregates of opaque minerals (magnetite, manganilmenite, sphene-ilmenite, and pyrite, which themselves are hosts for inclusions of radioactive accessories.

Minor and Trace Minerals

Manganilmenite

Ilmenite occurs in opaque aggregates with magnetite (Figs. 12,79) as subhedral to euhedral grains up to about 1 mm in size, or associated with micas and clusters of radioactive minerals as skeletal or partially skeletal grains in the same size range. The skeletal grains may be part of the common sphene-ilmenite intergrowths (Figs. 74,75) or filled with quartz (Fig. 77) or feldspar (Fig. 21). In all of these occurrences, it is extremely manganese-rich with up to about 40 percent $MnTiO_3$ component substituting for $FeTiO_3$ (Tables 15,16). There is also limited substitution of Nb for Ti in the formula. Monazite, zircon, thorite, apatite, and quartz inclusions have been noted in manganilmenite in the opaque mineral concentrates and in the skeletal grain of Fig. 77. Sphene, white mica, zircon, apatite, and epidote have been noted in the sphene-ilmenite intergrowths.

Figure 30
Photomicrograph of the analyzed and leached mineral separate of biotite-chlorite, containing approximately three percent muscovite. Most of the bright grains are biotites which appear light due to reflections from their cleavage faces. A muscovite grain can be seen at the right edge of the photo about 2 cm up from the bottom edge. The diameter of the largest grains in the field is approximately 300 μm. Unmounted.

Figure 31
Photomicrograph of the high purity (99+ percent) muscovite concentrate utilized in the isotopic analyses. The mean grain diameter is about 150 μm. Unmounted.

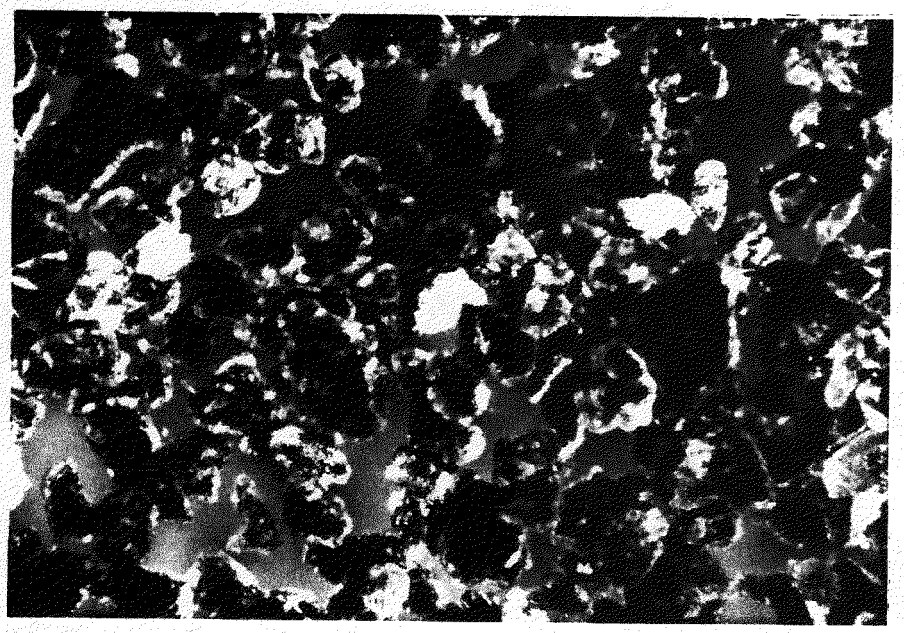

Figure 30

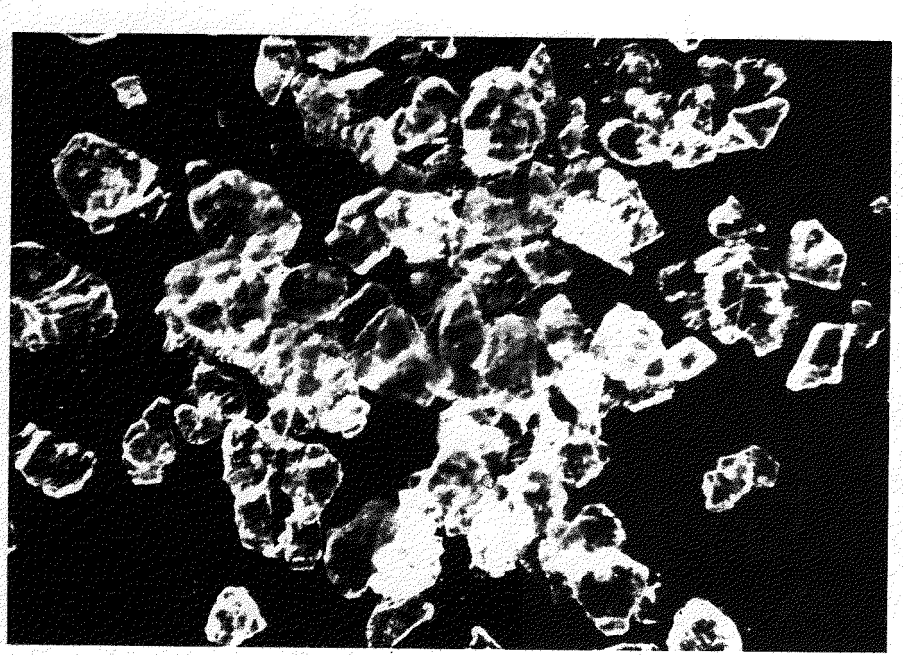

Figure 31

TABLE 15a

Selected high-density mineral microprobe analyses

Mineral	Mangan-ilmenite	Niobian Rutile	Magnetite	Pyrite[6]	Oxidized Pyrite	Epidote	Fluorite[6]	Apatite	
								Colorless	Gray
SiO_2	tr	—	0.2	—	4.8	37.8	0.1	—	0.1
TiO_2	51.3	70.6	—	—	—	—	—	—	—
Al_2O_3	—	—	—	—	—	24.6	—	—	—
FeO[1]	29.5	8.7	92.5[1]	48.1	81.4[1]	12.6	0.2	0.4	0.2
MnO	17.6	—	0.2	0.1	—	1.4	—	2.2	1.4
MgO	—	—	—	—	0.3	—	—	—	—
CaO	—	—	—	—	0.2	23.3	52.8	56.0	56.1
Na_2O	—	—	—	—	—	—	—	tr	0.1
P_2O_5	—	—	—	—	—	na[4]	—	40.5	41.8
F	—	—	—	—	—	—	47.0	2.3	3.8
PbO	—	—	—	0.4	—	—	—	—	—
ThO_2	—	—	—	—	—	—	—	—	—
UO_2[1]	—	—	—	tr	tr	—	—	—	—
ZrO_2	—	—	—	—	—	—	—	—	tr
Nb_2O_5	0.6	14.1	—	—	—	—	—	—	—
Y_2O_3	—	—	—	—	—	—	—	0.4	0.4
La_2O_3	—	—	—	—	—	—	—	—	—
Ce_2O_3[1]	—	—	—	—	—	—	—	—	0.3
Nd_2O_3	—	—	—	—	—	—	—	—	—
Sm_2O_3	—	—	—	—	—	na	—	—	—
Gd_2O_3	—	—	—	—	—	na	—	—	—
Tb_2O_3	—	—	—	—	—	na	—	—	—
Dy_2O_3	—	—	—	—	—	na	—	—	—
Ho_2O_3	—	—	—	tr	—	na	—	—	—
Er_2O_3	tr	—	1.4	1.0	1.5	na	—	—	—
Yb_2O_3	—	—	—	—	—	na	—	—	—
Lu_2O_3	—	—	—	tr	—	na	—	0.4	—
Hf_2O_3	—	—	—	—	—	—	—	—	—
Ta_2O_5	—	2.9	—	—	—	—	—	—	—
TOTAL	100.3	97.0	95.3	49.6[7]	88.8	99.8	100.1	103.3	99.5

[1] cation oxidation state not determined

[2] —; below detection limit

[3] tr; trace amount detected

[4] na; not analyzed for

[5] beam excited area within zircon broader than the narrow Th-rich band

[6] for pyrite and fluorite, abundances given as elemental percentages.

[7] S calculated by difference: 50.4%.

TABLE 15b

Selected high-density mineral microprobe analyses

Mineral	Zircon			Xenotime	Monazite		Sphene	Sphene in
	Central	Edge	Th-rich band		Central	Edge		Sphene-Ilmenite
SiO_2	33.1	31.3	31.6	1.2	1.7	1.9	30.5	31.9
TiO_2	—	—	0.3	—	—	—	27.8	28.0
Al_2O_3	—	—	1.1	—	—	—	6.6	7.1
FeO[1]	—	0.3	0.7	0.1	—	—	1.4	1.3
MnO	—	—	0.1	—	—	—	—	0.2
MgO	—	—	—	—	—	—	—	—
CaO	—	0.6	2.1	0.1	0.1	0.5	28.7	29.3
Na_2O	—	—	—	—	—	—	—	—
P_2O_5	—	0.5	1.4	33.0	29.1	27.0	—	—
F	—	—	0.3	—	0.5	0.5	0.8	1.7
PbO	—	—	—	0.6	0.3	0.4	—	—
ThO_2	—	—	2.7	1.1	2.6	8.1	—	—
UO_2[1]	—	1.2	1.4	2.7	—	—	—	—
ZrO_2	63.7	59.4	52.7	—	—	—	—	—
Nb_2O_5	—	—	0.3	—	—	—	0.6	—
Y_2O_3	tr	0.8	3.6	41.3	0.5	0.6	0.8	—
La_2O_3	—	—	—	tr	15.0	13.7	—	—
Ce_2O_3[1]	—	—	tr	—	32.5	29.8	—	—
Nd_2O_3	—	—	0.2	tr	12.6	11.6	—	—
Sm_2O_3	—	—	—	0.6	2.0	1.6	—	—
Gd_2O_3	—	—	—	1.3	1.6	1.4	—	—
Tb_2O_3	—	—	—	0.5	—	—	—	—
Dy_2O_3	—	—	—	5.1	—	—	—	—
Ho_2O_3	—	—	0.4	1.4	—	0.8	—	—
Er_2O_3	—	—	—	3.7	—	—	—	—
Yb_2O_3	—	—	0.7	4.9	—	—	—	—
Lu_2O_3	—	tr	0.7	0.5	—	—	—	—
HfO_2	1.7	3.4	3.0	—	—	—	—	—
Ta_2O_5	—	—	—	—	—	—	—	—
TOTAL	99.8	98.6	103.9[5]	98.8	98.5	97.9	98.1	99.5

TABLE 15c

Selected high-density mineral microprobe analyses

Mineral	Uranium Titanate--Brannerite?					Thorite	Uranium Silicate--Coffinite?	
	Zone A	Zone A	Zone B	Zone C	Zone D		U-rich zone	U-poor zone
SiO_2	3.0	3.3	9.5	4.1	14.7	17.7	13.7	15.5
TiO_2	32.1	34.7	38.3	63.4	23.4	0.6	—[2]	0.2
Al_2O_3	—	—	0.2	0.5	3.9	0.7	—	0.7
FeO[1]	1.3	1.2	1.9	5.4	27.2	0.6	2.1	16.0
MnO	0.5	0.4	0.4	0.2	0.4	—	—	—
MgO	—	—	—	—	0.6	—	—	0.1
CaO	3.8	3.0	3.4	1.6	2.8	1.5	5.4	3.9
Na_2O	—	—	—	—	—	tr	—	—
P_2O_5	—	—	0.4	0.2	0.4	1.1	—	0.4
F	—	—	—	—	—	0.7	0.5	1.0
PbO	1.2	2.6	5.3	2.3	5.0	—	0.3	0.3
ThO_2	2.8	5.9	6.4	6.5	3.6	47.7	3.6	17.3
UO_2[1]	50.4	41.6	22.2	3.9	5.2	2.2	63.3	36.4
ZrO_2	0.1	0.2	0.8	0.5	1.1	5.6	—	—
Nb_2O_5	1.0	0.9	1.4	2.6	1.5	0.6	—	—
Y_2O_3	1.0	1.0	0.7	0.4	0.3	5.1	tr[3]	1.1
La_2O_3	—	—	tr	—	tr	0.1	0.7	1.2
Ce_2O_3[1]	—	—	0.7	—	0.7	0.5	tr	0.7
Nd_2O_3	—	—	0.9	—	tr	0.4	—	0.6
Sm_2O_3	tr	tr	—	—	—	—	—	—
Gd_2O_3	—	tr	—	—	—	0.5	—	tr
Tb_2O_3	—	—	—	—	—	—	—	—
Dy_2O_3	—	—	—	—	—	1.3	—	—
Ho_2O_3	—	tr	—	tr	tr	—	0.8	0.7
Er_2O_3	—	—	—	—	0.4	0.5	—	tr
Yb_2O_3	—	—	—	—	—	0.7	—	—
Lu_2O_3	0.4	—	—	—	—	0.6	0.3	0.3
HfO_2	—	—	—	tr	—	0.2	—	—
Ta_2O_5	—	tr	—	—	—	0.3	—	—
TOTAL	98.6	97.1	93.7	92.9	92.1	90.1	91.4	96.5

TABLE 16

Approximate formulae of high-density minerals based on selected microprobe analyses

Manganilmenite	$(Fe_{.62}Mn_{.38})[Ti_{.98}Nb_{.01}]O_3$
Niobian Rutile	$(Ti_{.78}Fe_{.11}Nb_{.09}Ta_{.01})O_2$
Magnetite	$(Fe_{2.96}Si_{.01}Mn_{.01}Er_{.01})O_4$
Pyrite	$Fe_{.98}S_2$
Oxidized pyrite (hematite)	$(Fe_{1.84}Si_{.13}Mg_{.01}Ca_{.01}Er_{.01})O_3$
Epidote	$Ca_{1.94}(Fe_{.94}Mn_{.10})Al_{1.94}Si_{3.06}O_{12}(OH)$
Fluorite	$Ca_{.99}F_{1.87}$
Apatite	
Colorless	$(Ca_{4.91}Na_{.03}Mn_{.15}Fe_{.03}Y_{.02}Lu_{.01})[P_{.94}O_4]_3F_{.61}(OH,Cl)_{nd}$
Gray	$(Ca_{4.77}Na_{.02}Mn_{.10}Fe_{.01}Y_{.02}Dy_{.01}Ce_{.01})[P_{1.01}Si_{.003}]_3F_{1.03}(OH,Cl)_{nd}$
Zircon	
Central (clear)	$(Zr_{.95}Hf_{.02})[Si_{1.02}]O_4$
Edge (cloudy)	$(Zr_{.91}Hf_{.03}Ca_{.02}Y_{.014}U_{.01}Fe_{.01})[Si_{.984}P_{.014}]O_4$
High-Th (dark)	$(Zr_{.76}Hf_{.03}Ca_{.07}Y_{.06}Th_{.02}U_{.01}Fe_{.02}Yb_{.01}Lu_{.01}Ti_{.01}[Si_{.935}P_{.034}Al_{.037}]O_4F_{.03}$
Xenotime	$(Y_{.76}Dy_{.06}Yb_{.05}Er_{.04}U_{.02}Ho_{.02}Gd_{.02}Th_{.01}Sm_{.01})[P_{.96}Si_{.04}]O_4$
Monazite	
Central	$(Ce_{.47}La_{.22}Nd_{.18}Sm_{.03}Th_{.02}Gd_{.02}Y_{.01})[P_{.97}Si_{.07}]O_4$
Edge	$(Ce_{.45}La_{.21}Nd_{.17}Th_{.07}Sm_{.02}Ca_{.02}Gd_{.02}Y_{.01}Ho_{.01})[P_{.94}Si_{.08}]O_4$
Uranium Titanate—Brannerite?	
Zone A	$(U_{.72}Ca_{.27}Th_{.04}Y_{.03}Pb_{.02}Mn_{.03}Lu_{.01})[Ti_{1.56}Si_{.20}Fe_{.07}Nb_{.03}]O_{5.23}(OH)_{.77}$*
Zone A	$(U_{.60}Ca_{.20}Th_{.08}Y_{.03}Pb_{.05}Mn_{.02}Ho_{.01})[Ti_{1.66}Si_{.21}Fe_{.06}Nb_{.03}]O_{4.46}(OH)_{1.54}$*
Zone B	$(U_{.28}Ca_{.20}Th_{.08}Y_{.02}Pb_{.08}Mn_{.02}Zr_{.02}Nd_{.02}Ce_{.01}La_{.01})[Ti_{1.57}Si_{.52}Fe_{.09}Nb_{.04}]O_{2.63}(OH)_{3.37}$*
Zone C (Anatase)	$(Ti_{.74}Fe_{.07}Si_{.06}Ca_{.03}Th_{.02}Nb_{.02}U_{.01}Pb_{.01}Al_{.01})O_{0.74}(OH)_{1.26}$*
Zone D	$(Fe_{.33}Ti_{.25}Si_{.21}Al_{.07}Ca_{.04}Pb_{.02}U_{.02}Th_{.01}Nb_{.01}Zr_{.01}Mg_{.01})O_{0.60}(OH)_{1.40}$*
Thorite	$(Th_{.51}Zr_{.13}Y_{.13}Ca_{.08}Fe_{.03}U_{.02}Dy_{.02}Ti_{.02}Nb_{.01}Ce_{.01}Lu_{.01}Nd_{.01})[Si_{.84}P_{.05}Al_{.04}]O_4$
Uranium Silicate—Coffinite?	
U-rich zone	$(U_{.75}Ca_{.31}Fe_{.09}Th_{.04}RE_{.04}Y_{.01})[Si_{.73}]O_{.88}F_{.09}(OH)_{3.03}$*
U-poor Zone	$(U_{.33}Ca_{.17}Fe_{.55}Th_{.16}RE_{.06}Y_{.02}Ti_{.01}Mg_{.01})[Si_{.64}Al_{.03}P_{.01}]O_{2.64}F_{.14}(OH)_{1.22}$*
Sphene	$Ca_{1.00}(Ti_{.68}Al_{.25}Fe_{.04}Mg_{.01}Y_{.01}Nb_{.01})[Si_{.99}]F_{.08}O_{4.50}(OH)_{.42}$*
Sphene in Sphene-Ilmenite	$Ca_{1.00}(Ti_{.67}Al_{.26}Fe_{.03})[Si_{1.02}]F_{.18}O_{4.70}(OH)_{.12}$*

*(OH) by difference (Value is subject to overestimation if oxidation states of U, Fe, Ce assumed by program are incorrect or if unanalyzed elements present.)

Rutile

Rutile has two distinct occurrences in the Lawler Peak Granite. The major occurrence of rutile is as equant, nearly black grains up to about a millimeter in diameter. Near absence or subordinance of the prism faces to the pyramidal terminations causes the grains to have a pseudo-dodecahedral form (Fig. 29). EMP analysis shows the rutile to be extremely niobian and ferroan, as well as having a significant tantalum content (Tables 15a,16). Presumably the large degree of isomorphous substitution of $[Fe^{3+} + (Nb + Ta)^{5+}]$ for Ti^{4+} has affected the crystal growth and caused the unusual morphology.

The second occurrence of rutile as very fine, pale, transparent needles in rutilated centers of large quartz grains suggests that these grains may be nearly pure TiO_2, distinct from the niobian variety, even though they are too fine for microprobe analysis. EMP scan photographs show them to have negligible Nb contents.

Magnetite

Magnetite occurs as subhedral to euhedral octahedra up to about a millimeter in size with dull black faces which commonly exhibit growth steps on their surfaces (Fig. 32). In thin section the magnetite predominantly occurs in opaque aggregates with manganilmenite and Nb-rutile (Figs. 12,65). In the mineral separates magnetite occurs in the hand-magnetic fraction with most grains showing numerous inclusions (Figs. 28,78,79). EMP scan photographs and analyses and optical identification show inclusions in magnetite to be zircon, monazite, thorite, apatite and quartz. The magnetite itself is nearly pure Fe_3O_4 with slight Si and Mn contents (Tables 15a,16).

Pyrite-Hematite

Pyrite occurs as partially altered euhedral cubes up to a few millimeters square. The unbroken grains are uniformly rust-brown in color exposing little or no unaltered pyrite. Grains broken during mineral separation show an irregular pyrite core making up about 20 to 80 percent of the volume of the original crystal (Fig. 33). Most grains in thin section occur as individual grains isolated from the magnetite-ilmenite-Nb-rutile aggregates. Pyrite included in such aggregates has been observed in the mineral separates however (Fig. 79).

Partial EMP analysis (Tables 15a,16) shows the unaltered cores to be nearly pure FeS_2 with about 4000 ppm Pb. The oxidized outer zones are hematite with a small amount of silica and trace levels of uranium and lead. EMP scan photographs show the lead to be highest at the outer margins of the oxidized zone but still below the level of the sulfide zone.

Epidote

Epidote occurs as vein, crack (Fig. 51) and cleavage fillings (Fig. 20), along grain contacts (Figs. 75,76) and as anhedral to euhedral grain aggregates (Fig. 34) 100 to 1000 μm in size in thin section. The grains found

Figure 32
Photomicrograph of hand-picked octahedral magnetite crystals used in the preparation of ground magnetite for the isotopic analysis and leaching experiments. The largest grain is 700 µm across. Unmounted.

Figure 33
Photomicrograph of pyrite crystals showing their variable degrees of alteration to hematite. The largest grain is 1 mm long. Unmounted.

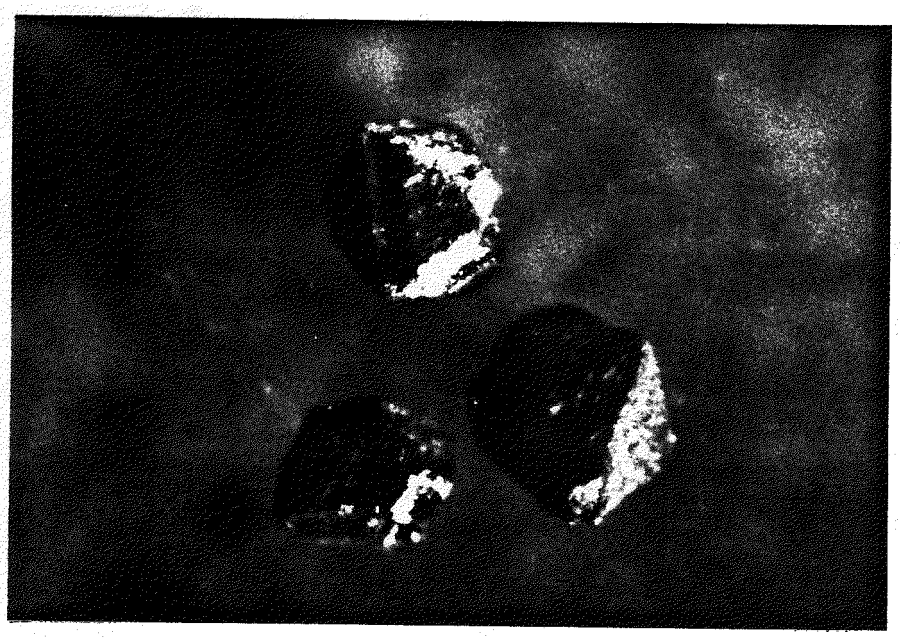

Figure 32

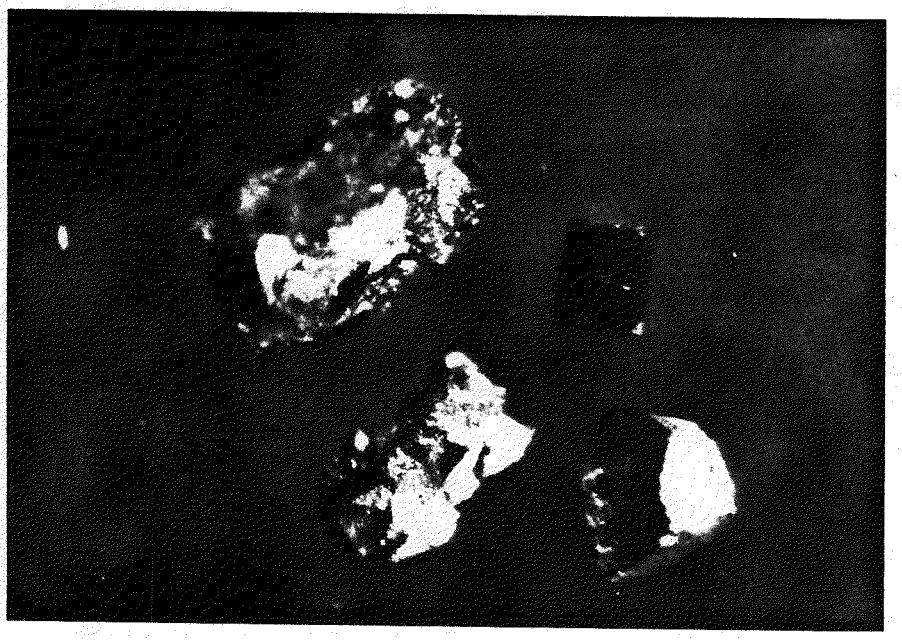

Figure 33

in the mineral separates are usually less than 150 μm but can be larger than 500 μm. They tend to be subhedral and very commonly are aggregates of tens of smaller crystals (Fig. 35). Such aggregates have angular, irregular shapes showing partial crystal forms with pronounced striations and often forming distinctly radiating clumps.

The color of epidote in the mineral separates may vary within single grains or aggregates, probably indicating compositional zonation. No crystallographic control over the zonation pattern is apparent. The most brilliant, transparent epidote grains are apple green and contain very few inclusions. Color varies from yellow-green towards buff-yellow on one hand and towards olive-green and brownish on the other. Both the yellow and more olive epidotes lack brilliance and are less transparent. The olive epidote commonly is particularly rich in opaque inclusions, which are aligned in planes, and contains dark brown centers, some of which appear to be allanite. A reduction in the order of interference colors in the allanite indicates it to be partially metamict.

One of the two principal occurrences of epidote aggregates in thin section is as large (several hundred microns) aggregates of radiating or randomly oriented crystals in the cores of plagioclase (Fig. 34) or associated with micas and clusters of radioactive accessories. The epidote is commonly associated with fluorite, apatite, and fine-grained white mica in these occurrences. A small patch of allanite at the aggregate's core is also common. The other principal occurrence of epidote is as considerably finer, less equant, radiating to irregular aggregates commonly containing allanite cores along the cleavages of micas, apparently as a secondary phase, where they are often associated with inclusions of radioactive accessories (Fig. 20).

EMP scan photographs show epidote to have a third principal occurrence filling narrow fractures in micas and most of the radioactive accessories, at grain contacts between the radioactive accessories and the opaque aggregates, and even in veins and cracks in feldspar and quartz.

EMP analyses show the apple green transparent epidote associated with feldspar to have a relatively high manganese content but otherwise to be normal in composition (Tables 15a,16). Its uranium and thorium contents are below the detection limits of the microprobe. Analyses of a full range of epidote colors and occurrences have not yet been made.

Allanite

Allanite occurs in thin section associated with coarse epidote both in micas (Fig. 20) and in clusters with micas and other radioactive minerals. It can be identified by its brown color and near isotropy (an indication that it is nearly metamict). It often occurs as small (<100 μm) anhedral masses near the center of much larger radiating masses of yellow or pale green epidote. It has also been noted in narrow centers where haloes of epidote are adjacent to radioactive species such as monazite (Figs. 56,57). In such occurrences, EMP scan photographs show it to contain appreciable U, Th, Pb, Fe, and REE levels. No EMP analysis of an allanite has been made.

Figure 34
Photomicrograph of coarse epidote in a plagioclase core. Clean grains of this epidote type were selected for isotopic analysis. The small (about 50 µm) brown grain in the epidote aggregate about 5 mm up to the left of the central opaque grain may be allanite. The epidote aggregate is about 1 mm long. Thin section, crossed nicols.

Figure 35
Photomicrograph of transparent epidote crystal fragments and aggregates handpicked for isotopic analysis. The largest grain is 300 µm long. Unmounted.

Figure 34

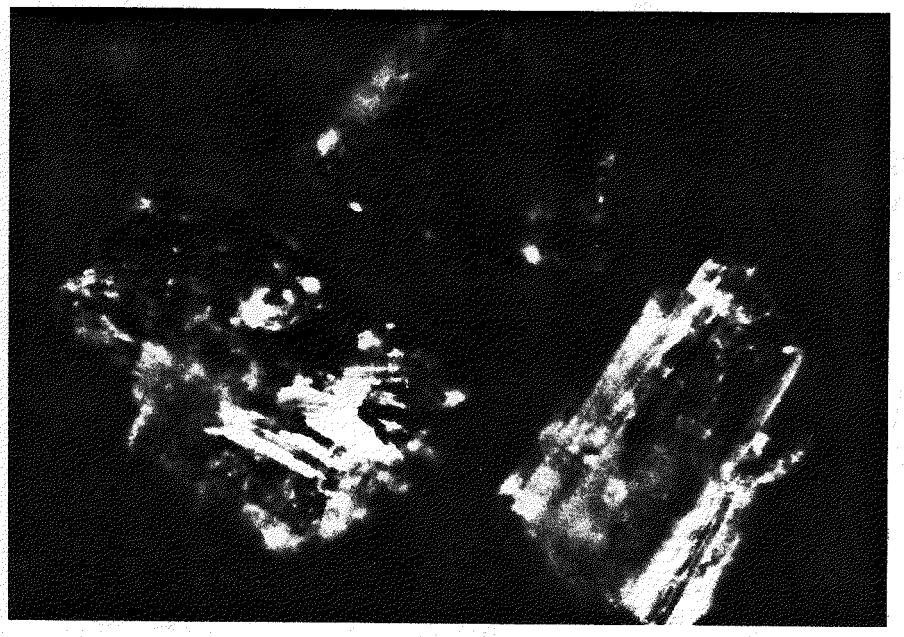

Figure 35

Fluorite

Fluorite occurs as anhedral grains, the majority finer than 150 μm. Its color is extremely variable (Fig. 36). Much of the fluorite is virtually colorless; the remainder ranges from the palest mauve for the most part, through to mauve so intense that the crystal is nearly opaque. Rare grains show the same variability but in blue-gray hues. Intense coloration is not common and tends to be limited to small areas of any particular grain. In thin section the color is seen in some cases to be a function of proximity to crystals which are highly radioactive, so it may be an effect of radiation damage.

The crystals show no visible compositional zoning, and little internal fracturing. Inclusions are common, ranging in size from a few microns to the finest dust. The majority of the inclusions are euhedral apatite crystals, but small grains of opaque minerals are also present. Rare inclusions are rounded, irregular in form and isotropic. They may well be non-crystalline. In thin section the fluorite is seen to occur in two principal sites; as inclusions in biotite and as inclusions in plagioclase. In both sites the grains may be large (on occasion as large as 1 mm) but because of the constraints of the crystal form of their host mineral, they differ significantly in proportion. Grains in biotite are elongate parallel to the mica cleavage plans; grains in plagioclase are more equant and commonly very irregular. In plagioclase the close association of fluorite with sericite, fine-grained muscovite, and epidote is very common (Fig. 17).

EMP analyses show no detectable compositional differences between colored and uncolored fluorite. Uranium and thorium are below detectable limits (Tables 15a,16).

Apatite

Apatite is present in an extreme range of grain sizes. Prism diameters range from a few microns to more than 0.5 mm. The majority of the crystals are well-formed hexagonal prisms (Figs. 37,38). The color and proportions of the crystals vary as a function of grain size. The finest crystals (less than 100 μm diameter) tend to be elongate, brilliantly transparent and colorless (Fig. 38) or translucent and pale gray. The intermediate sized crystals are stubbier, gray to dark gray and clouded. Length to width ratios average 3:1. The coarsest crystals (greater than 300 μm diameter) mostly are close to equidimensional, milky, gray to dark gray and rarely dark gray-brown (Fig. 39).

The reason for the color and clarity variation is not readily apparent; no internal zoning can be seen and the grains are not intensely fractured. The darkest grains do show some planes of internal reflection. Many of the darker grains contain a myriad of fine inclusions ranging from a few tens of microns down to the finest dust (Fig. 40). Those inclusions large enough to be optically identifiable are monazites, tiny zircons and opaque minerals. The fine inclusions in the apatite tend to be distributed randomly or in thin sheets not obviously related to internal growth zones.

The great majority of the apatite occurs in close association with the aggregates of micas and opaque minerals. Finer apatite is particularly abundant as inclusions in biotite-chlorite, where it frequently is oriented parallel to

Figure 36
Photomicrograph of hand-picked fluorite fragments showing a color range from colorless to deep purple due to different degrees of radiation damage. The dark grain in the center is 600 μm long. Unmounted.

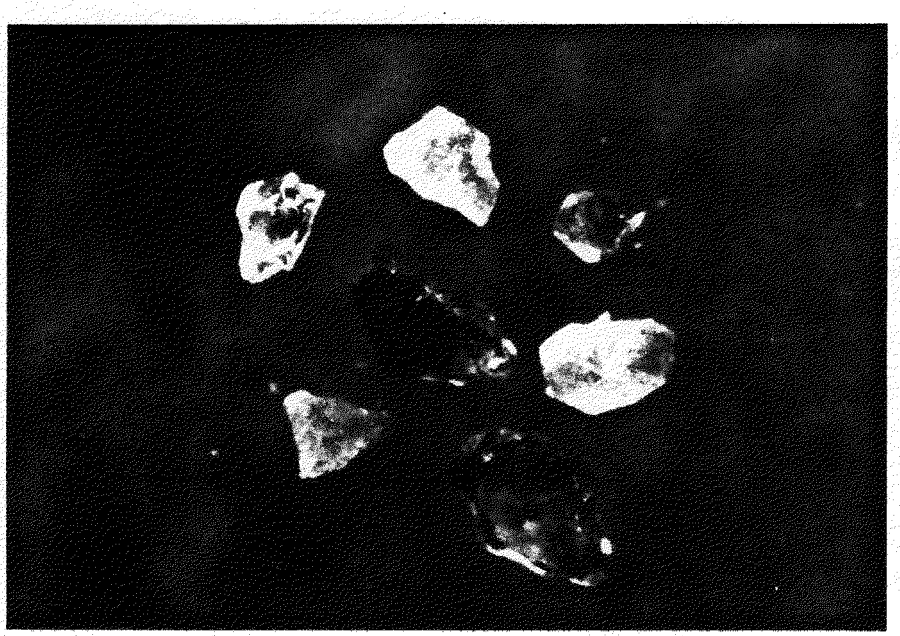

Figure 36

Figure 37
Photomicrograph of the mineral concentrate of clear colorless apatite prepared for isotopic analysis. The mean crystal length is about 250 µm. Mounted in covered medium (n = 1.65).

Figure 38
Photomicrograph of limpid colorless apatite crystals with characteristic prismatic form, typical of the analyzed concentrate of clear apatite. The crystal in the lower left of the field is 400 µm long. Unmounted.

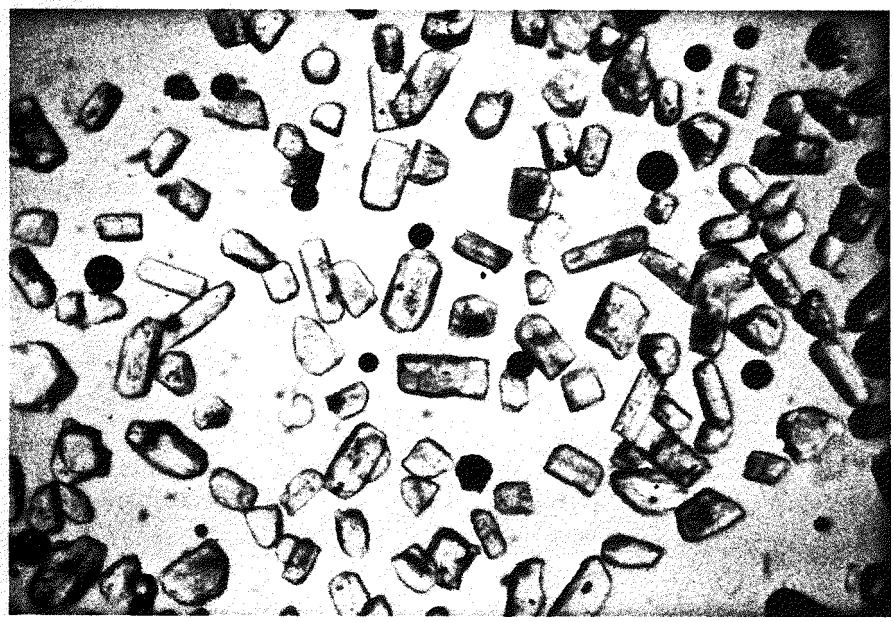

Figure 37

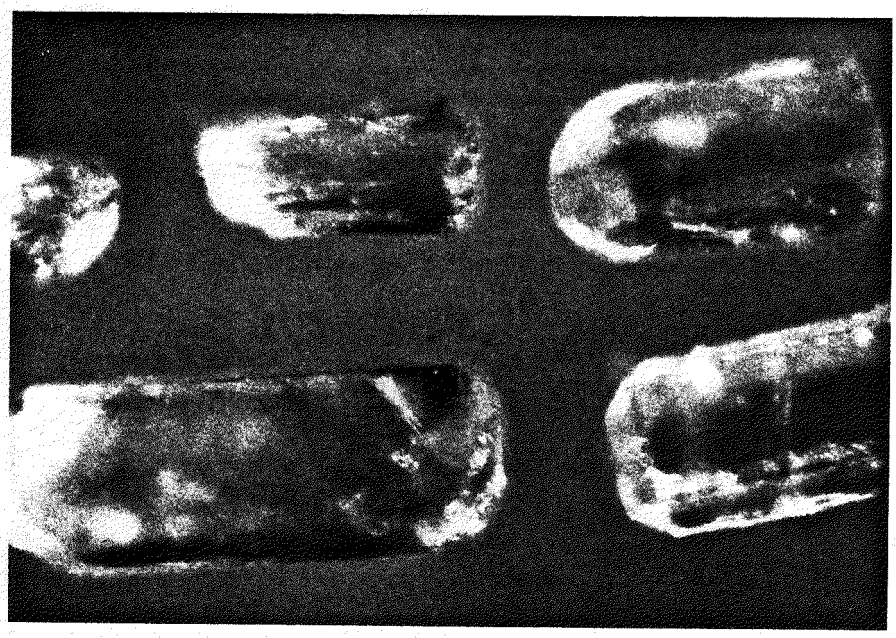

Figure 38

Figure 39
Photomicrograph of stubby gray smoky apatite crystals of variable translucence typical of the analyzed concentrate of gray apatite. The large crystal in the upper center of the field is 800 µm long. Unmounted.

Figure 40
Photomicrograph showing, in detail, inclusions of two distinct size ranges in a mounted gray apatite crystal. Finer dark opaque dust is unidentified. Coarser crystals include an orange monazite at the lower left and an out-of-focus zircon to its right. The apatite crystal is 400 µm across.

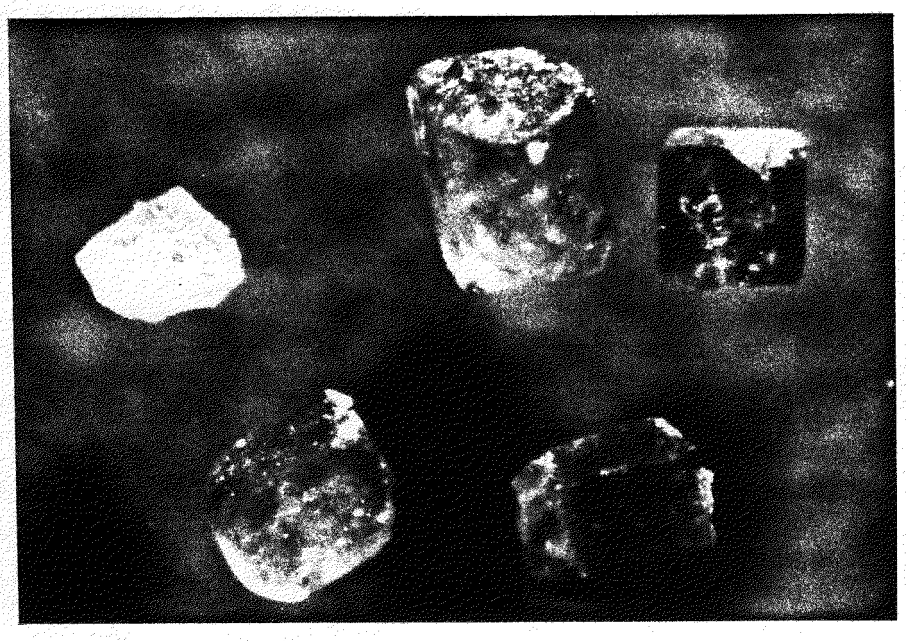

Figure 39

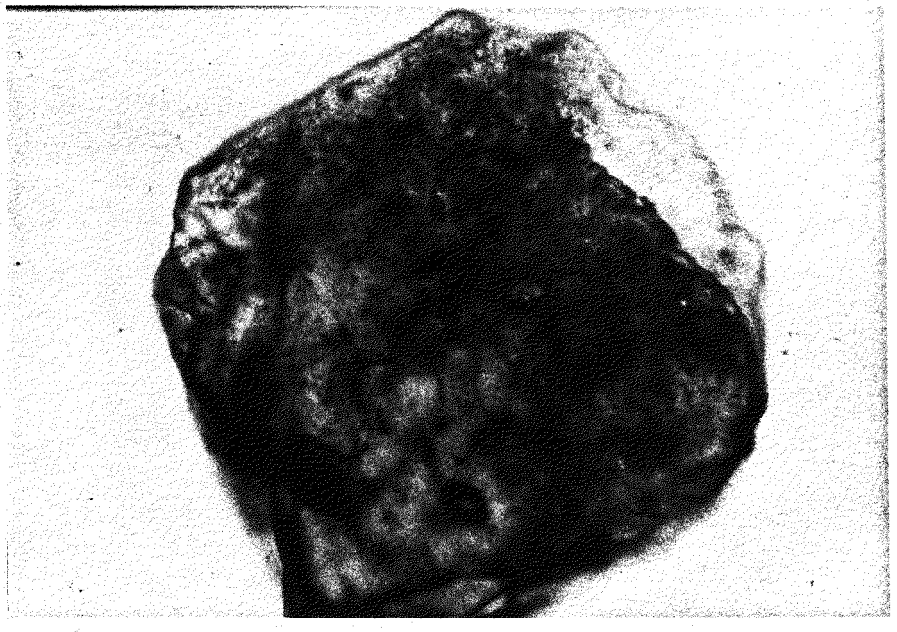

Figure 40

the mica's cleavage (Fig. 20). The large equant apatite grains tend to occur as independent crystals. EMP scan photographs show the additional widespread occurrence of apatite included in and associated with zircon, monazite, magnetite and manganilmenite (Figs. 51,57,66). Apatite also occurs as a fracture filling in zircon and at grain boundaries between several accessory minerals and opaque minerals.

EMP analyses show the apatites to be fluorapatites with few detectable differences in composition between the colorless and the gray varieties (Tables 15a,16). The gray apatite does have slightly higher fluorine and lower manganese and iron contents. Uranium and thorium in both are below EMP detection limits. Isotope dilution studies suggest somewhat higher U and Th in the darker apatite.

Scheelite

Scheelite, $CaWO_4$, has been identified by EMP scan photos and by qualitative analysis on the SEM as rare, colorless, transparent, anhedral grains in the zircon mineral separates (Fig. 44). EMP analysis is pending establishment of an adequate tungstate standard. As scheelite is not known to contain detectable uranium, thorium, or lead, its rare presence in the zircon concentrates would merely produce a negligible dilution effect.

Zircon

Most of the zircon grains recovered are less than 150 μm in prism diameter. The crystal morphology is very uniform; euhedral simple (110) prisms with simple (111) pyramidal terminations (Fig. 41) A very few crystals have a flattened habit. Length to width ratios of the majority of grains are in the range 2:1 to 3:1. Approximately 20 percent of the grains are stubbier and 10 percent more elongate, up to 7:1. Most of the grains have a well developed crystal form, although distinct blunting of corners and edges and pitting of crystal faces is common. Most imperfect grains are obviously fractured, probably during the mineral separation procedure (Fig. 42). There is no evidence of resorption or embayment that might indicate chemical instability.

The zircon crystals show a very considerable range in color and clarity from limpid deep hyacinth to clouded buff or pale gray (Fig. 43). The internal zonation of the crystals is complex, and made particularly striking by the color and clarity differences between various zones (Fig. 42). Most of the zoned crystals have a clear hyacinth core displaying both (110) and (100) faces with blunted edges and rounded terminations. Irregular or rounded cores are common and simple prismatic ones less so. A small fraction of grains exhibit cores which are not parallel to the outer zones (Fig. 48). The rims of zoned grains show varying development of purplish gray to light gray cloudiness, ranging from a slight discoloration of the crystal terminations, through discoloration along all edges, to completely clouded (Fig. 45). The transition between layers of transparent and clouded zircon commonly occurs over very narrow intervals (<2-3 μm). The zircon core may itself be zoned in refractive index and birefringence (Fig. 50). Some crystals have an additional very thin, yellowish, low-order birefringence, sharply euhedral zircon outer zone which is partially

Figure 41
Photomicrograph of zircon crystals selected to show the ranges of color, opacity, form and zonation. Color values of this and the following color photograph tend to be too yellow. The largest crystal, on the right side of the group, is 500 µm long. Unmounted.

Figure 42
Photomicrograph, a detail of Fig. 41, showing some intricate patterns of zonation in color and opacity in zircon. The crystal in the center of the field is 350 µm long. Unmounted.

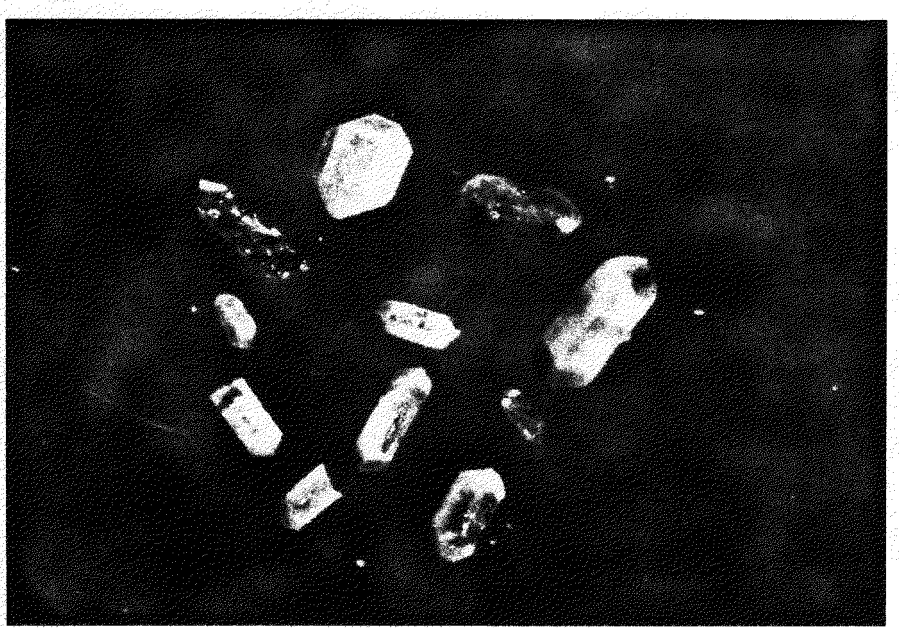

Figure 41

Figure 42

Figure 43
Photomicrograph of a detail of Fig. 41, showing contrasts in opacity and color in zircon. The pale opaque crystals are up to ten times more radioactive than the hyacinth transparent ones. The hyacinth crystal is 350 μm long. Unmounted.

Figure 44
Photomicrograph of a concentrate of more magnetic and radioactive zircons showing variations in form, inclusions, internal structures, color and opacity. The dark zircon in the center (as well as the three grains to its right) exhibits a clear, euhedral outer zone on its unbroken tip. The irregular colorless grain with lower relief is a fragment of scheelite. It is 100 μm across. Mounted mineral separate (n = 1.65), transmitted light.

Figure 43

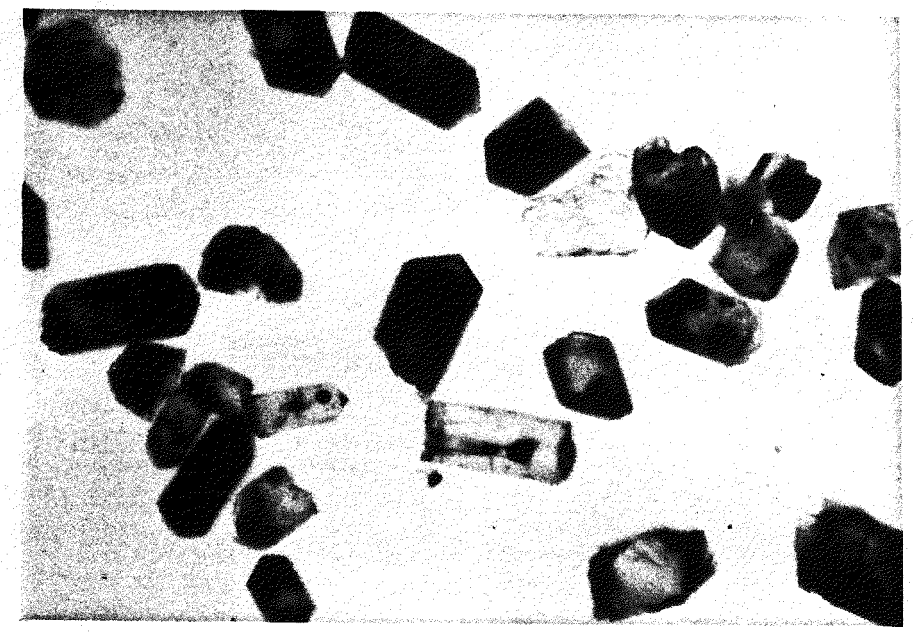

Figure 44

Figure 45
Photomicrograph of part of the same zircon population as shown in Figure 44, illuminated with side lighting to emphasize the variability in turbidity (and radioactivity) in and among individual crystals. The mean crystal length is about 100 μm.

Figure 46
Photomicrograph of a detail of the center of Figure 21, showing a zircon crystal with emergent c-axis. The crystal has been analyzed by EMP scans, which have deposited brown sublimate on the polished thin-section surface. Small uncommon granules of brown sphene and colorless apatite near the prismatic zircon are identified in Figure 47(a). The large zircon crystal is 50 μm across. Polished thin section, plane light.

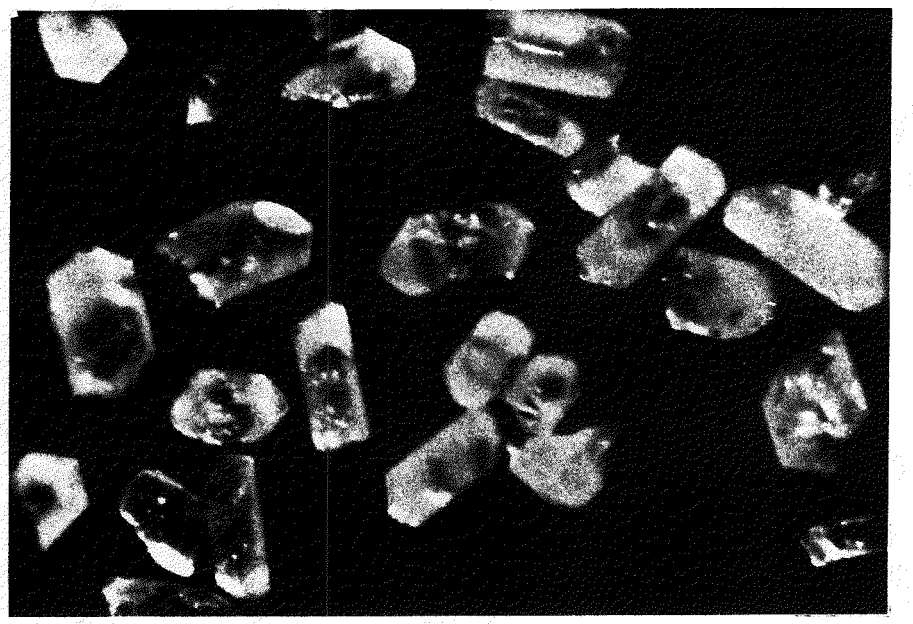

Figure 45

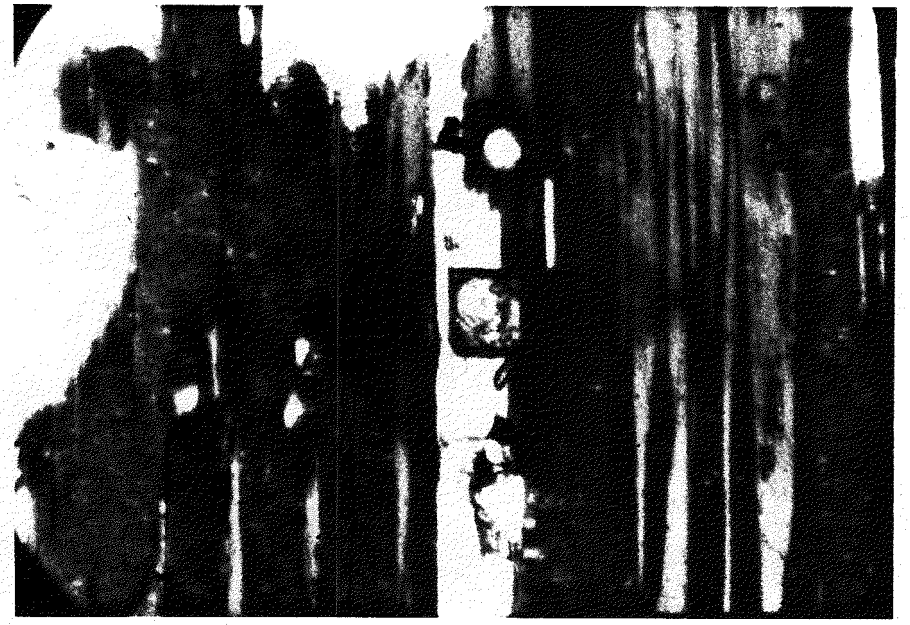

Figure 46

Figure 47
Electron Microprobe Scan Series--Zircon and associated phases.

a. Index sketch of the zircon and associated phases in Figure 46.
b. Zirconium distribution.
c. Thorium distribution. Note the zonation with enrichment in the outer zone.
d. Calcium distribution. Note the zonation and the central apatite inclusion indicated by the Ca-rich spot.
e. Uranium distribution. Note the zonation and the uranium enrichment in the outer zone differing in detail from that of thorium.
f. Titanium distribution. Note the sphene adjacent to the zircon and parallel to the biotite-chlorite cleavage planes.
g. Phosphorus distribution. Note the zonation and the apatite inclusion in the center of the zircon, as well as the apatites in opposite corners of the field.
h. Hafnium distribution. Note the zonation, which is less sharp than that of the other elements.
i. Yttrium distribution. Note the zonation, similar to that of P.

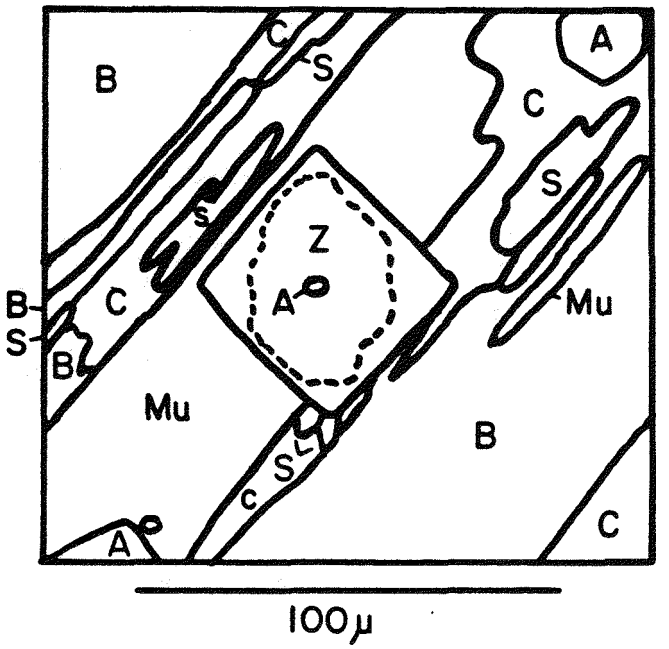

Figure 47(a)

A -- Apatite

B -- Biotite

C -- Chlorite

Mu -- Muscovite

S -- Sphene

Z -- Zircon

Figure 47 (continued)

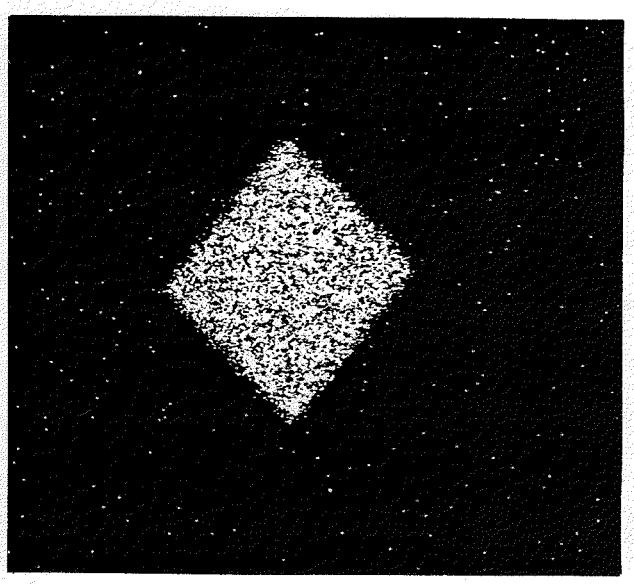

b - Zr

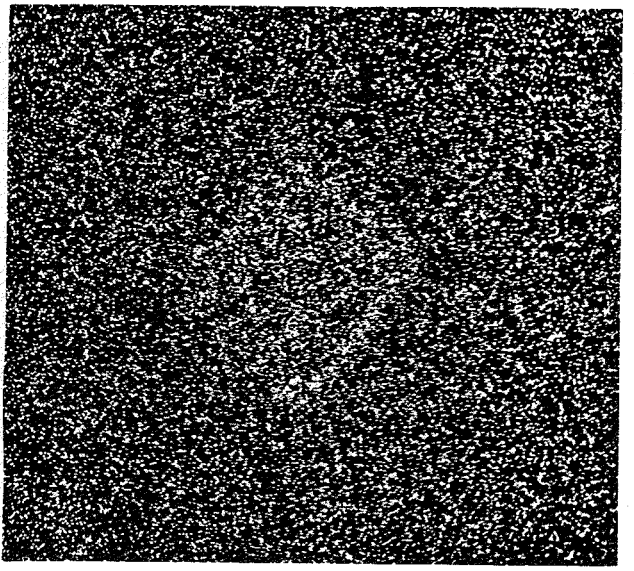

c - Th

d - Ca

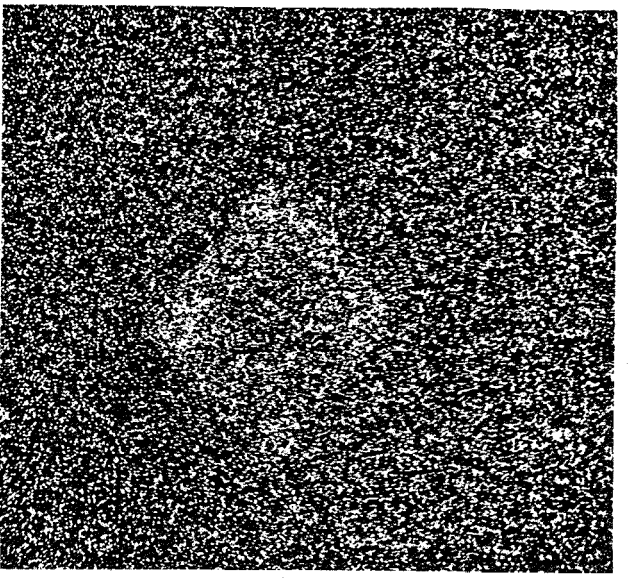

e - U

Figure 47 (continued)

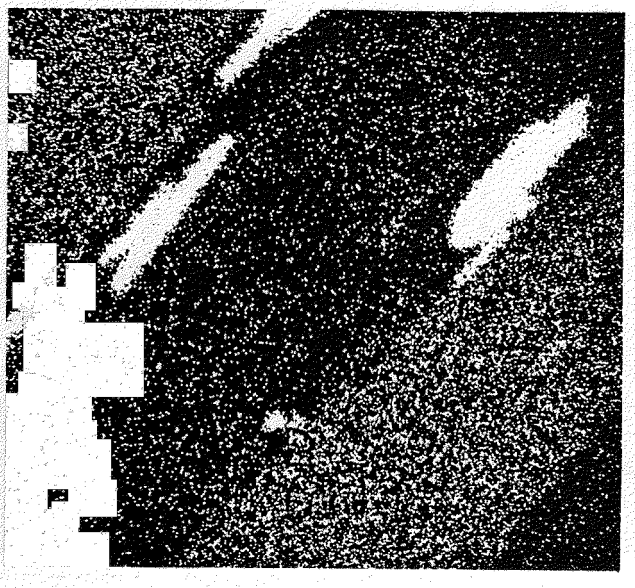

f - Ti

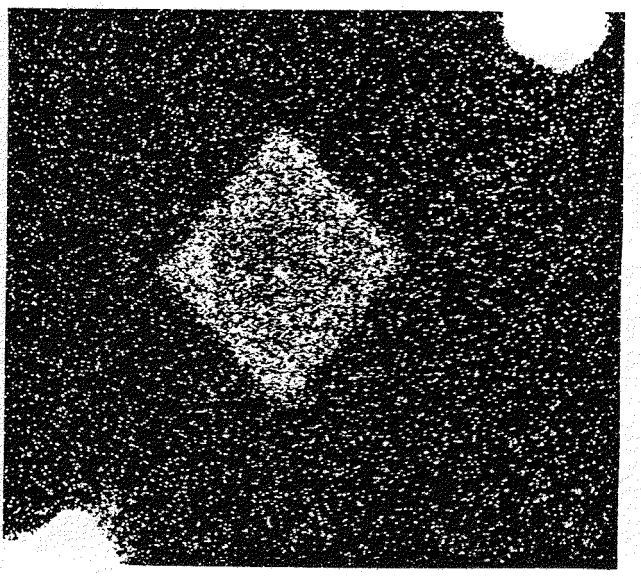

g - P

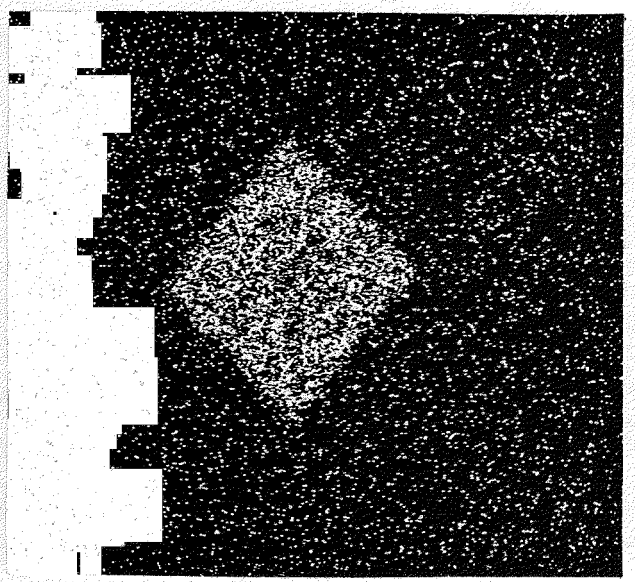

h - Hf

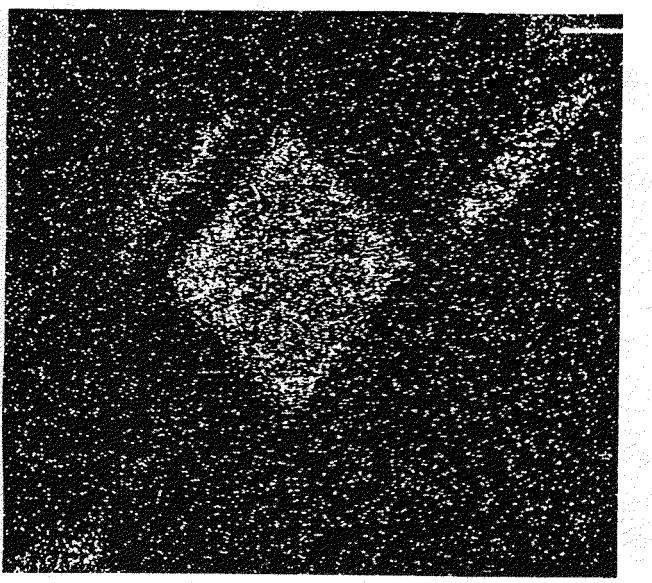

i - Y

Figure 48
Photomicrograph of a large, complexly zoned zircon crystal with an irregular inclusion of apatite near its lower termination. The outer zircon zones have overgrown disconformably a slightly rotated zircon core which lacks sharp form. The outermost zone is incomplete where an adjacent manganilmenite crystal has impinged on the zircon. Fracturing in the core may have contributed to the disconformable growth. Several other small grains of radioactive species including epidote, thorite and zircon, appearing elsewhere in the field, are identified in Fig. 51(a). Note the brown (Fe-rich) halo adjacent to the uraniferous faces of the zircon and around the thorite grains. The length of the crystal is 400 μm. Polished thin section, plane light. The EMP scan stain is visible.

Figure 49
Photomicrograph of the same field as Fig. 48. Oblique illumination reveals the systematic internal distribution of opacity, which is most strongly developed in the outer crystal growth zones of the zircon.

Figure 50
Photomicrograph of the same field as Fig. 48. Zonation of the interference colors, with decreasing anisotropy in outer zones, reveals increased radiation damage in those regions. Polished thin section, crossed nicols.

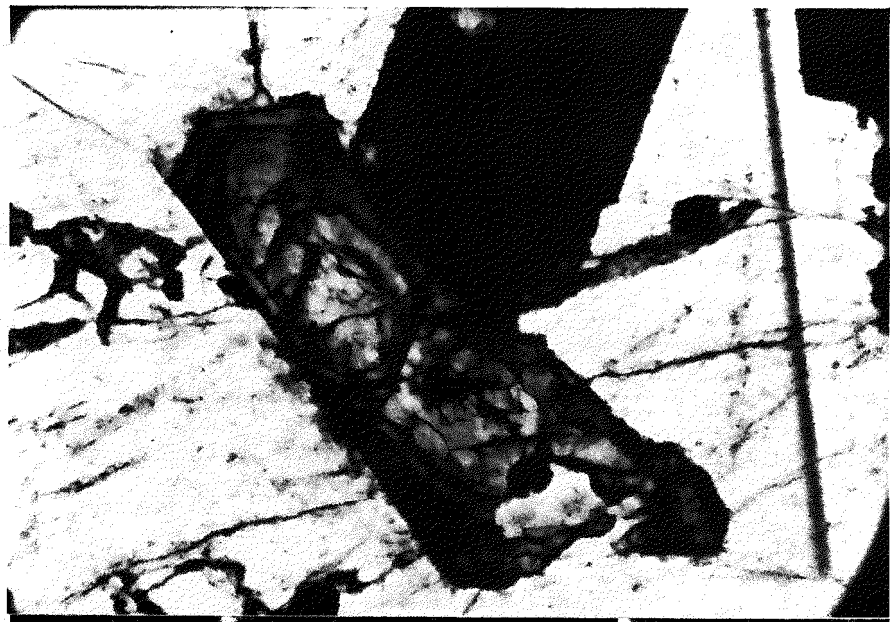

Figure 48

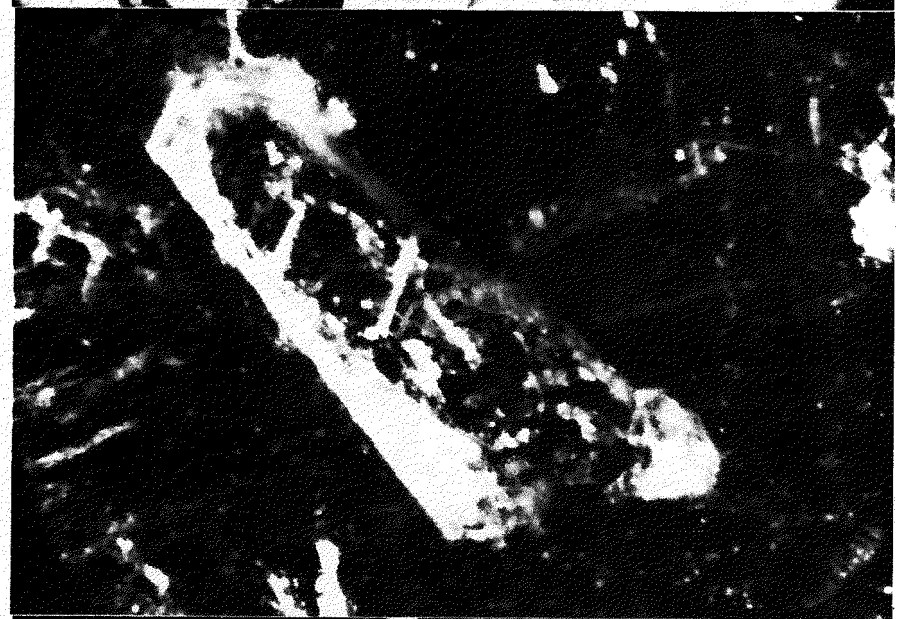

Figure 49

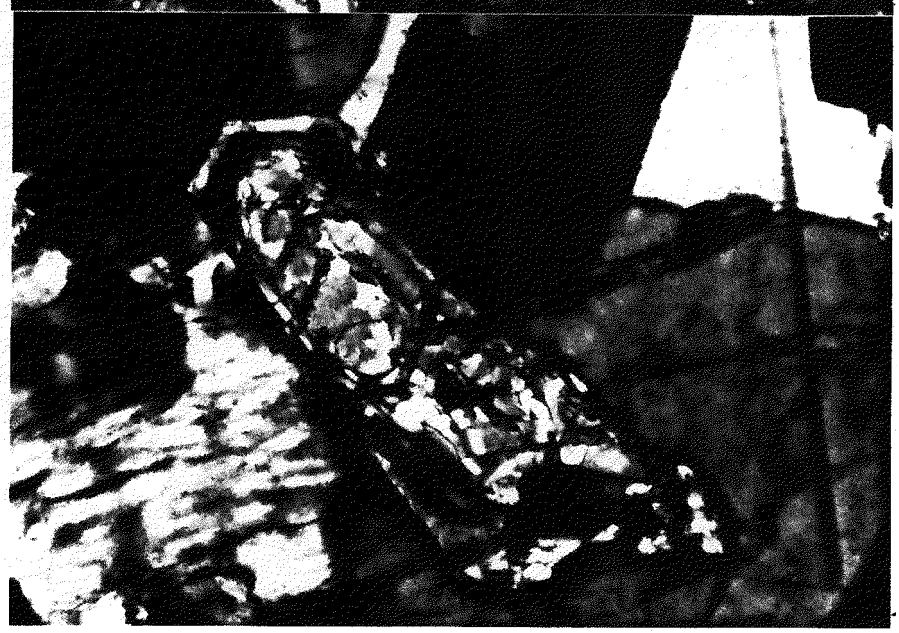

Figure 50

Figure 51
Electron Microprobe Scan Series--Zircon

a. Index sketch of zircon and associated phases shown in Figure 48.
b. Zirconium distribution. Note the two small zircons in the adjacent upper right field.
c. Thorium distribution. Note the narrow thorium-rich bands in the outer growth zone, especially near the upper tip, with distinctly lower levels of thorium in most of the outer zone. A half dozen minute thorite grains are also visible.
d. Calcium distribution. Note the general zonation in the zircon and the high calcium concentrations in fractures and at grain contacts.
e. Uranium distribution. Note the marked increase in uranium in the outer zones, over a broader area than the narrow Th-rich bands, as well as the high uranium levels in thorites. The apparent increase in uranium concentration in the manganilmenite is due to interference by a second order Fe peak which becomes significant only in very high Fe phases.
f. Iron distribution showing a moderate zonation in zircon, with enrichment along epidote-filled fractures in the zircon, in a narrow halo at its left side, and in the vicinity of thorite grains. The high-iron grain is manganilmenite.
g. Phosphorus distribution, showing increased phosphorus concentrations in the outer zones, several apatite inclusions and fracture fillings.
h. Hafnium distribution, showing increased hafnium concentration in the outer zones. There is some evidence for an inverse correlation between Hf and Th abundances in the Th-rich bands.
i. Yttrium distribution, showing increased yttrium concentration in the outer zones, reflecting, along with phosphorus, an increased xenotime component in solid solution. Note also that the several small thorite crystals have an even larger xenotime component.

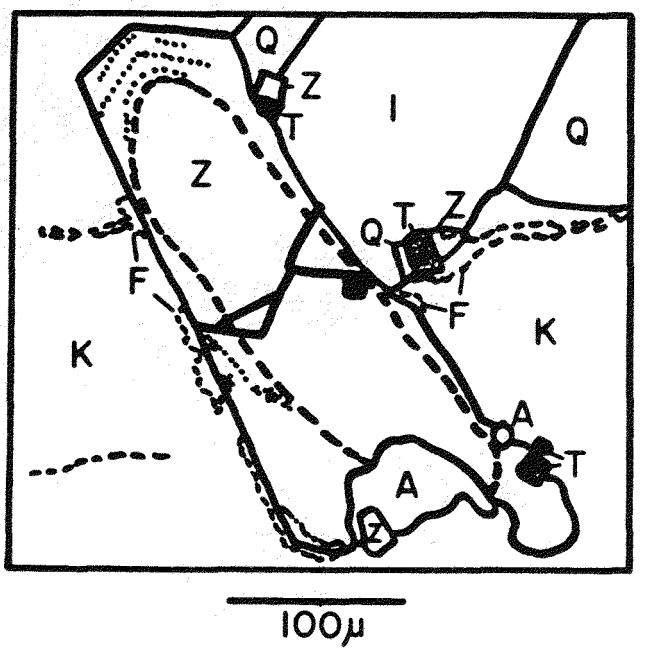

Figure 51(a)

A -- Apatite

F -- Iron-rich fractures and haloes

I -- Manganilmenite

K -- Microperthite

Q -- Quartz

T -- Thorite

Z -- Zircon

Figure 51 (continued)

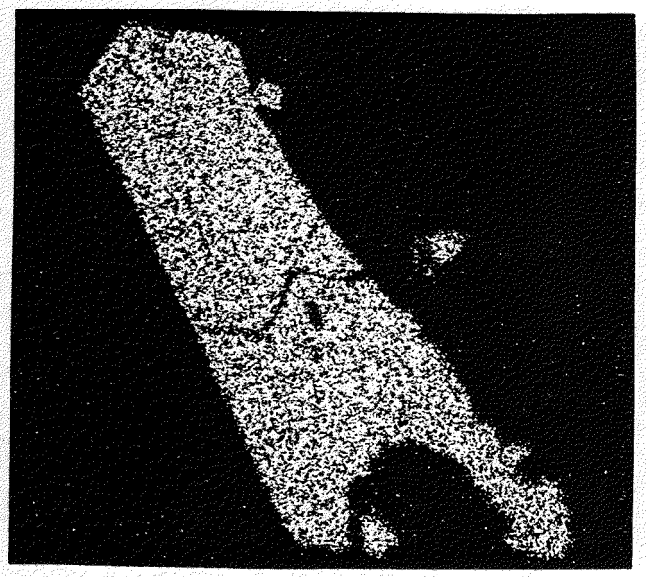

b - Zr

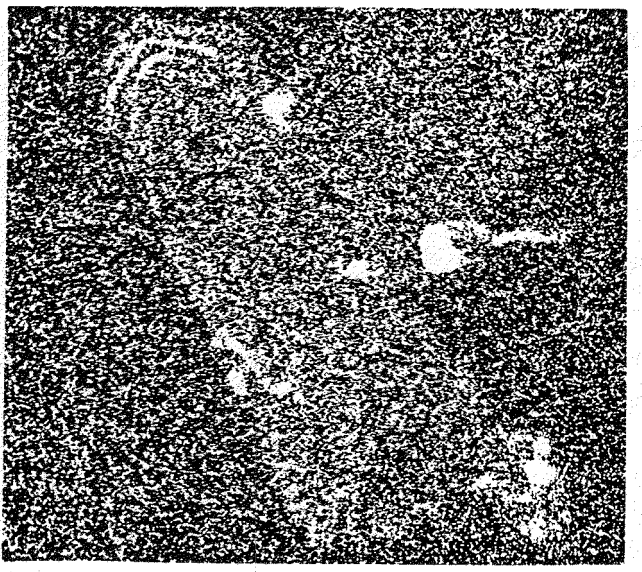

c - Th

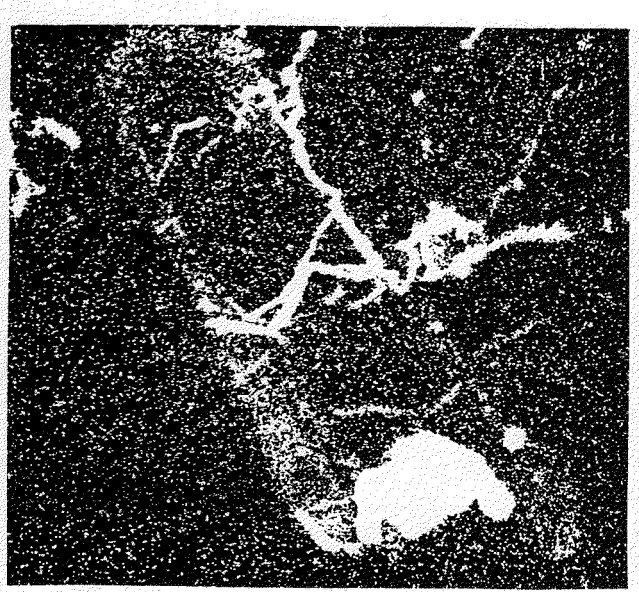

d - Ca

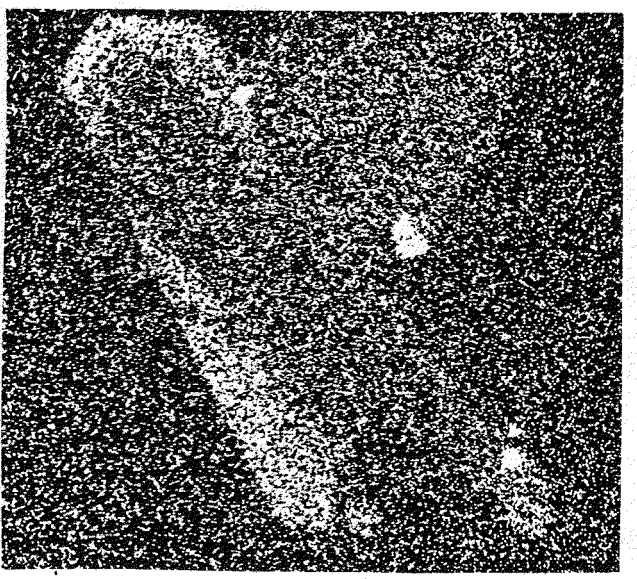

e - U

Figure 51 (continued)

f - Fe

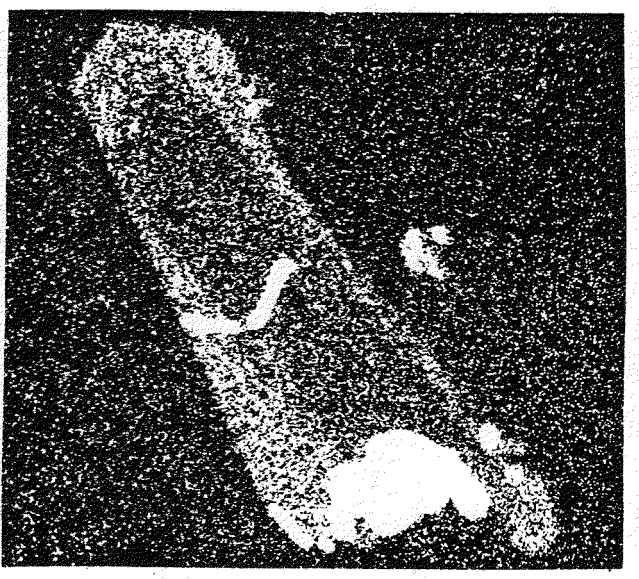

g - P

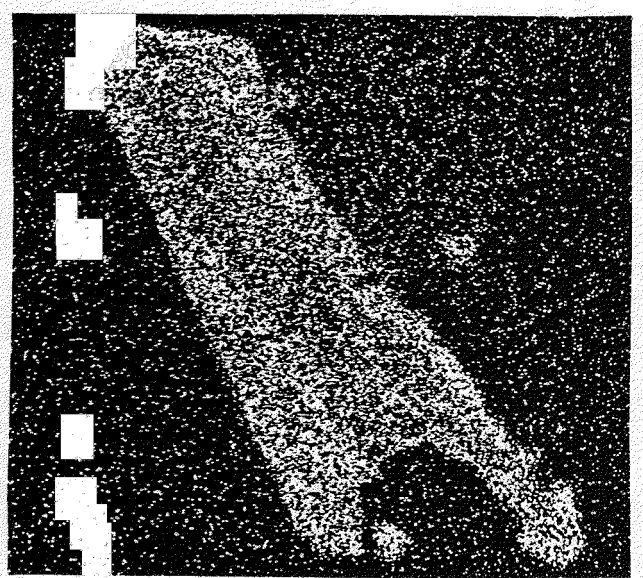

h - Hf

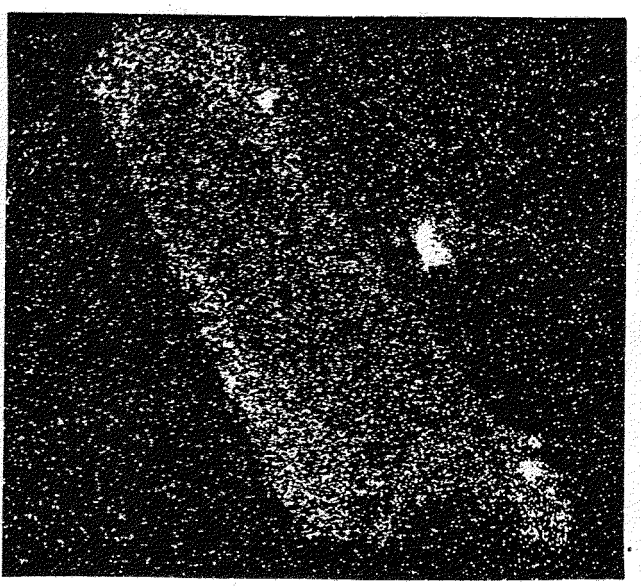

i - Y

metamict (Fig. 44). Zircon fractions with higher radioactivity contain higher proportions of clouded grains.

Many of the zircons contain a network of internal fractures. The two principal sets are aligned perpendicular and parallel to the prism faces. Finer, apparently randomly oriented cracks are also present. Inclusions in the zircon crystals are very common, with few grains being wholly inclusion-free (Fig. 44). Three types of inclusion are readily distinguishable: opaque equidimensional crystals?, transparent needle-like crystals (some of which are extremely small) and irregular transparent inclusions with a rounded form. Generally, the largest of the elongate inclusions are oriented parallel to the prism of their host zircon or parallel to the internal zones. There are many exceptions however, especially in those zircons in which growth zones are not visible. It is in just such crystals that the fine inclusions are the most abundant. EMP scan photographs of zircons in thin section show inclusions of apatite and thorite to be common. They are absent in the acid-washed grain separates. Apatite and also epidote can be seen filling fractures within zircon and at contacts between zircon and opaque mineral grains.

Zircon occurs in a variety of sites. Of 313 crystals observed in four thin sections, 46 percent were hosted in the major minerals and 54 percent in the micas and accessory minerals (Table 17). Many of the largest grains, accounting for the bulk of the zircon in the rock, occur in or against aggregates of magnetite and manganilmenite (Fig. 78) along with other radioactive phases such as monazite, xenotime, apatite and sphene-ilmenite (Fig. 24) or in clusters of these phases in biotite-chlorite (Fig. 26) or muscovite (Fig. 25). The zircon in such aggregates comprises a small number of larger grains, surrounded by a swarm of smaller grains in the host mica, quartz or plagioclase. Less commonly, finer euhedral zircon crystals are located as isolated inclusions in plagioclase and quartz, both within the host crystals, and near grain boundaries. Isolated zircon is rarely found in K-feldspar. As inclusions in biotite-chlorite or muscovite, zircon is surrounded by distinct pleochroic haloes, and generally is oriented preferentially, parallel to the cleavage.

EMP analyses and scan photographs (Figs. 46,47,48-51) show the zircons commonly to be sharply zoned in calcium, yttrium, phosphorus, uranium, thorium and iron and less so in hafnium (Tables 15b,16). The chemically defined zones coincide with the color and opacity zonation. In those crystals studied in detail, the hyacinth core has relatively low uranium and thorium, (<1000 ppm); negligible calcium, iron and xenotime (YPO_4) component; and a high Zr/Hf ratio (62.5). The cloudy outer zones contain as much as 3.6 percent xenotime component, and have a Zr/Hf ratio more than a factor of two lower (27.3). Uranium and thorium are high in the outer zones at the corners of the prism (outside the (100) faces of the inner zones) and at the tips of the grains. Uranium is commonly 10,000 to 12,000 ppm in these areas, and reaches 22,000 ppm; thorium is less strongly enriched, up to 2300 ppm. Th/U is inversely proportional to U content, averaging about 0.1. Narrow thorium-rich (high thorite component) zones parallel to growth faces and only a few microns wide have been identified within the cloudy outer zones of zircons in thin section (Figs. 48-51) and from the more radioactive grain separates. These zones contain up to 23,000 ppm Th with Th/U ratios of 2 to 4. They are entirely metamict; the cloudy high-U zones in which they occur are also strongly radiation damaged (1st order birefringence); and even the inner hyacinth zones may have only 2nd order colors (Fig. 50).

TABLE 17

Distribution of zircons in various other minerals of Lawler Peak Granite #1

Host Phase	Phase Abundance Vol%	No. of Zircons		No. of zircons/ 1% Vol of rock
Quartz	34.	103		3.0
Perthite	37.5	18	147	0.5
Plagioclase	21.7	26		1.2
Muscovite	3.7	82		22.
Biotite-chlorite	2.1	46		22.
Opaques (in or against)	0.4	36	166	95.
Apatite	0.1	2		20.

Xenotime

Xenotime occurs principally as relatively large (150-200 μm) euhedral to subhedral tetragonal dipyramids (Fig. 52). The crystal edges and corners are sharp, but the faces are frosted by fine pitting. The xenotime ranges in color from gray to buff to buff-orange. A few grains are transparent; the great majority are translucent. Most crystals contain a myriad of tiny opaque rust-brown inclusions and also internal surfaces coated to various extents by gray to black or rust-brown stains. Both these features affect the color and opacity of the individual grains. Internal compositional zoning is not visible, although some crystals do contain areas of diffuse gray discoloration.

The very few xenotime crystals found in thin section (Figs. 53,65) were associated with aggregates of magnetite, and manganilmenite in clusters of radioactive minerals including zircon, monazite, thorite, apatite and uranium titanate. The grains show low-order birefringence and are therefore inferred to be partially metamict.

EMP analyses show the xenotime to have a relatively uniform composition (Tables 15b,16) with no regular internal zonation. Heavy rare earths, uranium, and thorium substitute for yttrium to the extent of 20 to 25 atom percent. Ranges in ThO_2 content from 0.8 to 1.1 weight percent and UO_2 content from 1.3 to 2.7 weight percent have been measured, but EMP scan photographs (Fig. 54) show that these elements are distributed very irregularly and that in some areas uranium concentrations are significantly lower.

The EMP scan photographs also reveal numerous tiny inclusions (smaller than 10 μm), many of thorite, others of K-feldspar, epidote, apatite, zircon, quartz, white mica and magnetite.

Monazite

Monazite is present as approximately equant grains, some as large as 150 μm but most finer than 75 μm. The grains generally are rounded or subhedral crystals with few identifiable crystal faces and only a gross suggestion of monoclinic form (Fig. 55). The grain surfaces are reflective, although deeply pitted. The crystals range in color from transparent straw yellow through orange to turbid orange-brown. The turbidity appears to be related to internal granularity and in some cases clearly is restricted to the crystal rims. A few grains are yellow to orange opaque, have a dull chalk-like appearance and are friable. The few inclusions present are tiny opaque crystals that are too small for optical identification.

Those monazites identified in situ occur associated with aggregates of magnetite and manganilmentite (Figs. 28,56) or included in apatite (Fig. 40). Many of the inclusions in mica, surrounded by pleochroic haloes, are monazite (Fig. 25). The turbidity of the monazite crystals obscures their optical properties, but where birefringence is visible it is low-order and the monazite is inferred to be partially metamict. EMP scan photographs (Figs. 57,66) reveal that the monazite commonly is intergrown with apatite and is host to inclusions of thorite. The dark haloes surrounding monazite in feldspar (Figs. 56,65) are iron rich and contain elevated lead, uranium and thorium levels.

Figure 52
Photomicrograph of tetragonal dipyramids of xenotime from the hand-picked concentrate used for isotopic analysis. The crystals are 250 µm across. Unmounted.

Figure 53
Photomicrograph showing a euhedron of xenotime in host plagioclase with a dark, rusty (Fe-rich) halo characteristic of the more radioactive species. The numerous minute inclusions are characteristic of xenotimes seen in thin section. The large opaque inclusion is magnetite. A smaller xenotime grain is at the lower right of the large grain. This figure is a detail of Figure 65 and includes a brannerite? grain (also shown in Figure 63) in the upper-right corner. The large xenotime crystal is 100 µm long. Polished thin section.

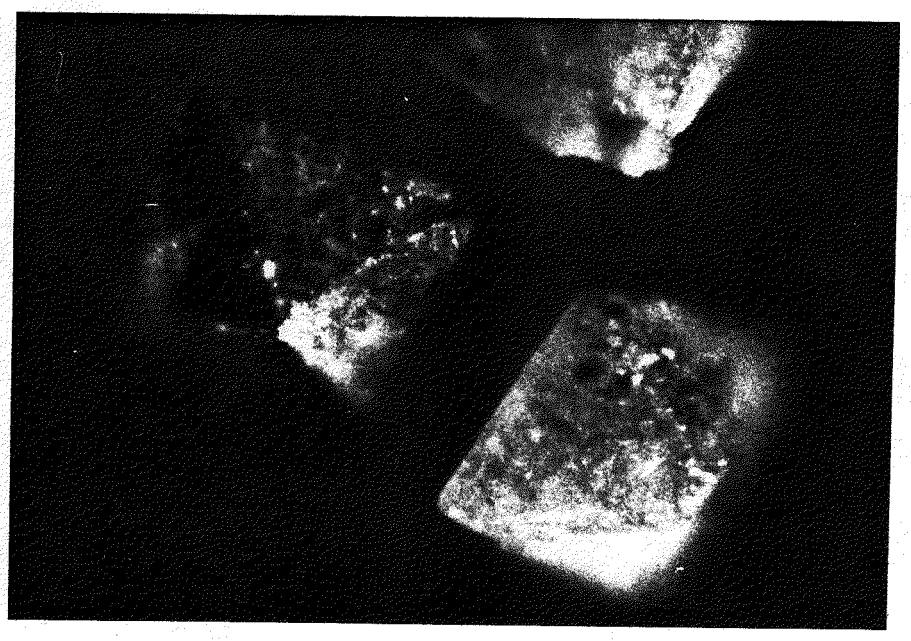

Figure 52

Figure 53

Figure 54
Electron Microprobe Scan Series--Xenotime

a. Index sketch of xenotime and several inclusions (see Fig. 53)
b. Phosphorus distribution
c. Yttrium distribution
d. Silicon distribution; note the many silicate inclusions.
e. Zirconium distribution; note the zircon inclusion at the lower right.
f. Iron distribution; note the iron-rich halo and magnetite inclusion.
g. Thorium distribution; note the two thorite inclusions and the thorium enrichment in parts of the iron-rich halo.
h. Lead distribution; note the patchy zonation pattern correlated with those of uranium and thorium and the detectable increase in lead in the iron-rich halo.
i. Uranium distribution; note the distinct zonation which is paralleled by the thorium variation and the uranium enrichment in the iron-rich halo. Note that the two thorite inclusions differ strikingly in uranium content.

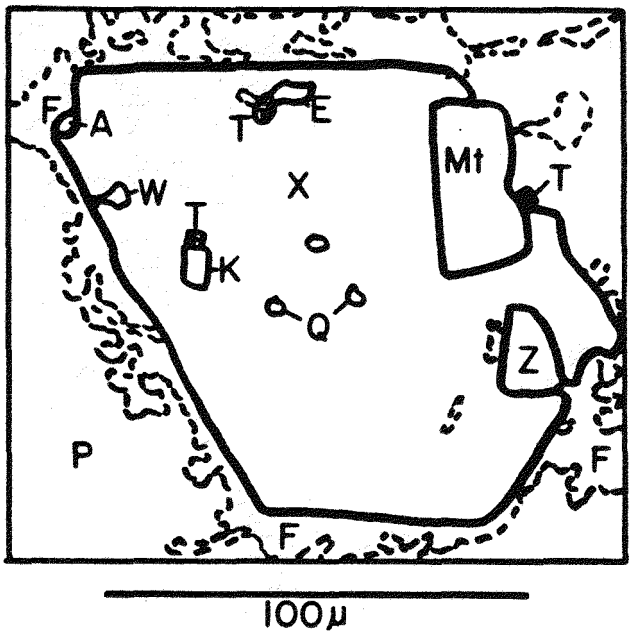

Figure 54(a)

A -- Apatite

E -- Epidote

F -- Iron-rich halo

K -- Potassium feldspar

Mt -- Magnetite

P -- Oligoclase

Q -- Quartz

T -- Thorite

W -- White mica

X -- Xenotime

Z -- Zircon

Figure 54 (continued)

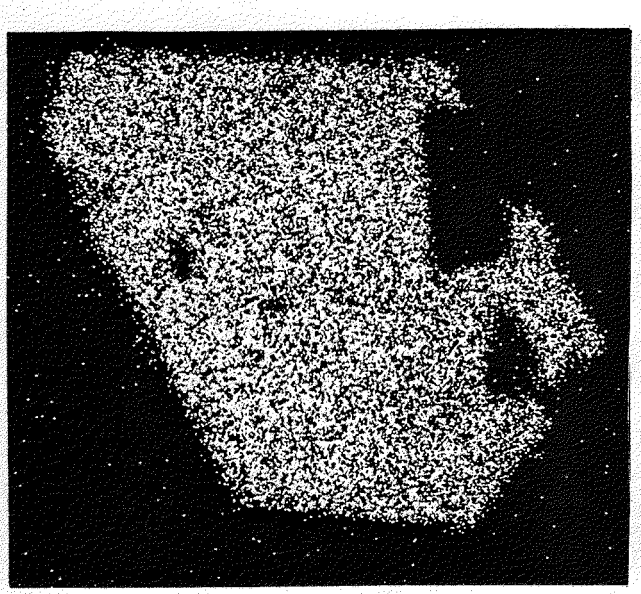

b - P

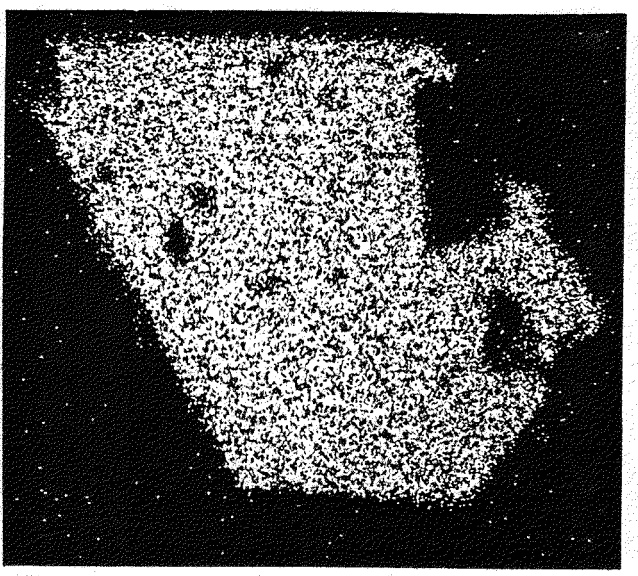

c - Y

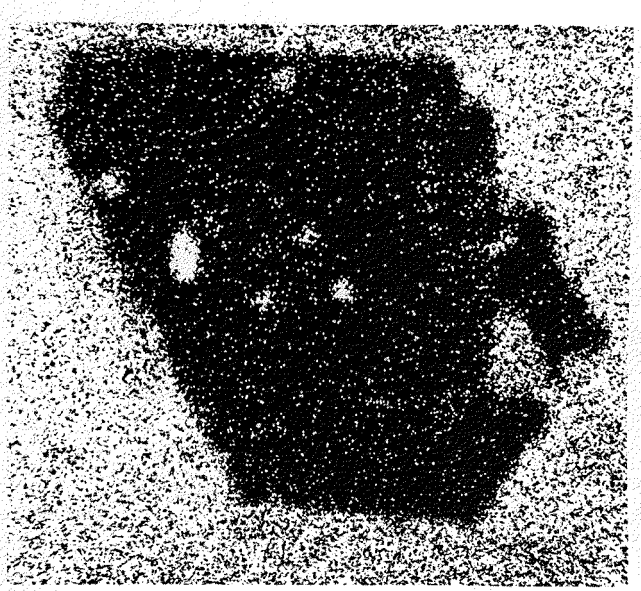

d - Si

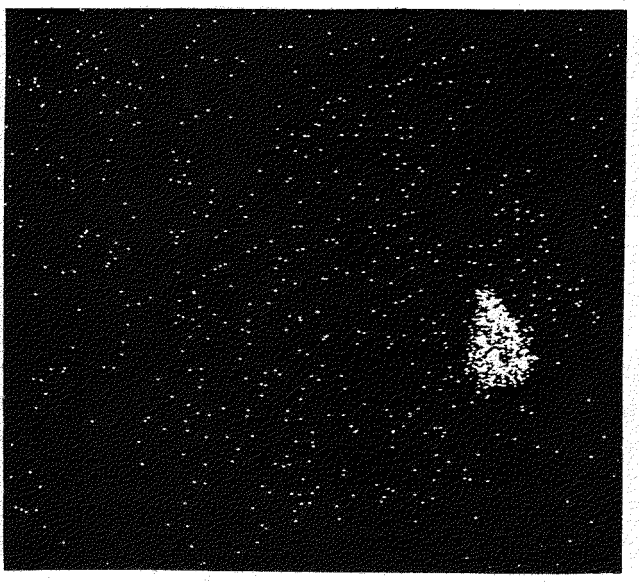

e - Zr

Figure 54 (continued)

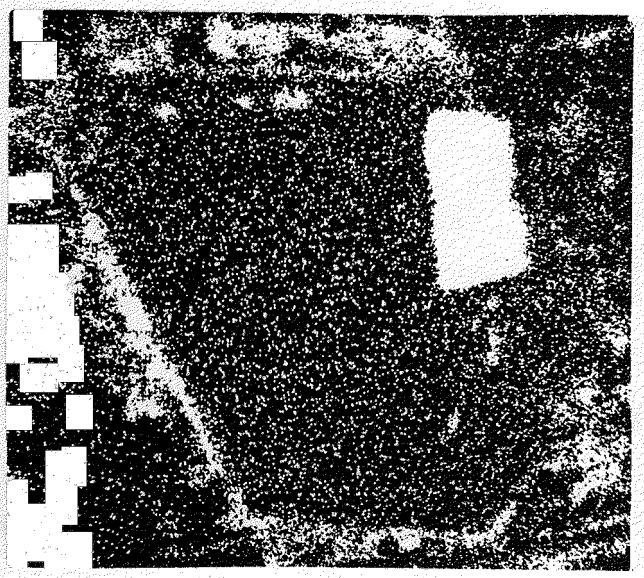

f - Fe

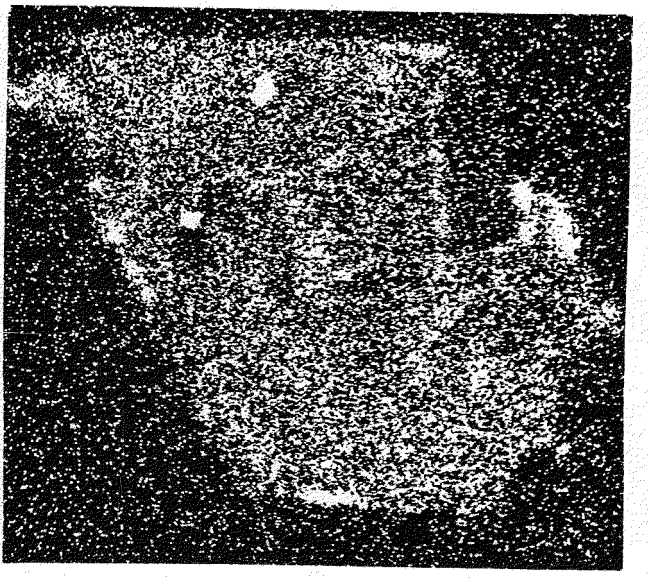

g - Th

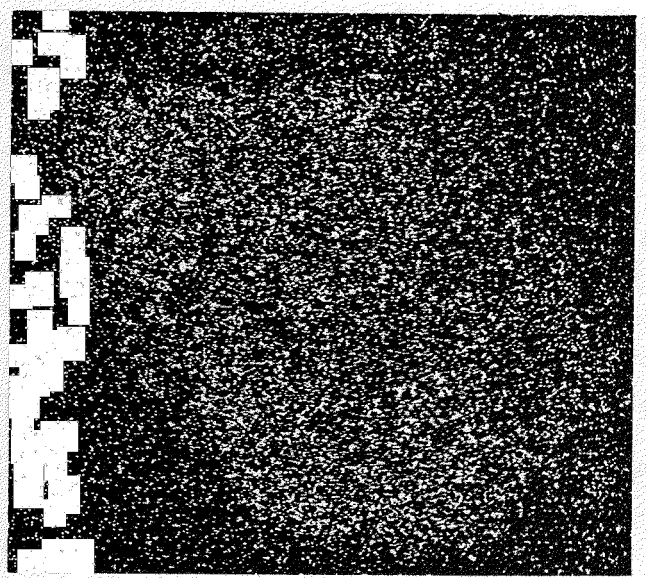

h - Pb

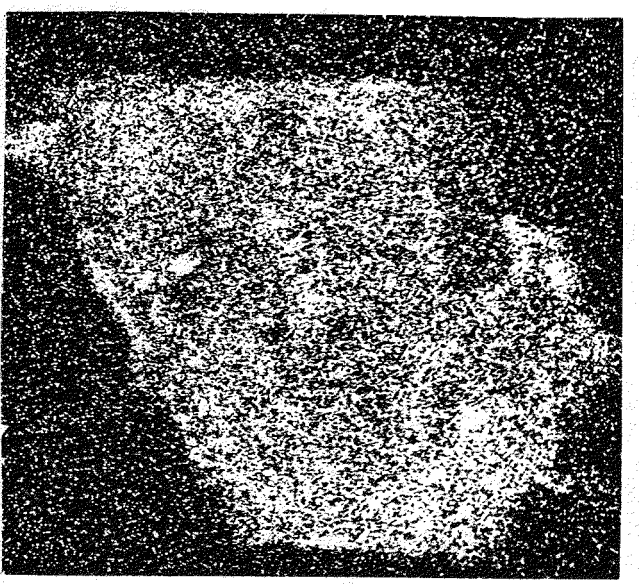

i - U

Figure 55
Photomicrograph of orange, subhedral to euhedral monazite crystals showing the variation in color, opacity and grain size. The large crystal in the upper center of the field is 150 μm long. Unmounted.

Figure 56
Photomicrograph of a monazite crystal adjacent to zircon and magnetite. The rectangular brown stain shows the EMP scan area. Note the dark (Fe-rich) areas at either end of the grain. The crystal is 150 μm long. Polished thin section, plane light.

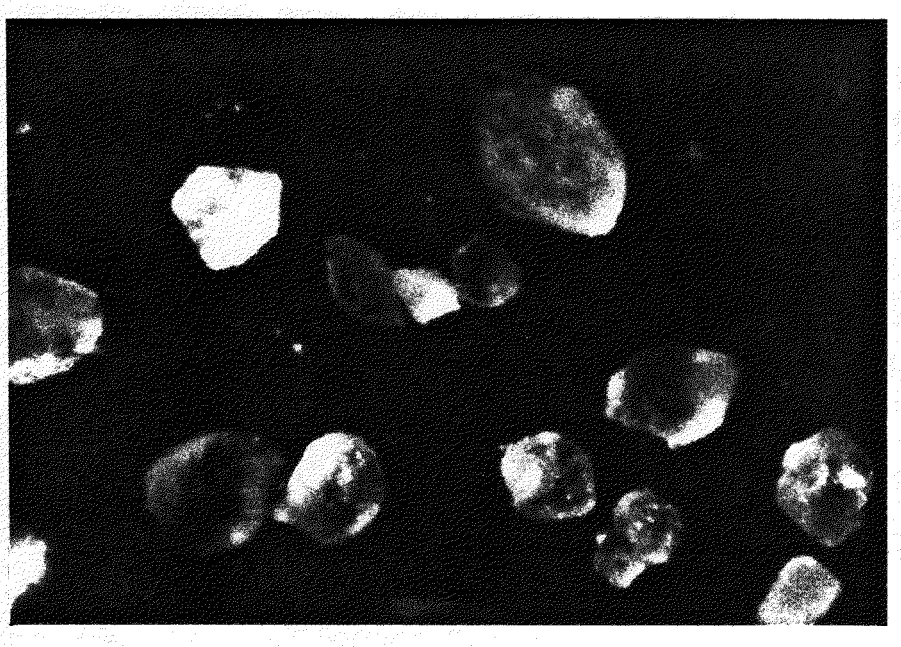

Figure 55

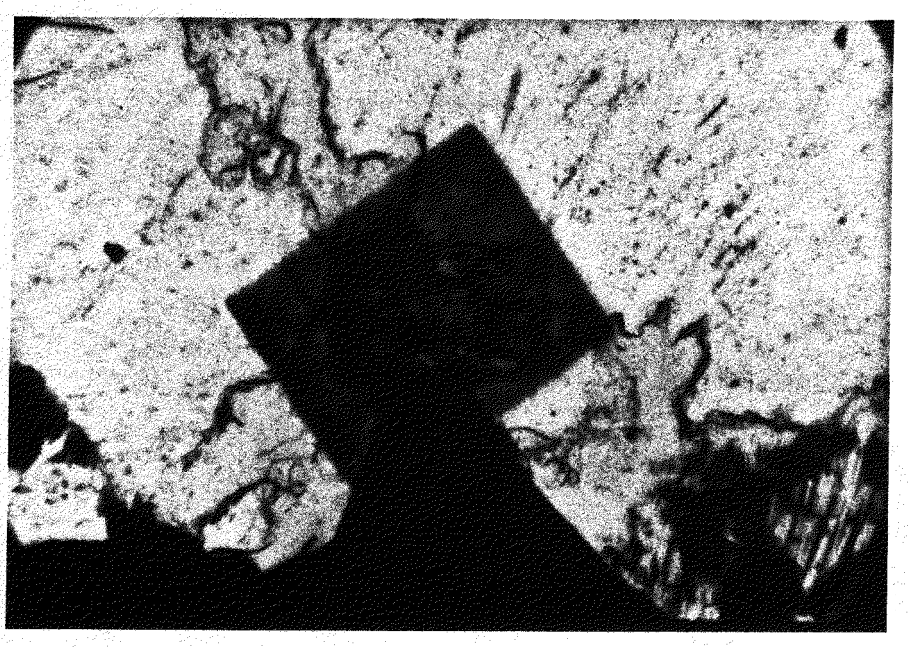

Figure 56

Figure 57
Electron Microprobe Scan Series--Monazite

a. Index sketch of the monazite, inclusions and neighboring phases (see Fig. 56).
b. Cerium distribution; note the obvious intergrowth with a second phase (see calcium distribution).
c. Calcium distribution; note the complementary relationship to cerium.
d. Phosphorus distribution; note the distinct differences in concentration which correlate with Ca and Ce distributions. The large crystal form is primarily a monazite-apatite intergrowth.
e. Silicon distribution; note the positive correlation with cerium. Monazite accepts more Si than apatite.
f. Zirconium distribution; note the two zircon euhedra adjacent to the phosphate. Also note the two other areas, one associated with a fracture, with significant Zr levels.
g. Thorium distribution, note the positive correlation with cerium-rich monazite. Also note the two high-thorium areas which appear to be thorites.
h. Yttrium distribution; note the irregular distribution following monazite, and the higher levels in the thorites and zircons.
i. Uranium distribution; note the general enrichment correlated with thorium in the monazite phase, and the even higher levels in the thorites. The phases rich in Th, U, Zr, Y and Si appear to be unusually uraniferous thorite with extensive zircon and xenotime solid solution.
j. Lead distribution; note the correlation with thorium and uranium within the monazite and the lower lead level in the thorites.
k. Iron distribution; note the low iron content of the monazite and the higher iron content of the dark halo (Fig. 56) at either end of the monazite grain. Enrichment of U and Pb above surrounding rock levels in this halo can be seen in Figures 57(i) and (j).
l. Neodymium distribution; note the neodymium enrichment in the halo.
m. Fluorine distribution; shows the intergrown apatite to be fluorapatite.

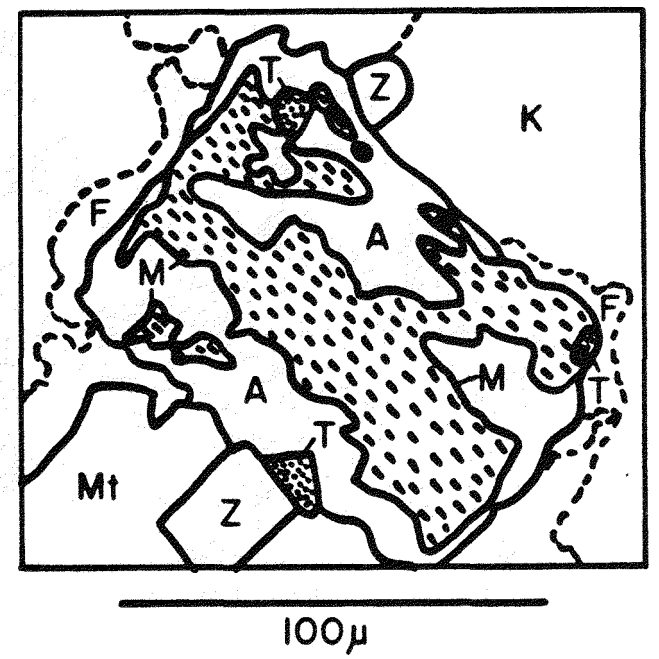

Figure 57(a)

A -- Apatite

F -- Iron-rich halo around grain

K -- Microperthite

M -- Monazite

Mt -- Magnetite

T -- Thorite

Z -- Zircon

Figure 57 (continued)

b - Ce

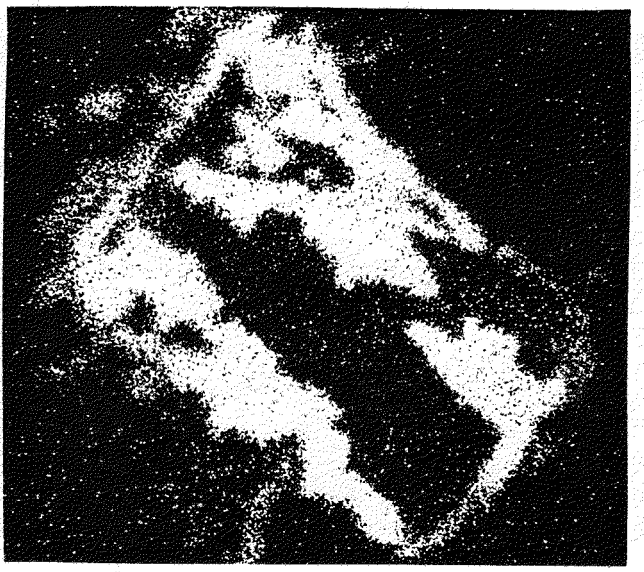

c - Ca

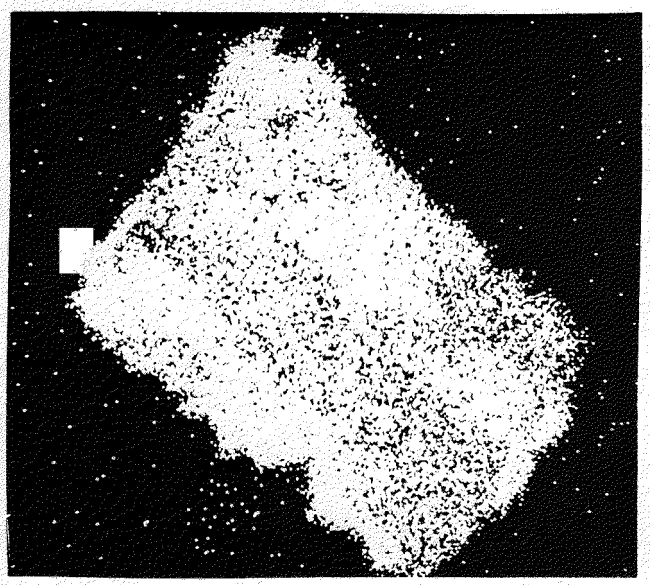

d - P

e - Si

Figure 57 (continued)

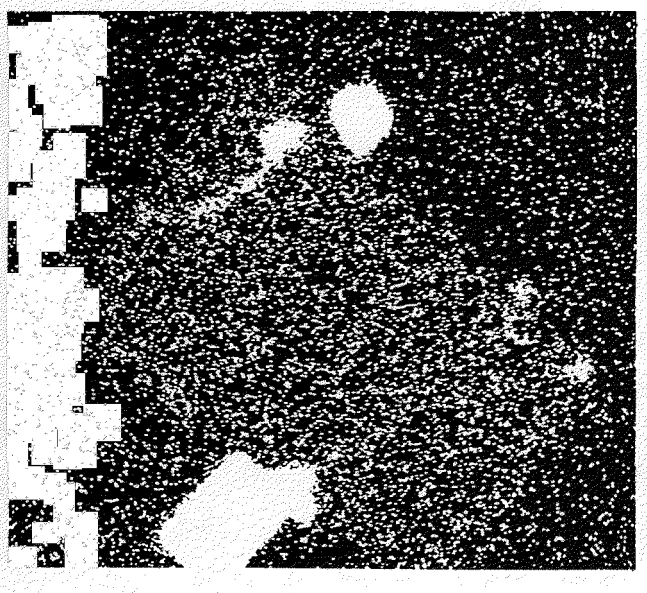

f - Zr

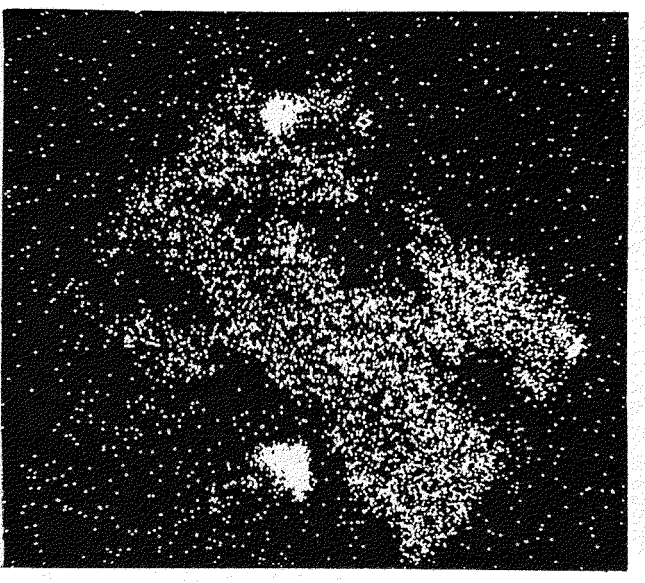

g - Th

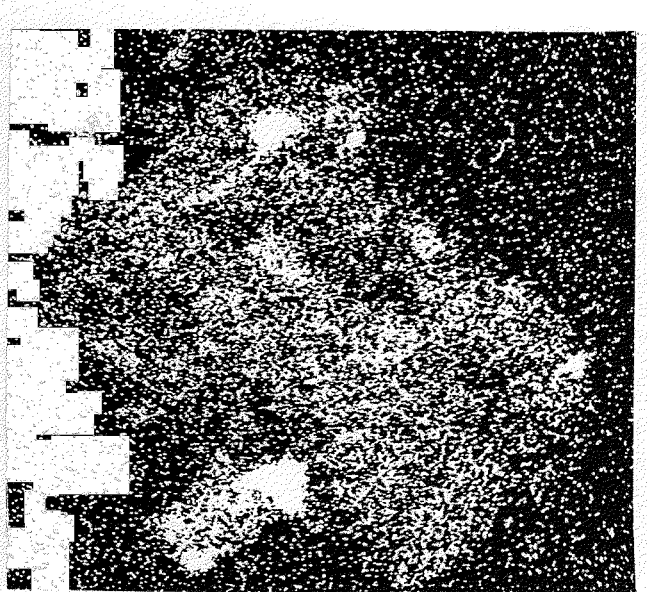

h - Y

i - U

Figure 57 (continued)

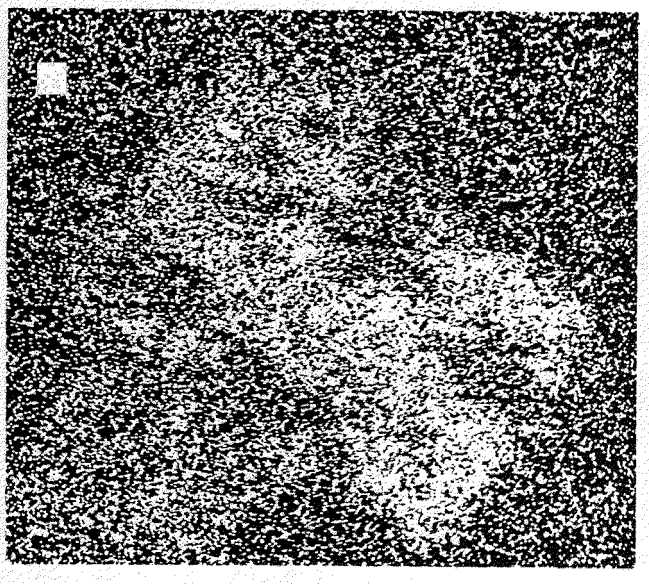

j - Pb

k - Fe

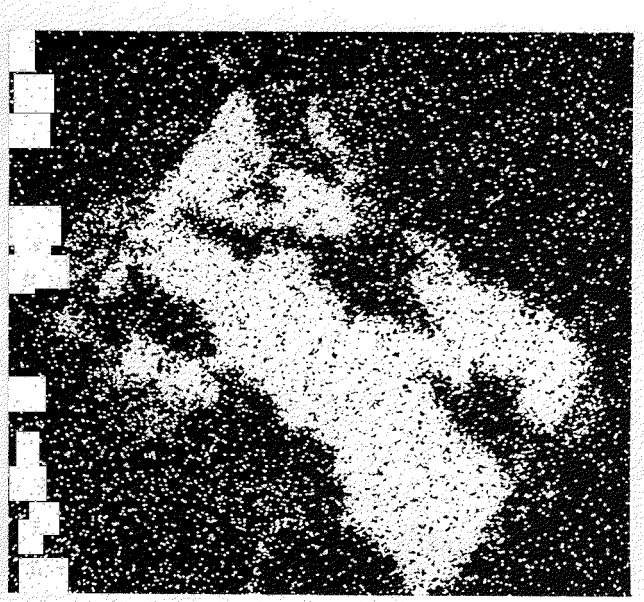

l - Nd

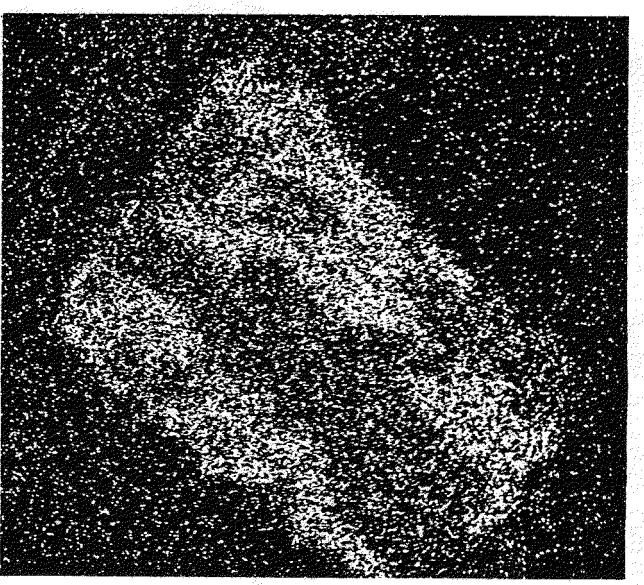

m - F

EMP analyses (Tables 15b,16) show the monazite to have nearly equal neodymium and lanthanum levels, their sum being about equal to the cerium content. Internal chemical zonation is present (Fig. 57), notably an increase in ThO_2 from about 2.5 to over 8 weight percent core to rim. The EMP scan photographs show a correlated zonation in uranium, yttrium and lead.

Uranium Titanate--Brannerite?

Calciferous uranium titanate has been identified both in thin section and the mineral separates. It is present as relatively large tabular crystals, generally broken by the liberation process, up to approximately 1mm in maximum dimension (Figs. 58,59). The unbroken grains in the mineral separates are commonly subhedral to euhedral with rounded edges and pyramid terminations, possibly orthorhombic (Figs. 60,61). The surface of the grains may be dull black-brown, yellow-white or rusty orange. Broken surfaces have a shiny resinous luster and show the same color range. The only grain of U-titanate seen in thin section occurred as a randomly oriented euhedral inclusion in plagioclase, in close association, but not aggregated, with xenotime, monazite, zircon, thorite, apatite, magnetite and ilmenite (Fig. 65). The plagioclase in its vicinity shows distension and iron staining along albite twin planes and fractures leading away from the opaque iron-rich halo which surrounds the grain (Fig. 63). Elevated lead, uranium and thorium levels can be seen in the iron-rich halo, fractures, and cleavage planes on the EMP scan photographs of Figure 64.

EMP analyses (Tables 15c,16) have shown the U-titanate crystals to contain as many as four chemically distinct internal zones (Figs. 62,64) corresponding to the areas of different color:

Zone A, black, lustrous and isotropic, forms the center of most grains. It consists of highly uraniferous titanate with 40-50 percent UO_2, 3-6 percent ThO_2 and 0.7-3 percent PbO. Some grains are almost exclusively Zone A material, suggesting that it may represent the original mineralogy of those crystals which now are compositionally zoned.

Zone B, brown, lustrous and isotropic, commonly occurs outside of or intergrown with Zone A. It contains 20-25 percent UO_2, 5-8 percent ThO_2 and 4-6 percent PbO. The composition of both Zones A and B can be expressed by a brannerite formula, $(U,Ca,Th,REE)(Ti,Si,Fe)_2O_6$. Together they comprise over 80 percent of most grains. Both zones appear to be totally metamict.

Zone C, pale, yellowish-brown, is probably a multiphase aggregate of more than one species. It forms a thin outer layer on Zones A and B or may be intergrown with them. It is highly enriched in titanium (54-64 percent TiO_2), and contains 2-7 percent UO_2, 4-6 percent ThO_2 and 1-3 percent PbO. X-ray diffractometry indicates the presence of anatase, but does not distinguish whether uranium and thorium present are substituted in the anatase or are in an intergrown, metamict, uranium-thorium-titanium-bearing phase. In thin section the birefringence of the crystalline anatase clearly is visible.

Zone D, rust-brown and also probably a multiphase aggregate, sometimes is present as an irregular outer zone on Zone C. Relative to Zone C, it is

Figure 58
Photomicrograph of hand-picked fragments of calciferous uranium titanate (brannerite?) showing the typical light yellow and orange outer zones around irregular dark brown to black cores. The largest fragment is 900 µm long. Unmounted.

Figure 59
Photomicrograph of a brannerite? crystal in cross-section showing in detail the irregular zonation of dark brown and yellow phases. A thin outermost orange layer is visible. The grain is 500 µm long. Unmounted.

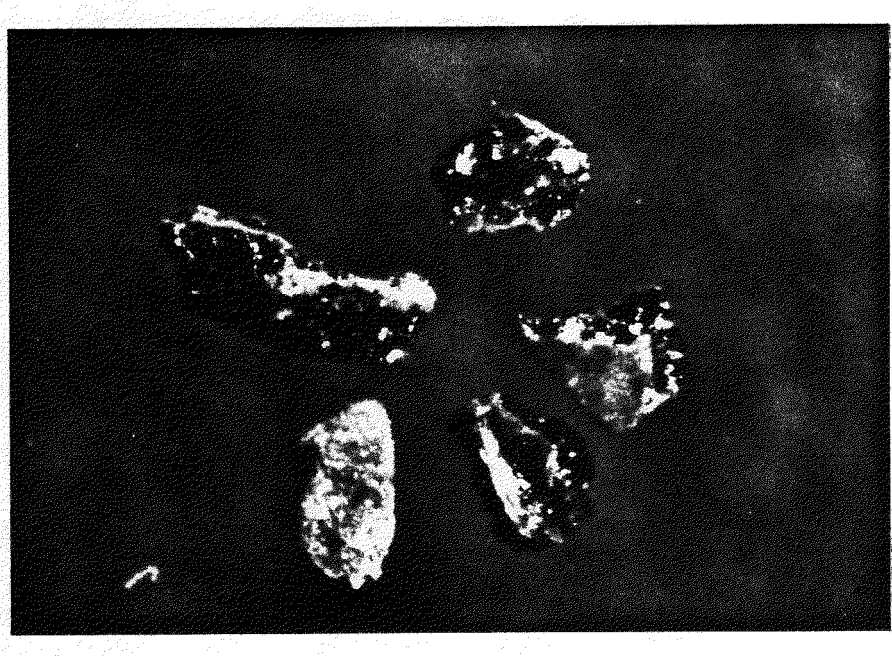

Figure 58

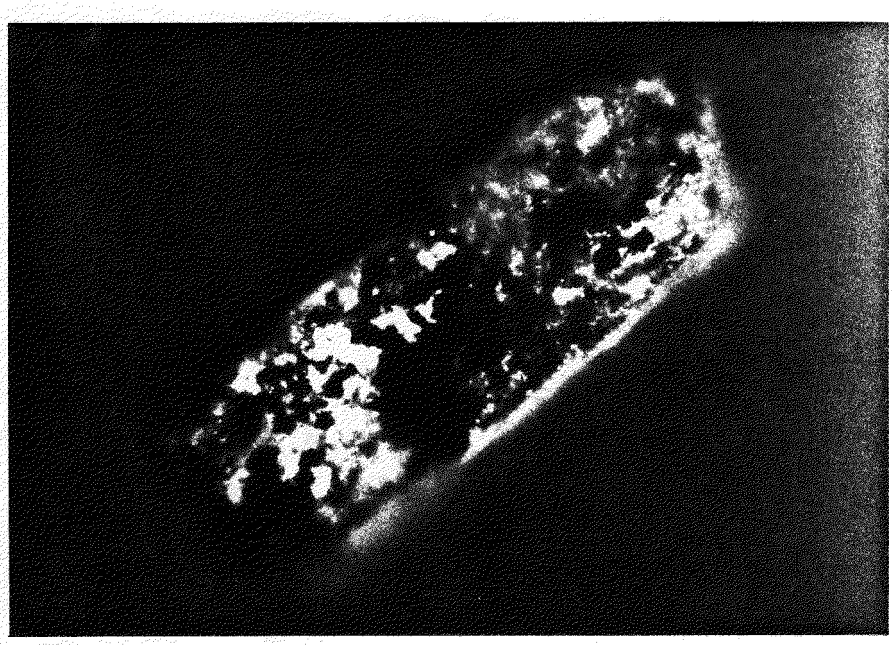

Figure 59

Figure 60
Photomicrograph of brannerite? cut approximately parallel to the long axis and polished close to the large crystal face showing the irregular internal color distribution. The characteristic crystal form is visible. The grain is 800 µm long. Polished grain mount.

Figure 61
Photomicrograph of brannerite? viewed on a polished surface cut approximately perpendicular to the long axis. The interior varies irregularly in color and composition. The thin, rusty outer zone is enriched in Fe and Ti. The off-white region at right center is predominantly anatase. The grain is 550 µm long on the polished surface. Polished grain mount.

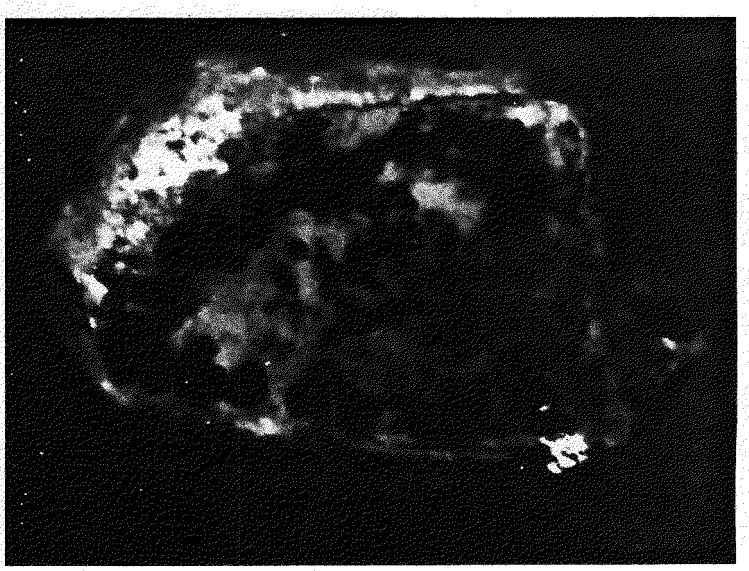

Figure 60

Figure 61

Figure 62
Electron Microprobe Scan Series--Brannerite?

a. Index sketch of the brannerite? grain shown in Figure 61.
b. Photomicrograph in reflected light of the polished surface of the grain in Figure 61. In general the more uraniferous zone stands higher, with a better polish. The grain is 470 μm long.
c. Titanium distribution; with the exception of obvious high concentrations in the anatase in a Zone C area in the center-right part of the grain and in the outer zone, titanium is quite uniform. (The apparent outward decrease is an artifact of beam defocussing due to the large area scanned.)
d. Uranium distribution; the concentration of uranium is much more heterogeneous than that of Ti. Compare with reflectance properties in (b).
e. Thorium distribution; note the negative correlation between thorium and uranium.
f. Calcium distribution; calcium tends to be uniform with some enrichment in the high Th core and at the inner edge of the outer zone, and with depletion in the anatase.
g. Iron distribution; enrichment of iron is apparent in the outer rusty zone of the crystal and in the anatase. A slight enrichment also occurs in the thorium-rich central zone.
h. Silicon distribution; note the distinct zonation in silicon content showing strong negative correlation with uranium. Several types of silicate inclusions are visible.

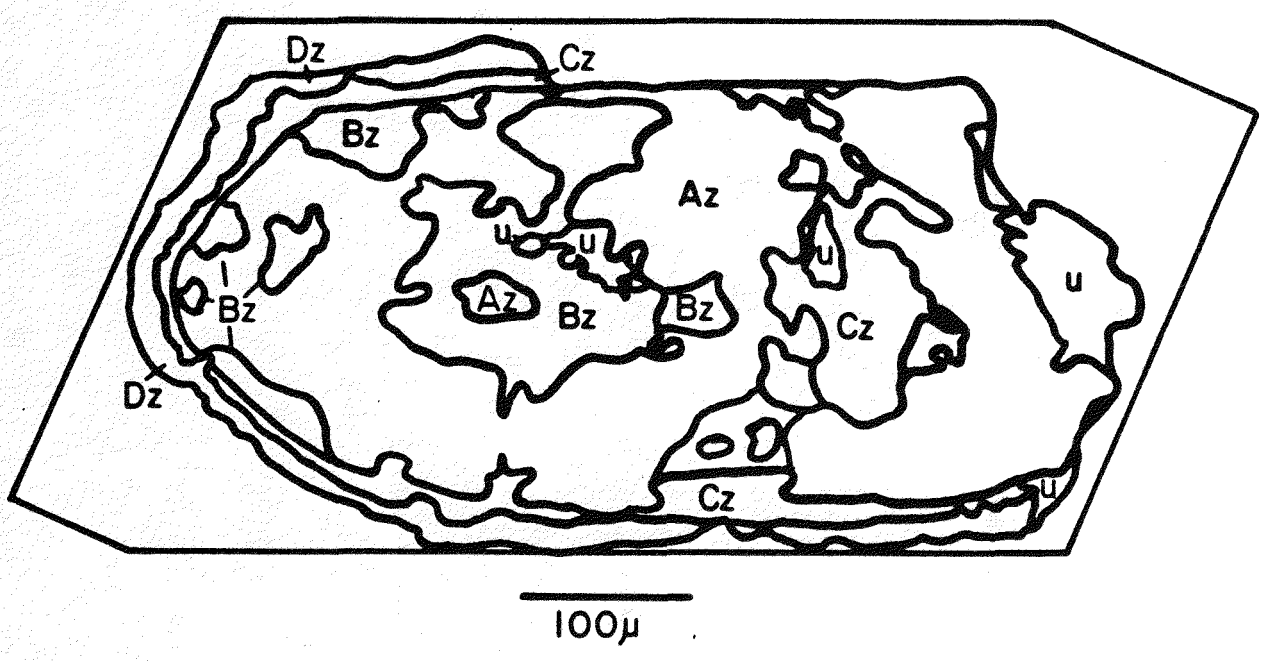

Figure 62(a)

Az - U-titanate, highest U zone

Bz - U-titanate, intermediate zone

Cz - Titaniferous zone with anatase, low U

Dz - High iron zone, low U

u -- Various silicate inclusions

Figure 62(b)

Figure 62 (continued)

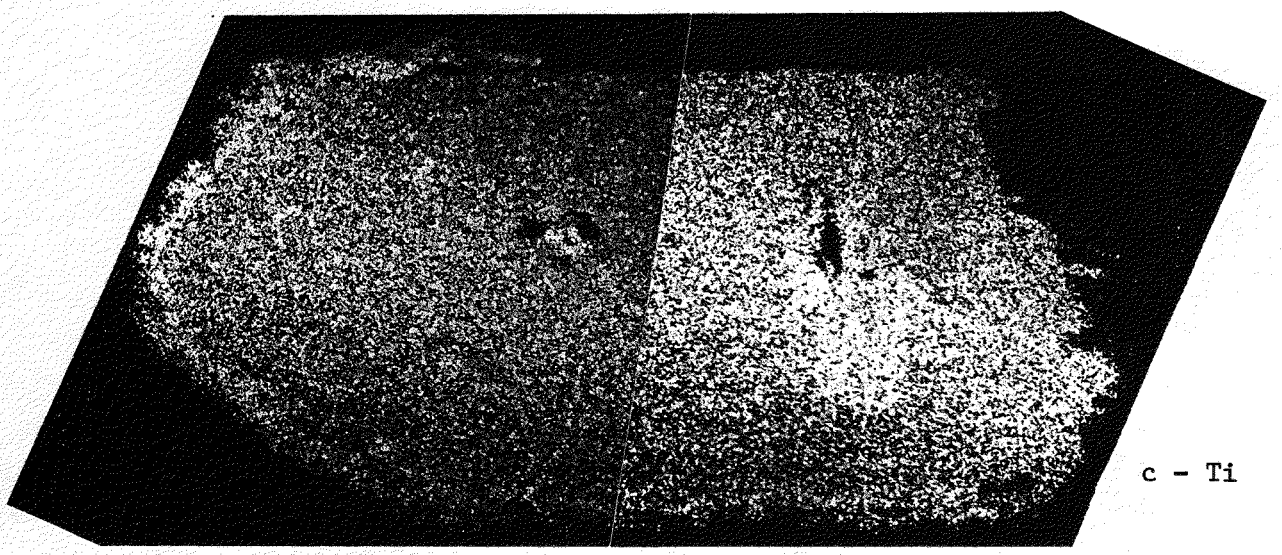

c - Ti

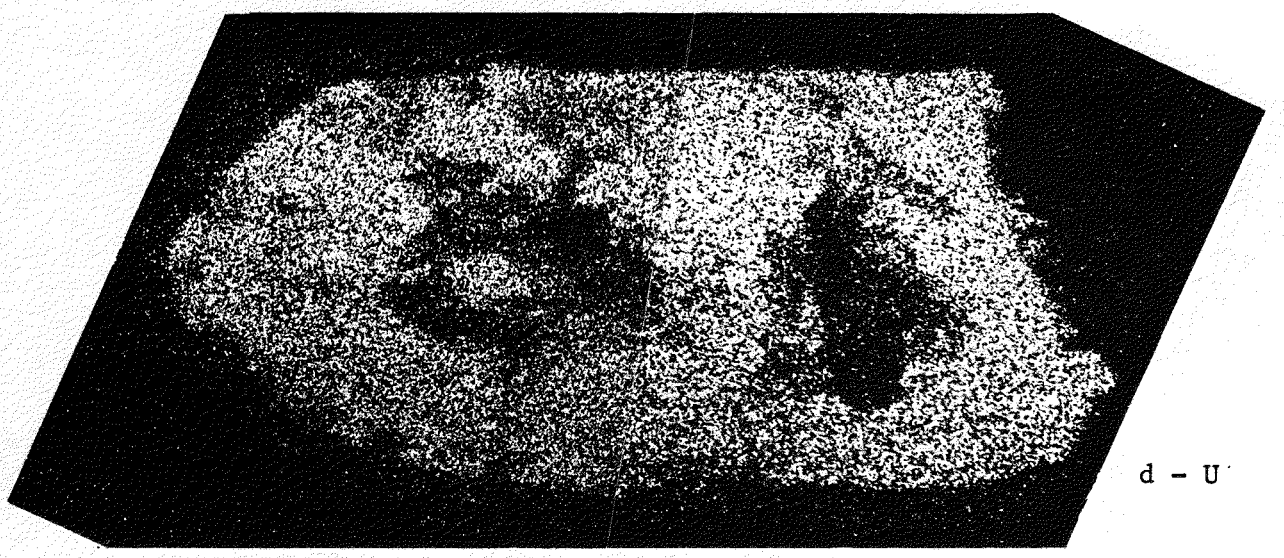

d - U

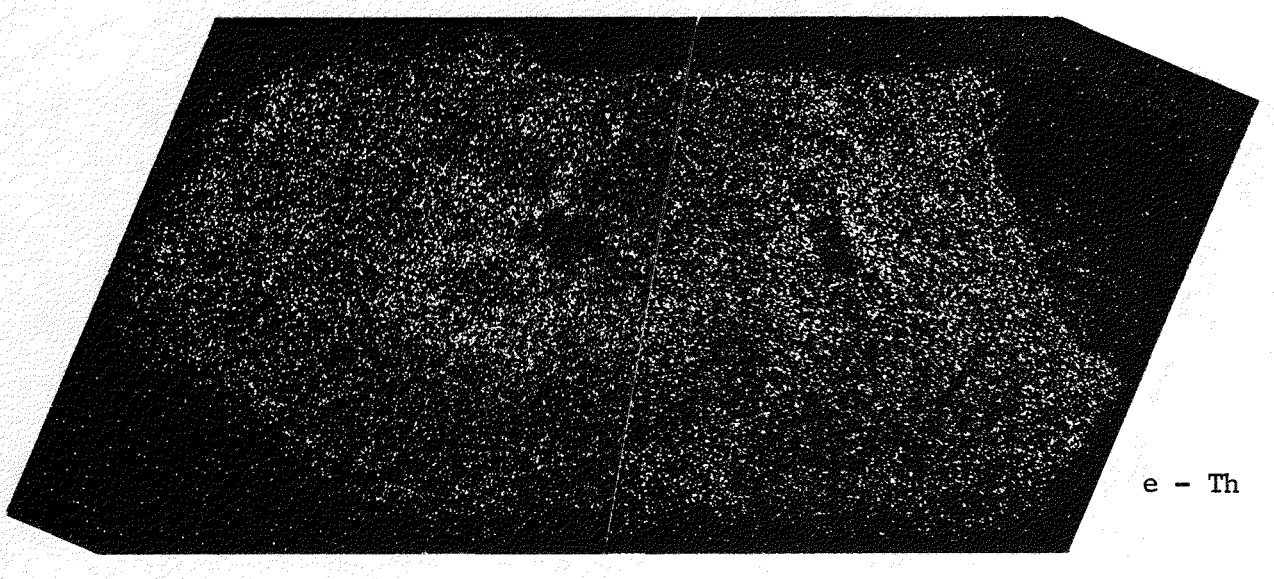

e - Th

Figure 62 (continued)

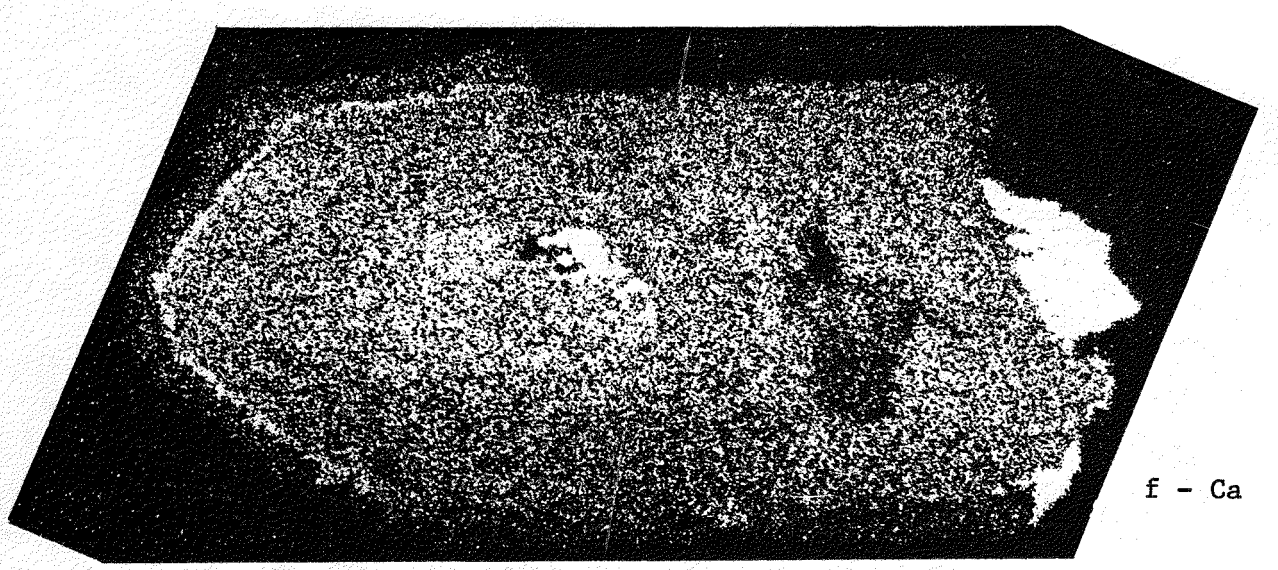

f - Ca

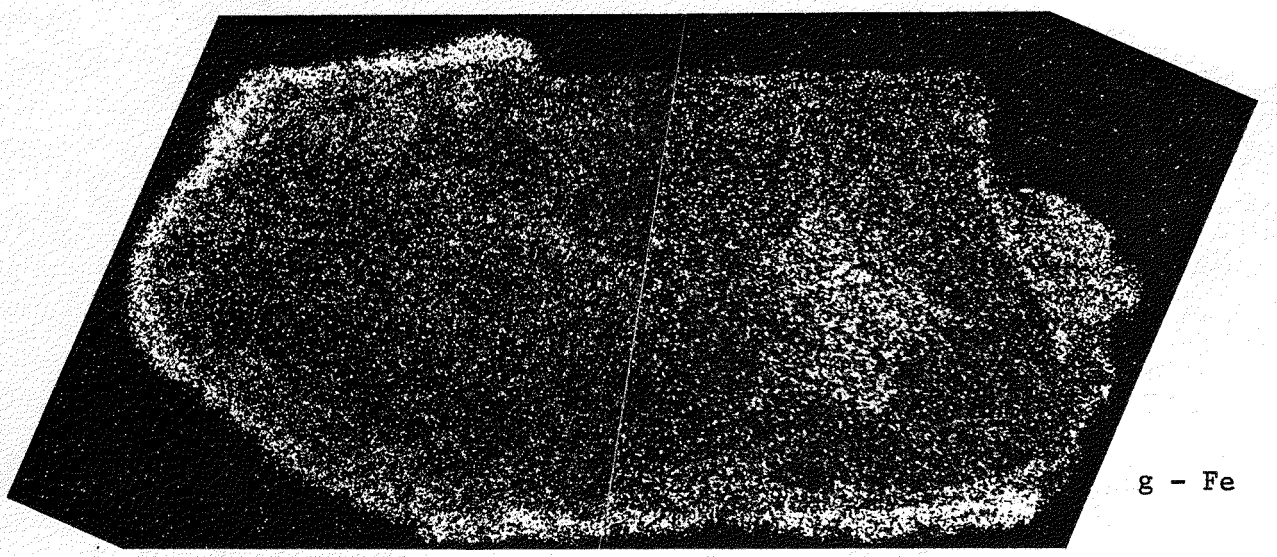

g - Fe

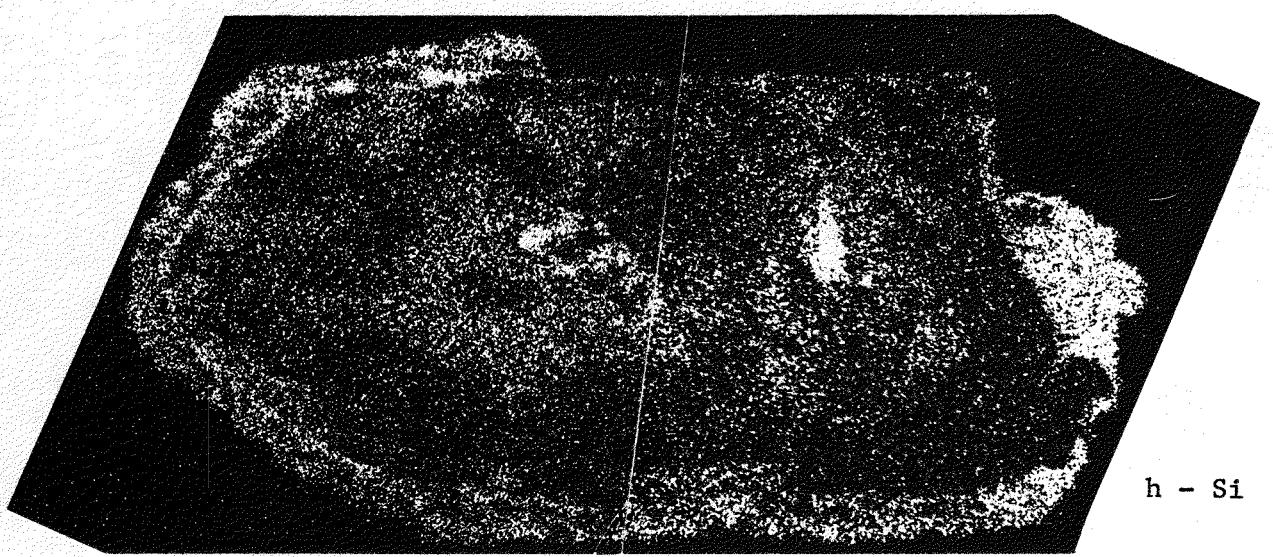

h - Si

Figure 63
Photomicrograph of brannerite? showing the hour-glass zonation in color and opacity, internal fracturing and opaque (Fe-rich) halo. Note the opaque halo appears to have penetrated cleavages and fractures in the surrounding host plagioclase. The grain is 470 μm long. Polished thin section, plane light.

Figure 63

Figure 64
Electron Microprobe Scan Series--Brannerite?

a. Index sketch of the brannerite? grain shown in Figures 63 and 64.
b. Photomicrograph of the brannerite? grain after the EMP scan showing the surface desiccation caused by the energy of the electron beam and the characteristic stain over the scanned area. Polished thin section, reflected light.
c. Uranium distribution; note the high but extremely variable concentration levels (the range is a factor of 20). Uranium is highest in the darkest interior zones visible at the top of Figure 63.
d. Thorium distribution; the concentration variation is more limited than that of uranium, and is negatively correlated with it.
e. Titanium distribution; showing a uniformly high concentration with some marked enrichment around the crystal waist.
f. Silicon distribution; showing zonation with the lowest values in the highest uranium zones and the highest values in the translucent brown hourglass shaped zone (intermediate U) and in the narrow outer zone.
g. Iron distribution; showing enrichment around the waist of the grain and especially in the outermost zone. An external, dark iron-rich halo extends into fractures and cleavages of the host feldspar.
h. Yttrium distribution; yttrium tends to be depleted where uranium is lowest.
i. Lead distribution; surprisingly, lead (which isotopic studies show largely to be radiogenic) does not show a positive correlation with uranium. There also is distinct evidence for lead migration into iron-rich fractures in the host feldspar.
j. Phosphorus distribution; phosphorus is lowest in the highest uranium regions, but appears to correlate with uranium in the waist regions. Phosphorus correlates negatively with yttrium.
k. Calcium distribution; calcium is fairly uniform except for a depletion around the waist and in the high-Ti outer zone. The calcium-rich inclusions may be fluorite. (The apparent diagonal enrichment is an artifact of beam defocussing.)
l. Magnesium distribution; magnesium is generally uniform except for enrichment in the outer iron-rich zone at the sides of the grain.
m. Manganese distribution; manganese is generally uniform except for a depletion around the waist.
n. Niobium distribution; niobium shows distinct enrichment in the titanium-rich outer zone and extends into fractures in the host feldspar.

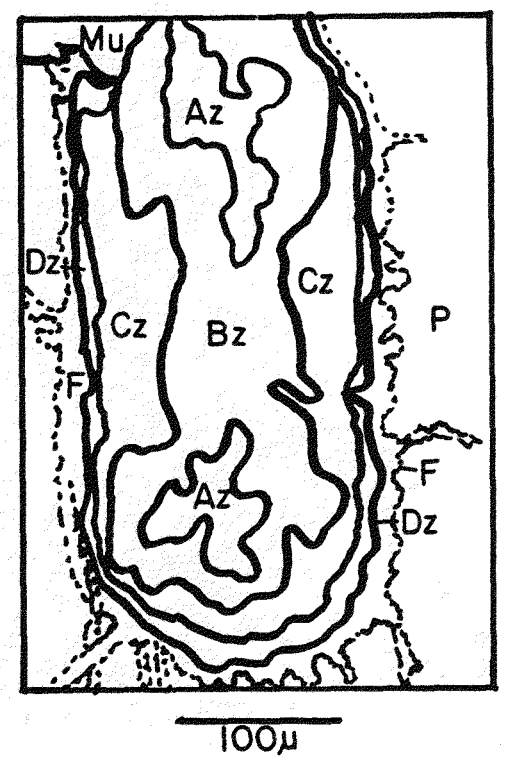

Figure 64(a)

Az - U-titanate, highest U zone

Bz - U-titanate, intermediate zone

Cz - Titaniferous zone with anatase, low U

Dz - High iron zone, low U

F -- Iron enrichment halo

Mu - Muscovite

P -- Oligoclase host

Figure 64(b)

Figure 64 (continued)

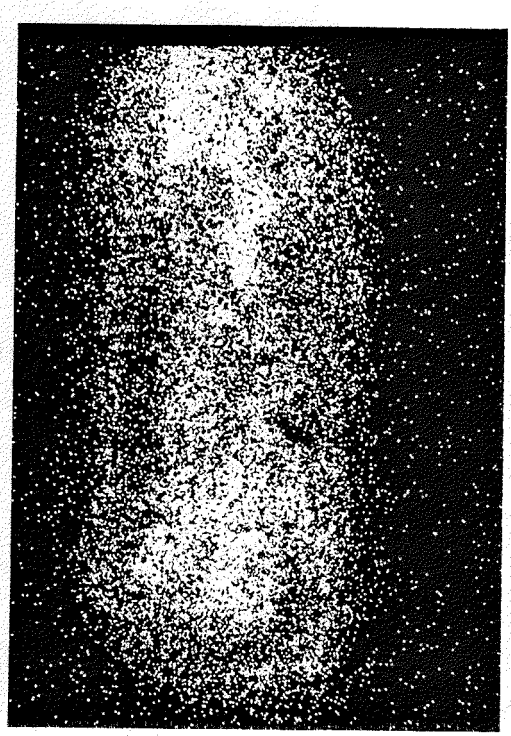

c - U

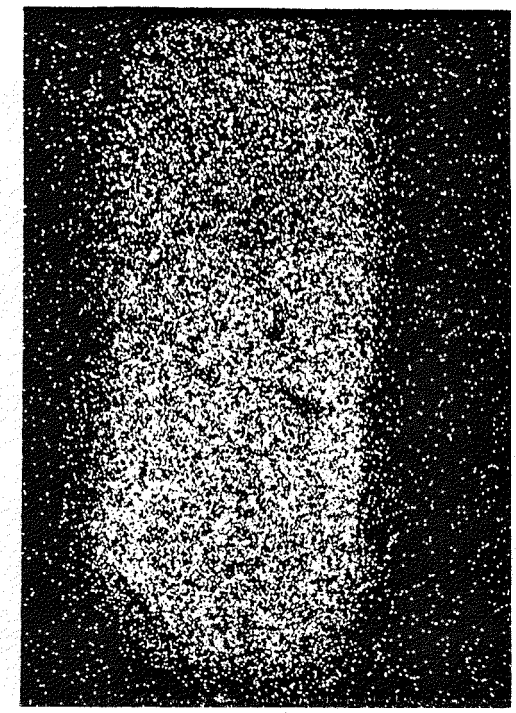

d - Th

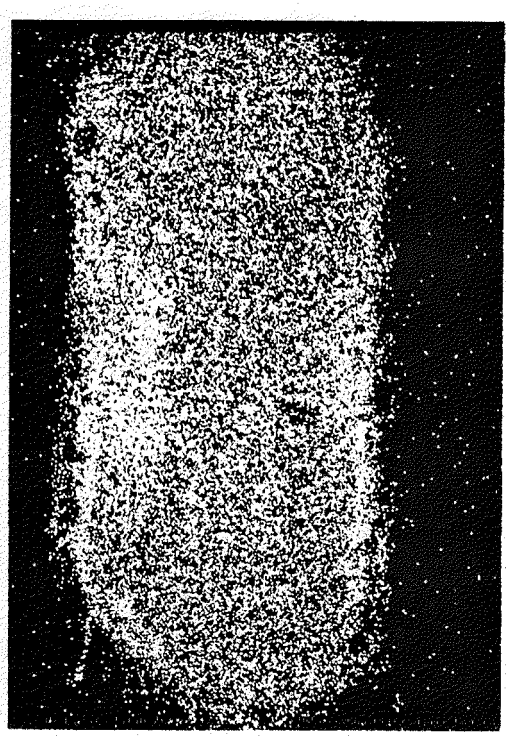

e - Ti

f - Si

Figure 64 (continued)

g - Fe

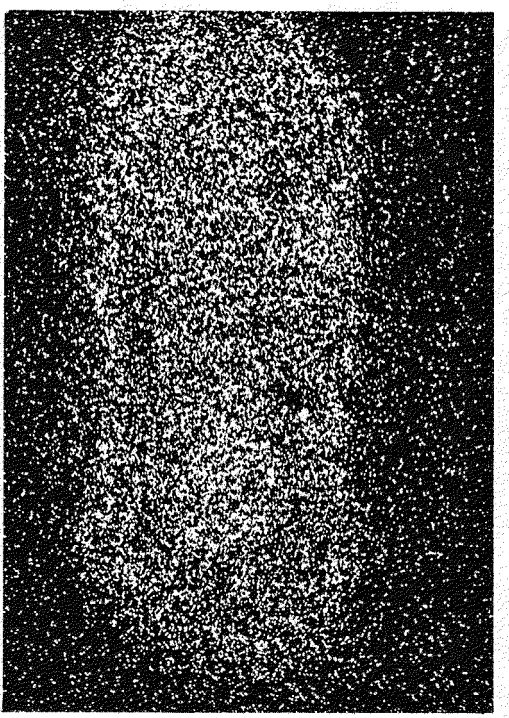

h - Y

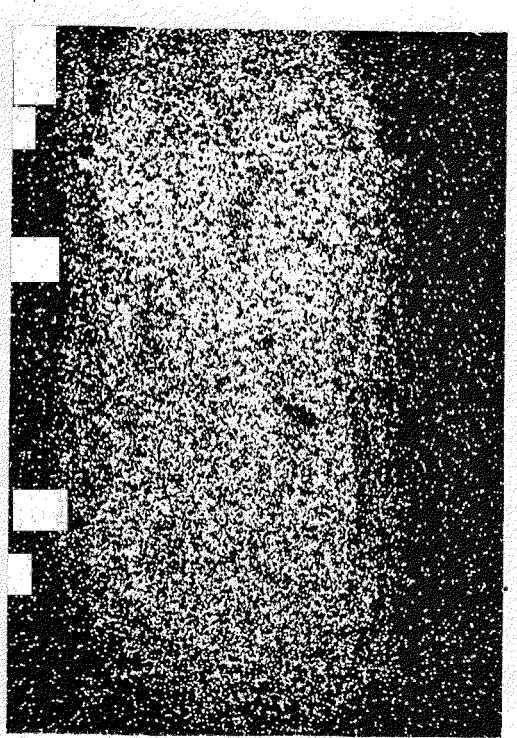

i - Pb

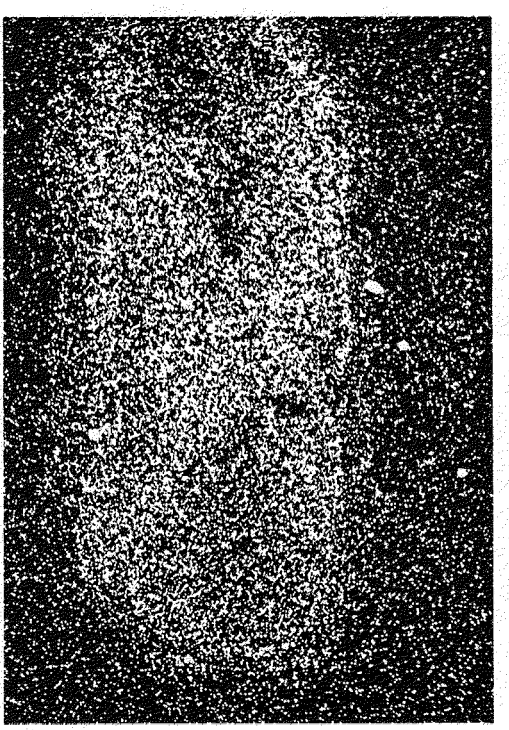

j - P

Figure 64 (continued)

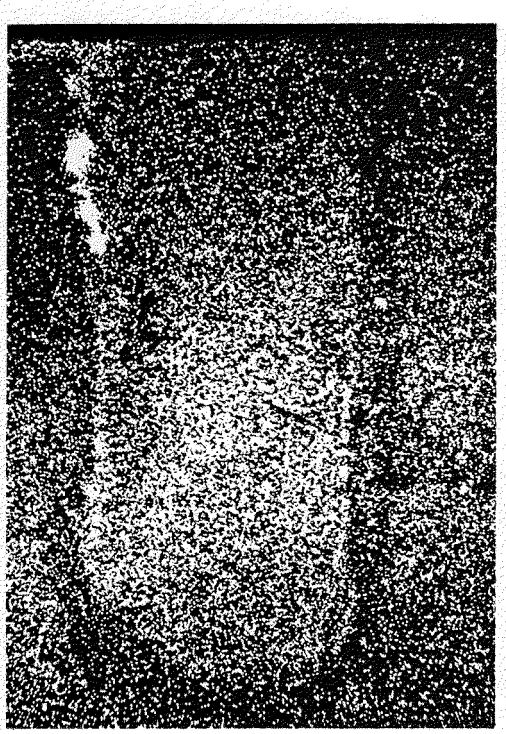

k - Ca

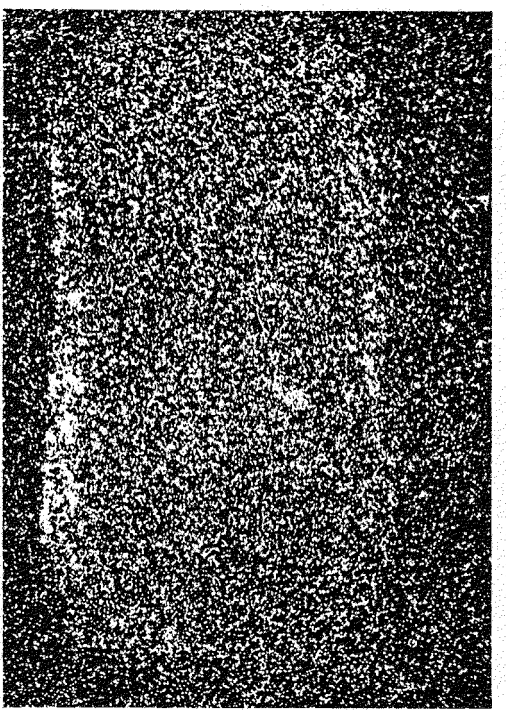

l - Mg

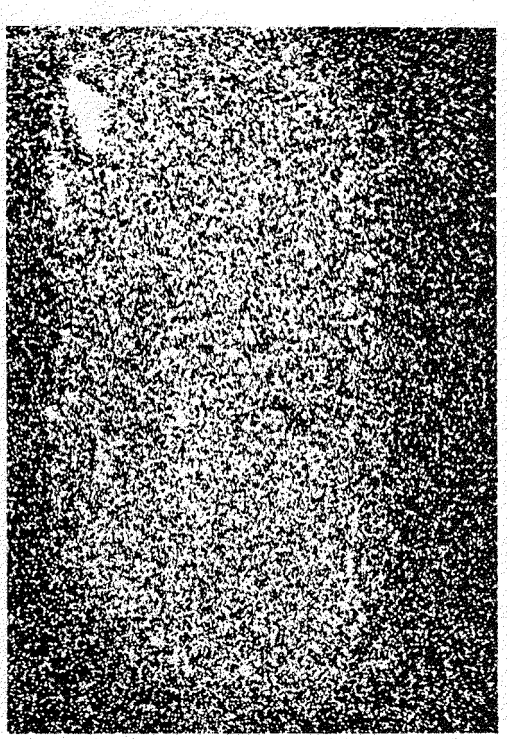

m - Mn

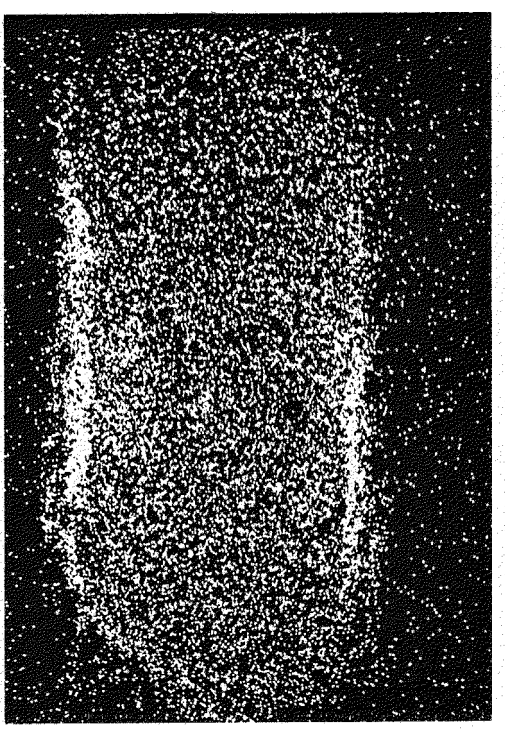

n - Nb

Figure 65
Photomicrograph showing textural relationships among brannerite? (Fig. 63), xenotime (Fig. 53), and an association of accessory minerals with a manganilmenite-magnetite aggregate (upper right; see also Fig. 66). The brannerite? in the upper left of the field is 470 µm long. Polished thin-section, plane light.

Figure 65

enriched in iron, silicon, and lead (~5 percent PbO) and depleted in titanium. The uranium and thorium contents of Zones C and D are similar.

The EMP analysis sum decreases progressively from Zone A through to Zone D, suggesting an outward increase in water content. This is corroborated by the significant desiccation of the grain surface observed after the EMP scans were made (Fig. 64b). From the EMP data however, it does not appear that Zones A through D represent a simple sequential alteration of Zone A material; the uncorrelated and irregular changes in uranium, thorium and lead content being a case in point (Fig. 64) If the measured lead is assumed principally to be radiogenic, relative to the presently observed uranium contents and the 1411 m.y. age, Zone A may be about 90 percent lead deficient, while Zone D may contain a lead excess of more than a factor of four.

Anatase

Anatase has been detected by X-ray diffraction in the relatively low uranium and thorium Zone C of U-titanate, brannerite? (Figs. 61-64). The zone appears to be finely multicrystalline, but EMP analyses and X-ray diffraction results do not indicate whether the uranium, thorium, and lead present in Zone C occur in the anatase itself, in a metamict phase mechanically mixed with anatase, or along grain boundaries and fractures. Its textural occurrence suggests that the anatase was formed secondarily by breakdown or alteration of primary brannerite? but does not rule out original chemical zonation of the brannerite?.

Thorite

Thorite has been identified in EMP scan photographs of thin sections (Figs. 65,66) but not in the high-density mineral separates. It is probable that grains in the zircon separates were removed by acid-washing procedures in preparation for isotopic analysis. It occurs as minute subhedral to euhedral stubby prismatic crystals, up to about 25 μm in width, in clusters of other radioactive accessory minerals in micas and associated with aggregates of magnetite and manganilmenite. Larger thorite crystals commonly contain inclusions of xenotime and zircon, apparently grown in crystallographic continuity with their host. Thorite itself occurs as micron-size inclusions in xenotime (Fig. 54) and zircon (Fig. 51), and commonly occurs in contact with zircon in apparent epitaxy. Thorium silicate inclusions seen in EMP scan photographs of monazite (Fig. 57) have been identified as thorite by their apparent chemistry but the monoclinic dimorph huttonite, which is isostructural with monazite, has not been ruled out.

Because of the thorite's fine grain-size, its full compositional range has not yet been determined. Available analyses indicate the presence of up to 47.7 weight percent ThO_2 and 3.7 weight percent UO_2, between 6 and 10 atom percent rare earths substituting for Th, and significant solid solution components of both zircon and xenotime (Tables 15b,16). EMP scan photography (Fig. 51) suggests that grains with even higher uranium and thorium contents probably are to be found.

Figure 66
Electron Microprobe Scan Series--Accessory Mineral Group

a. Index sketch of the accessory mineral group shown in Figure 65, upper right stained region. The thorite grain in the upper left of the field is 25 μm across.
b. Thorium distribution; a euhedral thorite with a low-thorium core is present in the lower left of the field. Thorium-rich monazite with two thorite inclusions and a Th-rich crack are found in the upper right.
c. Zirconium distribution; three zircons appear in the field. The largest zircon has a low-Zr inclusion. The zircon at the lower left is hosted in thorite. All thorite grains have distinct Zr enrichment.
d. Yttrium distribution; enrichment in the core of the large thorite indicates a xenotime crystal. The other thorites have yttrium levels similar to the large thorite, and some enrichment is seen in the monazites and zircons.
e. Phosphorus distribution; the high phosphorus concentration in the core of the larger thorite indicates a xenotime grain. Other high concentrations are seen in the monazites and in an apatite crystal included in the large zircon, and in apatites intergrown with monazite. The thorites show a higher phosphorus content than the P-enriched corners of the large zircon.
f. Cerium distribution; cerium defines the monazite grains. Compare the outline of the larger monazite at the upper right with those in Figures 66(b) and (e). Faint cerium enrichment is visible in the larger thorite.
g. Calcium distribution; calcium shows the apatite inclusions in zircon and monazite. The Ca level in the larger thorite is higher than that in the zircon.
h. Iron distribution; a large manganilmenite with a small magnetite at its left is clearly defined. A striking iron-enriched halo is visible around the larger thorite; smaller enrichments occur in the vicinity of the other thorites, monazites and zircons.
i. Uranium distribution; highest uranium concentrations are found in the thorites. Other high levels are found in the xenotime, monazites and zircons. Note the uranium and thorium enriched fracture filling which extends from the large zircon to the largest monazite in the upper right field.

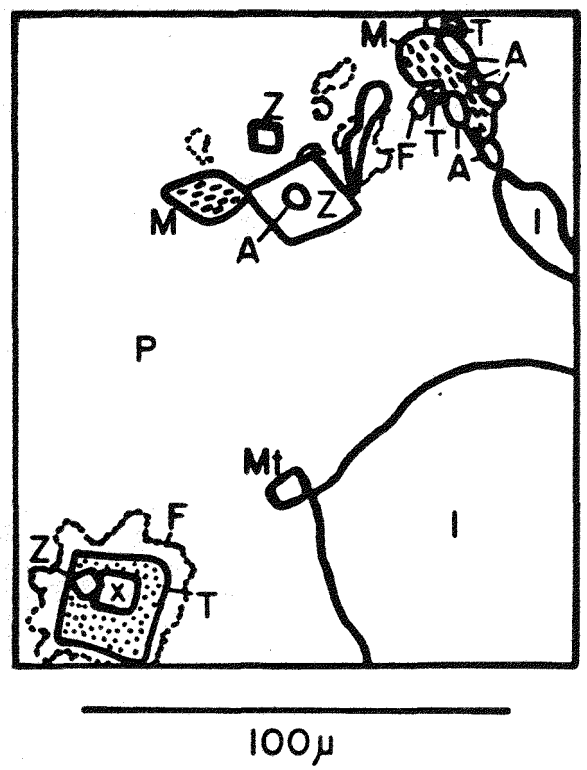

Figure 66(a)

A -- Apatite

F -- Iron-enriched haloes

I -- Manganilmenite

M -- Monazite

Mt -- Magnetite

P -- Oligoclase

T -- Thorite

X -- Xenotime

Z -- Zircon

Figure 66 (continued)

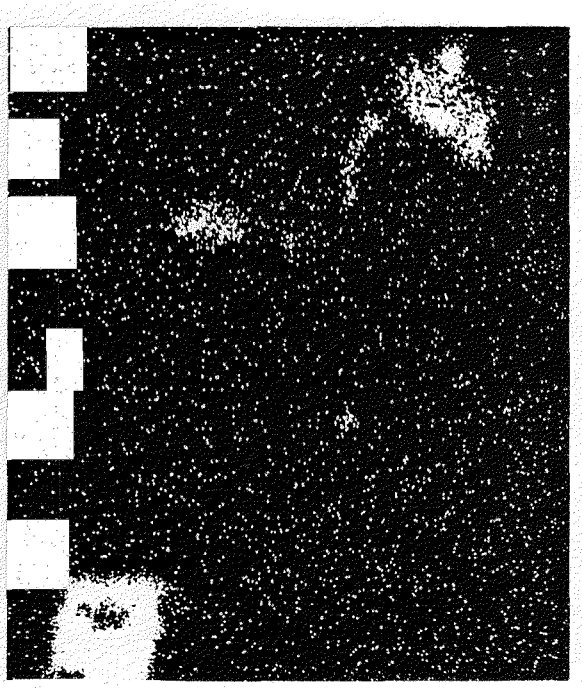

b - Th

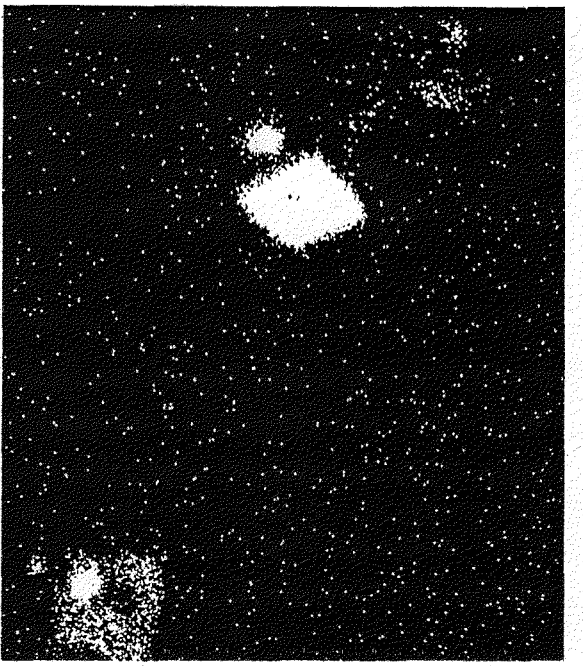

c - Zr

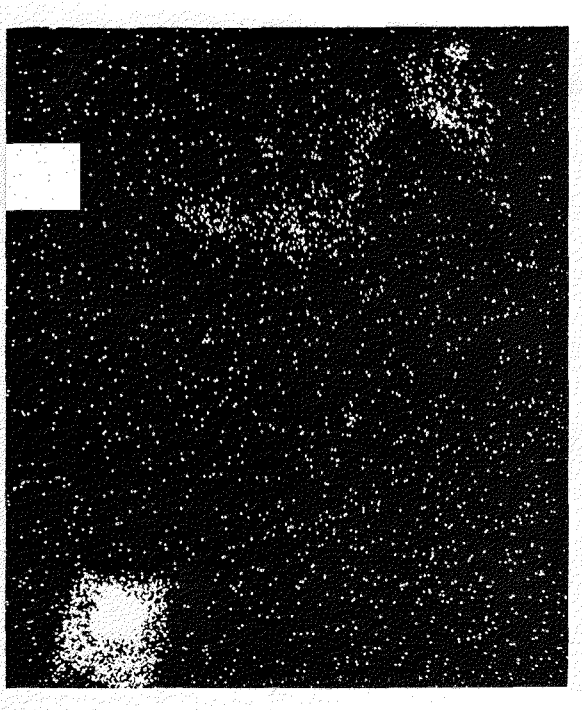

d - Y

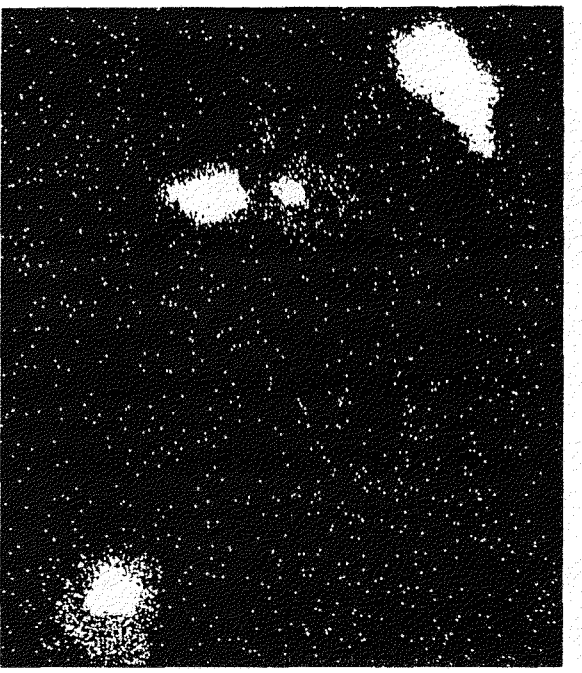

e - P

Figure 66 (continued)

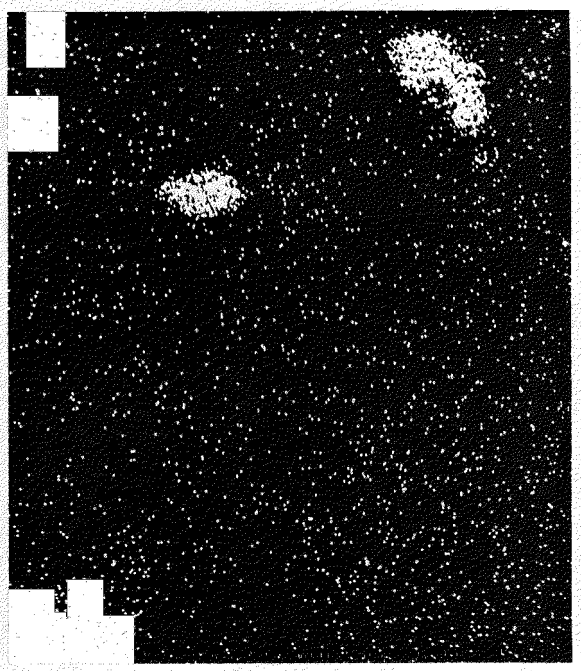

f - Ce

g - Ca

h - Fe

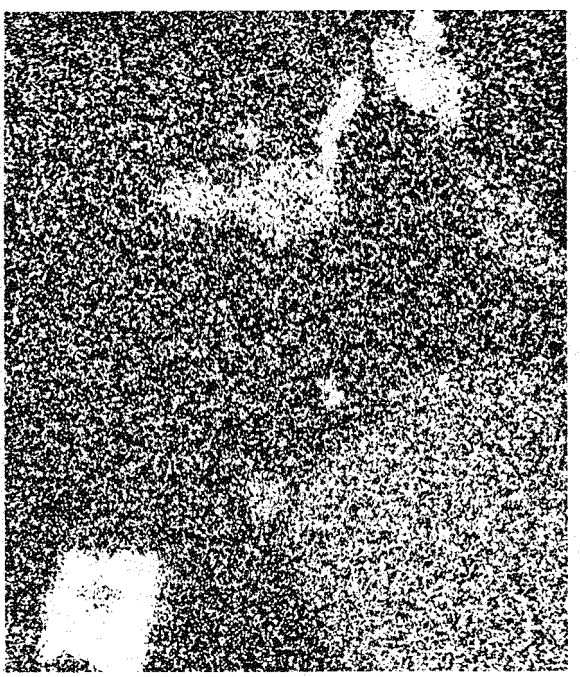

i - U

Uranium Silicate--Thorian coffinite?

A single grain of uranium-rich silicate was identified in thin section by EMP analysis. None has been distinguished in the mineral separates, perhaps because the mineral's brown-black color, near isotropy and opacity make it similar in appearance to the numerous crystals of uranium titanate. The identified grain is 300 μm in cross section and occurs as a euhedral inclusion in muscovite (Fig. 67) with a form suggestive of a cut through a tetragonal dipyramid. In the vicinity of the uranium silicate, the muscovite shows distension along cleavages and has an abnormally high iron content. The grain is very weakly anisotropic in patchy zones, possibly reflecting the presence of some alteration phases.

EMP analyses (Tables 15c,16) and probe scan photographs (Fig. 69) show the uranium silicate crystal to be zoned irregularly in uranium, thorium, iron, calcium, yttrium, phosphorus and several rare earth elements. The outermost zones tend to be richest in uranium, while the central areas are highest in iron. Irregular areas of thorium enrichment also are higher in yttrium and phosphorus, suggesting the presence of a xenotime component. Spot analyses show wide ranges in uranium and thorium proportions, from 558,000 ppm U and 32,000 ppm Th to 252,000 ppm U and 145,000 ppm Th. Correspondingly, the Th/U ratio ranges at least from 0.06 to 0.6. Lead in the mineral is uniformly low, between 1300 and 3000 ppm. Assuming the silicate to be the same age as the granite, this is less than 2 percent of the lead that should have accumulated in it from uranium and thorium decay.

The following contrasts in apparent mobilization behavior can be inferred from the Fig. 69 series of scan photographs:

1) Uranium, calcium, and iron have migrated beyond the grain along the muscovite cleavages, but thorium, zirconium, yttrium and phosphorus apparently have not.

2) Thorium, zirconium, yttrium and phosphorus are concentrated along some internal fractures within the coffinite? but uranium and calcium show no similar effects. Iron appears to be depleted on some internal fractures.

The crystal's chemical composition, its inferred habit and the presence of possible isostructural xenotime are consistent with a tentative identification as thorian coffinite?. Pronounced desiccation of the surface of the grain by the electron beam during EMP analysis (Fig. 68) suggests it has a high water content. Calculated by difference from the low sums of the EMP analyses (Table 8), water, expressed as OH, amounts to 4 (OH) for each Si in the high-uranium zone and 2 (OH) per Si in the low-uranium zone.

Bismutite-Bismuthinite

Bismutite ($Bi_2(CO_3)O_2$) has been observed only in a coarse fraction of the mineral separates where it stands out from other grains due to its distinctive smoky green color (Fig. 71). The grains are large (200-300 μm), anhedral, and commonly broken (Fig. 70). Some grains exhibit a tannish-yellow outer zone or coating, and most have irregular lead-gray inner zones about which the bismutite

Figure 67
Photomicrograph of the uranium silicate, coffinite?. The euhedral, nearly opaque, black to dark brown crystal is surrounded by an irregular brown halo in the host muscovite. Brown stains extend away from the grain along the muscovite cleavages. The grain is 300 μm across. Polished thin section, plane light.

Figure 68
Photomicrograph of the coffinite? grain seen in Figure 67 (rotated about 70° clockwise relative to Figure 67). The reflected light reveals the well-defined grain, distinct from its halo. Some internal variability is visible. The desiccated appearance has developed in response to the energy of the EMP beam during the probe scanning of Figure 69 and is probably due to water loss. Polished thin section, reflected light.

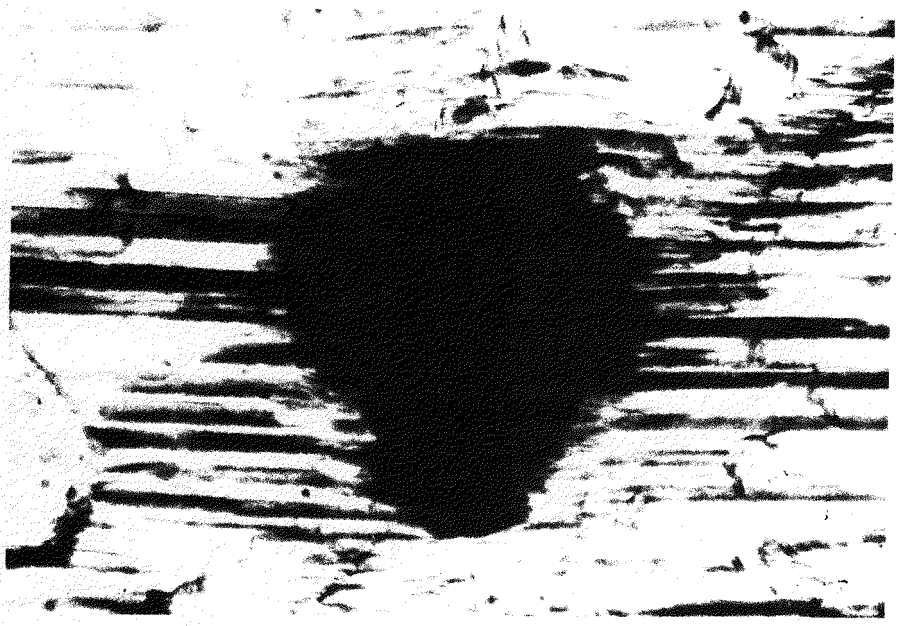

Figure 67

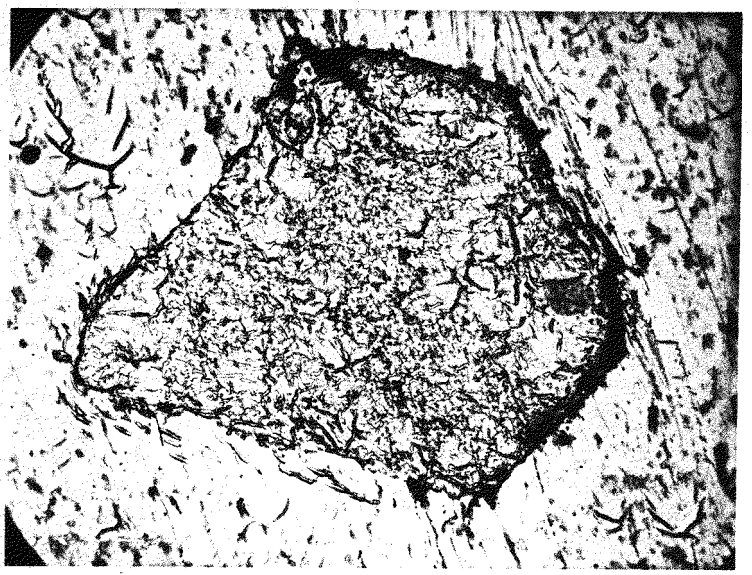

Figure 68

Figure 69
Electron Microprobe Scan Series--Coffinite?

a. Index sketch of uranium-silicate, coffinite? shown in Figures 67 and 68.
b. Uranium distribution; displays mottling with a range of 28 to 63 percent UO_2.
c. Iron distribution; the internal variation is from 2 to 16 percent and correlates negatively with uranium. A very striking halo of iron-rich material penetrates the cleavages of the adjacent muscovite. Close inspection of Figure 67(b) reveals that some uranium follows the iron halo into the muscovite.
d. Calcium distribution; the internal variations closely parallel those of uranium, with extensions into the muscovite.
e. Silicon distribution; silicon is uniform at approximately 15 percent.
f. Thorium distribution; thorium shows a patchwork distribution crudely negatively correlated with Fe. Thorium concentration ranges from 4 to 22 percent.
g. Zirconium distribution; zirconium is present at low levels and tends to correlate directly with thorium.
h. Yttrium distribution; yttrium shows a mottled pattern similar to that of thorium. Concentrations range from trace to about 1 percent.
i. Phosphorus distribution; phosphorus closely parallels yttrium.

The following contrasts in apparent mobilization behavior can be inferred from the Figure 69 series of scan photographs:

1) Uranium, calcium, and iron have migrated beyond the grain along the muscovite cleavages, but thorium, zirconium, yttrium and phosphorus apparently have not.
2) Thorium, zirconium, yttrium and phosphorus are concentrated along some internal fractures within the coffinite? but uranium and calcium show no similar effects. Iron appears to be depleted on some internal fractures.

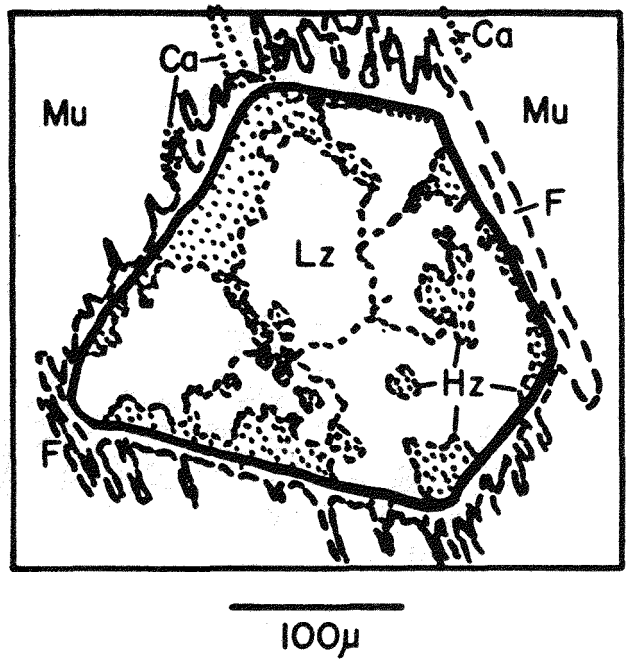

Figure 69(a)

Ca - Calcium-enriched cleavages and fractures

F -- Iron-enriched cleavages and fractures

Hz - High-iron zone

Lz - Low-iron zone

Mu - Host muscovite

Figure 69 (continued)

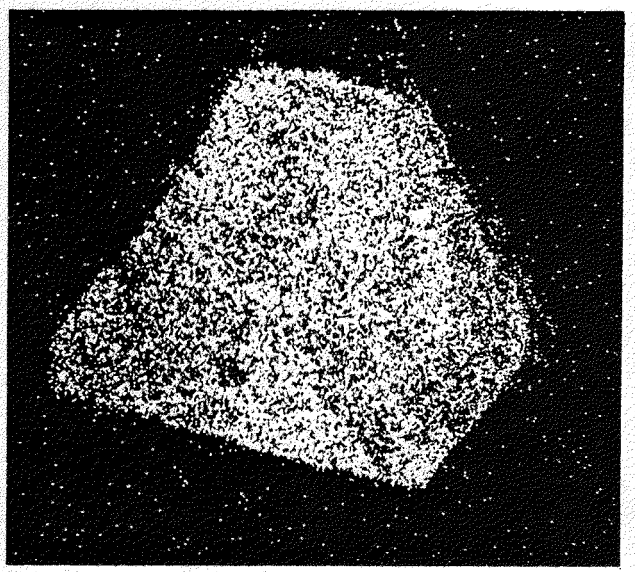

b - U

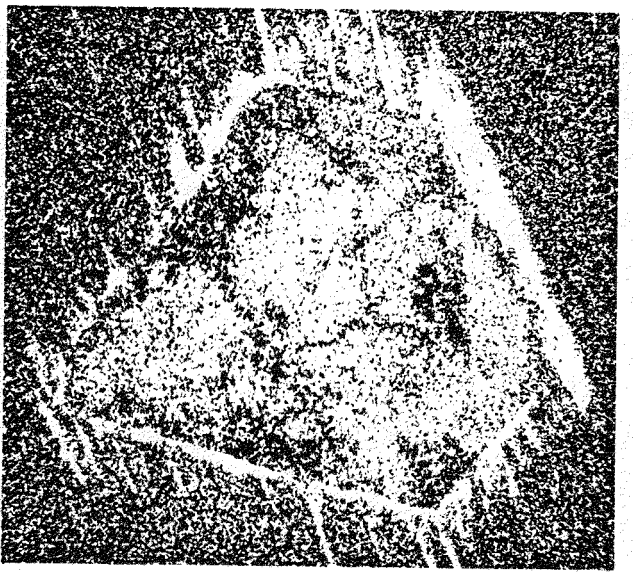

c - Fe

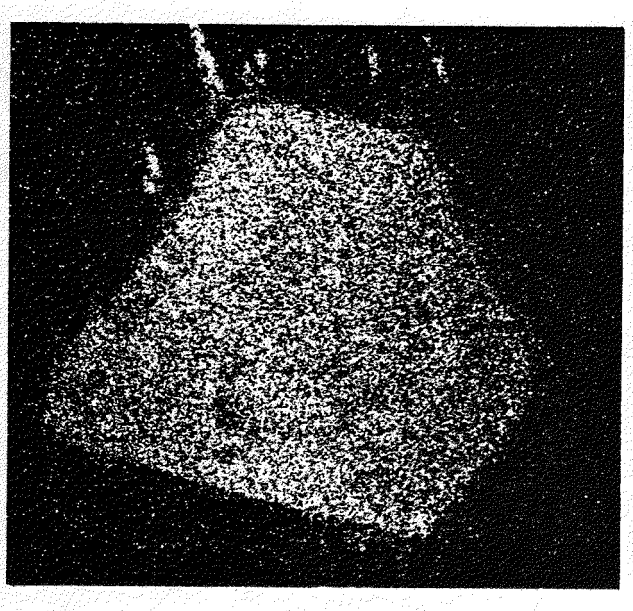

d - Ca

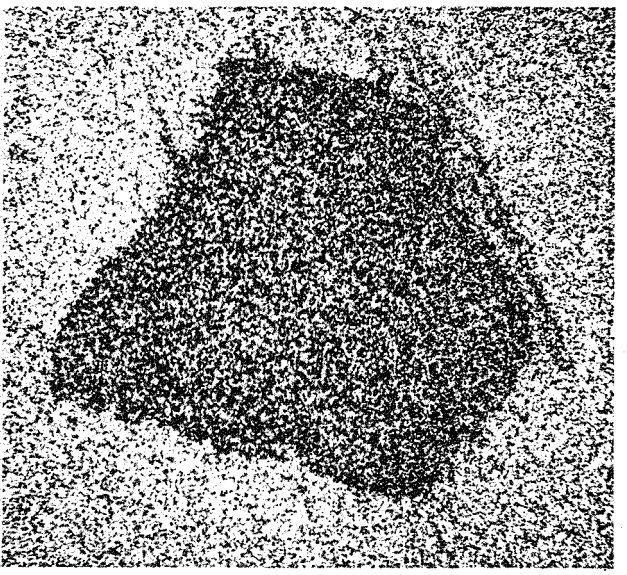

e - Si

Figure 69 (continued)

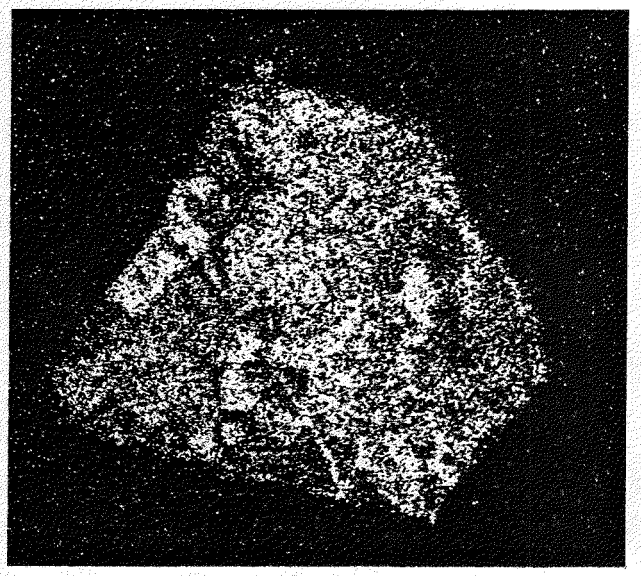

f - Th

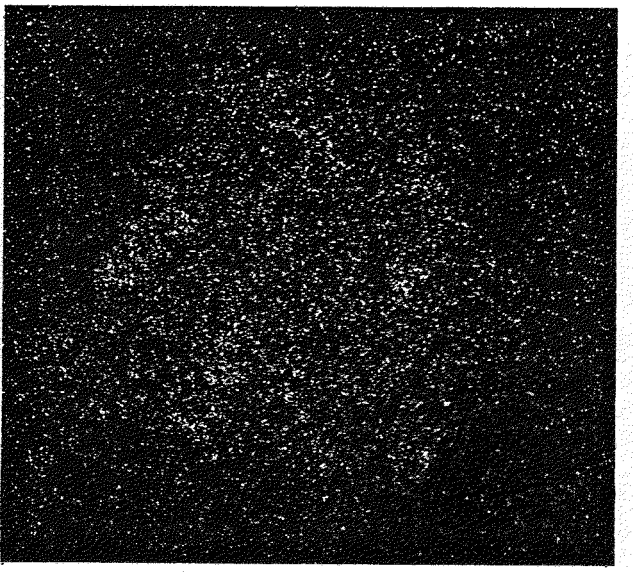

g - Zr

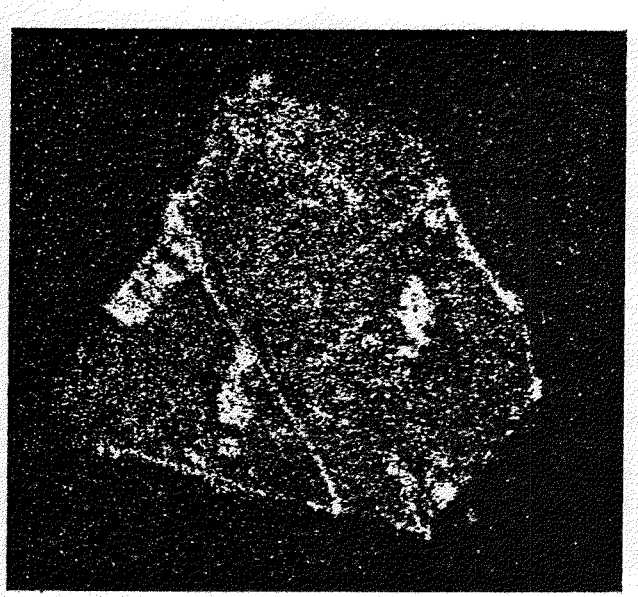

h - Y

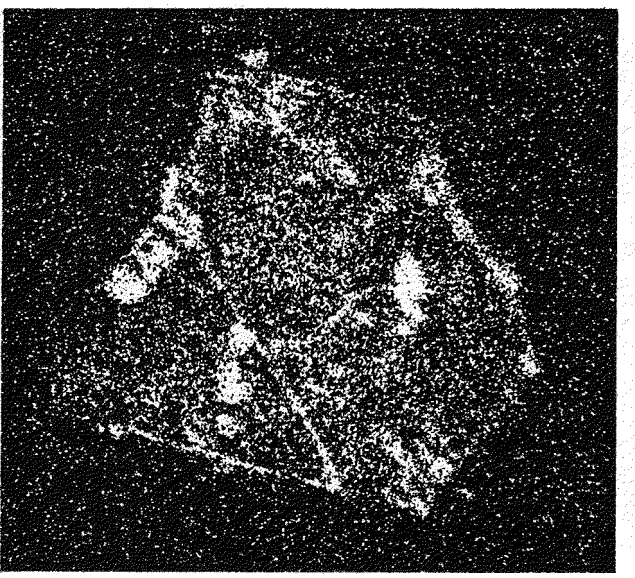

i - P

is concentrically zoned, suggesting that it is an alteration product of the core material (Fig. 72).

EMP scan photographs (Fig. 73) show the lead-gray core of several grains to be bismuthinite (Bi_2S_3) and to contain an appreciable amount of Pb. It is low in U and especially Si. The outer, bismutite, zone is lower in Pb with an increase near the rim. It is enriched in U and Si significantly over the bismuthinite. Partial EMP analyses show the bismutite to contain 9.5 percent PbO, 1.8 percent SiO_2, and about 0.2 percent UO_2 by weight. A complete analysis requires establishment of a bismuth standard.

Sphene

Sphene has been identified in thin section by EMP, but not as individual grains in the high-density mineral separates. It occurs as minute grains 5 to 10 μm wide and less than 20 μm long associated with zircon, epidote and chlorite in micas, where it is oriented parallel to the mica's cleavage (Figs. 46,47). Sphene also occurs as an intergrowth with ilmenite in distinctive aggregates as discussed in the following section. The sphene crystals appear to be honey-brown in color and free of inclusions. Their textural relationships suggest that they are secondary.

The sphene's fine grain size made EMP analysis difficult. The possibility that the sphene analysis listed in Tables 15b and 16 may have been affected by the chlorite host must be considered in the light of the high aluminum content. However, its close agreement with the analysis of the sphene in sphene-ilmenite intergrowths argues against any significant effects. Uranium and thorium both were below the quantitative detection limits, but scan photographs suggest that the uranium and thorium contents of the sphene were similar to those of the host chlorite and lower than those of an adjacent zircon.

Sphene-ilmenite

Distinctive intergrowths, presently composed of alternating layers of sphene and manganilmenite, have been identified in abundance in thin section by EMP (Fig. 74) but are less common in the high-density mineral separates. The intergrowths suggest possible pseudomorphs of stubby prismatic crystals. They occur in groups in close association with micas, where they may be present as randomly oriented inclusions in the micas, in nearby minerals (for example quartz and feldspar), or as independent mineral grains.

The pseudomorphs consist of disjointed layers of manganilmenite laths, alternated with layers of microcrystalline sphene and rarely, muscovite and apatite, enclosed in a thin skeletal outer shell of manganilmenite (Fig. 75). The fact that the intergrowths were recovered in such small amounts in the high-density mineral separates, despite their relative abundance in thin section (c. 0.05 volume percent) is probably attributable to their being too fragile to survive the crushing procedures. EMP analysis (Tables 15b,16) shows both the sphene and ilmenite to have essentially the same compositions as independent grains of the same phases in Lawler Peak Granite #1. EMP scan photographs (Fig. 76) reveal the manganiferous ilmenite and aluminous sphene compositions as well as an epidote rim developed against biotite at the lower end of the intergrowth.

Figure 70
Photomicrograph of bismutite-bismuthinite intergrowths. The upper two fragments have irregular lead-gray cores of metallic bismuthinite which is surrounded by the pale gray-green bismutite. The largest grain is 200 μm across. Unmounted.

Figure 71
Photomicrograph of a bismutite crystal split before analysis. The lower portion was analyzed for Pb, U and Th. The upper portion was shown to be bismutite (without bismuthinite) by X-ray diffraction. The color in this photograph is a truer representation of the actual color than that in Figure 70. The crystal is 300 μm long.

Figure 70

Figure 71

Figure 72
Photomicrograph of a bismutite-bismuthinite in a polished grain mount in oblique reflected light. The outer smoky green bismutite shows concentric alteration zones around the lead gray bismuthinite core. The brown rectangular scar on the plastic mounting medium shows the EMP scan area. The crystal is 280 μm long.

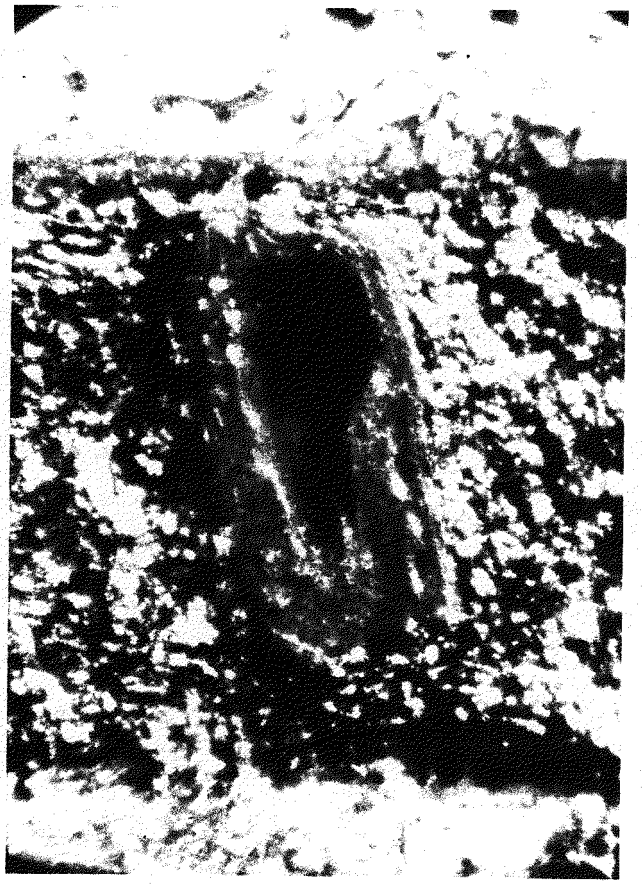

Figure 72

Figure 73
Electron Microprobe Scan Series--Bismutite-bismuthinite

a. Bismuth distribution; the Bi content is nearly uniform in both phases.
b. Sulfur distribution; the inner bismuthinite core is distinct.
c. Silicon distribution; there is a modest enrichment of Si in the outer, bismutite, zone.
d. Lead distribution; the bismuthinite core is richer in lead than the bismutite, but a distinct lead enrichment in the rim of the bismutite is visible.
e. Uranium distribution; bismutite is clearly enriched in uranium above the level in the bismuthinite core.
f. Silver distribution; a more-or-less uniformly low silver content is visible in both bismuth minerals.

Figure 73

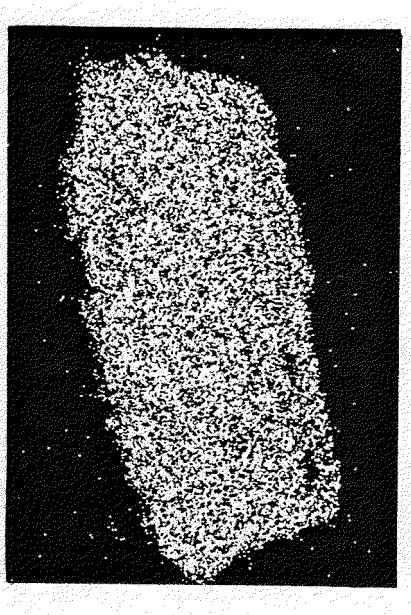

a - Bi

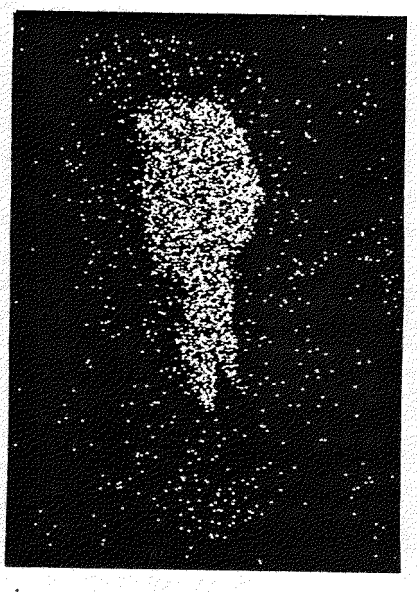

b - S

c - Si

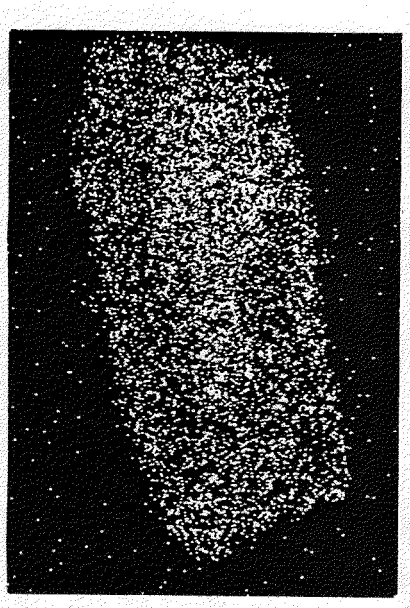

d - Pb

e - U

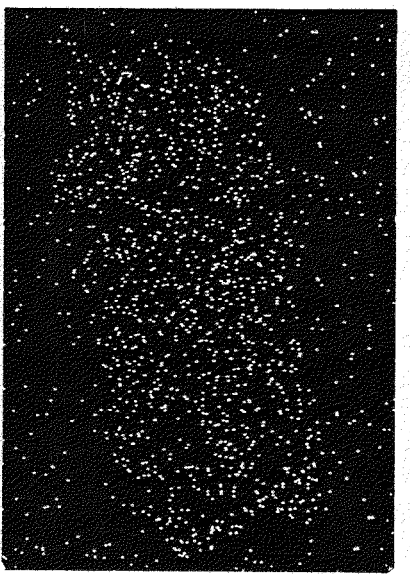

f - Ag

Figure 74
Photomicrograph of several distinctive sphene-ilmenite intergrowths which may be pseudomorphs of earlier phases. They are located in both muscovite and biotite. The field of view is 3 mm by 2 mm. Thin section, plane light.

Figure 75
Photomicrograph of a typical sphene-ilmenite intergrowth showing the rim and internal laths of manganilmenite and the microgranular sphene interlayers. The sphene-ilmenite intergrowth is surrounded by a rim of epidote and white mica at its contact with biotite. The grain is 550 μm long. Thin section, plane light.

Figure 74

Figure 75

Figure 76
Electron Microprobe Scan Series--Sphene-ilmenite (lower half of the intergrowth shown in Figure 75)

a. Titanium distribution; the pattern shows the higher Ti content of the ilmenite.
b. Manganese distribution; this shows the opaque phase to be manganilmenite.
c. Calcium distribution; calcium defines the layers of sphene and an outer rim of epidote.
d. Aluminum distribution; the sphene is unusually aluminous. White mica, present as inclusions among the sphene-ilmenite layers and intergrown with the epidote, is identifiable by its high Al content.

Figure 76

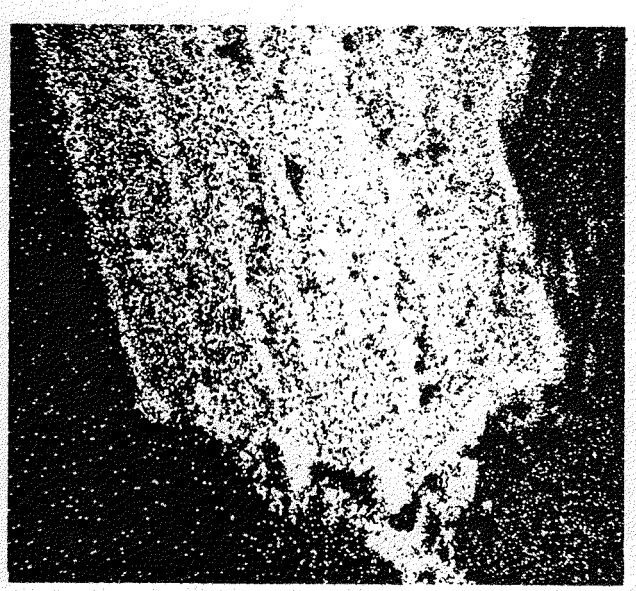

a - Ti

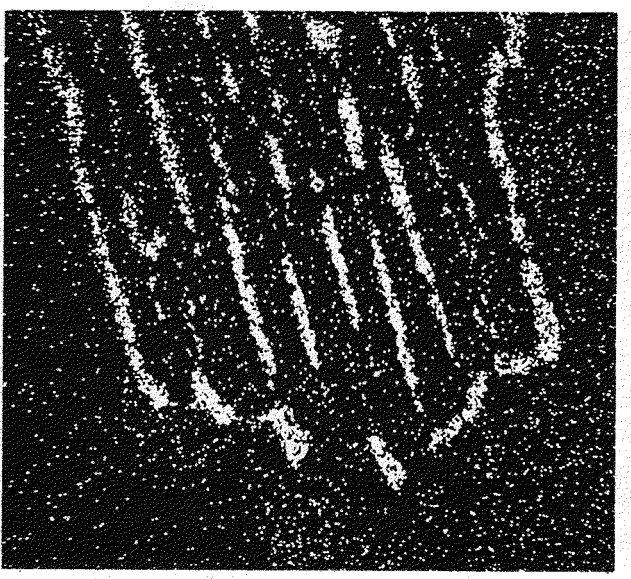

b - Mn

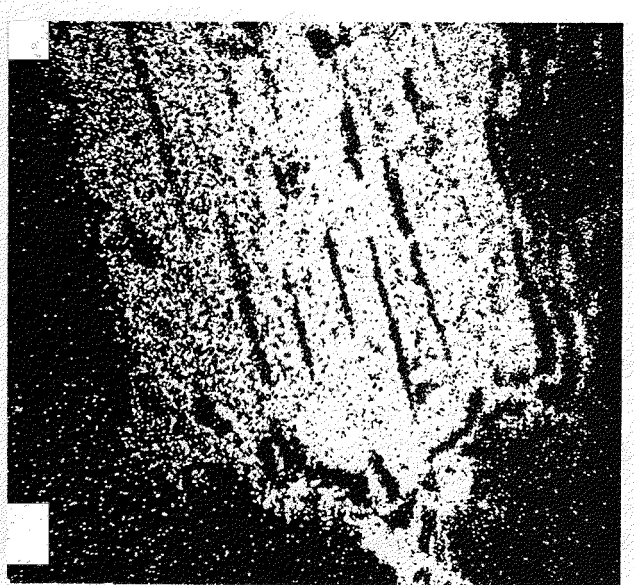

c - Ca

d - Al

Figure 77
Photomicrograph of a skeletal manganilmenite grain filled and overgrown with coarse quartz. This suggests the possibility that some sphene-ilmenite intergrowths may represent two-stage growth rather than pseudomorphs. Dark orange-brown monazites are intergrown with the manganilmenite at either end. The small pale brown euhedral zircon in the upper skeletal rim has an epitaxial dark brown thorite at its lower left. The skeletal grain is 500 µm long. Polished thin section, plane light.

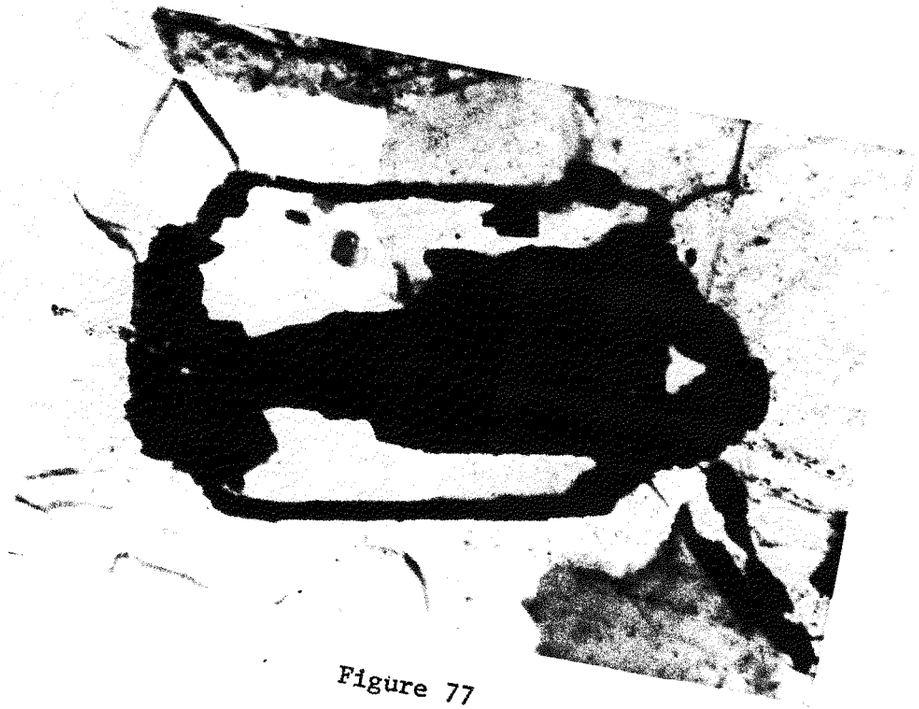

Figure 77

Figure 78
Photomicrograph of typically complex particles of ferromagnetic minerals and other phases in the granite, illustrating the intricate intergrowths common in the strongly ferromagnetic mineral separates. The left particle contains a small pale turbid zircon euhedron; the right particle has a brownish orange monazite on its upper surface. A significant fraction of the ferromagnetic separates extracted from this rock consist of such aggregates, which contain an important component of the total radioactivity of the rock. This type of intergrowth was avoided when selecting handmagnetic material for the isotopic studies. The larger grain is 1 mm across. Unmounted grains.

Figure 79
Photomicrograph of a split from the isotopically analyzed concentrate of high density, weakly ferromagnetic opaque minerals showing the diversity of complex intergrowths. This material contains, in unisolated form, a significant fraction of the radioactivity and radiogenic lead in the sample. The mean grain size is about 400 µm. Unmounted grains.

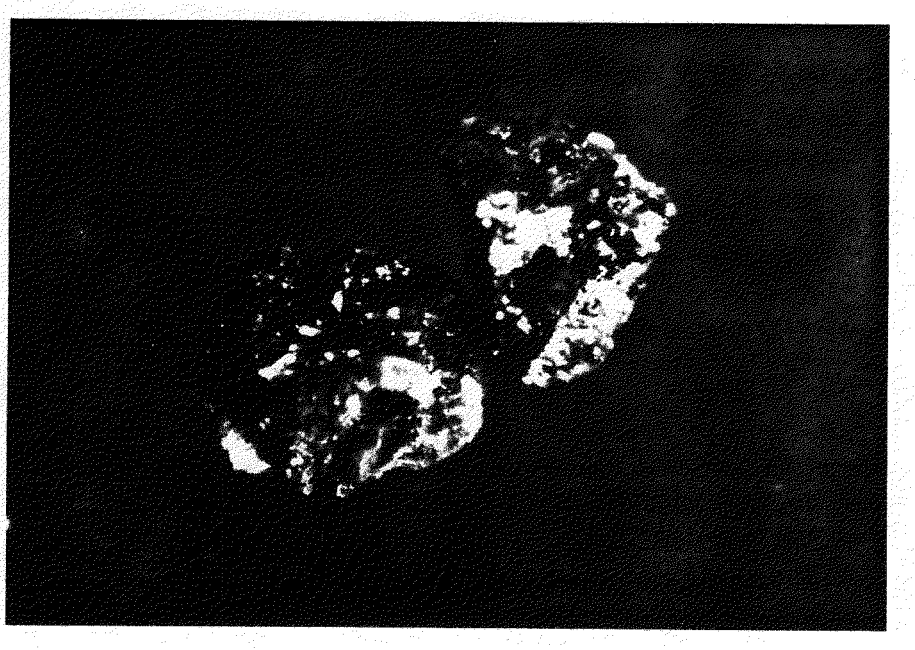

Figure 78

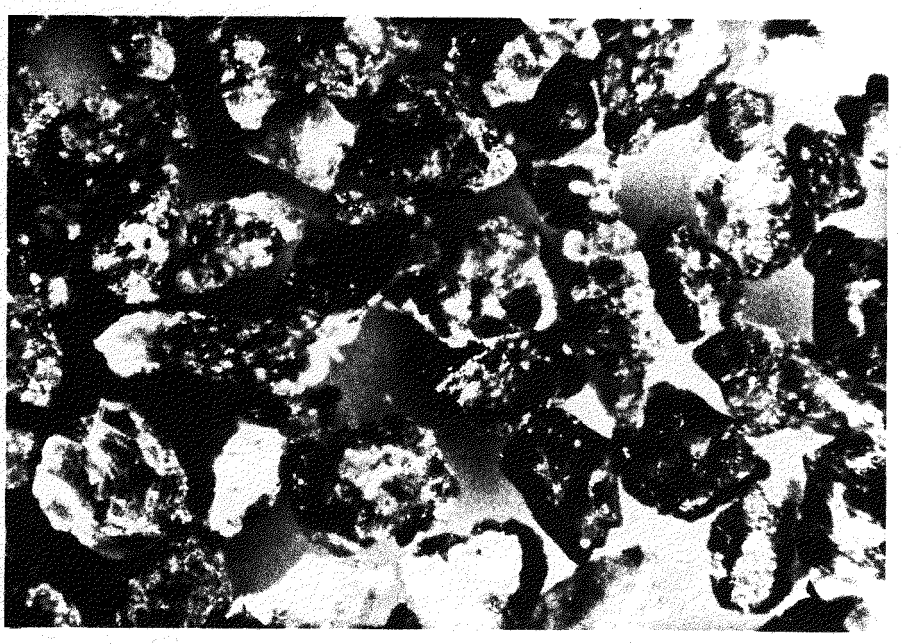

Figure 79

U-TH-PB ISOTOPIC STUDIES

Introduction

Lead, uranium and thorium isotopic analyses were made on carefully selected components of the Lawler Peak Granite in order to provide data bearing simultaneously on a number of key questions:

What is the granite's age and the timing, nature and effects of isotopic disturbances throughout its history?

What is the isotopic balance in the rock as a whole and what are the implications of that balance for parent and daughter mobilization?

What are the nature and contents of mineralogical sites for uranium, thorium and radiogenic lead and the implications for differential migration of elements and isotopes in different chemical environments, past, present and future?

What are the nature and contents of non-mineralogical sites for uranium, thorium and radiogenic lead and the implications for the migration of a labile component or components within and out of the granite?

Analytical Procedures for Isotopic Studies

The analytical procedures employed in the determination of lead, uranium and thorium differed from sample to sample, principally because the samples varied in size and degree of resistance to decomposition.

The zircon fractions, monazite and weakly ferromagnetic opaques concentrate were prepared for mass spectrometry by the techniques used regularly in this laboratory for zircon analysis. Two splits of the sample were processed in parallel; one was spiked before decomposition with lead, uranium and thorium and the other was run unspiked for lead composition. The samples were fused in platinum crucibles with sodium tetraborate flux. Lead was extracted as lead dithizonate (Silver et al., 1963) and uranium and thorium separated by nitrate form anion exchange (Tatsumoto, 1966).

The samples of xenotime, epidote, biotite-chlorite, muscovite and magnetite were prepared similarly as parallel fused spiked and unspiked splits, but uranium, thorium and lead were separated by small scale anion exchange. The technique used to isolate lead was modified after the hydrobromic acid procedure described by Manhes et al. (1978), with resin beds of 0.2 and 0.02 cc respectively. Uranium and thorium were separated on similar columns in chloride and nitrate forms respectively.

The samples of U-titanate and bismutite were so small that it was not possible to prepare pairs of equivalent samples by splitting. Those samples therefore were fused in their entirety, then the resultant solutions divided into two parts, one of which was spiked. Lead, uranium and thorium were extracted from the U-titanate samples by dithizone extraction and nitrate form anion exchange respectively and from the bismutite by small scale anion exchange.

Fusion was not necessary for apatite, which dissolved readily in 9 N hydrobromic acid while the included quartz, monazite and zircon did not. The apatite samples were dissolved in their entirety and then the solutions split before spiking. Lead, uranium and thorium were extracted by small scale anion exchange.

Extensive leaching experiments were performed on the two mineral concentrates, quartz plus feldspar, and magnetite. The quartz plus feldspar was purified by selecting grains in a very narrow density range (2.53 to 2.57 g/cc) and size range (75-150 μm) and with the least magnetic susceptibility. The resultant concentrate was of quartz and feldspar better than 99 percent free of discolored crystals. The starting material for the magnetite concentrate was coarse (300-600 μm) magnetite handpicked to be free of all crystals with visible inclusions. The magnetite was crushed in an agate mortar to finer than 75 μm, immersed in acetone and the handmagnetic separation repeated. Two splits of the handmagnetic powder were analyzed complete, a third split was leached.

The leaches to which the two mineral concentrates were subjected were the same. For Leach I the mineral concentrate was placed in room temperature 1 N nitric acid for one hour. The leachate was then decanted and the minerals washed with several rinses of distilled water, which were added to Leach I. For Leach II the mineral concentrate was placed for an additional hour in 14 N nitric acid held close to its boiling point. The decanted leachate and several distilled water rinses comprised Leach II. Each leach was mixed by prolonged heating then split into two aliquots, one of which was spiked with lead, uranium and thorium.

Preliminary leaching experiments were conducted on concentrates of several other mineral species. The conditions for these experiments varied somewhat but all were conducted in 1 N nitric acid at 25° C for one hour or less.

Lead, uranium and thorium from the quartz-feldspar leaches were prepared for mass spectrometry by solvent extraction and nitrate form anion exchange respectively. The processing of the magnetite leaches was by small scale anion exchange. The other, preliminary, leach data were obtained by solvent extraction.

For the whole-rock sample, approximately 2 kg of granite was crushed to pea size and quartered. 500 g was then ground to pass 200 mesh (75 μm) in a Spex "Shatter box" mill and tumbled to improve the mixing. Further aliquotting was by a coring technique through the total reservoir of powder.

The whole rock was prepared for chemistry by two methods, dissolution in a mixture of hydrofluoric and perchloric acids and fusion. The two sets of concentrations measured were the same within the sampling error. The fused sample was processed by the techniques described above for the zircon samples. Because of the size of the sample of whole rock dissolved, (over 2 g) a lead concentrate was prepared from the initial solution prior to the organic extraction by co-precipitation with barium nitrate.

The mass spectrometric analyses were performed on 12-inch, single focusing, solid source mass spectrometers built at the California Institute of Technology. Data were obtained using both simple collector and electron multiplier and have been corrected for a very slight non-linearity in shunt factors. A mass

discrimination correction also has been applied, based on the 0.1 percent per mass unit difference between isotopic ratios measured on the Caltech spectrometers and the nominated values for NBS lead and uranium standards.

The zircon fractions, with the exception of P200 1.7NM 2.5 II, were analyzed in 1964 (and the results reported in Silver, 1966). The lead from those samples was loaded for mass spectrometry as lead sulfide. The latter fraction and all other samples were analyzed recently and the leads loaded by the silica gel technique. The uranium and thorium isotopic analyses for the zircons, monazite, brown lustrous U-titanate and whole rock were performed using a triple filament nitrate load and analyzing the oxides. Uranium and thorium from the remainder of the samples were analyzed using a single filament phosphoric acid-carbon load, which emitted metal ions. Within the precision limits reported below, no distinction can be recognized between analyses obtained on lead sulfide and on lead in a silica gel-phosphoric acid substrate.

The assignments of uncertainties to individual analyses were made on the basis of several factors. Mass spectrometric precision for ratios up to several hundred was usually 0.05 to 0.5 percent and for ratios in excess of 1000, the standard error of the observations increased by approximately 1 percent for every thousand. Evaluation of replicate analyses in this laboratory suggests that determinations of $^{206}Pb/^{238}U$, $^{207}Pb/^{235}U$ and $^{208}Pb/^{232}Th$ are reproducible analytically to within about 1 percent. Sample gravimetry, and therefore the determination of absolute concentrations of lead, uranium and thorium, was also similarly accurate, except for sample weights approximately 1 mg or less, in which cases the gravimetric uncertainty became a very significant factor.

Minimum uncertainties assigned to each analysis were 1 percent for the determination of $^{206}Pb/^{238}U$ and $^{208}Pb/^{232}Th$, and 0.5 percent for the determination of radiogenic $^{207}Pb/^{206}Pb$. In those cases where the correction for common lead was large, uncertainties in the composition of the common lead became significant and the appropriate propagation of error in the analysis was calculated. Only in cases of measured $^{206}Pb/^{204}Pb$ less than 100 was this additional uncertainty of any significance. Assessment of what were effectively replicate determinations of $^{207}Pb/^{206}Pb$ from the lead concentration and lead composition analyses for each sample provided an additional indication of analytical precision in every case. The uncertainties allotted to each analysis are plotted in Figures 80 and 81.

For the calculation of apparent ages and for various other geochemical systematics and balances, we have used the following decay constants for ^{238}U, ^{235}U and ^{232}Th, respectively:

^{238}U, λ: 1.55125×10^{-9}/year

^{235}U, λ: 0.98485×10^{-9}/year

^{232}Th, λ: 0.049475×10^{-9}/year

$^{238}U/^{235}U$ is taken as 137.88.

These are the values adopted by international convention (Steiger and Jäger, 1977) and are taken from the works of Jaffey et al. (1971) and Le Roux and Glendenin (1963).

Figure 80
A plot of $^{206}Pb/^{238}U$ versus $^{207}Pb/^{235}U$ isotope ratios for various radioactive mineral concentrates from the Lawler Peak Granite #1 sample. The diagram is called a "Concordia" diagram after the smooth curve which represents the locus of all ideal isotope systems in which the two Pb-U isotope ratios yield ages in agreement (are concordant). The Concordia is plotted for systems from zero to more than 1900 million years old. In most natural systems the two Pb-U isotope ratios do not give ages which are in agreement, as is illustrated here. Such systems are termed "discordant". However, the remarkable linear arrays commonly generated by the analyses of related isotope systems can be used in precise geochronological interpretations (see the text) and to evaluate open system behavior for uraniferous minerals.

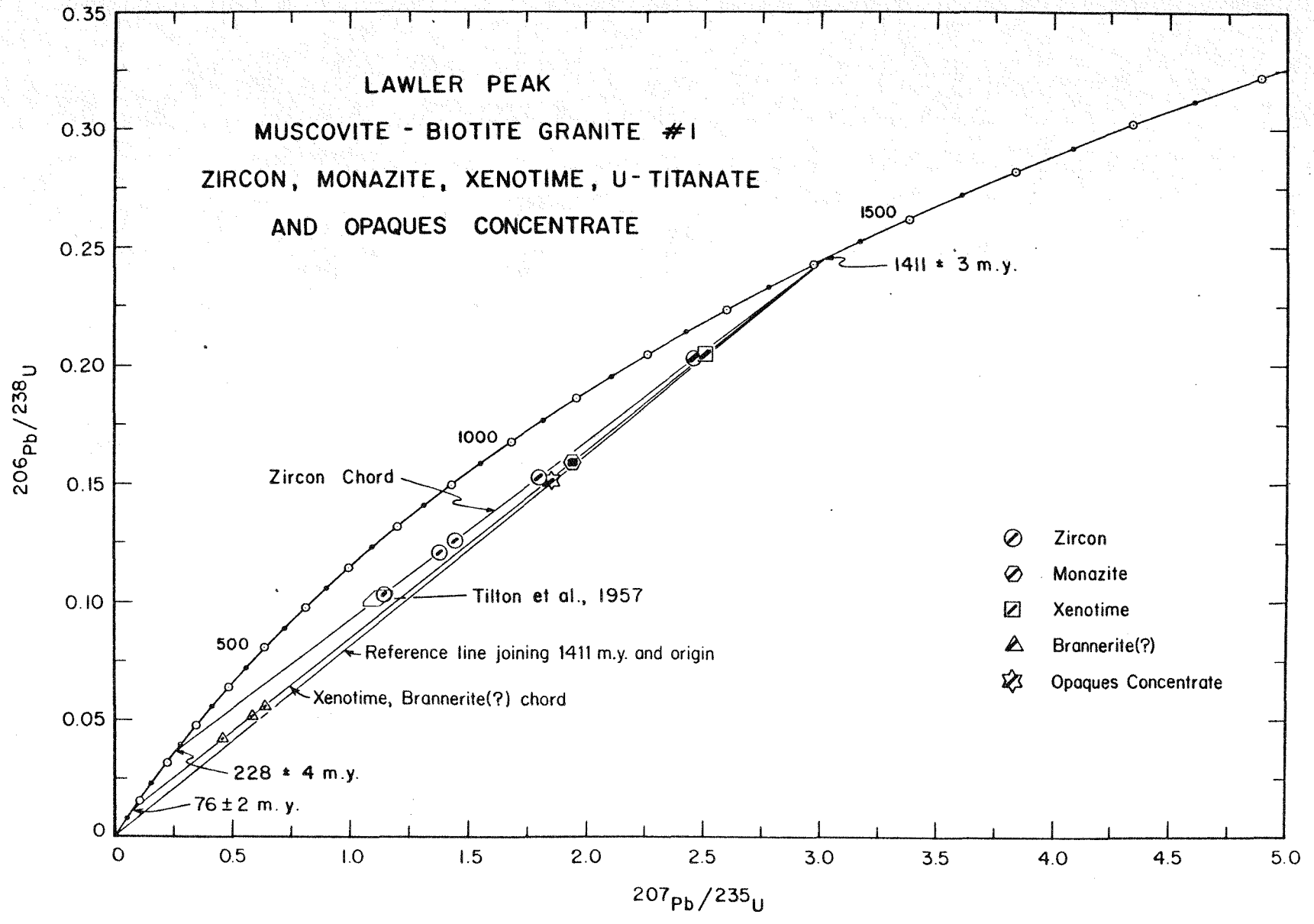
LAWLER PEAK
MUSCOVITE - BIOTITE GRANITE #1
ZIRCON, MONAZITE, XENOTIME, U-TITANATE
AND OPAQUES CONCENTRATE
1500
1411 ± 3 m.y.
1000
Zircon Chord
Tilton et al., 1957
500
Reference line joining 1411 m.y. and origin
Xenotime, Brannerite(?) chord
228 ± 4 m.y.
76 ± 2 m.y.
Zircon
Monazite
Xenotime
Brannerite(?)
Opaques Concentrate
0.35
0.30
0.25
0.20
0.15
0.10
0.05
0
0.5
1.0
1.5
2.0
2.5
3.0
3.5
4.0
4.5
5.0
$^{206}Pb/^{238}U$
$^{207}Pb/^{235}U$

Figure 80

Figure 81
A Concordia diagram similar to Figure 80, but with extended axes, showing the relations among Pb-U isotope systems for the whole rock, some minerals and two leached mineral concentrates, Lawler Peak Granite #1 sample. Those analyses plotting above the Concordia are termed "reverse discordant" and indicate systems in which uranogenic lead is present in excess of uranium. The linear chords plotted are the extensions of the chords defined in Figure 80, which comprises only a small portion of this field, close to the origin.

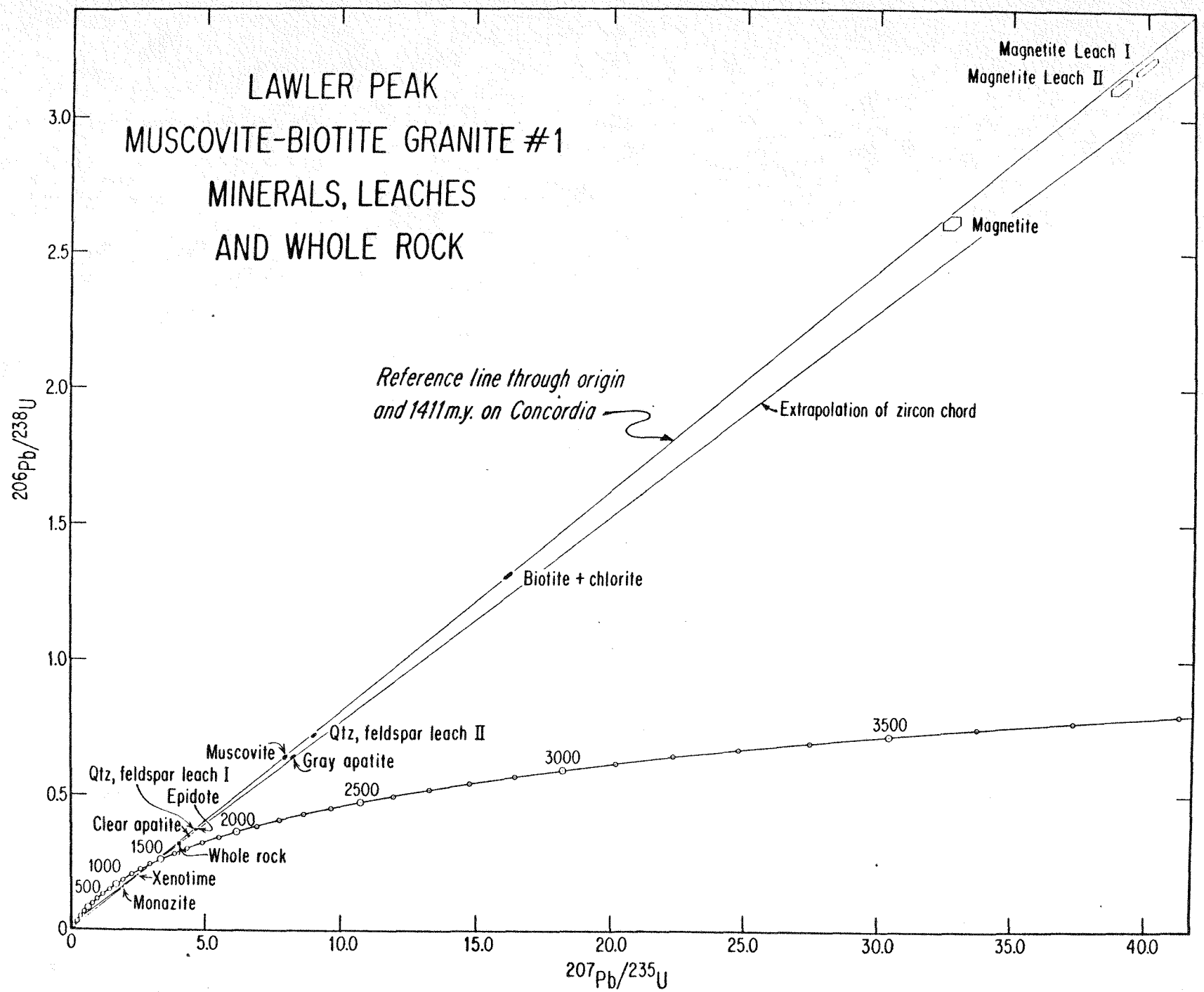
LAWLER PEAK
MUSCOVITE-BIOTITE GRANITE #1
MINERALS, LEACHES
AND WHOLE ROCK
Magnetite Leach I
Magnetite Leach II
Magnetite
Reference line through origin
and 1411m.y. on Concordia
Extrapolation of zircon chord
Biotite + chlorite
Qtz, feldspar leach II
Muscovite
Gray apatite
Qtz, feldspar leach I
Epidote
Clear apatite
Whole rock
Xenotime
Monazite
500
1000
1500
2000
2500
3000
3500
0
0.5
1.0
1.5
2.0
2.5
3.0
5.0
10.0
15.0
20.0
25.0
30.0
35.0
40.0
$^{206}Pb/^{238}U$
$^{207}Pb/^{235}U$

Figure 81

Results of the Isotopic Analyses

The Whole Rock

The whole-rock lead-uranium-thorium isotopic analysis listed in Tables 18a and 19a is that determined on the fused split. It shows Lawler Peak Granite #1 to be particularly uranium-rich, its uranium content of 20.9 ppm being eight to ten times the average crustal uranium abundance. While thorium (26.7 ppm) also is higher than the crustal average, it is so by only a factor of two or three and the granite thereby has an unusually low thorium to uranium ratio (1.3, in contrast to a more common value of about 4). In this respect the Lawler Peak Granite resembles many others of the 1440-1400 m.y. old generation of granitic rocks that are within the region of the Colorado Plateau uranium anomaly. The rock's μ value ($^{238}U/^{204}Pb$) of 44.5 is extraordinarily high.

Subtraction of the common lead component from the whole-rock analysis using the composition of common lead determined from analyses of feldspar ($^{206}Pb/^{204}Pb$ = 16.15, $^{207}Pb/^{204}Pb$ = 15.38, $^{208}Pb/^{204}Pb$ = 35.75; Ludwig and Silver, 1977) gives a calculated radiogenic lead concentration of 8.00 ppm, 22.4% of the whole-rock lead. Using that radiogenic lead, model ages for the rock's lead-lead, lead-uranium and lead-thorium isotopic systems can be computed. The $^{206}Pb/^{238}U$ and $^{207}Pb/^{235}U$ apparent ages, 1784 and 1638 m.y. respectively, are greater than the age of the Lawler Peak Granite inferred, as will be discussed below, from the zircon isotopic systems, 1411 ± 3 m.y. The rock contains an apparent excess of radiogenic lead with respect to uranium. Conversely, the $^{207}Pb/^{206}Pb$ and $^{208}Pb/^{232}Th$ apparent ages, 1453 and 1414 m.y. respectively, are very close to the interpreted age of the granite. This near concordance is not believed to be a unique coincidence but is a phenomenon observed in a number of Precambrian granitic plutons of the same generation in the Southwest. A first order assumption can reasonably be made that the Lawler Peak Granite #1 whole rock has remained closed throughout its history for thorium and thorogenic lead.

Thorogenic leads are associated with uranogenic leads in all sites identified in this work and vice versa (Tables 18a,b,c). No natural mechanisms of lead isotopic fractionation are known. It follows, therefore, that if the bulk rock has been effectively closed to thorogenic lead loss, limits on the magnitude of significant selective uranogenic lead loss from the total rock can be postulated. Although some phases (e.g. brannerite? and zircon) contain low ^{208}Pb radiogenic leads and are demonstrably open systems as individual grains, it does not appear that the whole-rock system has lost uranogenic lead relative to uranium. Assuming no radiogenic ^{206}Pb loss, which probably is an oversimplification, the bulk-rock Pb-U system appears to be out of balance, suggesting instead extensive uranium loss (~24 percent). If some modest selective uranogenic lead loss has occurred also, then the calculated uranium loss must be increased further by a factor of 1.24 times the ^{206}Pb radiogenic loss.

It appears therefore that the whole-rock system has lost a minimum of 24 percent of its earlier uranium content, or about 5 grams of uranium per tonne of granite. This loss would imply an initial Th/U ratio for the rock of 1.0, or less.

TABLE 18a

Isotopic data for whole rock and minerals,

Lawler Peak Muscovite-biotite Granite #1.

Sample	Weight (mg)	Observed Lead Ratios			Radiogenic Pb* Atom%			Concentrations (ppm)				$\frac{238U}{204Pb}$
		206/204	207/204	208/204	206	207	208	Pb^{rad}	U	Th	Th/U Ratio	
WHOLE ROCK	2016	29.84	16.59	39.87	71.84	6.57	21.59	8.00	20.89	26.72	1.28	42.95
BRANNERITE?												
R100 1.0M 10												
Brown Lustrous	0.8	367.5	43.08	62.12	87.11	6.87	6.02	9419	226,500	19,500	0.086	8342
Brown-orange Coated	0.3	211.9	31.37	58.35	83.53	6.82	9.65	14,460	272,300	25,750	0.095	3796
White-yellow Coated	0.6	274.7	36.82	60.38	84.88	7.04	8.08	16,860	297,900	31,460	0.106	4631
XENOTIME												
R100 0.34M 10	1.0	3652	338.6	675.8	79.05	7.03	13.92	2018	9066	9286	1.02	17,780
MONAZITE												
P200 1.0 M 10	1.4	209.9	32.50	1423	12.12	1.07	86.81	5109†	4493†	125,400†	27.9	1218
ZIRCON												
P200 1.7NM 2.5 II	7.4	1780	165.9	203.2	84.73	7.23	8.04	194.6	1256	400.2	0.319	11,560
P200 1.7NM 2.5 I	25.0	771.6	81.74	114.5	83.89	7.37	8.74	263.9	1267	--	--	3720
R200 1.7NM 5	9.3	1568	144.3	130.5	87.40	7.26	5.34	264.4	2133	--	--	12,320
P200 1.7 M 2.5	36.2	2808	245.9	236.1	86.63	7.15	6.22	345.4	2877	--	--	23,090
P200 1.7 M 6	35.2	2096	181.9	181.9	86.93	6.96	6.11	422.1	4129	--	--	20,130

† See text for discussion of element concentrations in monazite.

* Lead compositions are corrected assuming the common lead composition determined from K-feldspar from Lawler Peak Granite #1.

206/204 = 16.15 207/204 = 15.38 208/204 = 35.75 (Ludwig and Silver, 1977)

TABLE 18b

Isotopic data for minerals,

Lawler Peak Muscovite-biotite Granite #1.

Sample	Weight (mg)	Observed Lead Ratios			Radiogenic Pb* Atom%			Concentrations (ppm)				$\frac{238U}{204Pb}$
		206/204	207/204	208/204	206	207	208	Pb^{rad}	U	Th	Th/U Ratio	
BISMUTITE												
R100 1.0NM 10	0.02	101.3	23.24	54.34	77.53	7.16	15.31	32,070	3313	14.71	0.0044	9.765
OPAQUES CONCENTRATE												
R100 0.29M 10	24.0	126.3	25.13	71.63	71.39	6.32	22.29	249.7	1374	1303	0.948	731.6
EPIDOTE												
R100 0.36M 10	9.7	93.01	22.41	57.53	72.74	6.65	20.61	35.59	80.90	24.43	0.302	206.9
MAGNETITE												
R50 Ground	6.0	99.98	22.98	56.50	74.72	6.78	18.50	78.24	26.03	72.23	2.77	32.14
APATITE												
R200 1.7M 10 Clear	5.4	64.68	19.85	64.01	59.73	5.50	34.77	10.86	21.67	77.68	3.58	139.8
R50 1.0M 10 Gray	9.1	94.29	22.68	66.97	66.98	6.26	26.76	21.43	25.99	105.3	4.05	121.9
BIOTITE + CHLORITE												
R200 0.3M 10	22.4	100.9	22.95	54.68	76.18	6.81	17.01	30.48	20.61	35.39	1.72	64.74
MUSCOVITE												
R200 0.9NM 25	15.8	48.39	18.28	54.32	60.03	5.40	34.57	4.22	4.58	18.82	4.11	50.24

* Lead compositions are corrected assuming the common lead composition determined from K-feldspar from Lawler Peak Granite #1.
206/204 = 16.15 207/204 = 15.38 208/204 = 35.75 (Ludwig and Silver, 1977)

TABLE 18c

Isotopic data for leaches,

Lawler Peak Muscovite-biotite Granite #1.

Sample	Weight (mg)	Observed Lead Ratios			Radiogenic Pb* Atom%			Concentrations (ppm)				$\frac{238U}{204Pb}$
		206/204	207/204	208/204	206	207	208	Pb^{rad}	U	Th	Th/U Ratio	
GROUND MAGNETITE	14.9											
LEACH I 1N, 1hr, 25°C	--	100.6	23.03	56.79	74.64	6.76	18.60	11.09	3.01	9.74	3.24	26.39
LEACH II 14N, 1hr, 90°C	--	99.94	22.93	56.20	74.93	6.78	18.29	62.98	17.54	56.44	3.22	26.89
COMPOSITE OF LEACHES	--	100.0	22.94	56.29	74.89	6.78	18.34	74.07	20.55	66.18	3.22	26.82
CLEAN QTZ, FELDSPAR	997											
LEACH I 1N, 1hr, 25°C	--	67.87	20.07	48.76	74.50	6.75	18.75	0.196	0.456	1.106	2.42	139.1
LEACH II 14N, 1hr, 90°C	--	63.27	19.66	52.04	71.20	6.43	22.37	0.088	0.100	0.847	8.43	65.11
COMPOSITE OF LEACHES	--	66.44	19.94	49.78	73.48	6.65	19.87	0.284	0.556	1.953	3.51	115.5
BIOTITE-CHLORITE	376											
LEACH I 1N, 1hr, 25°C	--	95.55	22.48	54.12	75.71	6.77	17.52					
MUSCOVITE	112											
LEACH I 1N, 1hr, 25°C	--	79.79	21.16	52.17	74.13	6.74	19.13					
STAINED QTZ, FELDSPAR	980							DATA INCOMPLETE				
LEACH I 1N, 1hr, 25°C	--	77.07	20.89	51.16	74.44	6.73	18.83					
OPAQUES CONCENTRATE	336											
LEACH I 1N, 15m, 25°C	--	105.4	23.43	57.72	74.84	6.75	18.41					
LEACH II 1N, 45m, 25°C	--	106.5	23.57	56.95	75.46	6.84	17.70					

* Lead compositions are corrected assuming the common lead composition determined from K-feldspar from Lawler Peak Granite #1.
206/204 = 16.15 207/204 = 15.38 208/204 = 35.75 (Ludwig and Silver, 1977)

TABLE 19a

Atomic ratios and apparent ages for whole rock and minerals,

Lawler Peak Muscovite-biotite Granite #1.

Sample	Atomic Ratios				Apparent Ages (m.y.)			
	$^{206}Pb/^{238}U$	$^{207}Pb/^{235}U$	$^{207}Pb/^{206}Pb$	$^{208}Pb/^{232}Th$	$^{206}Pb/^{238}U$	$^{207}Pb/^{235}U$	$^{207}Pb/^{206}Pb$	$^{208}Pb/^{232}Th$
WHOLE ROCK	.31873	4.0184	.09143	.072480	1784	1638	1453	1414
BRANNERITE?								
R100 1.0M 10								
Brown Lustrous	.04212	.45763	.07880	.032729	266	383	1167	651
Brown-orange Coated	.05157	.58078	.08168	.060948	324	465	1238	1196
White-yellow Coated	.05583	.63833	.08291	.048728	350	501	1267	962
XENOTIME								
R100 0.34M 10	.20447	2.5067	.08891	.034008	1199	1274	1402	676
MONAZITE								
P200 1.0 M 10	.15906	1.9381	.08836	.039495	952	1094	1390	783
ZIRCON								
P200 1.7NM 2.5 II	.15256	1.7953	.08534	.043992	915	1044	1323	870
P200 1.7NM 2.5 I	.20309	2.4599	.08784	--	1192	1260	1379	--
R200 1.7NM 5	.12595	1.4430	.08308	--	765	907	1271	--
P200 1.7 M 2.5	.12092	1.3767	.08257	--	736	879	1259	--
P200 1.7 M 6	.10334	1.1413	.08010	--	634	773	1199	--

TABLE 19b

Atomic ratios and apparent ages for minerals,

Lawler Peak Muscovite-biotite Granite #1.

Sample	Atomic Ratios				Apparent Ages (m.y.)			
	$^{206}Pb/^{238}U$	$^{207}Pb/^{235}U$	$^{207}Pb/^{206}Pb$	$^{208}Pb/^{232}Th$	$^{206}Pb/^{238}U$	$^{207}Pb/^{235}U$	$^{207}Pb/^{206}Pb$	$^{208}Pb/^{232}Th$
BISMUTITE								
R100 1.0NM 10	8.7196	111.02	.09234	375.20	14,660	4791	1474	119,900
OPAQUES CONCENTRATE								
R100 0.29M 10	.15057	1.8377	.08852	.047972	904	1059	1394	947
EPIDOTE								
R100 0.36M 10	.37154	4.6871	.09149	.33733	2037	1765	1457	5875
MAGNETITE								
R50 Ground	2.6085	32.621	.09069	.22521	8273	3569	1440	4105
APATITE								
R200 1.7 M 10 Clear	.34711	4.4052	.09204	.054567	1921	1713	1468	1074
R50 1.0 M 10 Gray	.64118	8.2563	.09338	.061148	3194	2260	1496	1200
BIOTITE + CHLORITE								
R200 0.3 M 10	1.3090	16.127	.08935	.16474	5394	2884	1412	3082
MUSCOVITE								
R200 0.9NM 25	.64167	7.9562	.08992	.086945	3196	2226	1424	1685

TABLE 19c

Atomic ratios and apparent ages for leaches,

Lawler Peak Muscovite-biotite Granite #1.

Sample	Atomic Ratios				Apparent Ages (m.y.)			
	$^{206}Pb/^{238}U$	$^{207}Pb/^{235}U$	$^{207}Pb/^{206}Pb$	$^{208}Pb/^{232}Th$	$^{206}Pb/^{238}U$	$^{207}Pb/^{235}U$	$^{207}Pb/^{206}Pb$	$^{208}Pb/^{232}Th$
GROUND MAGNETITE								
LEACH I 1N, 1hr, 25°C	3.2002	39.964	.09057	.23816	9251	3770	1437	4318
LEACH II 14N, 1hr, 90°C	3.1251	38.992	.09049	.22937	9135	3745	1436	4174
COMPOSITE OF LEACHES	3.1361	39.134	.09050	.23067	9152	3749	1436	4194
CLEAN QTZ, FELDSPAR								
LEACH I 1N, 1hr, 25°C	.37191	4.6479	.09063	.037383	2038	1758	1439	742
LEACH II 14N, 1hr, 90°C	.72368	9.0097	.09029	.026098	3510	2339	1432	521
COMPOSITE OF LEACHES	.43536	5.4346	.09053	.032488	2330	1890	1437	646
BIOTITE-CHLORITE								
LEACH I 1N, 1hr, 25°C			.08944					
MUSCOVITE								
LEACH I 1N, 1hr, 25°C			.09086					
STAINED QTZ, FELDSPAR	DATA INCOMPLETE				DATA INCOMPLETE			
LEACH I 1N, 1hr, 25°C			.09039					
OPAQUES CONCENTRATE								
LEACH I 1N, 15m, 25°C			.09017					
LEACH II 1N, 45m, 25°C			.09060					

Radioactive Accessory Minerals

Isotopic analyses were made of a selection of accessory mineral concentrates and high-purity mineral separates. The data obtained on the lead-uranium-thorium contents of and isotopic balances in the various minerals have been used first to deduce the age of the Lawler Peak pluton and the timing of significant events in its isotopic evolution and second to assess the minerals' respective roles as past and present repositories for radioactive and radiogenic elements. The results of the isotopic analyses and apparent ages calculated from them are listed in Tables 18a,b,c and 19a,b,c.

In all of the minerals studied the lead-uranium-thorium isotopic systems have been open at some stage in the granite's history; in no two minerals has the open system behavior been the same. Each mineral has responded to the same geological history differently, but there are sufficient isotopic data that it is possible to suggest both the timing of some isotopic events and the specific redistribution of radiogenic and/or radioactive isotopes that those events may have caused.

Zircon

Lawler Peak Granite #1 was collected originally for the purpose of measuring the age of the Lawler Peak pluton U-Pb isotope systematics in the zircon suite. Because isotopic discordance (parent-daughter imbalance) and radioactivity in zircon commonly are correlated (Silver, 1963), the zircon concentrate was divided, on the basis of grain size and paramagnetic susceptibility, into several subpopulations of different average radioactivities. Before analysis the zircon separates were washed for one hour in hot concentrated nitric acid to remove thorite impurities. Subsequent EMP scan photographs of the acid washed zircon show that the wash also was very efficient in removing thorite inclusions.

From isotopic studies (Table 18a) and radiometry the composite zircon population averages about 2700 ± 100 ppm uranium. Four zircon fractions were selected for lead-uranium analysis when the sample first was studied in 1964 (Silver, 1966). The fractions showed a considerable range in aggregate uranium content, 1267 to 4129 ppm. EMP analyses of grains in polished thin section reveal that the range in uranium content of zircon within individual grains or in zones within grains is at least an order of magnitude greater than this, from less than 1000 ppm to as much as 22,000 ppm. The range in thorium concentrations is similar, from less than 400 ppm up to 23,000 ppm. On a lead-uranium Concordia plot* (Fig. 80) the isotopic analyses are well dispersed. They range from 17 percent to 58 percent normally discordant ($^{206}Pb/^{238}U$ age < $^{207}Pb/^{235}U$ age) as a function of increasing radioactivity and are perfectly fitted, within the analytical uncertainties, to a straight line. The Concordia intersections of that line are 228 ± 4 m.y. and 1411 ± 3 m.y.

---

*For a discussion of the mathematical basis for the Concordia diagram and its use with discordant Pb isotope systems see Wetherill (1956).

To assess the compatibility of these data with more recent analyses, a fifth fraction was analyzed in conjunction with the samples prepared for the present study. That fraction (P200 1.7NM 2.5 II), prepared to have as low a radioactivity as possible, was an extract of the least magnetic zircon from the least magnetic fraction remaining from the earlier work. Fractions P200 1.7 NM 2.5 I and II were separated at the same Frantz magnet settings, but the latter fraction represents a resampling of a reservoir already severely depleted in lowest radioactivity zircon by the preparation of the earlier fraction. The analyses cannot be considered to be duplicates and the data emphasize that fact. Significantly however, the recent analysis, within the uncertainties, plots on the chord defined by the earlier data. There is no evidence for systematic error between the two generations of analyses and the results of the older work therefore are considered to be directly comparable with the results of work done more recently.

The recent zircon analysis included a determination of thorium and showed the fraction's lead-thorium system to be 70 percent normally discordant. The Th/U ratio measured was 0.32. An indication of the change in Th/U in zircon as a function of radioactivity is suggested by the several fractions' radiogenic $^{208}Pb/^{206}Pb$ ratios. As radioactivity increases, $^{208}Pb/^{206}Pb$ decreases; by implication, so does Th/U. This conclusion receives direct support from data obtained from EMP scan photographs and spot analyses. These show that, more than any other accessory mineral, zircon shows strong compositional zonation controlled by crystal geometry. Compositional changes most commonly are progressive from core to surface but locally may be oscillatory. The central areas of zircon crystals generally are lowest in radioactivity and incompatible elements (e.g. Hf, Y, P) and highest in Th/U. Outer zones show a progressive increase in radioactivity (by more than an order of magnitude) and incompatible elements and decrease in Th/U. The Zr/Hf ratio is inversely proportional to the uranium content. The average Th/U is probably 0.1 to 0.2.

The lead in the zircon is very radiogenic, showing that the mineral crystallized with a very small initial rock lead content and probably has not been open to isotopic exchange with rock lead through its subsequent history. Most importantly, the composition of the zircon's radiogenic lead is consistent with the Th/U ratio presently found in the mineral (Fig. 82). Accepting that lead in the zircon has not in any way equilibrated with lead in its environment, this implies that the zircon has maintained the same Th/U ratio throughout its history, except for the slight change due to the difference in uranium and thorium decay rates. In this vital respect, zircon appears unique amongst the minerals studied from Lawler Peak Granite #1.

This fact and the observation that reverse discordance ($^{206}Pb/^{238}U$ age > $^{207}Pb/^{235}U$ age > $^{207}Pb/^{206}Pb$ age) is rarely, if ever, found in zircon suggests that the apparent deficiency in radiogenic lead with respect to both uranium and thorium in the Lawler Peak zircons is predominantly due to loss of lead, rather than gain of uranium and thorium.

In view of the commonly observed complex intergrowth of zircon with thorite and xenotime (Fig. 66), it is necessary to consider the possibility that the zircon discordance is in fact a consequence of mixing between concordant zircon and other discordant phases. It is unlikely that the discordance is due to mixing with xenotime; that phase has a higher uranium and thorium content but lesser discordance than the zircon. Similarly, mixing with thorite is an

Figure 82

A log-log plot of the Th/U ratio observed in the Lawler Peak Granite #1 minerals and whole rock versus the Th/U ratio calculated to be consistent with the radiogenic $^{208}Pb/^{206}Pb$ in each. Evolution of the isotopic systems over 1410 m.y. has been assumed, although the calculations have relatively little age sensitivity. The comparatively limited range of the calculated Th/U ratios (that is, of the observed radiogenic $^{208}Pb/^{206}Pb$), with the notable exception of monazite, contrasts markedly with the great range in Th/U ratios observed. Zircon is the only mineral which appears now to retain its original Th/U ratio and is therefore a valuable indicator of the original Th/U ratio of the granite.

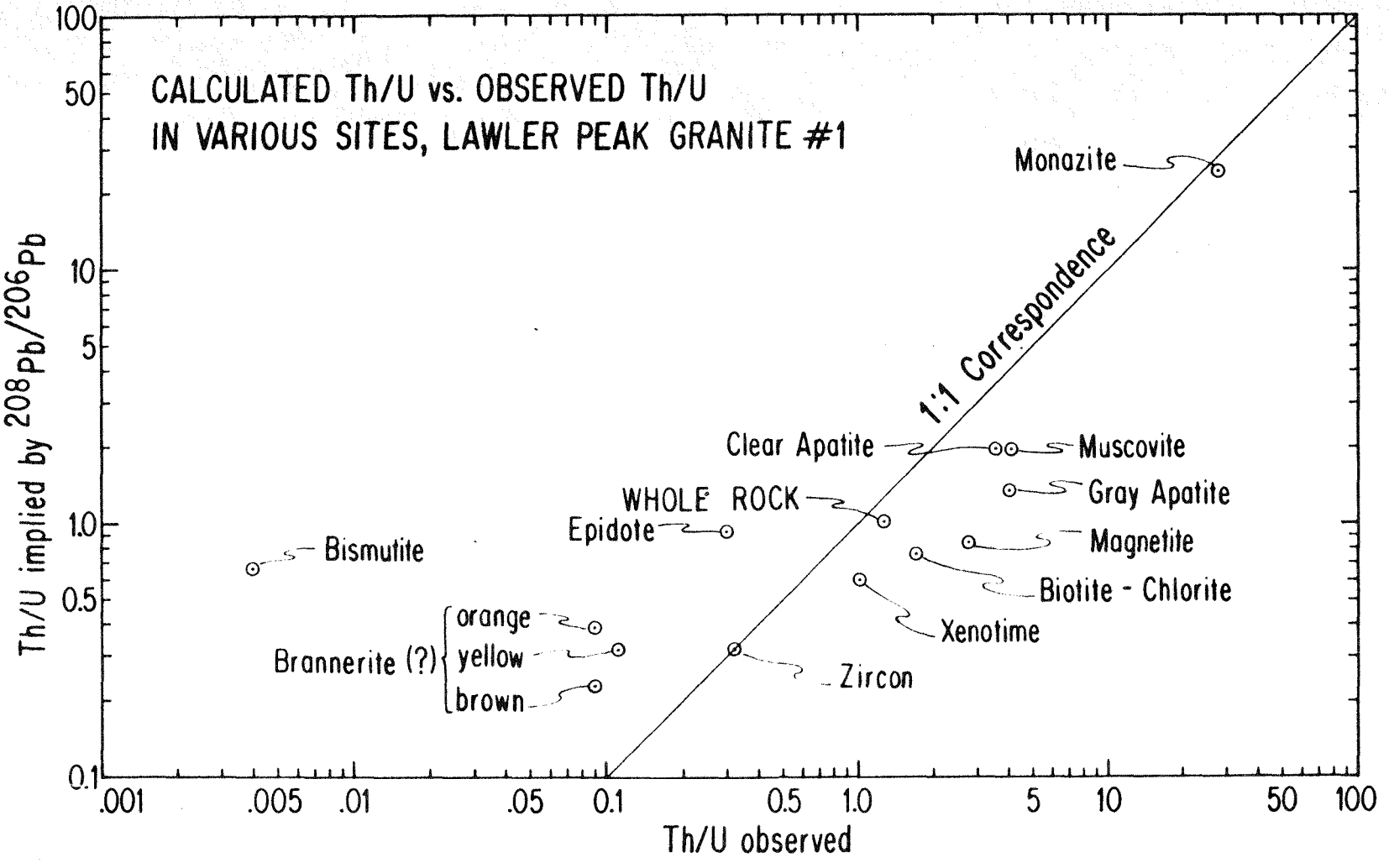
CALCULATED Th/U vs. OBSERVED Th/U
IN VARIOUS SITES, LAWLER PEAK GRANITE #1
Th/U implied by $^{208}Pb/^{206}Pb$
Th/U observed
100
50
10
5
1.0
0.5
0.1
.001
.005
.01
.05
0.1
0.5
1.0
5
10
50
100
1:1 Correspondence
Monazite
Clear Apatite
Muscovite
Gray Apatite
WHOLE ROCK
Epidote
Magnetite
Bismutite
Biotite - Chlorite
Xenotime
Brannerite (?)
orange
yellow
brown
Zircon

Figure 82

insufficient explanation; though the thorite's Th/U ratio is much larger than that of zircon, the zircon Th/U falls with increasing radioactivity.

The preferred interpretation of the zircon analyses is that the zircon first became closed for lead-uranium and lead-thorium at the time of primary crystallization of the zircon and the host granite 1411 ± 3 m.y. ago. This age is consistent with isotopic ages interpreted from several other systems in the rock, indicating that the zircon probably closed without incorporating any older radiogenic lead at the time of pluton emplacement. The system remained closed until 228 ± 4 m.y., when the zircon lost on average about 50 percent of its lead. The uranium and thorium levels may not have been altered substantially. The nature of the 228 m.y. event is not fully understood. There is no significant igneous or orogenic event that has been independently identified in the local geological history. The event has been recognized however by its effects on other isotopic systems in the rock. Silver (1966, and unpublished data) has found this event recorded in several other nearby granites. Its importance in the history of this granite is firmly established. There is no evidence for disturbance of the Lawler Peak Granite #1 zircon isotopic systems subsequent to 228 m.y., although zircon from other samples of the pluton clearly show the superimposed effects of at least one additional younger event (Williams and Silver, 1979).

Monazite

A single separate consisting of hand-picked fine-grained monazite was analyzed by isotope dilution. A few of the grains were clear yellow, but most were turbid orange to orange-brown (Fig. 55). EMP analyses show that there is a correlation between monazite turbidity and chemical composition, the clearer grains being higher in lead and uranium by factors of two or three and on average a few percent higher in thorium than the more turbid ones.

The isotope dilution analysis (Table 18a) shows the composite monazite concentrate to be highly enriched in radiogenic lead (5100 ppm), uranium (4500 ppm) and especially in thorium (125,400 ppm). EMP scan photographs and spot analyses show wide grain to grain variations in the mineral's lead, uranium and thorium contents but only minor compositional zonation in individual crystals. Uranium concentrations range from less than 1500 ppm to 4200 ppm, thorium values from 23,000 ppm to 72,000 ppm. Compared to these ranges the isotope dilution analysis is anomalous. Monazite however, clearly is a major repository for thorium and thorogenic lead in the rock.

The monazite lead-uranium and lead-thorium isotopic systems both are normally discordant*, the former by 35 percent and the latter by 45 percent, implying a net deficiency of radiogenic lead in both systems (Table 19a). The radiogenic lead has a very thorogenic component (radiogenic $^{208}Pb/^{206}Pb$ is 7.2), which is close to that expected from the mineral's high Th/U ratio of 28. The monazite has nearly 200 ppm common lead, in marked contrast to the very low common lead content of the zircons.

---

*Lead-thorium isotopic systems are considered normally discordant if the $^{208}Pb/^{232}Th$ age is less than the upper intercept age of the Pb-U systems.

The monazite isotopic systems from two other samples of the Lawler Peak pluton (Williams and Silver, 1979) contrast markedly with those of the present sample. They have lead and uranium contents which are lower by a factor of two, thorium which is lower by a factor of three and radiogenic $^{208}Pb/^{206}Pb$ ratios which are much lower (3.6 to 1.9). Most significantly, though, the lead-uranium systems are reverse discordant by a factor of two. It is possible that such differences could be no more than sample to sample variability, but the disparity between the Lawler Peak Granite #1 monazite isotope dilution and EMP analyses suggests otherwise. The isotope dilution data could be explained completely if the Lawler Peak Granite #1 monazite sample had contained as little as 15 percent thorite (Pb <3000 ppm, U ≈2.0 percent, Th ≈43 percent). This proposal receives direct support from the EMP scan photography. All monazites scanned were highly complex intergrowths of monazite and apatite, in volume proportions between about 6:1 and 1:1. It is possible that these intergrowths are exsolution phenomena. Apatite radiogenic systems occur in such low concentrations as to offer little but dilution effects to the monazite systems. However there is, in addition, a commonly observed association between monazite and thorite in this granite, with the latter occurring either juxtaposed to monazite grains or as internal inclusions. The scan photographs also show the monazite grains commonly to be surrounded by an iron-rich halo in which lead is visible.

On a lead-uranium Concordia diagram (Fig. 80) the monazite analysis plots significantly off the chord defined by the zircon analyses. Given the relatively large uncertainty in the radiogenic lead isotopic composition, reflecting the large common lead correction, the monazite could be construed to plot on the chord linking 1411 m.y. and the origin, which would imply undisturbed evolution of the isotopic system until very recently, and then an episodic reduction of the mineral's lead-uranium ratio. The analysis actually plots closer to a 1411 m.y.-75 m.y. chord. Interpretation of the analysis is not simple. All other monazites analyzed from the pluton have a $^{207}Pb/^{206}Pb$ age of 1411 m.y. and EMP determinations of thorite lead-uranium ratios show thorites to have lead-uranium ages probably less than 40 m.y.; a simple mixture of these two components would not appear to account for the observed monazite $^{207}Pb/^{206}Pb$. If the analysis is accepted at face value, the effects of at least one episode at or before 75 m.y. ago are recorded by the monazite isotopic system.

Xenotime

The analyzed concentrate of xenotime consisted of hand-picked dipyramidal crystals which were relatively uniformly translucent and buff yellow in color (Fig. 52). The isotope dilution analysis (Table 18a) shows xenotime to have more than 2000 ppm radiogenic lead, and nearly 1 weight percent uranium and thorium, making the mineral a major repository for radiogenic and radioactive elements in the rock. The measured Th/U ratio is close to 1, slightly lower than the observed whole-rock value (1.3). EMP analyses of xenotime in polished thin section show the grains to have only a small degree of relatively diffuse zonation in uranium and thorium, but the measured variations in concentration from grain to grain are considerable, 9000 ppm to 24,000 ppm for uranium and 7000 ppm to 10,000 ppm for thorium. The range in Th/U ratio determined by EMP is 0.4 to 0.6, consistently less than the isotope dilution value. The xenotime radiogenic $^{208}Pb/^{206}Pb$ is consistent with evolution in a system with a Th/U ratio of 0.5.

The lead-uranium and lead-thorium isotopic systems are both normally discordant, by 17 percent and 53 percent respectively (Table 19a). On a lead-uranium Concordia plot (Fig. 80), the xenotime analysis falls on the 1411 m.y. to 75 m.y. chord. However, the uncertainties in the analysis and the close proximity of the chord linking 1411 m.y. and the origin does not preclude the possibility of more recent disturbance.

EMP scan photographs of xenotime (Fig. 54) reveal a great many inclusions in the crystals, including quartz, feldspar, magnetite, epidote, zircon and thorite. Most of these act only as diluents to the xenotime isotopic systems, and the isotopic data do not suggest that the effect is significant. Thorite however could have a profound effect on the xenotime analysis because of its extreme normal discordance and high Th/U ratio. About 2 percent thorite mixed with concordant xenotime would be sufficient to account for the observed discordance in the analyzed xenotime lead-thorium system. Further, the presence of thorite in the isotope dilution sample could explain its having a slightly higher Th/U ratio than the EMP average value.

The difference between the degrees of discordance of the xenotime lead-uranium and lead-thorium isotopic systems cannot be explained by a simple loss of average radiogenic lead from the mineral, the apparent deficiency in ^{208}Pb being greater than that of ^{206}Pb. Loss of lead preferentially from ^{208}Pb-rich sites (such as thorite inclusions) is one possibility, but loss of intrinsic xenotime radiogenic lead accompanied by some loss of uranium relative to thorium also could account for the data. The lead-uranium analyses suggest that the disturbance of the xenotime isotopic systems occurred 75 m.y. ago, but the possibility of more than one period of open system behavior cannot be ruled out.

Uranium Titanate--Brannerite?

Despite its quite low abundance in the rock, brannerite? is potentially the most important mineralogical site for uranium in Lawler Peak Granite #1. The U-titanate's large grain size and consistently euhedral habit suggest that the mineral, now represented by complex intergrowths of brannerite? and more TiO_2-rich materials, was a primary phase which crystallized relatively early in the history of the granite.

Three hand-picked U-titanate separates were analyzed, each consisting of about one dozen grains selected on the basis of their mineral composition. The first separate consisted of black-brown grains, chosen to be only Zones A and B materials (as defined in the earlier discussion). The second separate was comprised of grains coated to a large extent by white and yellow Zone C material. The third separate was of grains with large areas coated by brown-orange Zone D, as well as Zone C, material. The zoning and coatings can be seen in Figures 58 and 59.

The three analyses are listed in Tables 18a and 19a and plotted on a Concordia diagram in Fig. 80. The thorium and radiogenic lead contents of the three separates are very high (1.95 percent to 3.1 percent and 0.9 to 1.7 percent respectively), and the uranium contents are enormous, 23 percent to 30 percent. Considering the extreme radioactivity of the mineral, the lead is unexpectedly non-radiogenic. The common lead contents of the three fractions, calculated assuming the ^{204}Pb to be associated with rock lead of the same composition

as that deduced from lead in the K-feldspar (Ludwig and Silver, 1977), are 1590 ppm for the brown-lustrous material, and 3780 ppm and 4220 ppm for the white-yellow and brown-orange coated grains respectively. Brannerite? has one of the highest radiogenic $^{206}Pb/^{208}Pb$ ratios measured in any mineral from Lawler Peak Granite #1 (up to 14.5) but even so it is not high enough to be consistent with the mineral's very low Th/U ratio (0.1).

EMP scan photographs and spot analyses show the internal mineralogical and chemical zonation of the U-titanate grains to be extremely complex. While the material in Zones A and B can be described using a brannerite formula, the material in Zones C and D appears to be anatase plus other phases. Broadly generalizing, the lead and thorium contents of all zones are relatively constant (variations of less than a factor of two) but there is a marked progressive outward decrease in uranium content in Zones A through D and increase in TiO_2 content in Zones A through C.

The three U-titanate lead-uranium analyses are quite similar and strongly normally discordant, the uranogenic lead contents being only about 20 percent of those expected for a 1411 m.y. old system. The discordance in the lead-thorium systems also is normal but to a lesser and variable extent. The apparent deficiency of thorogenic lead in the brown lustrous grains is 55 percent, decreasing successively to 32 percent and 15 percent in the grains with white-yellow and brown-orange coatings respectively. Considering the relatively constant lead and thorium concentrations and Pb/Th ratio measured in Zones A through D by EMP and the relatively constant $^{206}Pb/^{232}Th$ ratio in the isotope analysis samples, this change in $^{208}Pb/^{232}Th$ cannot readily be explained by changes in the mineral's lead-thorium balance. Rather the implication is that the radiogenic $^{206}Pb/^{208}Pb$ ratio becomes progressively lower in Zones A through D. The data indicate that the reduction in $^{206}Pb/^{208}Pb$ is accompanied by a progressive increase in $^{206}Pb/^{204}Pb$.

On the lead-uranium Concordia diagram the brannerite? analyses plot astride the 1411 m.y.-75 m.y. chord, there being a very slightly greater increase in $^{207}Pb/^{206}Pb$ with increasing Pb/U than is consistent with the slope of the chord. The simplest explanation of the data is that the brannerite? lost lead relative to uranium in an episode 75 m.y. ago, following undisturbed evolution since 1411 m.y. The complexity of the mineral, as seen in the EMP studies, the apparent heterogeneity in radiogenic lead composition and the incompatibility of the observed radiogenic $^{208}Pb/^{206}Pb$ with the observed Th/U ratio suggest that the migration of elements actually is more complex, with a loss of uranium and thorium strongly suggested. Whether the present isotopic balance is the consequence of a single disturbance 75 m.y. ago or the combined effects of additional older and younger disturbances is difficult to establish. The general colinearity of the three analyses on the Concordia diagram argues for the disturbance at 75 m.y. having been the most important episode of open system behavior in the brannerite?.

Coffinite? and Thorite

Neither coffinite? nor thorite have been positively identified, thus far, in the high-density mineral concentrates, so isotopic data for neither have been obtained. However, both minerals have been analyzed in polished thin section by EMP (Table 15c). They are of such importance to the lead-

uranium-thorium balance of the whole rock that limiting chemical calculations of their degree of isotopic imbalance, which can be made using the EMP Pb, U, and Th values (Table 15c), are very useful.

Coffinite? is the most radioactive mineral yet identified in the granite. The single crystal analyzed shows a patchy internal distribution in many elements, including lead, uranium and thorium. Lead concentrations range from 1300 to 3000 pm, thorium concentrations from 32,000 to 191,000 ppm and uranium concentrations from 252,000 to 558,000 ppm. Thorium and uranium variations are not correlated, so the range in Th/U ratio was 0.06 to 0.57. Taking estimated average values of Pb--2000 ppm, U--400,000 ppm and Th--150,000 ppm, and assuming all the lead to be radiogenic, the discordance in the composite isotopic systems must be at least 98%. The presence of common lead in the coffinite? system would make the calculated discordances even greater.

EMP analyses of thorite show it to be the most thorium-rich mineral yet identified in the granite. In scan photographs of polished thin sections it is seen to occur only as small grains (mostly less than 10 μm in diameter), very commonly in intimate association with other accessory minerals as epitaxial overgrowths or inclusions. The thorite itself contains yttrium, phosphorus, zirconium and uranium in such abundances that it may be considered to be 50 to 60 percent thorite component, 10 to 15 percent xenotime component, 10 percent zircon component and 2 to 3 percent coffinite component. EMP-determined element abundances in thorite are lead $\leq$3000 ppm (at or below the EMP detection limit), uranium--13,000 to 30,000 ppm and thorium--360,000 to 453,000 ppm. Taking estimated average concentrations of thorium--430,000 ppm and uranium--20,000 ppm, accepting the lead concentration of 3000 ppm as an upper limit, and assuming all the lead to be radiogenic, the discordance in the thorite isotopic systems must be a minimum of 91 percent in a normal sense. The probable discordances must approach the levels of those in coffinite?.

Given the extreme open system behavior demonstrable for coffinite? and thorite and the lack of lead isotopic data for either, it is not possible to establish the extent of uranium and thorium mobilization from each. Leaching experiments carried out in this laboratory on thorite from other granites have shown the mineral to lose uranium and thorium very readily in mildly acid solutions. Similar behavior is to be expected for coffinite?. Clear evidence of lead, uranium and thorium in transient sites in the vicinity of the coffinite? (and to a lesser extent near thorite) can be seen in the EMP scan photographs where dispersed lead, uranium and thorium is visible in the iron-rich halo which surrounds the coffinite? grain (Fig. 69).

Apatite

Because of the great range in the physical properties of the apatite in Lawler Peak Granite #1 two samples were analyzed isotopically. Each was comprised of hand-picked grains selected to represent relative extremes expected in the spectrum of compositions. The first separate consisted of 75 to 150 μm diamagnetic, prismatic, euhedral, inclusion-free, colorless, high-clarity apatite (R 200 1.7M 10 Clear) (Fig. 38). The second separate consisted of 300 to 600 μm, weakly paramagnetic, equant, euhedral to subhedral, gray to brown, translucent apatite which contained both small crystalline and unidentifiably fine dusty inclusions (R 50 1.0M 10 Gray) (Fig. 39).

The apatite in both fractions (Table 18b), with uranium contents of 22 and 26 ppm, is only slightly enriched in uranium over the whole-rock average (21 ppm). The apatite thorium contents, at 78 and 105 ppm, are a factor of three to four higher than the average whole-rock thorium. Such concentration levels are below the detection limits of the electron microprobe so the details of uranium and thorium variability and zonation in apatite could not be determined by that technique.

The uranium contents of the analyzed apatites are unusually low considering the above-average concentration of uranium in the rock as a whole. It is more normal to find apatite to be enriched in uranium over the whole rock by about a factor of ten to thirty (Altschuler et al., 1958); in Lawler Peak Granite #1 the apatite uranium content might be expected to be 200 to 600 ppm. Furthermore, the apatites' Th/U ratios are unexpectedly high considering the abnormally low Th/U ratio of the granite. The Th/U ratio in apatite more commonly is about a factor of two to four lower than that of the host granite, in contrast to the factor of four higher observed in the present case. The apatites' low uranium contents and high Th/U ratios both suggest that apatite has been depleted in uranium relative to thorium.

The apatite isotopic analyses are listed in Tables 18b and 19b and plotted on a lead-uranium Concordia diagram in Fig. 81. Both fractions show strong reverse discordance in lead-uranium (by 42 percent and a factor of 2.6 for the clear and gray apatite separates respectively) and moderate normal discordance in lead-thorium (24 percent and 15 percent respectively). Both lead-uranium analyses plot within the analytical uncertainties on the upward extrapolation of the chord defined by the normally discordant zircon analyses, the chord which intersects Concordia at 228 ± 4 and 1411 ± 3 m.y.

The lead isotopic compositions measured in the two apatite fractions are relatively similar. Neither lead is particularly radiogenic (common lead accounts for 46 percent of the lead in the less radiogenic clear apatite) and both fractions are characterized by radiogenic lead which is markedly enriched in ^{208}Pb. The radiogenic $^{208}Pb/^{206}Pb$ of the clear apatite (0.58) is exceeded only by that of monazite among the minerals analyzed isotopically. Nevertheless, the radiogenic $^{208}Pb/^{206}Pb$ in the apatite is 50 to 70 percent lower than that expected for lead generated in a system with the mineral's observed Th/U ratio.

In grain mount and thin section the gray apatite in particular can be seen to contain minute inclusions of monazite and zircon (Fig. 40). The presence of such inclusions (both of which would have normally discordant lead-uranium systems) cannot explain the apatite reverse discordance, given that the inclusion-rich gray apatite is more reverse discordant and has a lower radiogenic $^{208}Pb/^{206}Pb$ ratio than the clear apatite. The apatite discordance apparently is the consequence of differential loss of lead, uranium and thorium from the mineral. The observed discordances would result if uranium loss greatly exceeded lead loss, which in turn exceeded thorium loss. There is no evidence for uranium gain by the mineral. The lead-uranium isotopic analyses imply that the disturbance of the apatite isotopic system occurred about 230 m.y. ago. Uranium loss in that episode and an originally lower Th/U is supported by the observed $^{208}Pb/^{206}Pb$ ratio and by the inconsistency between the observed high apatite and low whole-rock Th/U values.

Epidote

The epidote fraction analyzed consisted of inclusion-free, brilliantly clear, apple-green grains handpicked from the concentrate of high-density minerals coarser than 150 μm. Such epidote represented only a small proportion of the epidote in the rock. The majority of the epidote recovered was considerably finer and translucent yellow or olive green, containing many fine opaque inclusions. The selection of only coarse, clear epidote limited both the composition of the epidote analyzed and the possible sites in the rock from which it may have originated. In thin section, coarse-grained clear epidote free of inclusions or allanite cores is found only in the center of large plagioclase crystals. It is probable that such epidote has formed as a secondary alteration after plagioclase. Epidote in other sites in the rock is extremely complex texturally and compositionally, suggesting its formation in late stage primary or much younger secondary episodes.

The uranium and thorium concentrations measured in epidote by isotope dilution (81 and 24 ppm respectively, Table 18b) are low, below the detection limits of the electron microprobe. Although epidote comprises about 0.4 weight percent of the granite, the mineral does not appear to constitute a major repository for radioactive elements in the rock. The analyses should be considered minimum values for average rock epidote however, for a greater enrichment in uranium and thorium is to be expected in that epidote which has an allanite component. The observed epidote Th/U ratio of 0.3 is unexpectedly low, even in the context of the very low Th/U ratio of the whole rock.

The epidote lead-uranium and lead-thorium isotopic systems are unusual for radioactive minerals in Lawler Peak Granite #1. They are both strongly reverse discordant, Pb-U by 52 percent and Pb-Th by almost a factor of five. This is seen in the Concordia diagram in Fig. 81. Like the apatite analyses, the epidote analysis falls on the upward extrapolation of the chord defined by the zircon data, intersecting Concordia at 228 ± 4 and 1411 ± 3 m.y. The inclusion of the combined zircon, epidote and apatite analyses in a redefinition of that chord increases the uncertainties in the intersection ages slightly but makes no significant change in their values (1413.7 ± 4.6 m.y. and 230.9 ± 7.0 m.y.), reflecting the very small deviation of the combined analyses from perfect fit.

Lead in the epidote is among the least radiogenic found in the granite's radioactive accessory minerals, exceeded in relative ^{204}Pb content by lead in clear apatite only. The radiogenic $^{208}Pb/^{206}Pb$ ratio (0.28) is very close to the whole-rock value (0.30) but given the mineral's very low Th/U ratio, is a factor of three higher than is to be expected. That observation, the lead's high common component and the reverse discordance of both isotopic systems combine to suggest that much of the radiogenic lead now in the mineral has not evolved *in situ*. The position of the lead-uranium analysis on the 1411 m.y.-230 m.y. chord is consistent with the mineral having formed at 1411 m.y. and then having lost uranium and thorium relative to lead 230 m.y. ago. In the light of the evidence for exogenous lead in the mineral, an alternative interpretation must be considered. The observed discordance could be explained if epidote had formed 230 m.y. ago, incorporating radiogenic lead available at that time. The isotopic composition of that radiogenic lead implies its evolution in an isotopic system characterized by a Th/U ratio very similar to that of the whole rock. The unusually low Th/U ratio of the epidote itself may reflect the abnormally low Th/U ratio of the medium from which it crystallized, or the phase which it has replaced.

Bismutite

A single grain of bismutite was analyzed isotopically. The grain in fact was one half of a 200 μm diameter crystal fragment that was cleaved into two parts so that a piece closely equivalent to the analyzed sample was preserved for EMP and X-ray diffraction examination (Fig. 71). Like many of the bismutite grains recovered, the analyzed grain showed pronounced concentric internal zonation that was not in any apparent way related to the crystal form of the mineral (Fig. 72). In many of the grains studied such zones were centered on a core of metallic lead-gray bismuthinite (Figs. 70,72), but as far as could be determined visually, there was no similar core in the fragment analyzed. An X-ray diffraction photograph of the second half of the grain showed no bismuthinite lines. Bismutite-bismuthinite has been recovered from the high-density mineral separates but has yet to be identified in thin section.

Because the weight of the analyzed sample was small (0.02 mg) and difficult to determine accurately, the uncertainties in the lead, uranium and thorium concentrations measured in the mineral by isotope dilution are large. It should be noted that these uncertainties do not extend to the ratios of the concentrations or to the isotopic properties. The values obtained were radiogenic lead--32,100 ppm, uranium--3300 ppm and thorium--15 ppm. The measured total lead content was 44,400 ppm. Only preliminary EMP data have been gathered for bismutite. A semi-quantitative lead analysis of the mineral suggests its lead content may reach as high as 10 percent.

EMP scan photographs of bismutite-bismuthinite show compositional differences between the two phases and possible compositional zonation within the bismutite. Bismuthinite is richer in lead and in fact has the highest lead concentration (>12 percent) found in the granite. Lead concentrations in the bismutite are the second highest and show a tendency to increase towards the grains' rims. Uranium is detectably enriched in the bismutite.

The bismutite isotopic analysis is listed in Tables 18b and 19b. The reverse discordant isotopic imbalance in the mineral is extraordinary. If the bismutite is 1411 m.y. old, it contains a factor of thirty-five times more uranogenic lead than would have been produced by the *in situ* decay of the observed uranium and more than three orders of magnitude more thorogenic lead than would have been produced by the thorium. *In situ* generation of the radiogenic lead seems improbable. If the mineral is in fact younger the imbalances are even greater, and strongly imply an extraneous site for the origin of the radiogenic lead.

The lead in bismutite is moderately radiogenic, about 30 percent of the lead being common. The radiogenic $^{208}Pb/^{206}Pb$ ratio of 0.02 is a factor of one hundred sixty-five times greater than that expected given the mineral's extremely low Th/U ratio. The bismutite radiogenic lead actually is comparable in composition to the radiogenic lead in the rock as a whole and the total lead $^{206}Pb/^{204}Pb$ is similar to that found in a number of other minerals. The bismutite lead-uranium system is so reverse discordant that it has not been plotted on a lead-uranium *Concordia* diagram. The analysis does not fall precisely on the extrapolation of any chord defined by other data from the granite. The chord linking the analysis and 1411 m.y. on *Concordia* would provide a lower intersection at 104 m.y.

A simple interpretation of the bismutite lead-uranium analysis would be that the mineral's isotopic system was disturbed 104 m.y. ago. If the reverse discordances are to be attributed to uranium and thorium loss alone, the data imply loss of 97.3 percent of the original uranium and 99.98 percent of the original thorium contents of the mineral. This amounts to 50 percent of the original sample weight and seems quite improbable considering the low uranium content of the bismuthinite. A preferred interpretation of the data is that bismutite has formed secondarily from bismuthinite which earlier had concentrated radiogenic and common initial lead from the granite. The bismuthinite, whose properties largely are inferred from EMP data, must have formed in the Cretaceous during an alteration or hydrothermal episode involving sulfide ions. If that initial lead were derived from a previously closed 1411 m.y. old source, its radiogenic $^{207}Pb/^{206}Pb$ implies its isolation from that source 104 m.y. ago. It is more likely however that a mixture of leads from several sources was incorporated, in which case the resultant radiogenic $^{207}Pb/^{206}Pb$ does not have the same time significance. It is plausible however, that the bismutite formed during the 75 m.y. episode from available radiogenic and common lead mixtures.

Other Phases and Sites

Uranium, thorium and radiogenic lead in readily definable radioactive accessory minerals comprise only a part of the total uranium-thorium-radiogenic lead content of Lawler Peak Granite #1. There are in addition significant radiogenic and radioactive components associated with the major minerals and with some very complex mixtures of high-density minerals from which it has not been possible to isolate specific radioactive phases.

These additional uranium, thorium and lead components apparently are present as labile elements now distributed as surface coatings along grain surfaces, microfractures and interstices. They appear to form significant items in the whole-rock lead-uranium-thorium budget. Through the analysis of a selection of the more common minerals, mineral mixtures and mineral leaches it has been possible to identify these components and gain valuable insights into their abundance and compositions.

Biotite-Chlorite

A sample of biotite-chlorite was prepared for analysis by subjecting a magnetically purified biotite concentrate to repeated shear-grinding in a small agate mortar, screening and electrostatic separation. Shear-grinding separated the mica grains along their basal cleavage and both liberated and crushed inclusions so that they subsequently could be removed by wet sieving under acetone. To ensure that only the thinnest and most inclusion-free sheets were included in the sample, the ground mica was placed on a weakly electrostatically charged vibrating glass plate to which only the thinnest mica sheets adhered and were recovered. The product of this separation procedure was a mica-sheet concentrate consisting predominantly of biotite, with about 25 percent chlorite and 3 percent muscovite, as free as possible of inclusions. The sample was attacked for analysis by total fusion in borate flux.

The biotite-chlorite analysis is listed in Tables 18b and 19b plotted on a lead-uranium Concordia diagram in Fig. 81. The sample has the same uranium content (20.6 ppm) as the average for the whole rock and a thorium content (35.4 ppm) only slightly higher than the average, resulting in a Th/U ratio of 1.7. A feature of the analysis is the high concentration of radiogenic lead (30.5 ppm), five times as much uranogenic lead as can be accounted for by 1411 m.y. of decay of the associated uranium and twice as much thorogenic lead as can be accounted for by the thorium. Both the lead-uranium and lead-thorium isotopic systems are markedly reverse discordant. The isotopic composition of the radiogenic lead is unusual in that it is one of the few leads measured from Lawler Peak Granite #1 in which the radiogenic $^{207}Pb/^{206}Pb$ is consistent with evolution in a closed 1411 m.y. old isotopic system. The radiogenic $^{208}Pb/^{206}Pb$ is similar to the whole-rock average. The isotopic composition of the biotite-chlorite total lead is remarkably similar to that of lead in several other minerals and sites, notably bismutite. This last observation suggests that the procedure used for preparing the biotite-chlorite for analysis was relatively efficient at excluding the many radioactive minerals to which biotite is host.

Although the radiogenic and radioactive element contents of the biotite-chlorite are relatively low, the abundance of biotite-chlorite in the rock is sufficiently high that one must conclude mica is host to a significant fraction of those elements in the granite, especially radiogenic lead. The imbalance in the isotopic systems could be explained by uranium and thorium loss relative to lead, but in view of the lead's isotopic composition, the alternative of lead gain is preferred. That composition implies that if lead was gained it was gained recently from a source which has remained essentially closed for lead and uranium for the history of the rock. The results of recently performed leaching experiments on the biotite-chlorite mixture show that there is a labile lead component in the biotite-chlorite which differs only slightly in composition from the total-sample lead (Table 18c). What proportion of the total mica lead-uranium-thorium the labile component represents has yet to be established.

Muscovite

The analyzed sample of muscovite was purified from a preliminary concentrate using the same multi-cycle grinding, screening and electrostatic separation procedure as used for biotite-chlorite. About 90 percent of the radioactive inclusions were removed from the mineral by that procedure and subsequent hand picking raised the sample's purity to about 99 percent. Only coarse-grained muscovite was retained, thereby excluding sericite from the analysis. The sample was attacked for analysis by total fusion in borate glass.

The muscovite isotopic analysis is listed in Tables 18b and 19b and plotted on a lead-uranium Concordia diagram in Fig. 81. The isotopic systems in the muscovite differ markedly from those in the biotite-chlorite or whole rock. The muscovite uranium content (4.6 ppm) is lower by about a factor of five times in both comparisons , but its thorium content (18.8 ppm) is lower only by about 47 percent and 30 percent respectively. As a corollary, the muscovite Th/U ratio (4.1) is, next to monazite and thorite, the highest found in any mineral in the rock. The muscovite radiogenic lead content is very low (4.2 ppm) and the total lead has a very large common component (56 percent). Like the lead in biotite-chlorite, the muscovite radiogenic $^{207}Pb/^{206}Pb$ is consistent with

evolution in a closed 1411 m.y. old isotopic system. A feature of the muscovite radiogenic lead however is its comparatively high $^{208}Pb/^{206}Pb$ (0.58, compared to 0.22 in biotite-chlorite). This may in part be a consequence of the muscovite's high Th/U ratio, but considering the size of that ratio, the mineral's radiogenic $^{208}Pb/^{206}Pb$ is about 60 percent less than would be expected.

Both the muscovite's lead-uranium and lead-thorium isotopic systems are reverse discordant, the former by about a factor of two and a half times and the latter by about 20 percent. This is the same sense of discordance as seen in the biotite-chlorite isotopic system, but it is of lesser magnitude. It is possible that the muscovite's high thorium and thorogenic lead contents reflect the presence of thorium-rich mineral inclusions in the analyzed sample, or that even if the inclusions were removed, some imprint of thorium and thorogenic lead from those inclusions may have remained. This is consistent with thin section observation that muscovite contains a disproportionately large fraction of the monazite in the rock. The reverse discordance cannot be explained by the effect of known thorium-rich inclusions, which are normally discordant. It is possible also that muscovite has lost significant amounts of uranium and thorium relative to lead. A preferred interpretation of the data is that muscovite has incorporated a mixture of radiogenic and common lead in a way similar to that inferred for biotite but that in muscovite there is an additional component of ^{208}Pb-rich lead. Although it is difficult to confirm at this time, it is possible that the incorporated exogenous lead was accompanied by uranium and thorium.

The results of recent leaching experiments on an aliquot of the analyzed muscovite sample are consistent with the concept of added radiogenic lead. A brief, moderate nitric acid leach removed from the muscovite a lead component with a much lower $^{208}Pb/^{206}Pb$ and higher $^{206}Pb/^{204}Pb$ than the lead in the total sample (Table 18c). The leached muscovite lead in fact closely resembles the composition of the lead leached from the biotite-chlorite mixture. This suggests that the labile lead components in the two mica samples may be quite similar to one another, despite the major differences between the two composite isotopic systems.

Magnetite

The preparation of a pure magnetite sample for isotopic analysis was made difficult by the widespread occurrence of radioactive accessory minerals included in, and aggregated with the magnetite crystals (Figs. 28,78). The sample was obtained by hand picking euhedral, apparently inclusion-free magnetite (Fig. 32), grinding it and reseparating handmagnetic material from an acetone suspension of the powder.

EMP analyses of magnetite show it to be virtually pure $FeO \cdot Fe_2O_3$ but nevertheless, it contains significantly more uranium (26.0 ppm), thorium (72.2 ppm) and radiogenic lead (78.2 ppm) than the whole rock. These concentrations are small by comparison with those in many other accessory minerals but magnetite, with ilmenite, is so abundant in the granite (about 0.4 weight percent) that in toto it constitutes an important reservoir, especially for radiogenic lead.

The magnetite isotopic analysis is listed in Tables 18c and 19c. The magnetite Th/U ratio (2.8) is significantly higher than that of the whole rock, yet the compositions of radiogenic lead in the mineral and whole rock bear a

close resemblance to one another. Lead in the magnetite is slightly more enriched in ^{208}Pb. The magnetite's radiogenic $^{208}Pb/^{206}Pb$ and present Th/U ratio are not mutually compatible, the lead composition indicating its origin in a system with a Th/U ratio of 0.8. Significantly however, the magnetite total lead composition is very similar to that of lead found in some other minerals and sites, in the biotite-chlorite, its leach and the bismutite for example.

Both the magnetite lead-uranium and lead-thorium isotopic systems are strongly reverse discordant. The former is reverse discordant by a factor of ten times and is exceeded in reverse discordance only by the lead-uranium system of bismutite. The latter is reverse discordant by a factor of three times and is exceeded in reverse discordance only by the lead-thorium systems in bismutite and epidote. On a lead-uranium Concordia diagram (Fig. 81) the magnetite analysis falls on the upward extrapolation of a chord which intersects Concordia at 1416 ± 5 and 76 ± 2 m.y., the chord defined by the analyses of xenotime, monazite and brannerite?.

The reverse discordance of the magnetite isotopic systems could be explained by the loss of large amounts of uranium and thorium from the mineral. The preferred interpretation of the data, considering that the magnetite lead is very similar in composition to leads in other minerals that appear to contain a significant labile component, is that a mixture of radiogenic and common lead (with, but in excess of some U and Th) has been added to the magnetite. Analyses of acid leaches of magnetite support this suggestion and indicate that most of the uranium and thorium also was labile. The isotopic composition of the lead suggests that the radiogenic component evolved in a lead-uranium system that remained essentially closed from 1411 m.y until 75 m.y. ago, at which time the lead was separated from its parent uranium.

Concentrate of High-density, Weakly Ferromagnetic Opaque Minerals

A systematic survey of the α-activity of the high-density mineral separates showed that a significant fraction of the total rock radioactivity was present in one large heterogeneous concentrate of weakly ferromagnetic particles dominated by opaque minerals (0.29 M 10). The concentrate consisted primarily of composite aggregates of opaque minerals tightly bound with most of the other major and minor phases in the granite (Fig. 79). It was not possible however, to identify within the concentrate a specific phase or phases to which the activity might be attributed. A representative split of the total concentrate therefore was analyzed in order to characterize the composite system. The analysis of the opaques concentrate served two purposes. On the one hand, the contribution of the fraction to the whole-rock lead-uranium-thorium system was determined. On the other, the fraction represented a distinctive site in the rock for the possible production and/or accumulation of labile components. The analysis has provided information on what the composition and magnitude of those components might be.

The analysis of the concentrate of high-density, weakly ferromagnetic opaque minerals is listed in Tables 18b and 19b. The concentrations of radiogenic lead (250 ppm), uranium (1370 ppm) and thorium (1300 ppm) are thirty to sixty times higher than the concentrations of the same elements in the whole rock. The amount of material comprising the fraction is such that by present best estimates it accounts for approximately 10 percent of the rock uranium,

thorium and radiogenic lead. The total lead composition is slightly more radiogenic than that of leads from the epidote, magnetite, biotite-chlorite and bismutite but clearly is generally similar to them. The radiogenic lead has a slightly higher $^{208}Pb/^{206}Pb$ than lead in those minerals, most closely resembling the $^{208}Pb/^{206}Pb$ of lead from epidote and the whole rock. Unusually, the radiogenic $^{208}Pb/^{206}Pb$ is very close to being compatible with the concentrate's composite Th/U ratio (0.95).

The analysis is plotted on a lead-uranium Concordia diagram in Fig. 80. Both the composite lead-uranium and lead-thorium isotopic systems are normally discordant, by 38 percent and 33 percent respectively. The analysis plots within the analytical uncertainties on the 1416 m.y.-76 m.y. chord defined by the xenotime, monazite and brannerite? analyses and is offset significantly from the chord linking 1411 m.y. and the origin.

The interpretation of the analysis is difficult because an obviously complex mixture of isotopic systems is contributing to the fraction. The observed concentrations of uranium, thorium and radiogenic lead are so large that, despite the similarity of the lead isotopic composition to that of lead which has been shown to be labile in other minerals, it cannot be assumed that only labile components are contributing. Clearly there are important concentrations of radioactive minerals present, perhaps including species not yet distinguished. It is noteworthy however that both the composite lead-uranium and lead-thorium isotopic systems are markedly more concordant than the systems observed in brannerite? or deduced for coffinite?. The radioactive systems, therefore, cannot be composed only of contributions from included grains of those minerals. From the levels of uranium, thorium and radiogenic lead, the isotopic composition of the lead and the pattern of discordance, it is surmised that this fraction is probably enriched in all of the radioactive accessories at up to fifty times the whole-rock level.

Cold, moderate strength acid leaches which have been performed on the concentrate show that there is a significant component of labile lead present which is accessible to acid solution (Table 18c). The composition of that lead is extremely close to that of labile lead identified in other minerals and markedly less radiogenic than the lead in the total fraction. Data are not presently available on the fraction's contents of labile uranium and thorium.

Magnetite leaches

Analysis of magnetite showed the mineral to contain very significant quantities of uranium, thorium and radiogenic lead. In order to assess what proportion of these elements was an integral part of the mineral and what was labile component, an aliquot of the magnetite ground powder was subjected to two nitric acid leaches. The procedure for the leaching experiments already has been described.

The first leach with cold 1 N nitric acid for one hour removed a component representing about 10 percent of the uranium, thorium and radiogenic lead in the total sample (Table 18c). Significantly, the relative proportions of the lead isotopes and uranium and thorium obtained in the leach were virtually identical to those in the total sample. A second leach with concentrated nitric acid held close to its boiling point for one hour removed more than 90 percent of the

remaining thorium and lead and more than 75 percent of the remaining uranium. The lead composition in the second leachate was remarkably similar to that in the first, as were the lead-uranium and lead-thorium ratios. Together, the two leaches removed 95 percent of the radiogenic lead, 79 percent of the uranium and 92 percent of the thorium from the magnetite, although they effected only minor obvious chemical attack on the magnetite concentrate.

The facts that such a large proportion of the total lead, uranium and thorium proved to be acid soluble, that each leach removed lead of the same isotopic composition as the lead in the total sample and that in each leach the proportions of lead, uranium and thorium were virtually the same as those in the total sample strongly suggest that these elements were present in the magnetite concentrate in a uniform state or matrix that dissolved progressively. That matrix may have been acid soluble inclusions, but none of the analyzed accessory minerals has the isotopic characteristics observed in the leaches. A far more likely explanation is that the leached lead, uranium and thorium were present in coatings on surfaces of the magnetite grains and therefore represent a labile component. An observation that the leach solutions were iron-rich and that the magnetite luster changed from dull to metallic on leaching suggests that a surface coating was dissolved. The profound similarity of the compositions of total lead recovered from the magnetite and its leaches to that of lead found in several minerals (biotite-chlorite, bismutite, epidote and the opaques concentrate) suggests that all may share significant common labile components. We believe it is significant that, in this instance, the labile lead, which appears to be readily identifiable, is accompanied by equally labile thorium and uranium, for which there are no unique isotopic tags.

Quartz-feldspar leaches

One of the more direct methods of isolating and measuring at least a part of the labile component in the granite was to leach high purity separates of minerals which themselves were known to be extremely poor in indigenous uranium, thorium and radiogenic lead. The mineral separate chosen for the experiment contained quartz and feldspar, the principal phases in the rock.

The preparation of a high-purity concentrate of quartz (25 percent) and feldspar (75 percent) for the leaching experiment and the experiment itself already have been described. The analyses of a cold, one hour 1 N nitric acid leach and a hot, one hour concentrated nitric acid leach are listed in Tables 18c and 19c and plotted on a lead-uranium Concordia diagram in Fig. 81. Both leaches removed uranium, thorium and radiogenic lead from the mineral concentrate, the majority being removed by the first acid attack. The acid caused no apparent change in the quartz-feldspar substrate. The composite content of the two leaches is radiogenic lead 0.25 ppm, uranium 0.56 ppm and thorium 1.95 ppm. Although the quantities removed are small as a fraction of the weight of mineral leached, quartz and feldspar constitute such a large fraction of the granite that the quantities suggest this leachable component may account for 3.6 percent of the radiogenic lead, 2.7 percent of the uranium and 7.3 percent of the thorium in the whole rock. Given that only the very cleanest quartz-feldspar obtainable was leached, these may be considered minimum estimates. A further reason for considering the quantities to be minimum estimates is the undetermined leaching effect on the quartz and feldspar of the water used during the mineral separation procedures.

The lead removed by both leaches has a rather similar isotopic composition, a composition which in turn is similar to, though slightly less radiogenic than, that of lead in the magnetite and its leaches, epidote, biotite-chlorite and its leach and the leach of the concentrate of high-density, weakly ferromagnetic opaque minerals (Tables 18b,c). The slightly higher common lead content of the quartz-feldspar leaches probably results from the leaching of a small amount of additional lead from the common-lead-rich feldspar in the substrate. That the stronger leach is less radiogenic supports this. The two leaches do differ significantly from one another, however, in their lead-uranium, lead-thorium and thorium-uranium ratios. The Th/U ratio of the weaker leach (2.4) is of the same order as that of the magnetite but the Th/U ratio of the stronger leach (8.4) is more than twice that of any other leach or phase. In both leaches the Th/U ratio is considerably higher than the value of approximately 1 which would be consistent with the radiogenic lead composition.

The lead-uranium systems in both leaches are reverse discordant, the weaker leach by a factor of one and a half times and the stronger even more so, by a factor of nearly three times. In contrast, the lead-thorium systems in both leaches are normally discordant, that in the weak leach by 48 percent and in the strong leach by 64 percent. These differences in leach compositions contrast with the similarity of the two magnetite leaches. It could be argued that the leaches are attacking differentially some inclusions within the quartz-feldspar but the constancy of the lead compositions suggests otherwise. It would appear that the relative accessibility of lead, thorium and uranium sites in the quartz-feldspar to oxidizing acid solutions varies. The constant tetravalent state of thorium ions is in contrast to the partially to completely? hexavalent state of uranium and may contribute to slower dissolution rates for thorium. The Th/U ratio of the composite of the leaches is in fact very close to the Th/U ratio of the leaches of magnetite. This may be an indication that although the proportion of lead in the labile component may vary, the component's Th/U ratio is relatively constant. It appears possible to test this inference.

Preliminary Results from Leaches of Other Mineral Separates

Preliminary lead isotopic composition data have been obtained for acid leaches of four additional mineral fractions. All of these are one hour, cold, 1 N nitric acid leaches, except the leach of the opaque minerals concentrate which was prepared in two steps, a fifteen minute leach followed by a forty-five minute leach. The sum of these two leaches (whose lead isotopic compositions are quite similar) is equivalent to the leaches of each of the other fractions.

In these leaches, particularly in the case of the sheet structure minerals, it is expected that some common lead was dissolved from the mineral substrate. Indeed the observed $^{206}Pb/^{204}Pb$ for leaches of the quartz-feldspar, muscovite and biotite-chlorite reflects the anticipated comparative solubilities of the substrate phases. Nevertheless, the radiogenic lead compositions of all leached systems (Table 18c) are remarkably uniform and even the $^{206}Pb/^{204}Pb$ range is surprisingly limited. Of particular interest is a leach of a mineralogically comparatively pure fraction of quartz-feldspar which differs from the original fraction in having a higher proportion of yellow-stained (Fe-oxides?) surfaces. Its labile lead composition is somewhat more radiogenic than, but clearly similar to, the composition of all of the other leach leads.

SOME CONCLUSIONS AND INTERPRETATIONS

Whole-Rock Trace Element Constraints on Accessory Mineral Abundances

In the earlier section which deals with the modal composition of Lawler Peak Granite #1, the inadequacy of conventional point counting as a method of determining modal abundances of trace minerals was noted. The principal difficulty with the method is the very large area of thin section and large number of points which must be counted in order to sample the accessory minerals effectively and to achieve sufficiently good counting statistics for abundances at the levels 0.0001 to 0.02 percent. It is possible to obtain better estimates of modal abundances using high-density mineral separates in which the accessory minerals are concentrated. Such abundances however, are subject to large uncertainties resulting from incomplete recovery and biasing of the sample at each step of the mineral separation procedure, and are usually minimum values only.

Upper limits can be placed on the abundance of some accessory minerals from the whole-rock major and trace element analysis of the granite (Table 10). This is done by using the observation that certain key elements in the rock are found dominantly in only one (or two) radioactive accessory minerals. The calculation is possible only if, for the rock in question, data are available on the major (and often trace) element composition of every significant major, minor and trace mineral phase. The whole-rock and EMP mineral analyses done for the present study make a first order calculation of certain accessory mineral abundances possible for Lawler Peak Granite #1.

The whole-rock composition of the granite is listed in Table 9, the EMP-determined mineral compositions are listed in Tables 15a,b,c and the results of abundance limit calculations that have been possible are listed in Table 20. The abundance of zircon is limited by the availability of zirconium, assuming all Zr occurs only in zircon, thereby placing an upper limit of 0.028 weight percent on the rock's zircon content. In many granitic rocks the abundance of monazite is limited by the quantity of cerium, but in Lawler Peak Granite #1 a greater constraint appears to be imposed by the concentrations of neodymium and lanthanum. Monazite cannot exceed 0.029 weight percent of the granite. The abundance of xenotime is limited by the concentration of yttrium. Xenotime cannot exceed 0.016 weight percent of the rock. An upper limit on the abundance of brannerite? (plus coffinite?) is imposed by the whole-rock uranium. Brannerite? cannot exceed 0.006 weight percent of the rock. A more realistic limit however is obtained by correcting for that uranium that is known to be present in many minerals and sites other than brannerite?. In this case the brannerite? abundance limit is reduced to 0.0045 weight percent. The situation is similar in the case of thorite. If all the thorium in the rock were in thorite, thorite abundance would be limited to 0.0069 weight percent. Considering the large thorium content of monazite alone, the limit on thorite is probably closer to 0.003 weight percent. Apatite is limited by the amount of phosphorous available and cannot exceed 0.2 weight percent of the rock.

The extent to which these upper limits approximate the actual abundances of the respective mineral species in the granite depends on the correct assessment being made of the distribution of the various key elements between the minerals in question and other significant sites. The calculated limits and actual abundances would coincide only when the enormous task of identifying all sites, mineralogical and non-mineralogical, for each of the appropriate

TABLE 20

Possible order-of-magnitude contributions of various minerals and sites to the Lawler Peak Granite #1 uranium-thorium-radiogenic lead balance

Mineral	Estimated Abundance (wt %)	Observed Concentration (ppm)			Possible contribution to whole rock (ppm)				
		Pb^{rad}	U	Th	$^{206}Pb^{rad}$	$^{207}Pb^{rad}$	$^{208}Pb^{rad}$	U	Th
Whole Rock		8.00	20.89	26.72	5.74	0.53	1.73	20.89	26.72
Quartz-feldspar	91.9[1]	0.28	0.56	1.95	0.19	0.02	0.05	0.51	1.79
Muscovite	4.1[1]	4.22	4.56	18.82	0.10	0.01	0.06	0.19	0.77
Biotite-chlorite	2.6[1]	30.48	20.61	35.39	0.60	0.05	0.13	0.54	0.92
Magnetite	0.4[2]	78.24	26.03	72.23	0.23	0.02	0.06	0.10	0.29
Epidote	0.36[1]	35.59	80.90	24.43	0.09	0.01	0.03	0.29	0.09
Opaques concentrate	0.2[2]	249.7	1374	1303	0.36	0.03	0.11	2.75	2.61
Apatite	0.09[1]	21.43	25.99	105.3	0.01	0.00	0.01	0.02	0.09
Monazite	0.029[3]	2200[5]	2000[5]	55,000[5]	0.08	0.01	0.55	0.58	15.95
Zircon	0.028[3]	300[5]	2500[5]	400[5]	0.07	0.01	0.01	0.70	0.11
Xenotime	0.016[3]	2018	9066	9286	0.26	0.02	0.04	1.45	1.49
Bismutite	0.01[4]	32,070	3313	14.71	2.48	0.23	0.49	0.33	0.00
Brannerite? & Coffinite?	0.0045[3]	15,000[5]	250,000[5]	25,000[5]	0.59	0.05	0.04	11.25	1.13

[1] Estimate from point count mode

[2] Estimate from high-density mineral recovery

[3] Abundance limit calculated from whole rock chemical composition (see text)

[4] Arbitrary quantity chosen to provide an approximate radiogenic lead balance

[5] Estimated average values

elements had been undertaken; a task beyond the scope of the present work. A calculation of even crude mineral abundance limits is important however when an attempt is made to assess the relative importance of each mineral as a repository for radioactive and radiogenic elements.

Mineral and Non-mineral Contributions to the Whole-Rock Uranium-Thorium-Radiogenic Lead

To determine the contribution of each mineral and non-mineral site to the whole-rock uranium-thorium-radiogenic lead balance is an almost impossible task, requiring first a comprehensive knowledge of the uranium, thorium and radiogenic lead content of every significant site and secondly an accurate quanitative estimate of the volume of that site in the rock. Neither set of data is complete for Lawler Peak Granite #1, but through the present study more information has been gathered on the distribution of radioactive and radiogenic elements in a granite than, to the authors' knowledge, has been available before. An order of magnitude calculation of site contributions therefore has been attempted and is listed in Table 20.

One of the most significant features of the data in the tables is the large fraction of the total radiogenic lead which appears to be located in minerals and sites not normally considered to be radioactive and hosts for such leads. They may instead contain a large labile component, quartz-feldspar, biotite-chlorite, magnetite, the weakly ferromagnetic opaques concentrate and bismutite for example. If the limiting calculations approach the actual case, they imply approximately 65 percent of the radiogenic lead to be, or have been labile. This conclusion rests in large part on the assumed abundance of bismutite of 0.01 weight percent, a value which may well be a significant overestimate. An analysis of the whole rock for bismuth is planned and when available will permit this estimate to be refined considerably.

It should also be noted that our initial selection and preparation of a quartz-feldspar concentrate may have been too "pure". We may well have minimized the concentration of labile lead calculated to be associated with many major mineral grains that in fact have surface stains. To answer this question we have prepared a "stained" fraction of feldspar, still quite pure, for comparison of leachable components.

A second feature of the data is the dominance of monazite as a thorium site. This dominance will be somewhat overestimated because the role of thorite has not been isolated. Together, thorite and monazite clearly are the most important sites for thorium in the rock.

It appears that the dominant uranium site in the rock is brannerite?, and, perhaps, the other much more rare stoichiometric uranium mineral, coffinite?. All other known sites combined can account for only approximately 34 percent of the rock's uranium. Commonly recognized accessory minerals such as zircon, monazite, xenotime and apatite account for a very small proportion of the uranium indeed.

Despite its obvious flaws, a rationalization of various site contributions such as has been undertaken here is of considerable importance to the understanding of mobilization of radioactive and radiogenic elements within the

granite. It would appear that the greater fraction of these elements is located within relatively few sites, and that for radiogenic lead, labile components may dominate. They appear significant for uranium and thorium as well. Understanding the geochemical stability of each type of mineral and surface site is crucial to understanding element mobilization in the rock under different natural and man-induced conditions.

URANIUM AND THORIUM DISTRIBUTION DURING PRIMARY CRYSTALLIZATION OF THE LAWLER PEAK GRANITE

Introduction

Some central observations about this uraniferous granite sample are that it contains a large number of radioactive phases; that uranium and thorium concentrations in the major, minor and trace mineral species range over seven orders of magnitude; and that three mineral species contain up to 50 percent uranium or thorium. The petrological processes responsible for these distinctive characteristics deserve close consideration.

Although fifteen phases were observed to possess higher radioactivity levels than the whole rock, only eight, or possibly ten, are inferred to result from primary igneous crystallization. The others owe their above-average radioactivity levels to secondary mineral-forming processes (hydrothermal events) or to secondary redistribution of uranium and thorium into non-crystallographic sites (surfaces, grain boundaries) during hydrothermal events or, perhaps, during supergene processes.

We interpret zircon, monazite, xenotime, apatite, thorite, brannerite? and coffinite? to have crystallized from the melt. We believe some sphene in the intergrowths with ilmenite may represent late magmatic reaction products. Possibly some epidote and allanite formed in the volatile-rich last stages of high-temperature near-solidus processes. On the other hand, several types of evidence suggest that bismutite-bismuthinite, additional epidote, and possibly allanite and apatite may be products of much younger hydrothermal reactions. This secondary paragenesis will be discussed in a later section.

The finding of many co-existing primary radioactive accessory minerals in one granite is a very significant one, but we believe that in this respect the Lawler Peak Granite is not unique. Our studies have emphasized that where the abundance of many minerals is at levels of 1-100 ppm, large samples and intensive examination are required to establish the diversity and identity of the phases present. The work on large samples of the other three granites reported here has shown thorite, for example, to be ubiquitous, and other exotic phases probably to be present.

Particular significance is attached to the demonstrated existence of rare mineral phases with stoichiometric uranium and thorium which appear to contain large to possibly dominant fractions of these elements in the total rock. This demonstration has unexpected implications for the behavior of U and Th during primary granitic crystallization. Comparably significant is the conclusion that large fractions of the U and Th subsequently have been labile.

The Associations of Radioactive Minerals and Primary Iron-rich Oxides

In the course of several different facets of the present study, an impression of a close spatial association of the radioactive minerals with the major primary iron-rich oxides, magnetite and ilmenite, developed. It developed as a result of thin-section petrography, detailed EMP studies, and the observation that in the mineral separates, a large fraction of the total radioactivity measured (~45 percent) was associated with separates of the ferromagnetic minerals (handmagnetics) and of crush-resistant, heterogeneous aggregates with smaller proportions of the iron-rich oxides (the concentrate of high-density, weakly-ferromagnetic opaque minerals, Tables 18,19; Figures 80,83,84). Illustrations of this close association between opaque and radioactive minerals can be found throughout the report, but special attention is called to Figures 24,25,56,65,77,78 and 79).

As an example, the systematic survey of the host mineral association for zircons in the rock (Table 17) showed that more than 10 percent of the observed zircons occur in direct contact with opaque phases, which represent only 0.4 volume percent of the rock. We estimate from the survey that another 30 to 40 percent of the zircons are grouped in the near vicinity (within 1 mm) of opaque grains.

We tentatively interpret the minute local volumes marked by such associations to represent the sites of late-crystallizing melt fractions, enriched in iron and the incompatible elements. Although the volumes are not distinguished by discontinuities in texture, miarolitic cavities or other obvious structural manifestations, we are encouraged to investigate further the chemical character of all minerals which occur in intimate textural association with aggregates of iron-rich opaque phases. This should test whether, indeed, we have established valid visual criteria for the identification of late-crystallizing elements of melt in a fractionating granitic magma. Validation would have profound implications for the study of the paragenesis of uranium and thorium and the other incompatible elements in granite.

Fractional Crystallization Considerations

It has been well established that during primary granite crystallization, the major phases (quartz and feldspar) accept comparatively little U and Th. In the Lawler Peak Granite, distribution coefficients for U and Th for these phases appear to be $K_D \ll 1$. For biotite and muscovite, it can be seen in Table 18b that the U and Th distribution coefficients are also no greater than, and probably considerably less than, one. The progressive crystallization of these principal mineral phases, constituting about 98 percent of the rock mass, therefore occurred to the exclusion of U and Th, and resulted in those elements' progressive concentration in the residual melt fractions.

The remarkably consistent euhedral to subhedral crystal forms of essentially all the primary radioactive mineral grains suggests to us that most of those grains nucleated and grew well above the granite solidus. In some species, zircon for example, the progressively more radioactive euhedral zonation towards the exterior of most crystals suggests growth throughout a major portion of the history of the fractionally crystallizing melt, with little or no continuing equilibration. Such a fractionating growth history, of course, precludes the calculation of true K_D values for zircon.

We believe other early-crystallizing radioactive phases may have tended to equilibrate with changing melt compositions more extensively than the zircon, (for example monazite and xenotime). Even so, none of those phases is now notably homogeneous for uranium and thorium, as has been documented in the EMP scan photographs. Even allowing for some post-crystallization redistribution of uranium or thorium, we conclude that distribution of the actinide elements among phases in the Lawler Peak Granite departed widely from equilibrium and that a model for the actinide distribution mechanisms can only be built about complex kinetic considerations and in a qualitative sense. It is in this context that we have not attempted to calculate U and Th distribution coefficients.

The Lawler Peak Granite contains several well-known radioactive accessory minerals (zircon, monazite and xenotime) at abundance levels greater than 100 ppm. These phases usually are suggested to be the principal sites for U and Th in various types of common granites. The observed upper levels of uranium and thorium in these minerals in our sample appear to be about as high as any concentrations observed in these species in other granites. We infer that well before the granite was completely crystallized, these phases (containing common diadochic sites accepting U and Th) with their abundances controlled by available zirconium, cerium and yttrium, attained their maximum limited solid solutions with U and Th. Nevertheless, they were insufficient in abundance to prevent saturation of the residual melt in uranium and thorium. An inevitable consequence was the direct precipitation of stoichiometric uranium and thorium phases such as brannerite?, coffinite? and thorite. Even those phases are not chemically uniform and individually reflect the changing chemistries, both generally and locally, in the final residual melts in which perhaps all eight primary radioactive phases were crystallizing simultaneously and, commonly, in close mutual proximity (Figs. 65,66).

Some Implications of the Presence of Stoichiometric Uranium and Thorium Minerals

Limiting chemical calculations (Table 20) have suggested that upper limits on the abundances of brannerite? + coffinite? and of thorite are probably 45 and 30 ppm respectively. Even if the actual abundances are half those values, these minerals remain among the most significant sites for U and Th in the granite. The post-crystallization geochemical behavior of U and Th in the bulk granite must have been proportionately influenced by the responses of these rarely recognized (and little understood) phases in the changing geochemical and geological environments to which the granite was exposed.

Despite the indicated uncertainties in the present abundances of brannerite?, coffinite? and thorite, it can be argued that much of the uranium and thorium now assigned to major and minor minerals is labile, located on surficial sites, and was probably derived from the more rare phases during two or more important secondary geochemical episodes which previously affected the granite. With the exception of the contents of zircon, monazite, xenotime and apatite it appears that most of the rest of the observed uranium (~85 percent of the total) and thorium (~35 percent of the total) is contained in, or was ultimately derived from three of the rarest phases in the rock. Therefore, primary distribution patterns for uranium and thorium in the Lawler Peak Granite have been modified significantly by the apparent responses to alteration of these unusual minerals.

URANIUM, THORIUM AND RADIOGENIC LEAD RESPONSES TO POST-CRYSTALLIZATION PROCESSES

Introduction

In the analysis of the post-crystallization history of the Lawler Peak Granite, the observed isotopic relations between the parent actinides and their stable radiogenic lead daughters in various sites provide valuable site-specific information. The interaction between radiogenic lead isotopes (generated after crystallization) and initial lead isotopes (reflecting the original igneous lead endowment of the granite) has supplied useful total-reservoir as well as site-characteristic information.

In the elapsed 1411 ± 3 million years since the crystallization of the granite there has been an apparent 30-35 percent increase in the whole-rock lead content over its original value (~25 ppm) as a consequence of the decay of the actinides. The uranogenic leads have been especially augmented (reflecting the low Th/U ratio in the rock), providing large isotopic contributions to the lead systems and, as a consequence, permitting great analytical sensitivity to the variations within them. In our analysis of post-crystallization processes and their products therefore, the information on the concentrations of U and Th in various sites can be supplemented with data on radiogenic lead abundances; $^{206}Pb/^{204}Pb$ ratios (reflecting the ratios of uranogenic to initial lead); $^{206}Pb/^{208}Pb$ ratios (reflecting the ratio of uranogenic to thorogenic lead); and $^{207}Pb/^{206}Pb$ ratios (reflecting the time intervals affecting the Pb-U systems).

It is an essential premise of the interpretation of the U-Th-Pb isotope systems introduced earlier that the differences in chemical response among the three elements determine all fractionations among the related systems. The differences in lead isotopic abundances reflect the chemical fractionations of U, Th and Pb and the physical and chemical mixings of leads over the geological history of the sample, not some process of isotopic fractionation.

We have observed in the earlier detailed discussions of the isotopic analyses that, for its inferred age, the whole-rock sample is markedly out of balance for the Pb-U isotope systems and in close balance for the Th-Pb isotope systems (Tables 18a,19a). We also observed that all identified radioactive mineral systems are out of balance for both Pb-U and Pb-Th isotope systems (see Figure 80 and Tables 19a,b). This applies especially to the most radioactive phases: brannerite?, thorite and coffinite?. Among the primary radioactive minerals, there are notable deficiencies (to more than 95 percent) of lead relative to both uranium and thorium. On the other hand, in the weakly and poorly radioactive phases there are many instances of notable excesses (to several hundred percent) of uranogenic or thorogenic leads, or both, relative to the low levels of radioactive parent isotopes (see Figure 81 and Tables 19b,c).

Leaching experiments on a number of the major and minor minerals using moderately strong acid showed that significant fractions of radiogenic lead and uranium and thorium can be removed from mineral fracture and cleavage surfaces without major attack on the mineral substrates (Table 18c). This leads to the inference that significant quantities of all three elements have been redistributed from various primary igneous mineral sites to several other types of sites within the bulk rock.

The apparent net effect of the widespread mineral open-system behavior on the bulk-rock system already has been noted. Special emphasis is directed toward the contrast between the imbalance in the uranogenic system, suggestive of net uranium loss, and the apparent balance in the thorogenic system. This divergent behavior was observed earlier for the whole-rock sample of the 1440 m.y. old Ruin Granite (Table 5). Even for the much less discordant 1400 m.y. Dells Granite, ^{208}Pb-^{232}Th is the most nearly in balance of all the whole-rock daughter-parent systems (Table 7). An explanation of the processes leading to these consistent differences bears directly on the long-term comparative stabilities of uranium and thorium in granites. It is particularly problematic given that, as previously noted, it appears that almost all mineral phases have been open systems for U-Th-Pb.

Discrepancies between Observed Th/U and Radiogenic $^{208}Pb/^{206}Pb$ Ratios

The general open-system behavior of thorium-uranium-lead is clearly indicated in Figure 82. When one calculates the Th/U ratio implied by the observed radiogenic $^{208}Pb/^{206}Pb$ ratios in each phase for which data are available and plots it against the observed Th/U ratio, the discrepancies are manifest. With uncertainties for each parameter being no more than 2 percent, only zircon plots precisely on the line of exact correspondence. Monazite is about 15 percent discrepant; all other phases and the whole rock are twenty-five to several hundred percent away from consistency. Notably, the brannerite? concentrates depart from agreement by factors of three or four. Lack of isotopic data precludes plotting coffinite? and thorite.

Excepting the monazite, the dispersion of the points suggests a much greater range of observed Th/U than the range of Th/U calculated from the lead isotopic ratios. This latter limited range has its focus close to a calculated value of Th/U = 0.85. The several leached leads yield calculated Th/U in the range 0.7 to 1.0. It would appear that labile leads may make significant contributions to the bulk leads of many of the mineral concentrates, leading to the convergence in calculated Th/U ratios.

In a positive sense, this analysis supports a major thesis of these investigations, i.e. in rocks which have suffered various types of alteration histories, zircon seems consistently to reflect the original mineral, and therefore, the original whole-rock endowment of thorium and uranium. This is especially relevant when considering the regional uranium basement anomaly defined by the high-uranium zircons in Precambrian granites of the Colorado Plateau, of which the Lawler Peak Granite is a component.

For those mineral species which show significant departures from a direct correspondence between calculated and observed Th/U ratios, it is not possible to argue from this diagram whether Th, U or Pb have moved into or out of each system. As noted earlier, small percentages of thorite contained as inclusions in monazite and xenotime could explain their discrepancies. A geologically recent loss of 24 percent of the original whole-rock uranium content (also postulated earlier) would remove the whole-rock Th/U discrepancy. For the other phases, the discrepancies are so large as to indicate either extensive exchanges of lead with reservoirs of very different isotopic composition, or major changes in their thorium and/or uranium concentrations. We will argue that in some species probably all of these modifications have occurred.

Timing of Isotopic Disturbances

Before pursuing the nature of the chemical changes, it is necessary to reaffirm that the Concordia diagrams of Figures 80 and 81 clearly demonstrate that the open system events are not random in time. In Figure 80, it can be seen that the normally discordant radioactive minerals form two populations. Both populations formed at 1411 m.y.; one subpopulation, the zircon suite, can be modelled as reflecting an open-system event at 228 ± 4 m.y.; the other subpopulation (brannerite?, xenotime and monazite) apparently is dominated by an open-system disturbance at 76 ± 2 m.y.

In Figure 81, the reverse discordant phases, epidote and the two types of apatite, seem to have shared the 228 ± 4 m.y. event recorded in the zircon. Bismutite cannot be plotted on Figure 81 because of its extreme reverse discordance. Assuming its radiogenic lead component began accumulating 1411 m.y. ago, the data would yield a lower intersection at a little over 100 m.y. This may result from bismutite incorporating lead from a mixture of sources during the 75 m.y. event, some of which may have been isolated in the earlier event. Most of the other systems (biotite-chlorite, muscovite and the magnetite), within analytical error, appear to represent younger open-system effects from 76 m.y. to more recently.

The same two events are represented more clearly perhaps in Figure 83. Utilizing the same data as employed in the Concordia diagram (Tables 18 and 19), the observed radiogenic ratio $^{207}Pb/^{206}Pb$ is plotted against the atom percent radiogenic ^{206}Pb for the lead in each phase (where $^{206}Pb^{rad} + ^{208}Pb^{rad} \equiv 1$). Shown as dotted open circles, these points are compared with three reference lines of fixed radiogenic $^{207}Pb/^{206}Pb$ ratios. The lowest ratio, 0.0893, represents uranogenic leads generated in a 1411 m.y. old system closed up to the present time. The second ratio, 0.0912, represents uranogenic leads in the 1411 m.y. old system 75 m.y. ago. The third ratio, 0.0958, represents uranogenic leads in the 1411 m.y. old system 230 m.y. ago. For each phase or site in Tables 18 and 19 for which complete data are available, the observed radiogenic leads have been recalculated to the values of $^{207}Pb/^{206}Pb$ they would have had 75 and 230 m.y. ago, assuming the observed uranium and thorium has contributed an immobile increment of radiogenic lead for the subsequent period.

Those observed isotopic systems which, when corrected for the 75 m.y. interval, fall closely on the corresponding 75 m.y. line are represented by the filled symbols. Similarly, those systems which, when corrected for 230 m.y., fall on or close to the 230 m.y. line are also represented by filled symbols.

It can be seen that monazite, xenotime, brannerite?, magnetite and the opaques concentrate show a much better correlation after correction to 75 m.y. ago. Zircon, epidote and the two apatite fractions correlate most closely after correction to 230 m.y. ago, suggesting their major sensitivity to an episode at that time. Bismutite seems to have formed close to or at the 75 m.y. episode, while incorporating some leads isolated earlier. Muscovite, biotite-chlorite and the two different types of leaches are not as definitive but seem to correspond most closely to a 75 m.y. or younger event. The uncertainties from the initial lead corrections for these phases are large enough to blur this tentative assignment. Similarly the large corrections necessary to calculate radiogenic $^{207}Pb/^{206}Pb$ for the whole-rock system preclude a unique interpretation in this case.

Figure 83

A plot of radiogenic $^{207}Pb/^{206}Pb$ vs. atom fraction radiogenic ^{206}Pb ($^{206}Pb^{rad} + {}^{208}Pb^{rad} \equiv 1$) for isotopic analyses of the whole rock, minerals and leaches from Lawler Peak Granite #1. The analyzed values are plotted showing uncertainties in $^{207}Pb/^{206}Pb$ as vertical bars. The effects of removing the last 75 m.y. and 230 m.y. of decay product accumulation, assuming the presently observed Th and U contents of each system for the appropriate period of time, are shown as triangles (apex up for 75 m.y., apex down for 230 m.y.). Lines have been drawn to show the radiogenic $^{207}Pb/^{206}Pb$ ratio of a 1411 m.y. old closed isotopic system 230 m.y. ago (0.0958), 75 m.y. ago (0.0912) and at the present day (0.0893). Those isotopic systems which, when appropriately age corrected, fall closely to the corresponding 230 m.y. or 75 m.y. line are shown as filled symbols. (They also, of necessity, fall closely to the corresponding 1411 m.y.-230 m.y. or 1411 m.y.-75 m.y. chord on the lead-uranium Concordia diagram). The age corrections do not appear to induce convergence in atom fraction radiogenic ^{206}Pb values.

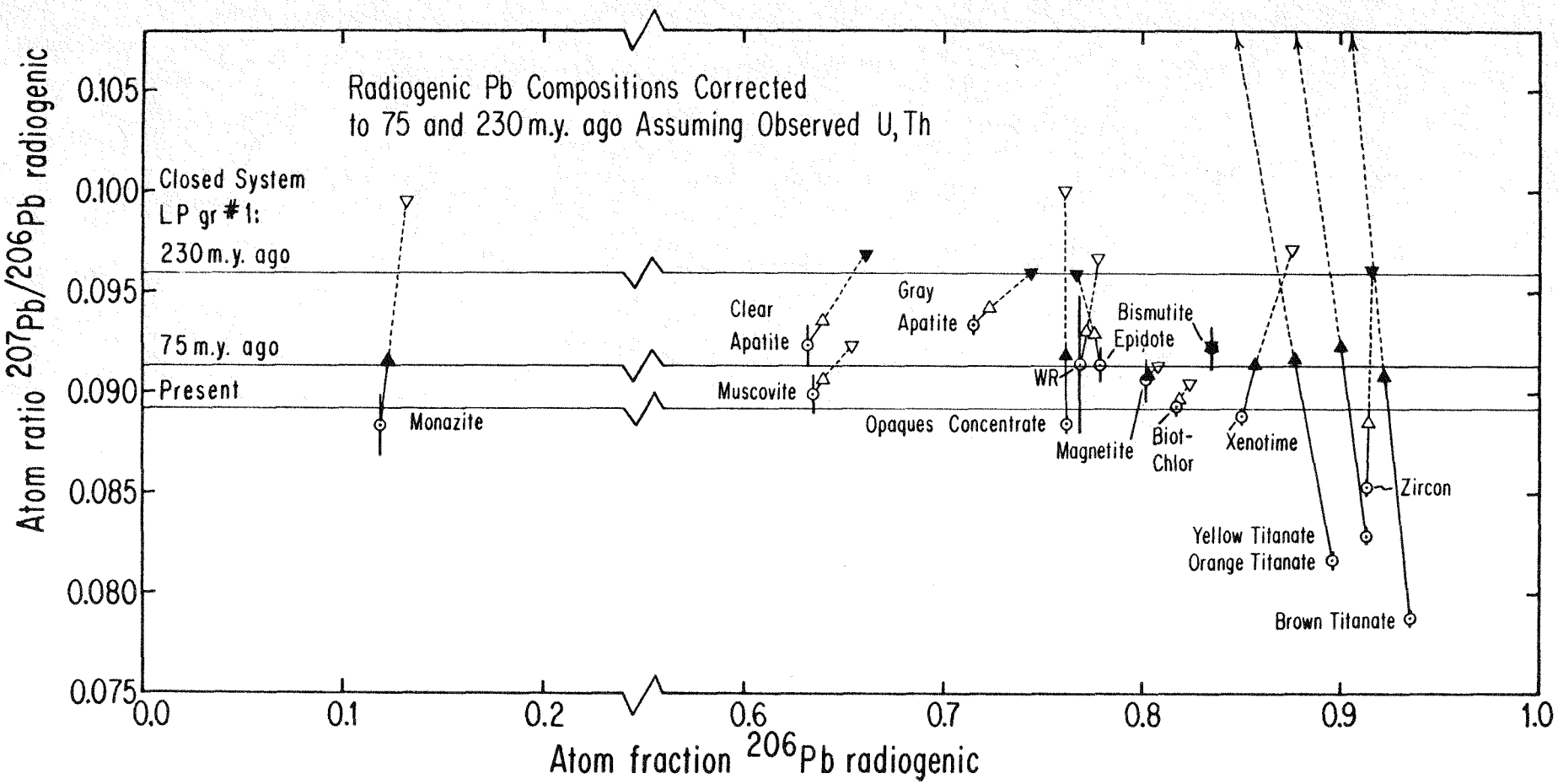
Radiogenic Pb Compositions Corrected
to 75 and 230 m.y. ago Assuming Observed U, Th
Closed System
LP gr #1:
230 m.y. ago
75 m.y. ago
Present
Monazite
Clear
Apatite
Muscovite
Gray
Apatite
Opaques Concentrate
WR
Magnetite
Bismutite
Epidote
Biot-
Chlor
Xenotime
Yellow Titanate
Orange Titanate
Zircon
Brown Titanate
0.105
0.100
0.095
0.090
0.085
0.080
0.075
0.0
0.1
0.2
0.6
0.7
0.8
0.9
1.0
Atom ratio $^{207}Pb/^{206}Pb$ radiogenic
Atom fraction ^{206}Pb radiogenic

Figure 83

These two presentations argue that in a temporal sense the major isotopic disturbances affecting the radioactive minerals in the Lawler Peak Granite occurred at about 230 and 75 m.y. ago, with some lesser suggestion of a more recent disturbance.

There is a lack of any stratigraphic information about the Early Triassic geological history in the immediate Bagdad area. The southern Colorado Plateau and adjacent Basin and Range Province was undergoing a major change in sedimentation patterns at the time. The Middle Permian Kaibab marine shelf environment had been disrupted. The Kaibab Formation was uplifted, eroded and covered unconformably by a thin section of continental sedimentary strata, the Moenkopi Formation, of Early to Middle Triassic age.

No distinct Early Triassic thermal episode has been recognized independently in the northern Arizona region. However, Early Triassic magmatism is well documented in southeastern California. The principal investigator (1966, and unpublished data) has observed similar temporal indications of apparent Early Triassic thermal disturbances in a number of Precambrian granitic zircon isotope systems throughout Yavapai County. Additional investigations in progress in our laboratory may shed further light on this shadowy event.

The 75 m.y. episode has a better identified independent manifestation in the immediate vicinity of the Lawler Peak Granite. Several stock-like masses of Tertiary-Cretaceous? quartz monzonite, quartz monzonite porphyry and diorite porphyry intrude the Precambrian section at Bagdad, including the southeastern perimeter of the Lawler Peak Granite (Anderson et al., 1955). The intensely mineralized Bagdad Porphyry Copper deposit is located in one of the quartz monzonite masses, 2 miles (3 km) south-southwest of the Lawler Peak Granite #1 sample locality. Published ^{40}K-^{40}Ar age measurements on biotite from the unaltered and the mineralized phases of the Bagdad Quartz Monzonite have yielded ages in the range 71-73 m.y. (e.g. Livingston et al., 1968). Similar ages are reported for other plutons in west-central Arizona. We are currently investigating the zircon U-Pb systems in a sample of slightly mineralized Bagdad Quartz Monzonite to obtain additional geochronological information. The existing data however, clearly support the occurrence of a significant thermal and hydrothermal episode in the appropriate time frame for the second disturbance apparent in the U-Pb isotope systematics of the Lawler Peak Granite #1 sample.

The possibility of still younger disturbance episodes related to the unroofing, weathering and volcanic episodes in the Cenozoic history of the Bagdad region also exists. Suggestions detected in some parts of our assemblage for such younger events can be rationalized but not independently verified.

In summary, the orderly separation of the daughter-parent isotope systematics of all the analyzed primary radioactive minerals into two distinct subpopulations is taken to reflect two distinct geological episodes in which significant geochemical disturbances are recorded. The more recent episode at 75 m.y. ago seems to be related to a prominent local and regional thermal and hydrothermal perturbation. The older episode, while more obscure in the geological record, seems fully as profound in its effect on the rock assemblage and is also taken to be a hydrothermal event.

Chemical Mobility of Lead, Uranium and Thorium

Mobile Lead Systems

Various types of evidence have been brought forward earlier which indicate a history of lead migration in the Lawler Peak Granite #1 sample:

1) All primary radioactive minerals appear to have lost some lead with respect to the observed U and Th. This seems to have taken place pricipally in two distinct episodes in the Early and Late Mesozoic.

2) Major minerals such as quartz and feldspar and the micas, and some minor minerals such as magnetite, all of which are non-radioactive, are marked by the presence of radiogenic leads which cannot be solely the products of the observed uranium and thorium (or Th/U ratios) in those minerals.

3) The minerals described in (2) respond to moderate acid leaching by readily yielding major fractions of their total radiogenic leads, while undergoing minor to negligible chemical dissolution.

4) Electron microprobe scan photographs have revealed unusual localized lead concentrations in Fe-rich haloes exterior to brannerite? (Fig. 64i), monazite (Fig. 57j) and xenotime (Fig. 54h), suggesting local fixation of lead which may be predominantly local-radiogenic in the immediate vicinity of the now lead-deficient radioactive minerals. Similar effects have been noted around thorite and coffinite? but have not been illustrated here.

5) Bismutite has been documented (Table 18a) to contain remarkable concentrations of radiogenic lead (3.2 percent) which cannot have been generated from its contained uranium and thorium. Since the bismutite commonly is localized around cores of bismuthinite with even higher lead concentrations and lower U and Th levels (Fig. 73d), it is inferred that both bismuth minerals contain radiogenic leads ultimately derived from radioactive sites elsewhere.

6) An epidote concentrate, selected to represent epidote replacing plagioclase, contains excessive quantities of lead with an isotopic composition that cannot have been produced by the present absolute and relative abundances of Th and U. Although the discordance effects are not so dramatic as for the bismutite, it is difficult to avoid the conclusion that the lead is exogenous. The lead is quite common; the radiogenic $^{208}Pb/^{206}Pb$ ratio implies evolution in a system very similar in Th/U to that of the whole rock; the radiogenic $^{207}Pb/^{206}Pb$ is similar to that which probably characterized the whole rock 230 m.y. ago. A plausible explanation for the epidote data is that epidote replaced plagioclase in a hydrothermal episode 230 m.y. ago, incorporating leads of composite common and radiogenic character available in the bulk rock at that time.

Citation of the several types of evidence for lead lability raises the general question: Which analyzed mineral leads in this sample are indigenous and which are exogenous to each mineral? To examine this question in more detail, the various observed mineral and whole-rock leads are plotted on the graph in Figure 84.

In Figure 84, the observed lead isotopic compositions have been represented by coordinates derived from the following relation: The atom sum of ^{204}Pb + ^{206}Pb + ^{208}Pb is taken as one. ^{207}Pb is neglected here because it is relatively minor and it does not depart from a constant ratio to ^{206}Pb by more than a few percent. The atom fraction of ^{204}Pb is small but it directly reflects the common, or initial, lead component in the sample. It can be measured with sensitivity and it is plotted as the ordinate in Figure 84. The abscissa is the atom fraction of ^{206}Pb. Since ^{204}Pb is generally less than one atom percent of this trio of isotopes, $^{206}Pb \approx 1 - {}^{208}Pb$. Therefore the atom fraction ^{206}Pb is a useful indicator of the abundance of uranogenic lead relative to thorogenic lead. If no ^{204}Pb is present, the lead is completely radiogenic and plots on the abscissa.

Mineral lead isotopic compositions plotted on this diagram represent, by their position, the relative contributions of initial lead and each end-member type of radiogenic lead. Specific examples include:

1) The lead in the alkali feldspar is nearly nonradiogenic. A best value for the corrected nonradiogenic lead composition is considered to be that of the initial lead. It is labelled "K-feldspar" at the top of the graph and represents the most ^{204}Pb-rich component known in the rock.

2) The observed lead for highly radioactive monazite has been generated principally by the decay of thorium (Th/U ~ 28), has very little ^{204}Pb (initial lead) and is ^{206}Pb-poor, ^{208}Pb-rich. It plots closest to the origin on this graph. Thorite, although not analyzed isotopically, has a Th/U ratio similar to that of monazite and probably has a quite similar lead composition. For this discussion it may be included with monazite.

3) The very radioactive zircon population is comparatively uranium-rich, thorium-poor (Th/U ~ 0.3) and ^{204}Pb-poor. It provides the most ^{206}Pb-rich lead compositions encountered, and plots on the lower right side of the graph. Brannerite? and xenotime are somewhat similar in their low Th/U ratios and ^{206}Pb-rich leads.

In Figure 84, the positions of the feldspar, monazite and zircon leads are linked to form a triangle, which includes the positions of all other observed mineral and whole-rock leads. An arbitrarily defined short-dashed line subdivides the triangle into a lower field containing the radiogenic leads of the highly radioactive minerals, and a larger upper field containing the more ^{204}Pb-rich leads of the moderate to low radioactivity minerals.

The character of the whole-rock lead is shown in the upper part of the triangle and is readily classified: it is ~75 percent initial lead (as found in feldspar) and ~25 percent radiogenic lead. Its uranogenic lead (^{206}Pb) is approximately 3 times more abundant than thorogenic lead (^{208}Pb). A long-

Figure 84

A diagram characterizing the lead isotopic composition of minerals and whole rock in the Lawler Peak Granite #1 sample in terms of initial lead, uranogenic lead and thorogenic lead components. The lead isotopes ^{204}Pb, ^{206}Pb and ^{208}Pb are summed equal to one. The calculated atom fraction ^{206}Pb directly reflects the uranogenic lead component. Because ^{204}Pb is very small, $^{206}Pb \approx 1 - {}^{208}Pb$ and is a good indication of the thorogenic component as well. The atom fraction ^{204}Pb, although small, directly reflects the initial lead component in a sample. All samples are limited by the compositions of the feldspar, monazite and zircon leads, which form a triangle. The large triangle is subdivided into two fields: a lower field for the leads in the radioactive accessory minerals with large radiogenic components, and an upper field for less radioactive minerals with smaller components of radiogenic lead. A line from the feldspar (initial) lead through the whole-rock lead to the abscissa defines the ratio of uranogenic to thorogenic leads in the radiogenic leads in the whole rock and reflects the integrated contribution of lead from all sites.

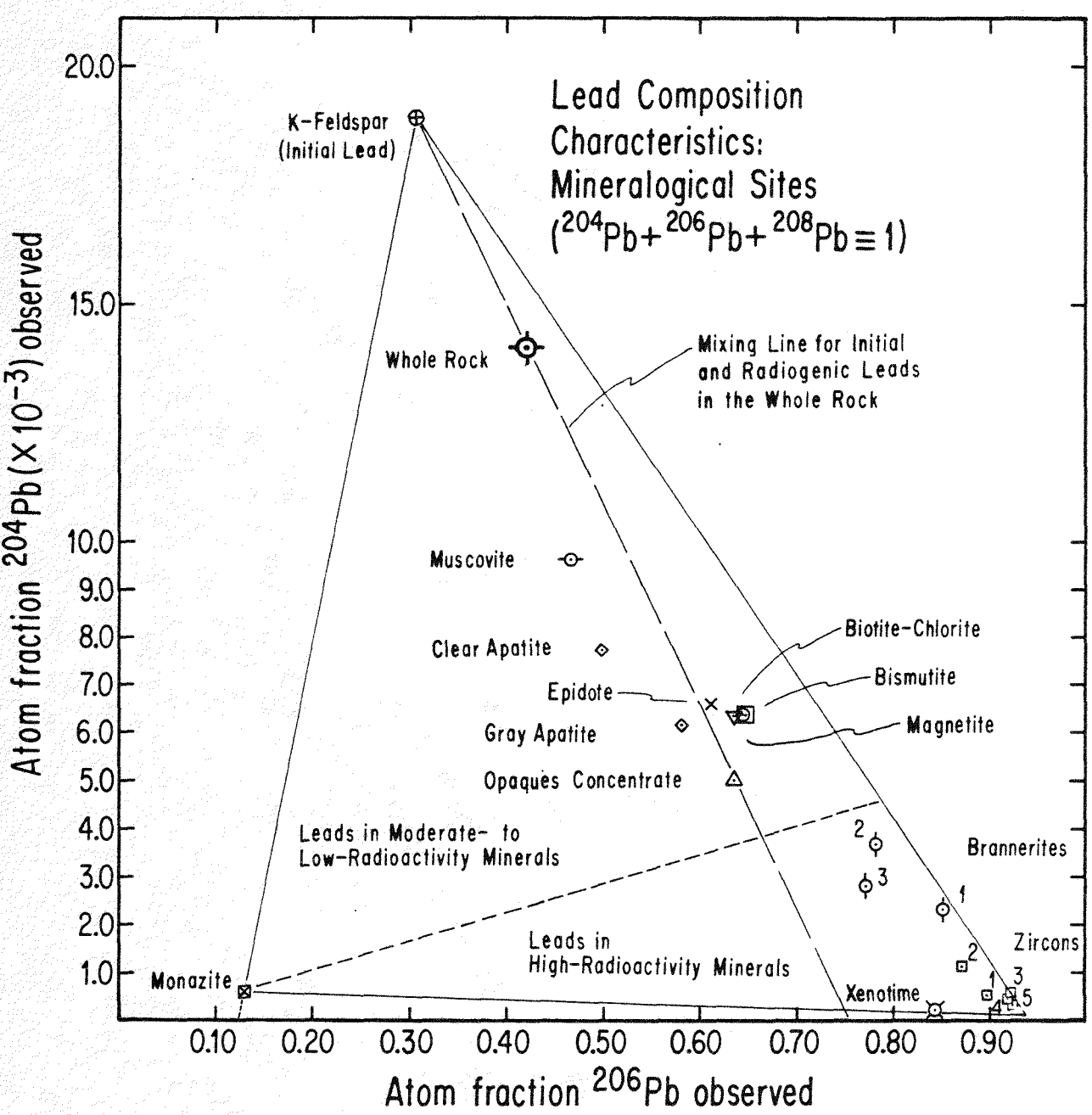
Lead Composition
Characteristics:
Mineralogical Sites
($^{204}Pb+^{206}Pb+^{208}Pb \equiv 1$)
K-Feldspar
(Initial Lead)
Whole Rock
Mixing Line for Initial
and Radiogenic Leads
in the Whole Rock
Muscovite
Clear Apatite
Epidote
Gray Apatite
Opaques Concentrate
Biotite-Chlorite
Bismutite
Magnetite
Leads in Moderate- to
Low-Radioactivity Minerals
Brannerites
Zircons
Leads in
High-Radioactivity Minerals
Monazite
Xenotime
Atom fraction ^{204}Pb ($\times 10^{-3}$) observed
Atom fraction ^{206}Pb observed
20.0
15.0
10.0
9.0
8.0
7.0
6.0
5.0
4.0
3.0
2.0
1.0
0.10
0.20
0.30
0.40
0.50
0.60
0.70
0.80
0.90

Figure 84

dashed line drawn through the whole-rock composition from the initial lead to the abscissa defines the radiogenic ^{206}Pb atom fraction (radiogenic $^{206}Pb/^{208}Pb$ ratio) in the whole rock.

Among the radioactive minerals, the various brannerite? separates occupy the most distinctive positions in the diagram. The atom fraction of ^{204}Pb in the brannerites? is surprisingly high, considering their age, mineralogy and extreme uranium and lead concentrations. It implies initial lead concentrations of 0.1 to 0.3 percent or more in a primary mineral whose crystal structure is expected to exclude large, singly-charged ions. The other analyzed primary radioactive phases, which contain considerably less uranium (zircon, xenotime), are much more radiogenic as expected.

Among the weakly to moderately radioactive minerals, the most prominent relation is a tight cluster of compositions for biotite-chlorite, magnetite and bismutite near which the rest of the leads are loosely grouped. Epidote lead is quite similar to the leads in the cluster. The apatite and muscovite leads, and the composite lead of the complex opaque minerals concentrate are more diverse in composition.

Consideration of the four minerals with nearly identical leads (biotite-chlorite, magnetite, bismutite and epidote) suggests mineralogical contrasts that underline the notable nature of the lead similarity. These minerals, two very different silicates, a transition metal oxide and a metal oxycarbonate differ widely in chemistry, crystal structure and chemical affinity for initial lead. They display, as expected, a great range of U and Th concentrations, and Th/U and $^{238}U/^{204}Pb$ ratios. As noted, the observed leads cannot have been generated by the associated actinides; they are in great excess and imply very different Th/U values. One must conclude that their shared lead compositions may be dominated by lead derived from some single external well-mixed lead reservoir. In as much as the bismutite and epidote have been argued to be clearly secondary, replacing earlier minerals, while the micas and magnetite are primary phases, it would appear that the entire group of leads should be evaluated for possible secondary derivation from one or more labile sources.

The muscovite, the two apatite populations and the opaque minerals concentrate show the diversity in lead composition that one might reasonably expect. They all have larger components of thorogenic lead than is characteristic of the lead in the tight mineral cluster, and their ^{204}Pb components are quite variable.

To examine the distribution and lability of the lead represented by the mineral lead cluster in Figure 84 the several leach experiments were undertaken, directed towards characterizing the soluble surface leads on both major and minor minerals of the rock. In addition to the leaches of the magnetite and biotite-chlorite aggregates, leaches were conducted on a concentrate of alkali-feldspar and quartz, estimated to be more than 0.9999 free of other minerals; on the purified muscovite concentrate; on a second quite pure quartz-feldspar concentrate but one with a distinct yellow cast due to surface staining; and on an aliquot of the complex weakly ferromagnetic opaques concentrate.

The leach data that we consider to be the most significant are those obtained using 1 N nitric acid at 25°C for one hour. In the case of the opaque minerals concentrate, the one hour leach was performed in 15 and 45 minute

increments. Additional leaches were performed for longer times or under more intense conditions, as noted earlier. In this discussion we wish to focus particularly on the soluble leads removed at the beginning of each leaching series.

In Figure 85 the compositions of the leach leads are plotted as open symbols on the base diagram shown in the preceding figure. The mineral leads are shown for comparison as solid points and are labelled only where relevant. The remaining identifications can be made by referring to Figure 84. A tie line in the form of an arrow connects the bulk lead of each mineral to the lead composition of that mineral's leach.

Some remarkable regularities become evident. In the case of the magnetite, the first leach (and the second, more intense leach) is indistinguishable from, and superimposed on, the magnetite point (inverted triangle). Nearly all the lead in the magnetite is leachable and probably surficial. The lead has the same composition as the cluster of mineral leads. The leach of biotite-chlorite is nearly identical to the bulk-mineral lead and plots just above the cluster.

The first-leached lead of the opaques concentrate is quite different from the bulk lead in the concentrate, but is very similar to the clustered mineral leads, plotting just below them.

The first leads leached from the "clean" quartz-feldspar concentrate, the "stained" quartz-feldspar concentrate and the muscovite concentrate are all significantly different from the leads in their respective substrates but are quite similar to each other. The leach leads plot systematically very close to the developing cluster, but fall neither on it nor in a random fashion around it. Instead, the leads of all first leaches generate a short, tight, linear array which includes the cluster and projects towards the feldspar (initial) lead composition.

The convergence of many of the first leach leads with several of the observed mineral leads forms an even more pronounced cluster in Figure 85 and indicates the existence of a significant widespread lead reservoir (consisting of closely related subreservoirs) which we call "Pool" lead(s). We will explore and develop the concept of pool leads further, but at this point they are considered to be labile leads of a remarkably restricted range of compositions (initial + uranogenic + thorogenic) forming a large reservoir (pool) which pervades many of the mineral phases and most of the non-mineralogical surface sites in this sample of granite.

Pool Leads

The composition of pool leads is evident from the tight clusters in Figures 84 and 85 and is so labelled in Figure 85. The prominent short linear array generated by the first leaches in Figure 85 projects precisely toward the initial lead from the pool leads. It can be interpreted geometrically as a mixing line between the pool leads of the tight cluster and initial lead represented by the feldspar lead composition.

Figure 85
A lead composition diagram similar to Figure 84, on which are plotted the compositions of acid-soluble leach leads (open symbols) for comparison with the mineral leads (closed symbols). Arrows form tie lines between mineral concentrate leads and the leads leached from them. A major cluster of leaches and minerals with uniform lead compositions is designated as well-mixed pool leads, which are inferred to be derived from a common, well-mixed labile lead reservoir. Extension of the mixing line of initial lead and pool leads to the abscissa defines the remarkably consistent radiogenic component in the pool leads.

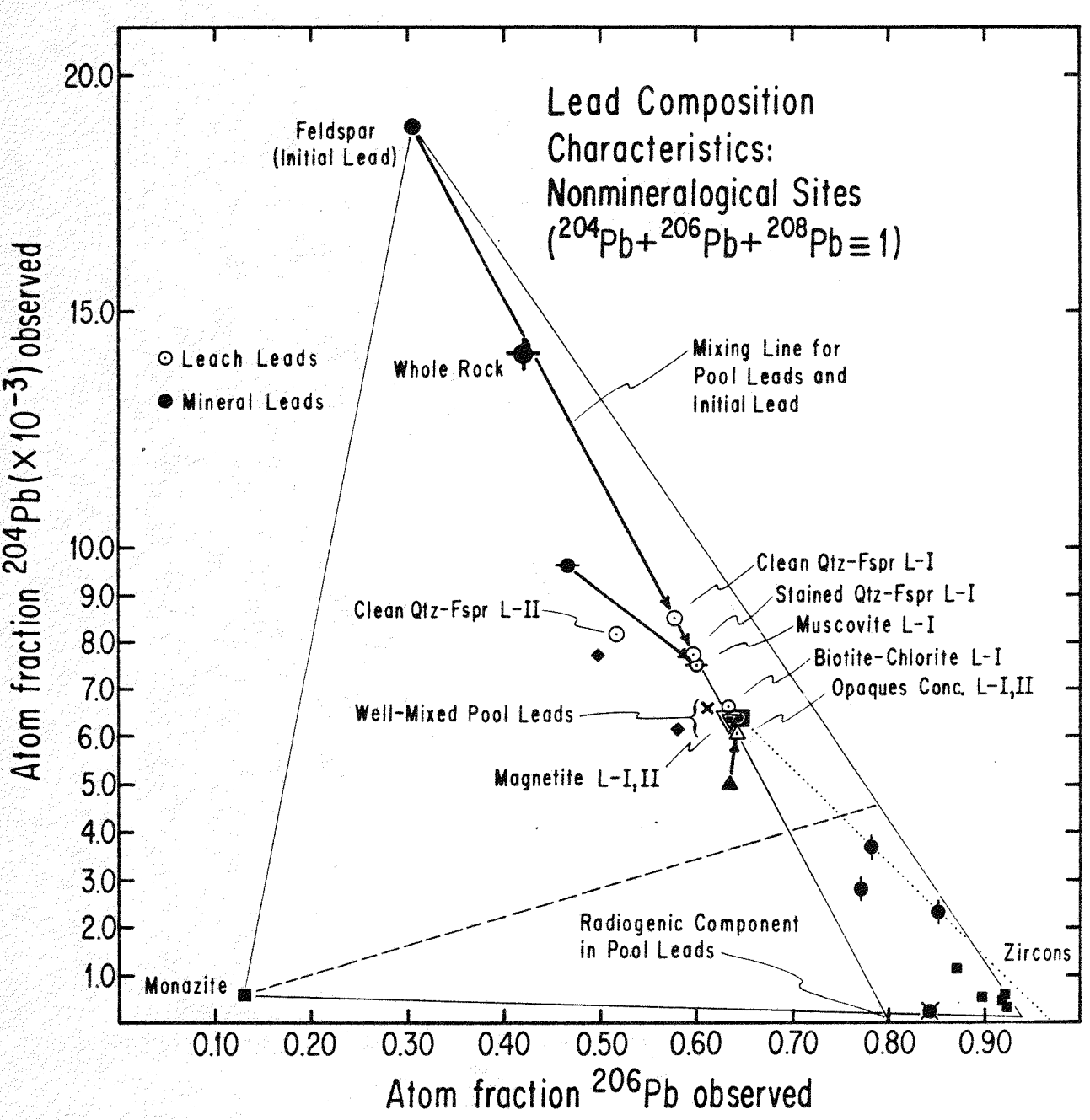
Lead Composition
Characteristics:
Nonmineralogical Sites
($^{204}Pb+^{206}Pb+^{208}Pb \equiv 1$)
Feldspar
(Initial Lead)
Whole Rock
Mixing Line for
Pool Leads and
Initial Lead
⊙ Leach Leads
● Mineral Leads
Clean Qtz-Fspr L-I
Stained Qtz-Fspr L-I
Muscovite L-I
Biotite-Chlorite L-I
Opaques Conc. L-I,II
Clean Qtz-Fspr L-II
Well-Mixed Pool Leads
Magnetite L-I,II
Radiogenic Component
in Pool Leads
Zircons
Monazite
20.0
15.0
10.0
9.0
8.0
7.0
6.0
5.0
4.0
3.0
2.0
1.0
0.10
0.20
0.30
0.40
0.50
0.60
0.70
0.80
0.90
Atom fraction ^{204}Pb ($\times 10^{-3}$) observed
Atom fraction ^{206}Pb observed

Figure 85

The minerals whose surfaces were leached to form the extended array are all potassium minerals (alkali feldspar and micas) with a significant initial lead content. It is possible that the leach acids have attacked the different mineral substrates, extracting different increments of initial lead. Other considerations lead us to infer that this effect is negligible and, instead, that the labile surface lead on these sites is indeed characterized by a larger component of initial lead. For example, the second, hot, concentrated acid attack on the quartz-alkali feldspar mixture removed only half as much lead as the first leach, moved the soluble lead composition to a position far removed from the mixing line, but did not increase the relative abundance of ^{204}Pb. In absolute terms the ^{204}Pb yield was reduced by a factor of two compared to the first leach and represented less than 0.1 percent of the ^{204}Pb in the feldspar. Experiments currently in progress involving weaker acids establish the magnitude of the contribution from the substrate to be very low.

It is important to develop other observational data which bear on the uniformity and variability in what we have called pool leads.

The most unifying element characterizing pool reservoirs is the remarkably constant atom fraction ^{206}Pb (0.805 ± 0.01) represented by all samples referred to as the pool leads. A second parameter that is almost as constant is the radiogenic ratio $^{207}Pb/^{206}Pb$ which averages 0.0903 ± 0.0004 for all leaches. For secondary minerals such as bismutite and epidote which are believed to represent samples of pool leads isolated in earlier events, the values of $^{207}Pb/^{206}Pb$ are appropriately somewhat higher. Examination of the atom percent radiogenic lead compositions in Table 18c, and comparison with the diversity of values for the mineral leads emphasizes the striking consistency of the composition of the labile radiogenic lead component. A third unifying parameter is the limited range of radiogenic to initial lead values, seen in the $^{206}Pb/^{204}Pb$ ratio. Individual mineral values range from less than 17 to more than 3000 but the leach and mineral leads referred to as pool leads form a range between 66 and 106 with a large number in the range 100 ± 8 (equivalent to atom fractions ^{204}Pb of $6.5 \pm 0.5 \cdot 10^{-3}$ in Figure 85).

A comparison of the pool leads with the whole-rock lead composition is informative. The whole-rock lead, of course, is the integration of lead in all the sites we have discussed, a composite mixture of the leads which limit, and are included in, the large triangle in Figures 84 and 85. The atom fraction of ^{206}Pb in the whole rock is 0.768 ± 0.003, slightly but distinguishably lower than the typical pool lead value. The radiogenic $^{207}Pb/^{206}Pb$, at 0.0914 ± 0.003, is the same as pool lead within the uncertainty but notably higher than found in any radioactive mineral (Table 19a). The material balance considerations require the whole-rock system to contain leads richer in ^{207}Pb than are presently found in the radioactive minerals. Pool leads and leads such as are found in bismutite and epidote, must represent large fractions of the radiogenic lead in the total rock.

Utilizing the abundance estimates for the radioactive accessories, their uranium, thorium and lead concentrations, and their radiogenic lead isotopic compositions, it is possible to calculate what fraction of the total radiogenic leads has been retained in the composite radioactive accessory mineral population. The data are organized in Table 20. Only about 25 percent of the total expected radiogenic lead is retained. With uncertainties based upon possible parent loss this number might be as low as 20 percent. Abundance estimates

contribute larger uncertainties but there is little question that about 75 ± 10 percent of the total radiogenic lead produced in the radioactive accessory minerals has moved out of them and into the larger volume of the rock. This provides an obvious important source for the radiogenic component of the pool leads.

The radiogenic $^{208}Pb/^{206}Pb$ ratio of the pool leads is quite uniform. It is intermediate between thorogenic leads from monazite (and thorite) and the uranogenic leads of brannerite? (and coffinite?), xenotime and zircon. The pool lead composition is appropriate for a well-mixed solution integrating the diversity of radioactive sources in the rock. As noted, pool leads are not quite as ^{208}Pb-rich as the whole rock. This can be rationalized by observing in Table 19a and in Figure 80 that monazite, the principal site for ^{208}Pb generation, shows a distinctly higher lead retentivity (about 55 percent) than brannerite?, the principal site for ^{206}Pb generation (retentivity less than 20 percent). It is not surprising, of course, that the lead release characteristics for such different phases are not the same.

Two minerals (bismutite and epidote), sharing the position of the cluster of leached leads in Figure 85, have been interpreted to be secondary minerals because of their textural relations to other minerals, bismuthinite and plagioclase respectively, which they appear to have altered and replaced.

The bismutite, with its extraordinary lead concentration and its radiogenic character, is particularly important to the concept of pool lead. It shares with the various leached leads the precise pool lead parameters (atom fractions of ^{204}Pb and ^{206}Pb), but occurs as discrete grains up to 200 μm in diameter commonly nucleated around Bi_2S_3 grains. It differs in its lead composition from the leach leads in its higher radiogenic $^{207}Pb/^{206}Pb$ ratio, 0.0923. This indicates a distinctly older age or interval of derivation of its lead from the radioactive mineral sources.

From its combination of lead isotope parameters, bismutite appears to be a candidate pool lead isolated from the rock reservoir more than 75 m.y. ago. Its lead seems to have been inherited from bismuthinite, which in turn has concentrated an appropriate mix of initial and radiogenic lead from the rock lead pool reservoir during a period of sulfide fixation. A simple one-step model suggests an age of 104 m.y. An equally plausible model suggests that, if the bismutite or its bismuthinite precursor formed 75 m.y. ago, it incorporated a significant fraction of pool lead isolated still earlier. If the earlier isolation episode was 230 m.y. ago, then this early lead would constitute about 25 percent of the mineral's present lead.

In Table 20, bismutite has been assigned an unusual role of contributing more than 40 percent of the radiogenic lead. This was done so as to achieve an approximate lead balance in the rock. Its actual abundance has been difficult to establish at this point, but it appears to be particularly important to the ^{207}Pb balance in the rock. As represented in the table, it may best be considered to represent itself plus other pool leads in unassigned sites.

At a more subdued level, epidote with a great excess of radiogenic lead over uranium and thorium, also appears to be a secondary mineral which has incorporated an earlier generation of slightly more thorogenic pool lead. The appropriate time appears to be 230 m.y. ago, from the relations shown in

Figures 81 and 83. The composition of the lead is quite incompatible with the very low observed Th/U ratio. The radiogenic ratio $^{207}Pb/^{206}Pb$ is 0.0915, a value higher than any found in the leads yielded by the leaches.

The identification of various types and ages of pool leads, as well as various types of mineral hosts for radiogenic lead and initial lead has suggested the need for a comprehensive diagrammatic flow sheet representing the relationships among the sessile and mobile leads in the Lawler Peak Granite #1 sample. Figure 86 attempts such a representation. Various important lead sites form four sides of a rectangle. At the top are the primary non- to low-radioactivity minerals which constitute the great mass of the rock. They contain the bulk of the initial rock lead endowment. They also contain at moderate to low levels intrinsic uranium and thorium partitioned into them during magmatic crystallization and from which some radiogenic Pb has been formed during the history of the granite. Alteration of these phases would release leads that are primarily ^{204}Pb-rich in character.

At the bottom of the diagram are the primary radioactive minerals, the principal production sites for radiogenic leads. All of the identified radioactive phases appear to have lost significant amounts of daughter leads compared to the observed parent isotope concentrations. They are characterized therefore as Lead Losers.

At least two of these primary accessory minerals have ^{204}Pb levels (common lead contents) that seem to be incompatible with their crystal structures. We have noted this anomaly for brannerite?, for example. Examination of Figure 85 shows that a line (dotted) can be drawn from the pool lead cluster, through two of the three brannerite? compositions, to an intersection with the abscissa at an atom fraction radiogenic ^{206}Pb of 0.97. One brannerite? sample plots some distance to the left of this line. The atom fraction radiogenic ^{206}Pb = 0.97 is of interest because that is the calculated value predicted by the observed Th/U ratio of 0.10 ± 0.01. It can be suggested that two of the observed brannerite? fractions owe their anomalous leads to a mixing of their indigenous radiogenic leads with leads of the pool. The degree of mixing implied can be calculated from Figure 85 to represent 35 to 55 percent additions of pool leads. The residual lead concentrations in the brannerite? are 2 percent or greater. Rather than accepting simple addition of pool leads to a system which apparently has lost 80 percent of its lead, it is inferred that extensive exchange has taken place between the general pool lead reservoir and the leads in various phases within the altered, metamict brannerite?. Exchange processes of more complex character involving more end-members may be required to explain the composition of the third brannerite?, which is marked by a distinctive yellowish outer coating.

Similar exchange processes during a period of open-system behavior may account for the comparatively high ^{204}Pb content of the two different types of apatite and the incompatibility of the apatite $^{208}Pb/^{206}Pb$ ratios with its observed Th/U values. The strong reverse discordance of the Pb-U system is in striking contrast to the normal discordance of the Pb-Th system. If indigenous, more thorogenic leads, have been partially exchanged with the more uranogenic pool leads, the discordance patterns can be explained. If such exchange has occurred, the isotope systematics would suggest it took place 230 m.y. ago.

Figure 86
A diagram illustrating major categories of lead sites in the Lawler Peak Granite #1 sample and their interactive relations with labile leads, including well-mixed pool leads, during the geologic history of the sample.

MAJOR CATEGORIES OF Pb SITES, LAWLER PEAK GRANITE #1
PRIMARY LOW-RADIOACTIVITY MINERALS
Pb SITES EXTERNAL TO SAMPLE
(REST OF PLUTON ?)
PRIMARY COMMON Pb SITES
FELDSPARS, MICAS
Pb^RAD FROM INTRINSIC LOW-LEVEL U & Th IN MANY MINERALS
Pb^RAD INCREMENTS PRODUCED IN POOL SITES FROM POOL U & Th
FE-RICH FIXATION SITES FOR Pb
FE-RICH HALOES AROUND RADIOACTIVE MINERALS, FE-RICH COATINGS ON MAGNETITE AND OTHER FE-OXIDES, HEMATITE(?) AFTER PYRITE
SURFACE DEPOSITION OR FIXATION OF Pb
FRACTURES AND CLEAVAGE SURFACES ON ALL MINERALS
NON-MINERAL SITES
LABILE Pb's NOT YET MIXED
WELL-MIXED POOL Pb's
SECONDARY MINERALS INCORPORATING POOL Pb's
BISMUTITE, BISMUTHINITE, EPIDOTE
ADJACENT ROCK
LAWLER PEAK GRANITE #1 SAMPLE
Pb EXCHANGERS (INCLUDING LOSERS)
BRANNERITE(?), APATITE
RADIOGENIC Pb LOSERS
ZIRCON, XENOTIME, MONAZITE, THORITE, COFFINITE(?), BRANNERITE(?)
PRIMARY RADIOACTIVE MINERALS

Figure 86

Returning to the distribution diagram in Figure 86, the right side of the rectangle is occupied by a class of lead sites designated non-mineralogical because they appear to be sites on surfaces rather than within the structurally continuous masses of each crystal.

Two of these non-mineralogical categories represent exogenous leads deposited on grain surfaces. One category includes the iron-rich haloes around radioactive minerals that are described and illustrated in this report, in which haloes EMP scan photographs reveal localized lead, as well as uranium and thorium fixation. Also in this category are dark films, apparently iron-rich, associated with the opaque oxides such as magnetite, in which significant quantities of leachable pool leads are fixed.

A separate non-mineralogical category includes deposition or fixation sites on the fracture and cleavage surfaces of the major minerals with little apparent iron staining. The chemical state of lead in this site is not yet understood. The leach experiments on "clean" alkali feldspar-quartz concentrates demonstrated the presence of pool leads on this type of site.

In both of these categories of surface sites, the presence of labile uranium and thorium has been confirmed. Therefore, it appears these surface sites may also contain a component of radiogenic lead generated in situ which may be distinguishable from the exogenous leads.

Completing the fourth side of the rectangle in Figure 86 is a class of secondary minerals formed during post-crystallization episodes, which owe their leads primarily to incorporation from the pool reservoir. Bismutite-bismuthinite and epidote seem to fall into this category.

Central to understanding the lead distribution in this rock is the concept of a geochemical history in which lead mobility has played a significant role. Therefore in the center of the rectangular distribution of various categories of lead sites in Figure 86 are concentric representations of the range of labile leads which appear to have moved through the rock. The outer circular zone represents the diverse compositions of labile leads derived from different individual mineral species and sites and contributed to the overall mobile lead reservoir. The central circular region represents the remarkably well-mixed pool leads which were synthesized during at least two different episodes of the general hydrothermal? circulation. Those events extracted leads from many radioactive accessory minerals, integrated them in a consistent manner, and then dispersed them throughout the entire granite sample.

From our present investigation, we cannot define the volume of rock from which the pool leads identified in this work were mobilized, mixed and redeposited. Our sample was extracted from a block less than 0.1 m^3 in volume. While we may have contributed some mechanical homogenization during sample preparation, several lines of evidence indicate earlier geochemical homogenization extended outside the sampled volume for an undefined distance. In the upper left part of Figure 86 we recognize this degree of extended lead communication, without having established any control on its dimensions in space, or an adequate understanding of the magnitude of the interactions. We feel that given our present stage of progress, it is practical to contemplate these questions in future work.

A summary statement on the mobile leads in this sample should note that on the order of seventy-five percent of the radiogenic lead, both uranogenic and thorogenic, has been mobilized out of the radiogenic accessory minerals. Extensive circulation, mixing and exchange of these leads has occurred in two distinct episodes with the formation of some significant new secondary mineral hosts for labile lead. The most significant lead reservoirs in the post-crystallization history, pool leads, are distinctive and ubiquitous. Their recognition and interpretation are essential to achieve successful application of the isotopic relations which previous workers have used to consider uranium and thorium mobility in granites.

Mobile Uranium and Thorium

One of the principal objectives of this study has been to evaluate the responsiveness of the primary uranium and thorium endowment of this granite to possible mobilization during various secondary processes. We have established that lead has been extraordinarily mobile within the limits of the sample volume on the scale of micrometers to centimeters or tens of centimeters, but we have made no unique demonstration of net lead loss, gain or exchange, as yet.

Application of the same type of analysis as that applied to lead is not possible for uranium and thorium because those elements lack the distinctive isotopic signatures which permit the characterization of variable radiogenic and initial leads. We must rely on evidence for, and interpretation of, the chemical association of Pb, U and Th in the various mineralogical and nonmineralogical sites. Because of these elements' different chemistries, fractionation of lead relative to uranium and thorium, and thorium relative to uranium is generally to be expected in any significant geochemical process. In addition, laboratory chemical extractive processes such as the oxidizing acid leaches we have employed can be quite selective, and may provide a source of biased information on the composition and physical nature of a given site. Therefore, a suitably cautious approach must be applied to the observations reported here.

What evidence exists for uranium and thorium mobility? On the scale of individual grains or small aggregates of grains, extensive evidence has been found:

1) Textural and chemical evidence for uranium and thorium mobility was developed from EMP scan photographs, which identified uranium and thorium localized in distinctive iron-rich haloes around important radioactive accessory minerals (e.g. Figs. 62d,e; 64c,d; 66b,i; 69b,f). This evidence suggests migration outward from the local uranium and thorium sources on scales of micrometers to millimeters.

2) Crystals of brannerite?, a high-uranium mineral, display prominent progressive uranium depletion outward in several zones, with a slight enrichment in the outermost zone. This variation seems to correlate with other aspects of chemical variations, but does not appear to be a primary characteristic.

3) Thorium has migrated along fractures in thorian coffinite?, as recorded in EMP scan photographs (Fig. 69f). The scale is tens of micrometers.

4) Secondary minerals which clearly have incorporated mobile leads also have significant levels of uranium. Bismutite acquired 3000 ppm of uranium from sources external to its bismuthinite cores (Fig. 73e). Its thorium content is negligible, suggesting either mineralogical discrimination or an altering solution in which only mobilized uranium, but not thorium, was significant. Epidote, another secondary mineral, shows quite similar effects but at much lower concentration levels (Table 18b).

5) Leaches of surfaces of minerals with intrinsically low uranium and thorium levels (fractions of ppm) have yielded acid-soluble uranium and thorium at levels of one to many tens of ppm of the samples leached (Table 18c). If successful mineral separation was achieved for the clean quartz-feldspar concentrate and the magnetite concentrate, then introduced labile uranium and thorium dominates these phases. The scale of migration must be at least millimeters to centimeters.

6) The various types of apatite crystals separated and analyzed displayed levels of uranium no higher than the bulk rock. This is incompatible with many observations and laboratory demonstrations that apatite has significant positive distribution coefficients for uranium in silicate melts. It is inferred that uranium, and perhaps thorium, has been leached or exchanged from apatite in this sample subsequent to crystallization. Assuming a reasonable distribution coefficient, one can suspect a loss of as much as 90 percent of the primary uranium occurring on a scale of hundreds of micrometers.

We find a pervasive body of data which shows that both uranium and thorium have been mobile on the scale of individual crystals and slightly larger scales through the history of the rock. This is perhaps not unexpected for uranium, considering the well-known mobility of hexavalent uranium under various geologic conditions. The quantities of thorium observed in the leaches of magnetite and quartz-feldspar are at least three times greater than those of uranium however. The observed Th/U ratios are much higher than expected from the whole-rock value, or implied by the isotopic composition of the associated radiogenic leads.

Our current leaching studies will provide additional data on the extent of the apparent preferential enrichment of thorium in the acid-leachable sites.

Given a model for a pool of labile leads, well-mixed and therefore implying processes of solution homogenization over a scale of at least tens of centimeters, does this suggest that labile uranium and thorium have participated in the same circulating solution systems? We think the weight of evidence supports extensive actinide element participation in the hydrothermal systems.

The quantities of mobile uranium and thorium, as cautiously interpreted from the quartz-feldspar and magnetite leach data, cannot be dismissed as being insignificant. Using the former body of data and assuming the major salic minerals to represent the lowest background level of dispersed surficial uranium and thorium, it appears from the first leach that a little more than two percent of the whole-rock uranium and a little more than four percent of the whole-rock thorium is in labile sites. The second, much more intense leach added only slightly to the uranium, but brought the thorium up to about seven percent

of the whole-rock level. However, the second leach yielded a lead distinctly more thorogenic than the pool lead of the first leach, and suggests some contribution came from a non-pool mineral site. We would prefer to use the first leach yields as minimum values for labile uranium and thorium. If these values were representative of labile thorium and uranium on all surfaces of the rock, then they might be neglected in material balance calculations. The magnetite leaches demonstrate that for at least some sites, much higher levels of labile uranium and thorium are present. Until we can complete our study of acid-soluble surficial uranium and thorium in the important sites in the rock, we cannot assess accurately the fraction of whole-rock uranium and thorium in labile sites.

Returning to the whole-rock system, we are faced with the contrast in the apparent uranium and thorium behavior in the net balances of the whole-rock isotope systems. Our studies of labile leads showed that most of them (pool leads) have an impressively constant $^{208}Pb/^{206}Pb$ system. The close agreement of the radiogenic $^{208}Pb/^{232}Th$ whole-rock ratio (Table 19a) with the independently confirmed age of the rock, requires either no ^{208}Pb loss or gain in our sample or else its very close coupling with thorium loss or gain. We have no evidence to support the latter special situation; it cannot be completely ruled out.

If no ^{208}Pb has been lost or gained from the rock, then because $^{208}Pb/^{206}Pb$ is so uniform in the labile leads, no selective uranogenic lead loss or gain seems reasonable. Then the discrepancy represented by an excessive $^{206}Pb/^{238}U$ whole-rock value seems to be logically resolved by accepting a 24 percent uranium loss (5 μg/g) from the primary igneous system.

Until other evidence is found, it would appear that lead and thorium migrations are limited to scales of micrometers to centimeters, perhaps to meters at most, while labile uranium is much more wide ranging. A geochemical explanation for the close similarity of the active, but apparently limited, mobilities of lead and thorium still must be developed and tested.

Implications for Uranium Resources

It appears that in two specific episodes, 75 and 230 m.y. ago, the Lawler Peak Granite #1 sample lost about a fourth of its uranium. If the magnitude of loss extends to the entire pluton, then the raw material for significant uranium deposits was mobilized (up to 100,000 tonnes from the top 400 m of granite). The possibility that the nearby uranium mineralizations were emplaced at one of these times can now be tested.

More basic implications are to be found in the new insights into the processes which affect uranium and thorium distribution during crystallization of granitic magmas and into the susceptibilities of the diverse primary minerals hosting uranium to certain types of post-crystallization alteration. These insights can and will be tested on other samples from this pluton, and from other granite plutons, for more general validation. They appear to be fundamental to the improvement of several aspects of our current geochemical models for uranium fixation and mobilization.

REFERENCES

Aero Service (1979). Airborne gamma-ray spectrometer and magnetometer survey, Las Vegas, Williams, Prescott, and Kingman Quadrangles (Arizona). GJBX-59(79) (two volumes).

Aldrich, L. T., Wetherill, G. W., Davis, G. L. and Tilton, G. R. (1958). Radioactive ages of micas from granitic rocks by Rb-Sr and K-Ar methods. Trans. Amer. Geophys. Union 39, pp. 1124-1134.

Altschuler, Z. S., Clarke, R. S., Jr. and Young, E. J. (1958). Geochemistry of uranium in apatite and phosphorite. U.S. Geol. Survey Prof. Paper 314-D, 90 p.

Anderson, C. A., Scholtz, E. A. and Strobell, J. A., Jr. (1955). Geology and ore deposits of the Bagdad area, Yavapai County, Arizona. U.S. Geol. Survey Prof. Paper 270, 103 p.

Anderson, C. A., Blacet, P. H., Silver, L. T. and Stern, T. W. (1971). Revision of Precambrian stratigraphy in the Prescott-Jerome area, Yavapai County, Arizona. U.S. Geol. Survey Bull. 1324-C, pp. C1-C16.

Anderson, C. A. and Silver, L. T. (1976). Yavapai series - a greenstone belt. Arizona Geol. Soc. Digest, X, pp. 13-26.

Banks, P. O. (1963). Some systematics of uranium and lead distribution in relation to the petrology of the Mt. Rubidoux granites, Riverside County, California. Unpublished Ph.D. thesis, California Institute of Technology.

Banks, P. O. and Silver, L. T. (1964). Material balance in the whole rock U-Pb system of a young granite (abs.). Trans. Amer. Geophys. Union, 45, p. 108.

Banks, P. O. and Silver, L. T. (1966). Evaluation of the decay constant of uranium 235 from lead isotope ratios. Jour. Geophys. Res., 71, pp. 4037-4046.

Brown, H., Blake, W. J., Chodos, A. A., Kowalkowski, R., McKinney, C. R., Neuerburg, G. J., Silver, L. T. and Uchiyama, A. (1953a). Geochemical aspects of interstitial material in igneous rocks (abs.). Geol. Soc. Amer. Bull., 69, p. 1400.

Brown, H., Blake, W. J., Chodos, A. A., Kowalkowski, R., McKinney, C. R., Neuerburg, G. J., Silver, L. T. and Uchiyama, A. (1953b). Leaching studies of interstitial material in igneous rocks (abs.). Geol. Soc. Amer. Bull. 69, pp. 1400-1401.

Brown, H. and Silver, L. T. (1956). The possibilities of obtaining long-range supplies of uranium, thorium and other substances from igneous rocks. U.S. Geol. Survey Prof. Paper 300, pp. 91-95.

Butler, A. P., Jr., (1972). Uranium; in Mallory, W. W. (ed.) Geologic Atlas of the Rocky Mountain Region, pp. 315-317, Hirschfeld, Denver.

Damon, P. E. and Mauger, R. L. (1966). Epeirogeny-orogeny viewed from the Basin and Range Province. A.I.M.E. Transactions, 235, pp. 99-112.

Jaffey, A. H., Flynn, K. F., Glendenin, L. E., Bentley, H. W. and Essling, A. M. (1971). Precision measurements of half-lives and specific activities of ^{235}U and ^{238}U. Phys. Rev. C., 4, pp. 1889-1906.

Krieger, M. H. (1965). Geology of the Prescott and Paulden quadrangles, Arizona. U.S. Geol. Survey Prof. Paper 467, 127 p.

Larsen, E. S., Jr. (1948). Batholithic and associated rocks of Corona, Elsinore, and San Luis Rey quadrangles, southern California. Geol. Soc. Amer. Memoir, 29, 182 p.

Larsen, E. S., Jr., Phair, G. P., Gottfried, D. and Smith, W. L. (1956). Uranium in magmatic differentiation. U.S. Geol. Survey Prof. Paper 300, pp. 65-74.

Le Roux, L. J. and Glendenin, L. E. (1963). Half-life of ^{232}Th, Proc. Natl. Meet. on Nuclear Energy, Pretoria, South Africa, pp. 83-94.

Livingston, D. E. (1969). Geochronology of older Precambrian rocks in Gila County, Arizona. Doctoral Dissertation, University of Arizona, 224 p.

Livingston, D. E., Mauger, R. L. and Damon, P. E. (1968) Geochronology of the emplacement, enrichment and preservation of Arizona porphyry copper deposits. Econ. Geol., 63, pp. 30-36.

Ludwig, K. R. and Silver, L. T. (1977). Lead isotope inhomogeneity in Precambrian igneous K-feldspars. Geochim. Cosmochim. Acta, 41, pp. 1457-1471.

Ludwig, K. R. and Stuckless, J. S. (1978). Uranium-lead isotope systematics and apparent ages of zircon and other minerals in Precambrian granitic rocks, Granite Mountains, Wyoming. Contr. Min. Petr., 65, pp. 243-254.

Manhes, A., Minster, J. F. and Allègre, C. J. (1978). Comparative uranium-thorium-lead and rubidium-strontium study of the Saint Sèverin Amphoterite: Consequences for early Solar System chronology. Earth Planet. Sci. Lett., 39, pp. 14-24.

Picciotto, E. E. (1950). Distribution de la radioactivité dans les roches eruptives. Soc. Belge Geologie Bull., 59, pp. 170-198.

Pierce, H. W., Keith, S. B. and Wilt, J. C. (1970). Coal, oil, natural gas and uranium in Arizona. Arizona Bur. Mines Bull., 182, 289 p.

Ransome, F. L., (1903). Geology of the Globe copper district, Arizona. U.S. Geol. Survey Prof. Paper 12, 168 p.

Rosholt, J. N. and Bartel, J. A. (1969). Uranium, thorium and lead systematics in the Granite Mountains, Wyoming. Earth Planet. Sci. Lett., 7, pp. 141-147.

Rosholt, J. N., Zartman, R. E. and Nkomo, I. T. (1973). Lead isotope systematics and uranium depletion in the Granite Mountains Wyoming. Geol. Soc. Amer. Bull., 84, pp. 989-1002.

Silver, L. T. (1963). The relation between radioactivity and discordance in zircons. Nat. Acad. Sci. Publ. 1075, pp. 34-39.

Silver, L. T. (1966). U-Pb isotope relations and their historical implications in Precambrian zircons from Bagdad, Arizona (abs.). Geol. Soc. Amer. Spec. Paper 101, p. 420.

Silver, L. T. (1967). Apparent relations in the older Precambrian stratigraphy of Arizona. in "Geochronology of Precambrian stratified rocks": abstracts of papers from a conference Dept. Geol., Univ. Alberta; Burwash, R. A. and Morton, R. D., eds., p. 87.

Silver, L. T. (1968a). Precambrian batholiths of Arizona (abs.). Geol. Soc. Amer. Spec. Paper 121, pp. 558-559.

Silver, L. T. (1968b). Annual Rept. to USAEC. Contract Cal T-AT (04-3)-767.

Silver, L. T. (1976). A regional uranium anomaly in the Precambrian basement of the Colorado Plateau. Geol. Soc. Amer. Abstracts with Programs, pt. 8, pp. 1107-1108.

Silver, L. T. and Deutsch, S. (1963). Uranium - lead isotopic variations in zircons: a case study. Jour. Geology, 71, pp. 721-758.

Silver, L. T., Mc Kinney, C. R., Deutsch, S. and Bolinger, J. (1963). Precambrian age determinations in the western San Gabriel Mountains, California. J. Geology, 71, pp. 196-214.

Silver, L. T., Anderson, C. A., Crittenden, M. and Robertson, J. M. (1977a). Chronostratigraphic elements of the Precambrian rocks of the southwestern and far western United States (abs.). Geol. Soc. Amer. Abstracts with Program, pt 9, p. 1176.

Silver, L. T., Bickford, M. E., Van Schmus, W. R., Anderson, J. L., Anderson, T. H. and Medaris, L. G., Jr. (1977b). The 1.4 - 1.5 b.y. transcontinental anorogenic plutonic perforation of North America. Geol. Soc. Amer. Abstracts with Program, pt 9, pp. 1176-1177.

Silver, L. T., Taylor, H. P., Jr. and Chappell, B. W. (1979). Some petrological, geochemical and geochronological observations of the Peninsular Ranges batholith near the international border of the U.S.A. and Mexico. in Mesozoic Crystalline Rocks, ed. P. L. Abbott and V. R. Todd, Manuscripts and road logs prepared for the Geol. Soc. Amer. Annual Meeting, San Diego. Dept. of Geol. Sciences, San Diego State University. pp. 83-110.

Steiger, R. H. and Jäger. E. (1977). Subcommission on Geochronology: Convention on the use of decay constants in geo- and cosmochronology. Earth Planet. Sci. Lett., 36, pp. 359-362.

Stuckless, J. S. and Nkomo, I. T. (1978). Uranium - lead isotopic systematics in uraniferous alkali-rich granites from the Granite Mountains, Wyoming: Implications for uranium source rocks. Econ. Geol., 73, pp. 427-441.

Stuckless, J. S. and Nkomo, I. T. (1980). Preliminary investigations of U-Th-Pb systematics in uranium-bearing minerals from two granitic rocks from the Granite Mountains, Wyoming. Econ. Geol., 75, pp. 289-295.

Tatsumoto, M. (1966). Isotopic compositions of lead in volcanic rocks from Hawaii, Iwo Jima, and Japan. J. Geophys. Res., 71, pp. 1721-1733.

Tilton, G. R., Patterson, C. C., Brown, H., Inghram, M., Hayden, R., Hess, D. and Larsen, E. S., Jr. (1955). Isotopic compositions and distribution of lead, uranium and thorium in a Precambrian granite. Geol. Soc. Amer. Bull., 66, pp. 1131-1148.

Wetherill, G. W. (1956). Discordant uranium-lead ages, I. Trans. Amer. Geophys. Union, 37, pp. 320-326.

Williams, I. S. and Silver, L. T. (1979). The U-Th-Pb system compared in coexisting zircon, monazite and xenotime (abs.). Trans. Amer. Geophys. Union, 60, p. 411.

Zartman, R. E. (1979). U, Th and Pb concentrations and lead isotopic composition of biotite granodiorite (sample 9527-2b) from LASL drill hole GT-2. Los Alamos Scientific Laboratory Report LA-7923-MS, 18 p.